EarthCARE JAXA

Level 2 Algorithm Theoretical Basis Document

(L2 ATBD)

December 2025

EARTHCARE

NICT JAXA
宇宙航空研究開発機構
Japan Aerospace Exploration Agency

Document Change Record

Revision	Date	Description of Changes
NC	18 January 2012	Baseline release
A	13 November 2012	Updated according to JFY2011 activity
B	September 2013	Updated according to JFY2012 activity
C	February 2015	Updated according to JFY2013 activity
D	December 2015	Updated according to JFY2014 activity
E	January 2017	Updated according to JFY2015 activity
F	January 2018	Updated according to JFY2016 activity
G	February 2019	Updated according to JFY2017 activity
H	September 2020	Updated according to JFY2018 activity
J	November 2021	Updated according to JFY2019 activity
K	January 2023	Updated according to JFY2021 activity
L	May 2024	Updated according to JFY2022 and JFY2023 activity
M	March 2025	Updated according to L2 data release
N	December 2025	Update for L2 major update and data release of ACM_CLP and ALL_RAD [3.1.1 CPR_ECO] - 3.1.1.2.1 3) AW3D DEM added - 3.1.1.2.1 7) mirror echo flag updated [3.2 ATL_CLA] - 3.2.1.3 Description of feature mask detection (aerosol, cloud or surface) added [3.3 MSI] - Table 3.3.1.3.1.2.1 and Table 3.3.1.4.2.1: solar zenith angle expanded to 80 degrees. - 3.3.1.4 Ice cloud properties replaced in the chapter of standard product 3.3.1. - 3.3.1.5 vicarious calibration added [4.4 All Four Sensor Synergy] - 4.4.1.1 and 4.4.1.2 updated.

EARTHCARE

NICT JAXA
宇宙航空研究開発機構
Japan Aerospace Exploration Agency

		- Figure4.4.2 added
		[6 Auxiliary Product]
		- Description added

Contents

Authors

Teruyuki Nakajima

Affiliation: Affiliation: Earth Observation Research Center, Japan Aerospace Exploration Agency

E-mail: nakajima.teruyuki@jaxa.jp

Sections: 1

Maki Kikuchi

Affiliation: Earth Observation Research Center, Japan Aerospace Exploration Agency

E-mail: kikuchi.maki@jaxa.jp

Sections: 2

Yuichi Ohno and Hiroaki Horie

Affiliation: Radio Research Institute, National Institute of Information and Communications Technology

E-mail: horie@nict.go.jp (corresponding author)

Sections: 3.1.1, 3.1.3

Hajime Okamoto

Affiliation: Research Institute of Applied Mechanics, Kyushu University

E-mail: okamoto@riam.kyushu-u.ac.jp

Sections:3.1.2, 3.1.4, 4.1, 4.3.1

Tomoaki Nishizawa

Affiliation: Center for Environmental Measurement and Analysis, National Institute for Environmental Studies

E-mail: nisizawa@nies.go.jp

Sections: 3.2, 4.2

Takashi Y. Nakajima

Affiliation: Research and Information Center, Tokai University,

E-mail: nakajima.takashi@tokai.ac.jp

Sections: 3.3.1, 3.3.2.2, 4.3.2

Kentaroh Suzuki,

Affiliation: Atmosphere and Ocean Research Institute, University of Tokyo

E-mail: ksuzuki@aori.u-tokyo.ac.jp

Sections: 3.3.2.3, 4.4

Masaki Satoh,

Affiliation: Atmosphere and Ocean Research Institute, University of Tokyo

E-mail: satoh@aori.u-tokyo.ac.jp

Sections: 5

Takuji Kubota,

Affiliation : Earth Observation Research Center, Japan Aerospace Exploration Agency

E-mail : kubota.takuji@jaxa.jp

Section : 6

1. Introduction

Earth observation by satellites is an important tool for us to investigate the earth's climate system perturbed by human activities such as global warming phenomenon and global air pollution phenomenon. The original concept of the EarthCARE (Earth Clouds, Aerosols and Radiation Explorer) satellite was built in 1990s when a new cloud profiling radar (CPR) technology became available. The CPR can detect cloud particles with its high frequency microwave radar pulse to measure the cloud stratification. The first satellite-borne CPR was proposed as the ESA's Earth Radiation Mission (ERM) in early 90s. Japanese ATMOS-B1 mission was also proposed as a project of JAXA's (Japan Aerospace Exploration Agency's) MDS (Mission Demonstration Satellite) program in mid-90s.

After these first generation mission proposals, the EarthCARE mission has been finally approved in 2006 in Europe and in 2007 in Japan for the Phase-B study of the third Earth Explorer core mission. This mission is a joint ESA (European Space Agency) -JAXA-NICT (National Institute of Information and Communications Technology) mission to carry a CPR and an atmospheric backscatter lidar (ATLID) on the same satellite platform accompanied by a multi-spectral imager (MSI) and a broadband radiometer (BBR). This package is the most advanced one to measure the vertical stratification of the atmosphere with clouds and aerosols. CPR and ATLID will measure the vertical stratification of the atmosphere. This capability is especially important to understand the phenomenon of aerosol and cloud interaction. MSI and BBR will add the information of horizontal distribution of aerosol and cloud and of broadband radiative fluxes. One of important tasks of the EarthCARE is to provide useful data to reduce the uncertainty in evaluation of the radiative forcing of aerosols and clouds. This will bring an enormous benefit for increasing a modeling ability of cloud and aerosol-laden atmospheres. The NICT's new technology of Doppler velocity sensing is another innovation of the EarthCARE platform that will produce a new data set of global cloud particle motion data.

This new mission is a good opportunity for the Japanese community to make a capacity building for the atmospheric science after the disastrous accidents of ADEOS-I and -II shutdown. We wish this innovative mission to lead us to the new remote sensing era.

In May 2008, the EarthCARE Mission Advisory Group of Japan drafted the Japanese science plan for the EarthCARE mission to present important science targets for the mission and activities to be performed as Japanese contributions. In March 2009, the draft version of the Algorithms Theoretical Basis Document (ATBD) was added by the EarthCARE Mission Advisory Group of Japan to present algorithms to be used in the mission product generation as Japanese activities. The NC version of the ATBD was officially released from JAXA in January 2012.

The purpose of the "EarthCARE JAXA Level 2 Algorithm Theoretical Basis Document" is to document the concept and the detailed description on the algorithms of the EarthCARE Level 2 products that JAXA is in responsible to develop. It also includes the description on the signal simulator of the sensors onboard EarthCARE, called "Joint-Simulator".

2. EarthCARE platform and the JAXA Product List

The EarthCARE platform is being developed by ESA.   The list of the orbit parameters during the nominal phase of the mission is given in Table 3.1.   JAXA and NICT are in charge of developing CPR system, whereas ESA is responsible for the development of ATLID, MSI and BBR systems.

Table 3.1 EarthCARE Nominal Orbit Parameter

Orbit Parameter	Nominal Orbit
Repeat Cycle [days]	25
Orbit Period (nodal) [s]	5552.7
Semi major axis [km]	6771.28
Eccentricity	0.001283
Inclination [°]	97.050
MLST Descending Node [hr]	13:45-14:00
Argument of perigee [°]	90.0
Means Semi-major axis Altitude [km]	393.14
Minimum Geodetic Altitude [km]	398.4
Maximum Geodetic Altitude [km]	426.0
Means Geodetic Altitude [km]	408.3

There are four sensors onboard the EarthCARE, each of which are designed to follow the following strategy:

- An Atmospheric Lidar (ATLID): to retrieve vertical profiles of aerosol physical parameters and, in synergy with the cloud profiling radar, vertical profiles of cloud physical parameters.
- A Cloud Profiling Radar (CPR): to retrieve micro- and macroscopic parameters of clouds and the vertical velocity of cloud particles.
- A Multi-Spectral Imager (MSI): to provide information of the horizontal structure of cloud fields in   support of the vertical profiles measured by the active instruments.
- A BroadBand Radiometer (BBR): to measure short-wave and total-wave (i.e. total wave = short-wave + long-wave) fluxes at the TOA.   Short-wave and derived long-wave considered to be used as a cross-check of the radiative flux derived from the cloud-aerosol profiles measured by the active instruments.

Regarding the development framework of EarthCARE scientific products, i.e. Level 2 products, JAXA and ESA agreed to develop their own products respectively. In this way, in case of failure in either algorithm of the agencies, EarthCARE mission may secure an alternative algorithm to derive scientifically important parameters.   In addition, keeping the algorithm development in Japanese science community will maintain and cultivate the techniques of the remote sensing

analysis in the country.   Despite the independency of the Level 2 product retrievals, JAXA and ESA will share the updates of the algorithm development on a regular basis.

Figure 3.1 and 3.2 is the list of the products that JAXA is planning to develop.   The strategy of JAXA's product development is to allot the respective products to either "Standard Product" or "Research Product", depending on the feasibility of the products.   The differences in the Standard Product and the Research Products are;

- Standard Product (ST)
    1. Majority of the algorithms in the Standard Products already being well researched and has heritage from past studies
    2. Strongly promoted to be developed and released
    3. Data that are decided to be released will be processed and released from JAXA Mission Operation System

- Research Product (ER/LR)
    1. The algorithms in the Research Products consists of new research development that are challenging, yet scientifically valuable
    2. Promoted to be developed and released
    3. Data that are decided to be released will be processed and released from either JAXA Earth Observation Research Center and/or Japanese Institute/Universities

Standard Product

Sensor	Process. Level	Product	Priimary Parameter	Grid Spacing		Spatial Resolution		Release Accuracy	Standard Accuracy	Target Accuracy
				Horizontal	Vertical	Horizontal	Vertical			
CPR	L1b	CPR one-sensor Received Echo Power Products and Doppler Product	Received Echo Power	0.5km	0.1km	0.765km*3 (Cross-track) 0.840km*3 (Along-track)	0.5km	＜4.7dB	＜2.7dB	–
			Radar Reflective Factor					＜4.7dB	＜2.7dB	＜2.7dB
			Surface Radar Cross Section		–		–	–	–	–
			Doppler Velocity/Covariance of Pulsepair/Spectrum Width		0.1km		0.5km	–	≦1.3m/s (Doppl. Vel)	＜0.2m/s (Doppl. Vel)
CPR	L2a	CPR one-sensor Echo Product	Integrated Radar Reflective Factor/Integrated Doppler Velocity/Gas Correction Factor	1km	0.1km	1km/10km	0.5km	–	≦1.3m/s (Int. Doppl. Vel.)	＜0.2m/s (Int. Doppl. Vel.)
CPR	L2a	CPR one-sensor Cloud Products	Cloud Mask	1km	0.1km	1km/10km	0.5km	±30%	±10%	±5%
			Cloud Particle Type					±100%	±50%	±20%
			Reff./LWC/IWC					–	±100% (LWC)	±50% (LWC)
			Optical Thickness					–	±100%	±50%
ATLID	L2a	ATLID one-sensor Cloud Aerosol Poducts	Feature Mask	L1b min. unit/1km	0.1km	L1b min. unit/1km/10km	0.1km	±100%	±40%	±10%
			Target Mask	1km		1km/10km		±100%	±40%	±10%
			Aerosol Extinction Coeff./Backscat. Coeff./Lidar Ratio/Dep. Ratio			10km		±60%/±90%, ±150%/±150%	±40%/±70%, ±110%/±130%	±20%/±50%, ±70%/±100%
			Cloud Extinction Coeff./Backscat. Coeff./Lidar Ratio/Dep. Ratio			1km/10km		±50%/±90%, ±140%/±150%	±30%/±70%, ±100%/±130%	±15%/±50%, ±65%/±100%
			Planetary Boundary Layer Height		–		–	±500m	±300m	±100m
MSI	L2a	MSI one-sensor Cloud Poducts	Cloud Flag/Cloud Phase	0.5km	–	0.5km	–	±15% Ocean ±20% Land	±15%	±10%
			Optical Thickness of Liquid Cloud					±10%	±100% (Converting to LWP)	±50% (Converting to LWP)
			Reff. of Liquid Cloud					±30%		
			Cloud Top Temp./Pressure/Altitude					±1K (CTT)	±3K (CTT)	±1.5K (CTT)
CPR + ATLID	L2b	CPR-ATLID synergy Cloud Poducts	Cloud Mask/Cloud Particle Type	1km	0.1km	1km/10km	0.5km	–	root mean square of errors of one-sensor products	–
			Reff./LWC/IWC					–		±2μm(water)/ ±20%/±30%
			Optical Thickness		–		–	–		–
CPR + ATLID + MSI	L2b	CPR-ATLID-MSI synergy Cloud Poducts	Cloud Mask/Cloud Particle Type	1km	0.1km	1km/10km	0.5km	–	root mean square of errors of one-sensor products	–
			Reff./LWC/IWC					–		±2μm(water)/ ±20%/±30%
			Optical Thickness		–		–	–		–
CPR+ ATLID+ MSI+BBR	L2b	Four-sensors Synergy Radiative Products	SW/LW Radiative Flux	10km*2	–	10km	–	–	±25W/m2	±10W/m2
			SW/LW Radiative Heating Rate		0.5km*2		0.5km	–	–	–

Auxilary Product

Sensor	Process. Level	Product	Priimary Parameter	Grid Spacing	
				Horizontal	Vertical
CPR	Aux	ECMWF CPR Grid Product	Temperature/Specific Humidity (CPR Grid)	1km	0.1km
			Pressure（CPR Grid）	–	0.1km
			Surface Pressure/2m Temperature (CPR Grid)	1km	–
ATLID	Aux	ECMWF ATLID Grid Product	Temperature/Specific Humidity/Ozone Mass Ratio（ATLID Grid）	1km	0.1km
			Pressire（ATLID Grid）	–	0.1km
			Total Column Ozone/10m U-Velocity/ 10m V-Velocity（ATLID Grid）	1km	–
MSI	Aux	ECMWF MSI Grid Product	Temperature/Specific Humidity (MSI Grid)	10km	25 layers*1
			Pressure（MSI Grid）	–	25 layers*1
			Total Column Ozone/10m U-Velocity/ 10m V-Velocity/Surface Pressure/ Skin Temperature（MSI Grid）	10km	–

The accuracy is defined using the "Pixel Integration Length" in red italic numbers.
The accuracies of CPR L1b are defined by 10km integration.
Those accuracies except for CPR are assumed under the condition that sensors developed by ESA functioned as expected.
The accuracies of ATLID is based on the information before the change of specifications.
The length of a scene is defined as the length of an orbit divided equally.
CPR-ATLID-MSI Synergy Cloud Products and Four Sensors Synergy Radiation Budget Products are the final goal of the EarthCARE mission.
Therefore, they are defined as the standard products, although they will be released one year after the start of MOP.
NRT and Statistics （L2c) will be adjusted approopreately by taking user's needs into account.
*1 : Depends on the resolution of ECMWF data that JAXA will receive by the time of launch
*2 : The values shown are defined at the time of JAXA CDR. In future, the values may change if there are strong scientific requirements.
*3 : The values shown are defined when anntenna beam width was 0.095 degrees and satellite altitude was 460km.

Fig 3.1 JAXA Standard and Auxiliary Product List

EARTHCARE

NICT JAXA
宇宙航空研究開発機構
Japan Aerospace Exploration Agency

Research Product

Sensor	Process. Level	Product	Priimary Parameter	Grid Spacing	
				Horizontal	Vertical
CPR	L2a	CPR One-sensor Doppler Product	Doppler velocity correction value (considering inhomogeneity)/ Doppler velocity unfolding value	1km/10km	0.5km
		CPR One-sensor Rain and Snow Product	LWC*/IWC*/Rain Rate/Snow Rate/Attenuation Corrected Radar Reflectivity Factor		
		CPR One-sensor Vertical Velocity Product	Vertical air motion/ Sedimentation Velocity		
ATLID	L2a	ATLID One-sensor Aerosol Extinction Product	Aerosol Extinction Coefficient (Water Soluble/Dust/SS/BC)	10km	0.1km
MSI	L2a	MSI One-sensor Ice Cloud Product	Optical Thickness of Ice Cloud with Reflection method/Effetive Radius of Ice(1.6&2.2μm)/Ice Cloud Top Temperature/Pressure/Altitude	0.5km	–
		MSI One-sensor Aerosol Cloud Product	Aerosol Optical Thickness (Ocean/Land)/ Angst. Exp.		
CPR + ATLID	L2b	CPR-ATLID Synergy Particle Mass Ratio Product	Mass Ratio (2D_Ice/IWC)*	1km/10km	0.5km
		CPR-ATLID Synergy Rain and Snow Product	LWC*/IWC*/ Rain Rate/Snow Rate		
		CPR-ATLID Synergy Vertical Velocity Product	Vertical air motion/ Sedimentation Velocity		
ATLID + MSI	L2b	ATLID-MSI Synergy Aerosol Components Product	Aerosol Extinction Coefficient (Water Soluble/Dust/SS/BC) Mode Radius (Fine mode/Coarse mode)	10km	0.1km
		ATLID-MSI Synergy Aerosol Direct Radiave Forcing Product	Aerosol Direct Radiative Forcing (TOA/BOA)	10km	–
CPR + ATLID + MSI	L2b	CPR-ATLID-MSI Synergy Cloud Doppler Product	Cloud Mask/Cloud Particle Type/Cloud Effective Radius (Water·Ice)/LWC/ IWC(with Doppler)	1km/10km	0.5km
			Optical Thickness/LWP/ IWP(with Doppler)		–
		CPR-ATLID-MSI Synergy Rain and Snow Product	LWC*/IWC*/ Rain Rate/Snow Rate		0.5km
		CPR-ATLID-MSI Synergy Vertical Velocity Product	Vertical air motion/ Sedimentation Velocity		
		CPR-ATLID-MSI Synergy Ice Cloud Product	Ice Effective Radius/Optical Thickness	0.5km	–

The length of a scene is defined as the length of an orbit divided equally.

＊Including with/without Doppler

Fig 3.2 JAXA Research Product List

3. Stand-alone Product
3.1 CPR
3.1.1 Standard Product (CPR Echo Product)
3.1.1.1 Introduction

This section describes the algorithms that provide the Standard Product relating the basic physical correction of the radar reflectivity factor and Doppler information from CPR on EarthCARE.

3.1.1.2 Basic Physical Correction
3.1.1.2.1 Algorithm

Level 1 products of CPR include corrections caused by variation of radar performance and satellite movement. However, the errors caused by physical characteristic of the echo and physical environment still remain in both L1 products (reflectivity and Doppler velocities). So, basic corrections are provided in level 2 algorithms: Clutter echo correction and gas attenuation correction are provided for radar reflectivity, and Doppler unfolding correction is provided for the Doppler velocity. In addition, the warning flags are set such as Clutter echo regions, mirror echo and multiple scattering echo.

1) Horizontal Integration Concept

In CPR L2a processing, both 1-km and 10-km horizontally integrated products are produced from the 500-m horizontally integrated received echo powers and Doppler velocities. Fourteen 500-m horizontally integrated products are provided per second in CPR L1b product as shown in Figure 3.1.1.2.1-1. Note that there is gap time every second in CPR observation mode in order to change pulse repetition frequency and to measure calibration data. So, 1-km and 10-km horizontal integration are defined as follow.

1-km horizontally integrated products are averaged with two successive 500-m integrations, but in order to avoid integration between every 1-second gap time, seven 1-km horizontally integrated products are produced within a second as shown in Figure 3.1.1.2.1-1. Center locations of 1-km horizontal integration are selected to the middle point of two successive L1b products location.
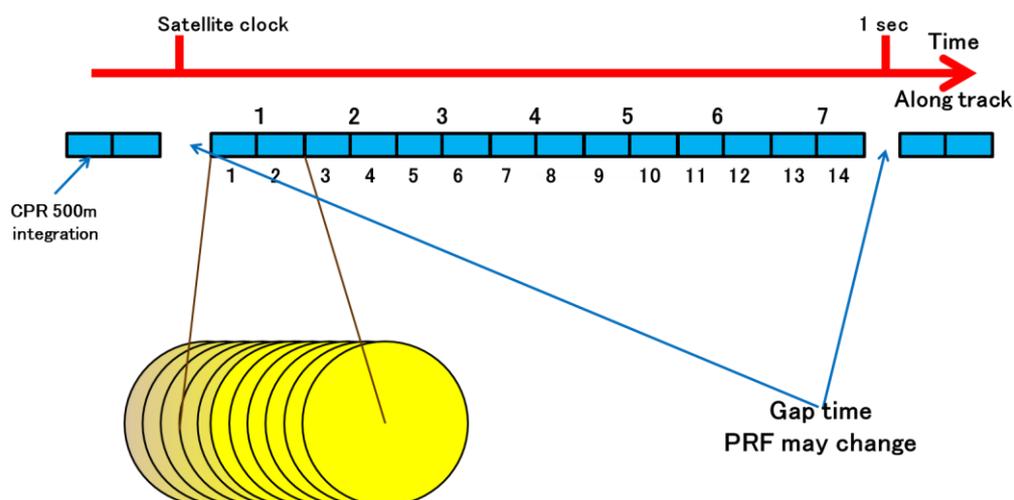
Figure 3.1.1.2.1-1 CPR 1 km Horizontal Integration

Center locations of 10-km horizontal integration are selected to be the same as those of 1-km integration, and 10-km horizontally integrated products are produced every 1 km along track distance using twenty successive 500-m integrations. It means that data across one or two gap time are integrated for 10-km horizontal integration (see Figure 3.1.1.2.1-2).
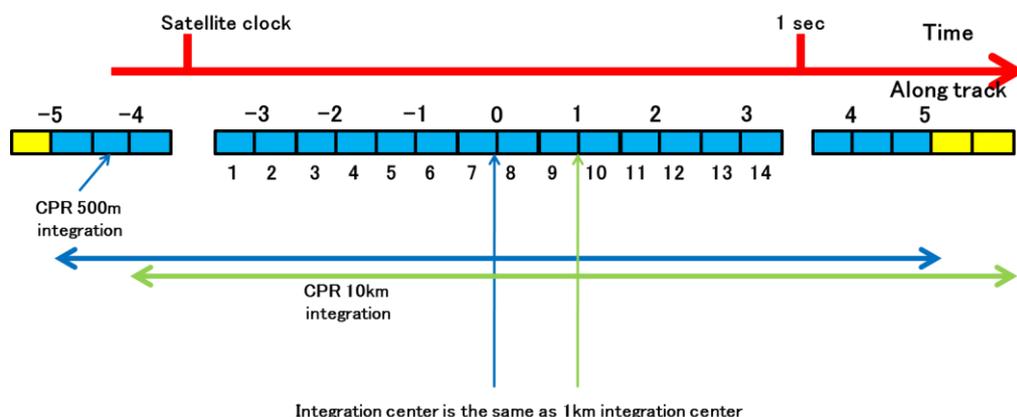

Figure 3.1.1.2.1-2 CPR 10 km Horizontal Integration

2) Integrated radar reflectivity factor products

Following the horizontal integration concept described 1), the 1-km and 10-km integrated radar reflectivity factor products are calculated. Echo signals and noise powers are averaged separately and 1-km and 10-km radar reflectivity factor are produced (see Figure 3.1.1.2.1-3). In case of 10km-avearage reflectivity calculation, since the integrated pulse number of L1b echo power may change at the 1-second gap time, pulse number weighted averages are applied for this calculation. The Signal to Noise ratio is calculated from the ratio of echo and noise power. The quality flags for the radar reflectivity factor products are implemented to show reliability of the radar reflectivity factors.
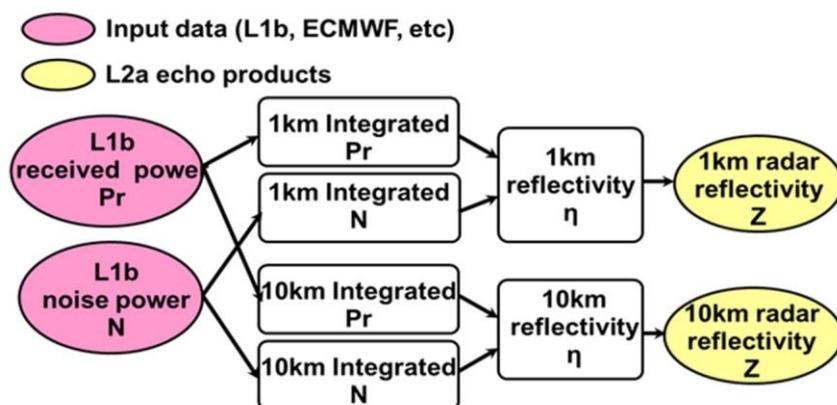

Figure 3.1.1.2.1-3 Processing flow of 1-km and 10-km averaged radar reflectivity factors

3) Surface detection and NRCS (normalized radar cross section)

1-km averaged surface positions (bin number and its fraction) and 1-km averaged NRCS are estimated from the 1-km integrated reflectivity profile calculated above. Roughly calculated ranges between the satellite and the surface calculated by 1-km averaged DEM (Digital Elevation Map) are used for the initial search for surface range. Currently the original DEM resampled by 1km from AW3D 30 DEM and added EGM2008 geoid height is used. L2a_echo products of surface location (bin number and its fraction) and NRCS are computed from the location of the maximum of received echo power around the surface. In the future, the surface detection with a fitting using surface echo patterns will be implemented.

On the other hand, 10-km integrated surface positions and NRCS are average of eleven 1-km integrated surface position and eleven 1-km averaged NRCS around the horizontal center (see Figure 3.1.1.2.1-4).

There is contamination of the strong echo from the surface in the echo power products near the ground surfaces as seen in the CloudSat data. In order to detect cloud echo near the ground as much as possible, similar clutter reduction algorithms is needed, but we expect that the contaminated height from the ground in EarthCRARE is less than that seen in the CloudSat. Clutter echo power products are estimated from the NRCS and the band pass filter feature. If measured echo power at the range near the ground is larger than the estimated clutter echo power, it is possible to detect echo power from the cloud. If measured echo power at the rage near the ground is less than the estimated clutter echo power, the echo power at the range may be caused by the clutter and not by the cloud. Clutter echo algorithm is now waiting for provision of band pass filter feature.

In the algorithm of public release version, since the clutter contamination such as the CloudSat CPR is not observed in the EarthCARE CPR, the clutter reduction algorithm is turned off. It is, however, the strong surface echoes due to the pulse response are observed as the mainlobe clutter so that the judgement of location of the mainlobe edge (called as clutter free bottom) is required to properly detect signals of low-level clouds. The mainlobe regions are located within a range of 500-600 m from the surface, the mainlobe areas are judged from the range-bin at surface to range-bin number at 600 m above the surface. Such results are contained in "integrated_radar_reflectivity_flag_(1km/10km)" and obtained of a bit flag 0x100 (= 256).
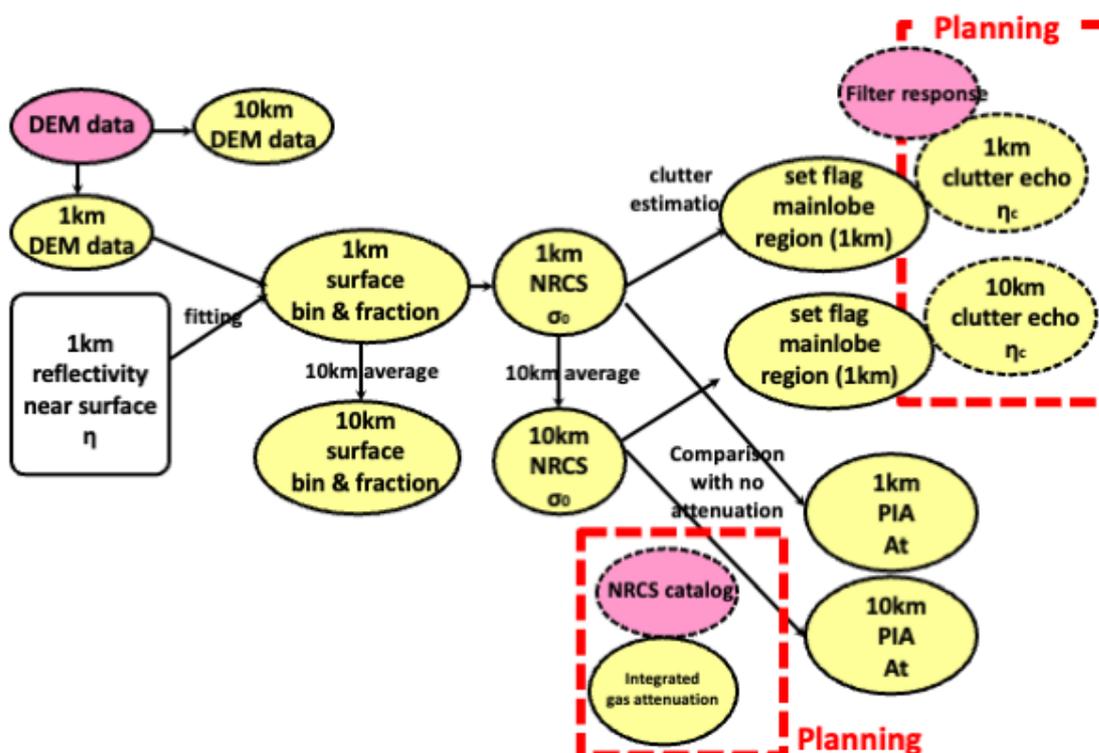
Figure 3.1.1.2.1-4 Processing flow of 1-km and 10-km averaged surface information

4) Horizontally integrated Doppler products

Following the horizontal integration concept described in 1), Doppler velocity products the 1-km and 10-km averaged Doppler velocity products are calculated. Doppler velocity is calculated from 1-km or 10-km integration of the real and imaginary part of the covariance of the pulse-pair processing of 500-m integration. In the case of 1-km integration, pulse repetition frequency (PRF) is always the same because the two 500-m integration products should be in the same one second. Then 1-km averaged Doppler velocity is easily calculated. In the case of 10-km integration, there is a case that twenty 500-m integrated products used different PRF. If two PRF are used in 10-km integration time, we use them of only one PRF, currently. Then 10-km integrated Doppler velocity is calculated with pulse number-weighted average (see Figure 3.1.1.2.1-5). The quality flag for the Doppler velocity products is also implemented.

Maximum Doppler velocity measured by pulse-pair method is defined by PRF. If speed of echo target is above maximum Doppler velocity, echo speed is observed as folded Doppler velocity. For example, in case of 6100 Hz PRF (maximum velocity: 4.8 m/s), 6 m/s of falling Doppler speed is measured as upward 3.6 m/s. The simple unfolding algorithm to avoid discontinuity velocity change normally used by ground Doppler weather radar is difficult to solve folding of isolated clouds. If ambient air velocity is negligibly small, target that exceeds the maximum Doppler velocity is only stronger rain. Then, we developed algorithm to identify strong rainfall from reflectivity and 0 degree-C temperature height and unfold its Doppler velocity. Last year, we found folded Doppler velocity with some heavy rain echo cannot detect because of its heavy rain

attenuation. We are planning to modify this algorithm next year. The estimation quality flag for Doppler velocity, folding correction is also implemented.

Doppler folding also appears with the error caused by the inhomogeneity of reflectivity. This correction method is discussed in the 3.1.2.2.1.
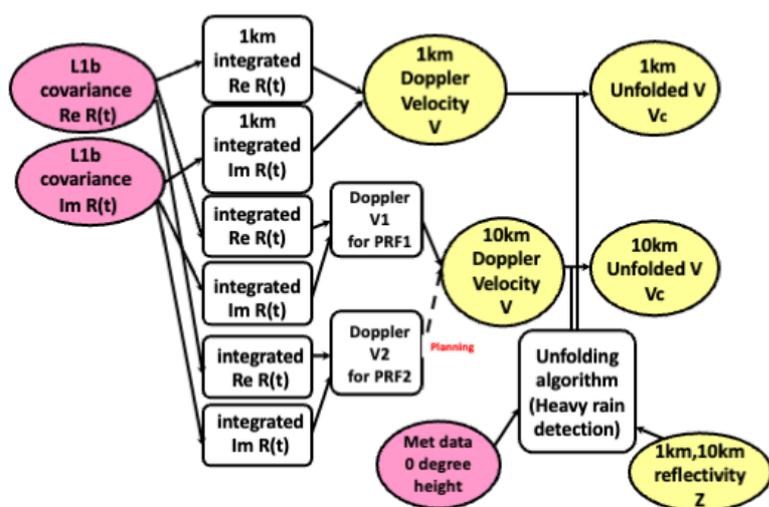

Figure 3.1.1.2.1-5 Processing flow of 1-km and 10-km averaged Doppler velocity

4-1) Horizontally integrated Doppler products with bias correction (temporary products)

Doppler velocity products are contaminated by the line-of-sight velocity due to antenna beam miss pointing for not corrected the effects of satellite attitude error and/or antenna thermal distortion, etc. Until antenna beam miss pointing correction is implemented to these products, the products applied for bias correction using surface velocity before horizontal integration are provided temporally. All integration process is same as 4) described above (see Figure 3.1.1.2.1-5b).
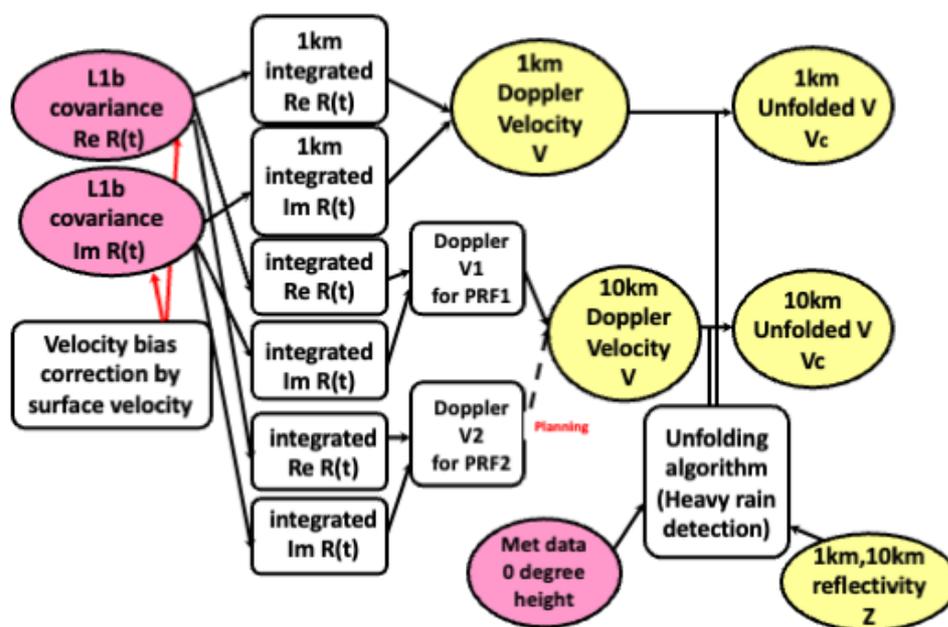
Figure 3.1.1.2.1-5b Processing flow of 1-km and 10-km averaged Doppler velocity with bias correction

5) Gas attenuation correction and PIA (Path Integrated Attenuation)

For the 90 GHz - 100GHz frequency radio wave, it is known as the relatively low absorption by atmosphere. However, the absorption by oxygen and water vapor is not negligible, so propagation loss correction is necessary to estimate the radar reflectivity factor. Pass attenuation products from the top of atmosphere up to each range are estimated from the profiles of water vapor content, air temperature and pressure. These profiles are estimated using data from numerical weather analysis (e.g. ECMWF) and interpolated to CPR grid. The gaseous attenuation at each range is calculated uses the equation described in the reference [Calculation of gaseous attenuation, ITU-R Recommendation P676-13 Annex 1] (see Figure 3.1.1.2.1-6).
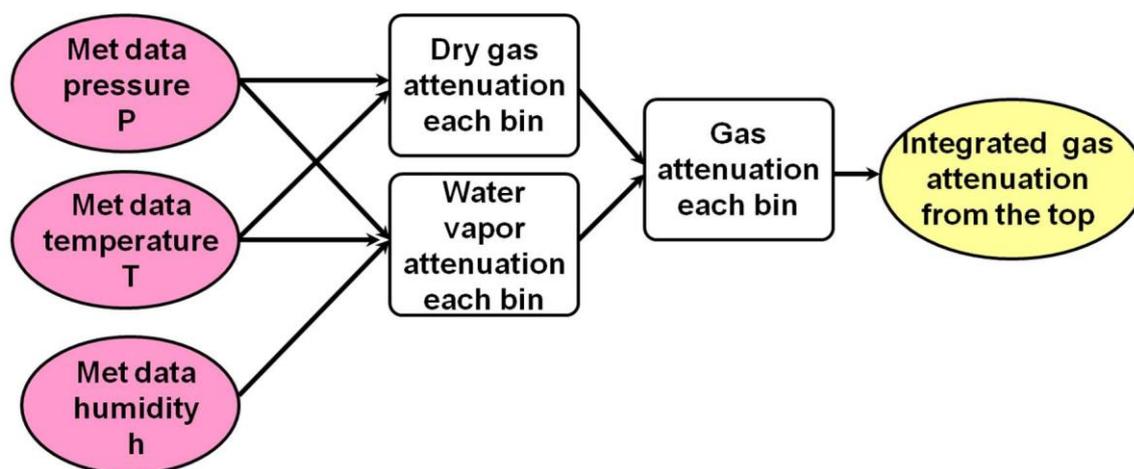
Figure 3.1.1.2.1-6 Processing flow of integrated gas attenuation correction

Estimation of PIA is helpful for estimating hydrometer parameters. Here, the PIA is estimated from the difference in surface echoes outside and within the areas where the surface echoes are attenuated by cloud and precipitation:

$$\text{PIA [dB]} = \sigma_{\text{ref}}^0 \text{ [dB]} - \sigma_m^0 \text{ [dB]}$$

where σ_{ref}^0 is the estimated NRCS in the clear-sky condition, and σ_m^0 is the observed NRCS. To estimate σ_{ref}^0, we plan to implement two methos for estimating σ_{ref}^0 in the algorithm. First one is the temporal reference method that σ_{ref}^0 is estimated from the catalogues of σ_m^0 in the clear-sky condition measured by the CPR. The catalogues are generated as geographical maps (as a function of longitude, latitude, and season) and as surface conditions (ocean surface wind, land surface vegetation, land use, etc.). Second one is the spatial reference method that σ_{ref}^0 is estimated from the neighborhood pixels in the clear-sky condition. Since two methods require the judgement of the clear-sky condition in the algorithm, a simple judgement of cloud and precipitation echoes are implemented. If range-bin where signal-to-noise ratio is higher than 0 dB above the clutter-free bottom and its situation is successively satisfied for 5 range-bins along the range-bin direction, the hydrometeor signals are flagged. Note that since the sampled number of the NRCS catalogue is limited after just the launch of satellite, only the spatial reference method is used in algorithm the first release (see Figure 3.1.1.2.1-4).

6) Reflectivity correction and JSG (Joint Simulator Grid) height conversion

Integrated gas attenuation from the top of the atmosphere calculated above is applied to the 1- km and 10-km radar reflectivity factor. The clutter echo correction is planning to implement as described in 3) for the 1-km and 10-km radar reflectivity factor. Then, reflectivity corrected 1-km and 10-km radar reflectivity factor are obtained. Because the heights of reflectivity and Doppler products are determined by CPR echo sampling bin and they are not the same as JSG height, these products converted to JSG height.
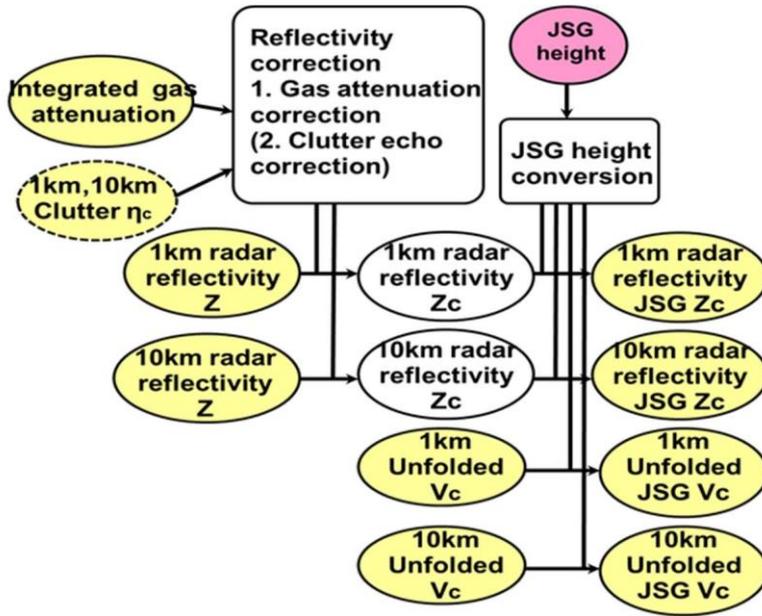
Figure 3.1.1.2.1-7 Processing flow of reflectivity correction and JSG conversion

7) mirror echo flag

CPR is designed to optimize PRF as much as possible due to establish better measurement accuracy of Doppler velocity. As a result, echoes that travel longer paths than usual—such as mirror images and multiple-scattering echoes—can overlap with the reception of subsequent pulses, leading to the appearance of more second-trip echoes at higher altitudes. The folding window, R_u, can be calculated as

$$R_u = \frac{c}{2 \times \text{PRF}}$$

where c is speed of light.

The most frequently occurring second-trip echo is the mirror image, which corresponds to a path that includes backscattering from the surface before reaching the cloud target. The estimated echo powers are calculated as follows (modified from Battaglia (2021)),

$$Z(r_m) = Z(r_t) - 20log_{10}\frac{r_m}{r_t} - 4A_{surface \to target} + 10log_{10}\left[\frac{(H_{sat} - H_t)^2\Gamma^4\sigma_0}{\sigma_0 H_{sat}^2 + 11.04\Gamma^2\frac{H_t^2}{\theta_{3dB}^2}}\right]$$

where the range of mirror echo $r_m = r_t + 2H_t$, r_t is the range of the target, H_t is its height above surface, Γ is its Fresnel reflection coefficient, A is one-way attenuation, σ_0 is NRCS, θ_{3dB} is antenna beam width. The fourth term of this equation is specular reflection property which depends on surface condition, ex. sea surface, land water and land. Since this term causes uncertainty in the estimation, the mirror reflectivity factor is not provided as a product. Instead, the estimated mirror occurrence regions are implemented as a mirror echo flag along with confidence levels. The third term is including the attenuation by liquid cloud and/or precipitation (Protat et al. 2019).

In addition, elongated tail-like echoes resulting from multiple scattering (MS tails) also appear at higher altitudes. The occurrence frequency of MS tails is significantly less compared to mirror images. But they cause significant contamination on deep convective clouds. First, it was determined whether multiple scattering was occurring in each radar reflectivity profile (Battaglia et al. 2011), and then the reflectivity of MS tails are calculated (Battaglia 2021). From the estimated reflectivity, MS flag is judged with probability information.

When the surface reflectivity is exceptionally high, a mirror image of the satellite, that is, an echo that has traveled two round trips between the satellite and the surface, appears as an artifact echo. This artifact echo frequently appears at a fixed altitude over regions such as sea ice, lakes, and large rivers. The altitude at which this echo appears, $z_{artifact}$, is given by

$$z_{artifact} = (-H_{sat} + 2z_s) \bmod R_u$$

where z_s is the surface height. Over sea-ice surfaces where $z_s = 0$, it appears around 2.5 km. The Doppler velocity of the artifact echo can be estimated from the Doppler velocity at the surface, and this information is also used for its identification.

3.1.2 Standard Product (CPR Cloud Product)

3.1.2.1 Introduction

There are two kinds of cloud products; standard and research cloud products. These will be distributed from JAXA. The standard CPR products include cloud mask, cloud particle type and cloud microphysics. These are derived mainly from radar reflectivity factor (Ze) without using Doppler velocity (Vd). The research products are similar to the standard products but derived by using Ze and Vd. The products will be processed in two horizontal and vertical grid spacings. The horizontal and vertical grid spacing of the fine scale version of the products are 1 km and 100 m, respectively. The coarse version of the products is provided after averaging over 10km and 100m horizontal and vertical resolution, respectively. Both of 1km- and 10km-products are reported at 1km.

This section describes the algorithms for the Standard Products, (1) the hydrometeor (cloud and precipitation) masks, (2) the cloud particle type discrimination scheme and (3) the cloud- and precipitation- microphysics retrieval scheme using the radar reflectivity factor from EarthCARE CPR. The flow of the algorithms to retrieve CPR cloud products is shown in Figure 3.1.2.1
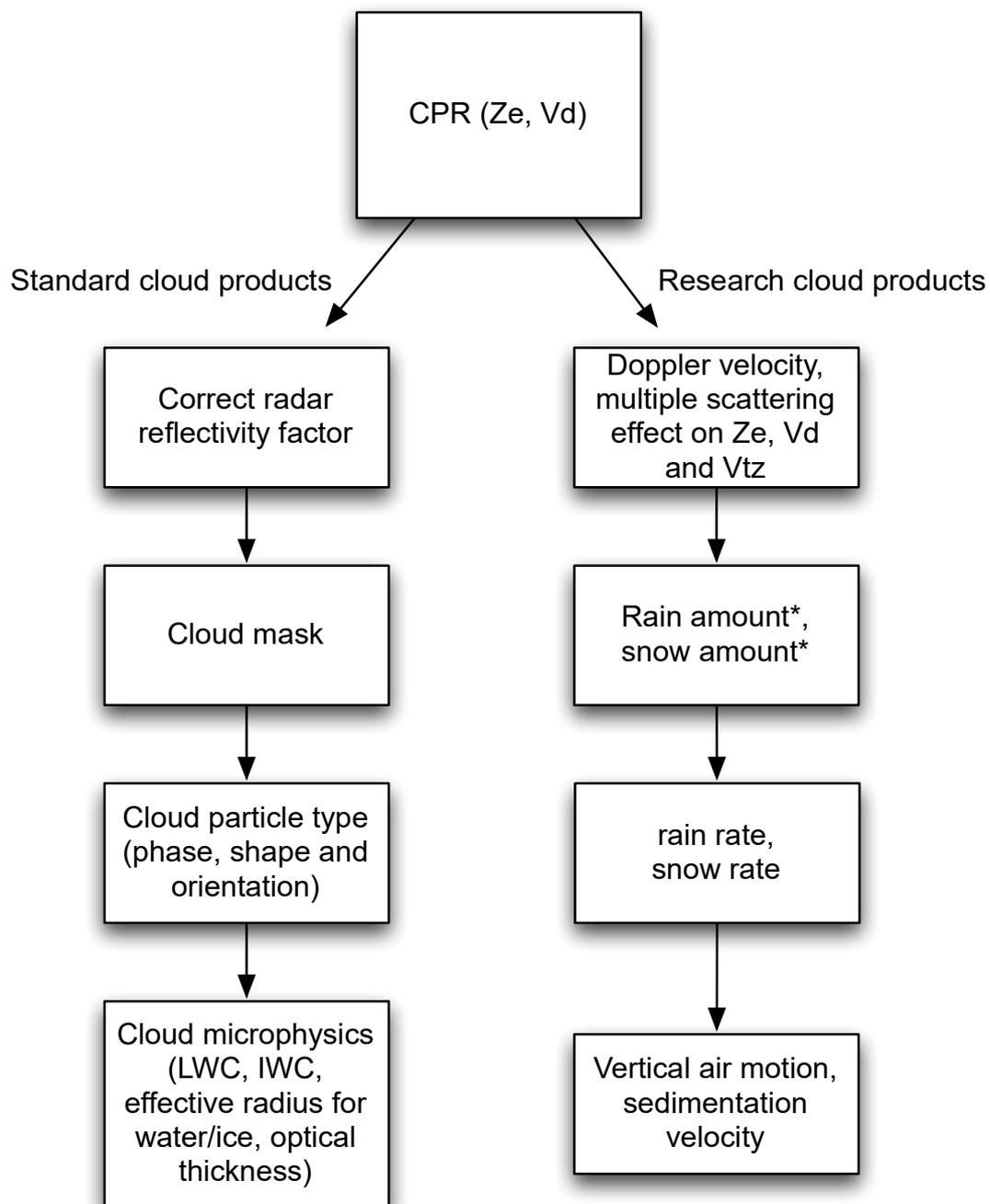
Figure3.1.2.1 Flow of the cloud products from CPR.

3.1.2.2 Cloud Mask

3.1.2.2.1 Algorithm

The CPR cloud mask algorithms are based on the algorithm originally developed for the analysis of 94GHz cloud radar on the vessel Mirai for the mid-latitude cruise near Japan [Okamoto et

al., 2007] and for the Tropical Western Pacific Ocean cruise [Okamoto et al., 2008]. The algorithm has been modified to analyze CloudSat 94GHz cloud radar [Hagihara et al., 2010]. There are several similarities between our cloud mask algorithm and the method developed in Marchand et al. [2008] which has been used for the hydrometeor detection by CloudSat. EarthCARE CPR cloud mask is extended version of one applied to CloudSat.

The algorithm considers the signal to noise ratio, spatial continuity (coherent test), and horizontal averaging to identify significant signals from noise and to assign a confidence level. In order to remove the effect due to surface echo and noise, we are planning to introduce the threshold method proposed by Okamoto et al., (2007).

$$P_t > P_{noise} + 2 \times \sigma_{noise} + P_{th} \qquad (1)$$

Where, P_t denotes the radar echo power measured at 94GHz. P_{noise} denotes the echo power due to noise. σ_{noise} is the standard deviation of noise, P_{th} is the threshold value to reduce contamination of noise signals into the signals from clouds and the value will be empirically determined from the analysis of EarthCARE after the launch. When P_t satisfies equation (1), the grid box is considered to be a candidate of a cloudy or precipitation grid.

Additional treatment, coherent filter, is considered to reduce the misclassification of clouds. We first create the sliding data window consisting of target bin, surrounding three bins in vertical and horizontal directions. The total number of bins in the window is 9. When more than half of the bins satisfies the criterion given by equation (1), the bin of interest is considered to be a cloudy or precipitation bin. In addition to the above criteria, Vd information will be used to further discriminate cloud signals from noise.

Reference

Hagihara, Y., H. Okamoto, and R. Yoshida, Development of a combined CloudSat/CALIPSO cloud mask to show global cloud distribution, J. Geophys. Res., doi:10.1029/2009JD012344, 115, D00H33, 2010.

Hagihara, Y., H. Okamoto, and Z. J. Luo, Joint analysis of cloud top heights from CloudSat and CALIPSO: New insights into cloud top microphysics, J. Geophys. Res. Atmos., 119, 4087-4106, doi:10.1002/2013JD020919.

Heymsfield, A. J., A. Protat, R. Austin, D. Bouniol, R. Hogan, J. Delaoe, H. Okamoto, K. Sato, G. Zadelhoff, D. Donovan, and Z. Wang, Testing and Evaluation of Ice Water Content Retrieval Methods using Radar and Ancillary Measurements, J. Appl. Meteor., 47, 135-163.,2008.

Okamoto, H., Information content of the 95GHz cloud radar signals: theoretical assessment of effect of non-sphericity by the discrete dipole approximation, Geophys. Res., 107(D22), 4628, doi:10.1029/2001JD001386, 2002.

Okamoto, H., S. Iwasaki, M. Yasui, H. Horie, H. Kuroiwa, and H. Kumagai, An algorithm for retrieval of cloud microphysics using 95-GHz cloud radar and lidar. J. Geophys. Res., 108(D7), 4226, doi:10.1029/2001JD001225, 2003.

Okamoto, H., T. Nishizawa, T. Takemura, H. Kumagai, H. Kuroiwa, N. Sugimoto, I. Matsui, A.

Shimizu, A. Kamei, S. Emori, and T. Nakajima, Vertical cloud structure observed from shipborne radar and lidar, : mid-latitude case study during the MR01/K02 cruise of the R/V Mirai, J. Geophys. Res, 112, D08216, doi:10.1029/2006JD007628, 2007

Okamoto, H., T. Nishizawa, T. Takemura, K. Sato, H. Kumagai, Y. Ohno, N. Sugimoto, I. Matsui, A. Shimizu, and T. Nakajima, Vertical cloud properties in Tropical Western Pacific Ocean: Validation of CCSR/NIES/FRCGC GCM by ship-borne radar and lidar, J. Geophys. Res., 113, D24213, doi:10.1029/2008JD009812, 2008

Sato, K., and H. Okamoto, 2006, Characterization of Ze and LDR of nonspherical and inhomogeneous ice particles for 95-GHz cloud radar: Its implication to microphysical retrievals, J. Geophys. Res., 111, D22213, doi:10.1029/2005JD006959, 2006.

Sato, K., Okamoto, M. K. Yamamoto. S. Fukao, H. Kumagai, Y. Ohno, H. Horie, and M. Abo 95-GHz Doppler radar and lidar synergy for simultaneous ice microphysics and in-cloud vertical air motion retrieval. J. Geophys. Res., 114, D03203, doi:10.1029/2008JD010222, 2009.

3.1.2.2.2 Evaluation of the detectability of clouds by CPR cloud mask

EarthCARE CPR has better sensitivity (-35dBZ) than CloudSat and detectability of clouds will be enhanced. Ground-based 94GHz cloud radar generally has higher temporal and vertical resolutions and some of the radar are more sensitive to low-level clouds compared with space borne systems. The data taken by such radars can be used to assess the performance of the EarthCARE CPR and the following ship borne data have been used for the evaluation. The ship-based 94GHz Doppler cloud radar (SPIDER) observations were conducted using the R/V Mirai, operated by the Japan Marine Science and Technology Center (JAMSTEC). The minimum sensitivity of SPIDER is about -30dBZ at 10km and -37dBZ at 5km after gaseous absorption in mid-latitude (Okamoto et al., 2007). This means that the SPIDER can detect more clouds than EarthCARE CPR below 5km and minimum detectable IWC for EarthCARE CPR is about 0.1 to 0.2mg/m^3. The radar and lidar measurements were conducted during the MR01-K02 and MR01-K05 cruises in 2001. In the MR01-K05, R/V Mirai departed from Sekinehama in northern Japan on 21 September 2001. The ship traveled southward to the equator, where it sailed near Indonesia during October and stayed in the warm pool region from 9 November to 9 December before returning to Japan. Stationary observation was performed for a month in the warm pool region at 2°N and 138°E from 9 November to 9 December 2001. The data obtained by the ship-based cloud radar data systems on R/V Mirai are used for the following comparison study.

We analyzed the cloud frequency of occurrence detected by ship-borne radar on R/V Mirai during MR01-K05 cruise. The radar-based cloud mask (hereafter, C1) with a radar threshold, the radar and lidar cloud mask (hereafter, C5), and schemes to derive hydrometeor and cloud occurrence are applied. C5 scheme used radar and lidar data. When the radar or lidar detected hydrometers (cloud or precipitation), the layer bin was considered to be the first candidate of clouds. When the altitude of cloud grid determined by the cloud radar was below the cloud bottom detected by the lidar, the grid box was considered to be contaminated by the precipitation. Mean occurrence frequencies were then estimated for the whole cruise period. The sensitivity of -30 dBZ$_e$ was approximately the same as that of CloudSat. The mean frequency of occurrence for -30 dBZ$_e$ was

the largest of the three cases, but it may have contained both precipitation and clouds. The difference between the fraction with -30 and -10 dBZ$_e$ thresholds was 6.5%. This could have corresponded to the cloud frequency, assuming that the frequency of occurrence with -10 dBZ$_e$ threshold corresponded to the actual precipitation frequency. This frequency was smaller than that of clouds derived from the C5 mask (7.5%). This underestimation might indicate that some cloudy regions were not detected using the -30 dBZ$_e$ threshold value. The underestimation of low-level clouds will be significantly minimized for EarthCARE case due to the higher sensitivity of the CPR than CloudSat. It is noted that the Doppler function can be used to improve discrimination between clouds and precipitation for the EarthCARE CPR observations.   HG-SPIDER has been in operation for years and it has higher sensitivity than EarthCARE CPR, e.g., -40dBZ at 10km. HG-SPIDER with co-located lidars will be used to evaluate cloud and precipitation detection from EarthCARE CPR.

Reference

Heymsfield, A. J., A. Protat, R. Austin, D. Bouniol, R. Hogan, J. Delaoe, H. Okamoto, K. Sato, G. Zadelhoff, D. Donovan, Z. Wang, Testing and Evaluation of Ice Water Content Retrieval Methods using Radar and Ancillary Measurements, J. Appl. Meteor., 47, 135-163.,2008

Okamoto, H., T. Nishizawa, T. Takemura, H. Kumagai, H. Kuroiwa, N. Sugimoto, I. Matsui, A. Shimizu, A. Kamei, S. Emori, and T. Nakajima, Vertical cloud structure observed from shipborne radar and lidar, : mid-latitude case study during the MR01/K02 cruise of the R/V Mirai, J. Geophys. Res, 112, D08216, doi:10.1029/2006JD007628, 2007

Okamoto, H., T. Nishizawa, T. Takemura, K. Sato, H. Kumagai, Y. Ohno, N. Sugimoto, I. Matsui, A. Shimizu, and T. Nakajima, Vertical cloud properties in Tropical Western Pacific Ocean: Validation of CCSR/NIES/FRCGC GCM by ship-borne radar and lidar, J. Geophys. Res., 113, D24213, doi:10.1029/2008JD009812, 2008

3.1.2.3 Cloud Particle Type
3.1.2.3.1 Algorithm

Cloud particle type is conducted by CPR. Details of the algorithm can be found in Kikuchi et al., [2017]. Algorithm for cloud particle type is as follows. The results of cloud particle types derived from cloud particle discrimination algorithm for CALIPSO lidar are used to develop CPR cloud particle type algorithm. The details of cloud particle type discrimination algorithm for ATLID are found in section 4. Cloud particle type algorithm for CPR uses information of radar Ze from CPR and temperature from the European Center for Medium-range Weather Forecasting (ECMWF) to infer cloud phase, shape and orientation, cloud or water or ice precipitation. Currently cloud particle types are obtained from CALIPSO for years [Yoshida et al., 2010]. The cloud particle type product has been used to develop the cloud particle type algorithm for CloudSat and it is extended to CPR. The algorithm used two-dimensional diagram of Z$_e$ and temperature to infer cloud particle type and the vertical profile of Ze and temperature. The first step used the Z$_e$ - temperature diagram for initial hydrometeor type classification. There are eight types; snow, rain,

mixed-phase drizzle, liquid drizzle, 2D-plate, 3D-ice, super-cooled water and warm water. For example, grid that indicates dBZe>10dBZ and temperature below 0°C is categorized as snow. Further, precipitation correction and special continuity test (as coherent filter) are introduced to the hydrometeor type algorithm in order to reduce the misclassification of cloud particle type. Information of V_d can be included for the hydrometeor type classification. Implementation of V_d will be described in the description of algorithms for the research cloud products. Evaluation of the algorithm was conducted by the comparison of radar-only classification with lidar-based classification assuming lidar phase classification to be correct, for September 2006. The phase misclassification was estimated to be about 25%. The misclassification will be corrected when CPR-ATLID cloud type algorithm will be applied.

Kikuchi, M., H. Okamoto, K. Sato, K. Suzuki, G. Cesana, Y. Hagihara, N. Takahashi, T. Hayasaka, R. Oki (2017), Development of algorithm for discriminating hydrometeor particle types with a synergistic Use of CloudSat and CALIPSO. Journal of Geophysical Research: Atmospheres, 122, 11,022–11,044. https://doi.org/10.1002/ 2017JD027113.

3.1.2.4 Cloud Microphysics

Here, we first describe the algorithm to retrieve ice microphysics in subsection 3.1.2.4.1, and the algorithm for water cloud microphysics will be described in subsection 3.1.2.4.2.

3.1.2.4.1 Ice cloud algorithm

After application of cloud mask and cloud particle type algorithm, microphysical retrievals of ice cloud and solid ice precipitation (snow) are performed using vertical profiles of Z_e and temperature for the standard products with the two-way path-integrated attenuation (PIA) using normalized radar cross section as follows;

$$PIA = \sigma^0_{clr} - \sigma^0_{att}$$

,where σ^0_{clr} and σ^0_{att} are the normalized radar cross section for clear sky and cloudy sky condition, respectively. σ^0_{clr} is obtained by searching the closest cloud free profiles within about 5 km consecutive pixels along-track. When the same land or ocean type continues within about 5 km, mean value of σ^0_{clr} is estimated. Then PIA for the cloudy record of interest is estimated by using the σ^0_{att} of the record and σ^0_{clr} in the closest records.

The retrieved properties are effective radius of ice particles and ice water content. To develop algorithm for cloud microphysics, the results from the radar-lidar algorithm can be used to formulate the empirical relationships between Z_e and cloud bottom and top altitudes and temperature where vertical structure of Z_e, cloud top and bottom altitudes and temperature are used as input. The details of the radar-lidar algorithms for ice clouds can be found in [Okamoto et al., 2003, Okamoto et al., 2010, Sato and Okamoto 2011] and some description for radar-lidar algorithms can be found in subsection 4.1. For actual cloud microphysics retrievals, we can use the framework of the Levenberg-Marquardt algorithm [Marquardt 1963] as one of the optimal estimation technique. The uncertainty of each cloud microphysical product is derived from the output of

EARTHCARE

NICT JAXA
宇宙航空研究開発機構
Japan Aerospace Exploration Agency

Levenberg-Marquardt algorithm [Sato and Okamoto 2011].

The ice particle model and scattering properties considered within the algorithm are provided in the followings. Ice particle models are taken from Sato and Okamoto [2006]. We consider the modified Gamma distribution function as standard size distribution function model (equation (2)).

$$\frac{dn(r)}{dr} = \frac{N_0}{\Gamma(p)} \left(\frac{r}{r_m}\right)^{p-1} \exp\left(-\frac{r}{r_m}\right),$$

(2)

and equivalent radius r_{eq} is first introduced as (3) .

$$r_{eq} = \left(\frac{3V_{ice}}{4\pi}\right)^{1/3}$$

(3)

Where, V_{ice} is the actual ice volume excluding internal air pocket. And the effective radius of the particle is defined in terms of using r_{eq} (4).

$$r_{eff} = \frac{\displaystyle\int_{r\min}^{r\max} r_{eq}^3 \frac{dn(r_{eq})}{dr_{eq}} dr_{eq}}{\displaystyle\int_{r\min}^{r\max} r_{eq}^2 \frac{dn(r_{eq})}{dr_{eq}} dr_{eq}}.$$

(4)

Several particle shapes are considered e.g., column, plate, bullet-rosette, aggregates of those, fractal aggregates with different orientations. The orientations of the non-spherical particles are considered as follows; horizontal oriented ice plate model (2D-plate) and randomly oriented ice particles in three dimensional space(3D-ice). We also considered horizontally oriented particles with Gauss-distribution with fixed standard deviation and also Klett type oriented model on the basis of aerodynamic properties of the falling ice particles [Klett 1995]. The aspect ratio for each particle shape varies and the parameterizations to construct ice particle models used in the algorithms are taken into account according to the measured ice particles [Sato and Okamoto 2006]. For these particle shapes and orientations, Z_e is estimated by the discrete dipole approximation (DDA). The accuracy of the DDA calculation to estimate Z_e for non-spherical ice particles is estimated to be smaller than 10% when the certain validity criteria are fulfilled [Okamoto 2002]. Note that the validity criteria depend on the shape and orientation and we follow the procedure to test the convergence of the DDA solutions [Okamoto et al., 1995] to obtain the secure solutions. The Z_e is tabulated as a function of particle radius and particle habits (shape and orientation). Currently the ice particle habit is fixed such as the mixture of 50% of the hexagonal column oriented randomly in the horizontal plane (2D-column) and 50% of the bullet rosette oriented randomly in space (3D-bullet-rosette) (hereafter the model is called CB50 model) in the retrieval algorithm. Size distribution function is further assumed to estimate Z_e for broad particle size ranges. Note that Ze for ice particles with perfectly distributed in horizontal plane such as plate-like ice or Voronoi ice is almost

the same as that for quasi horizontal distribution based on the DDA calculations. We also tested several different size distribution functions to assess the effect of size distribution function on the fixed function in the retrieval cloud microphysics. Snow particle is modeled as 2D-plate, 3D-ice and fractal aggregate models. Multiple scattering effect estimated by Monte Carlo method is also considered in the algorithm, though the effect is limited in the strong precipitation and convectively active regions.

3.1.2.4.2 Water cloud algorithm

The water cloud algorithm is similar to that for ice clouds. The algorithm uses look up tables of extinction, radar reflectivity factor as function of effective radius and temperature for a constant LWC and the vertical structure of Z_e, temperature and PIA are used as input parameters to derive effective radius and liquid water content (LWC) based on the synergy observations with cloud radar with Doppler function and lidar and also on the multi-wavelength Doppler radar observations and lidar. The empirical formula to provide water microphysics are derived on the basis of radar-lidar algorithm for water clouds where Z_e from CPR, β and depolarization ratio from ATLID will be used.

Reference

Marchand, R., G. G. Mace, T. Ackerman, and G. Stephens (2008), Hydrometeordetection using Cloudsat - An earth-orbiting 94-GHz cloud radar, *J. Atmos. Oceanic. Technol.*, *25*, 519-533, doi:10.1175/2007jtecha1006.1.

Heymsfield, A. J., A. Protat, R. Austin, D. Bouniol, R. Hogan, J. Delaoe, H. Okamoto, K. Sato, G. Zadelhoff, D. Donovan, Z. Wang, Testing and Evaluation of Ice Water Content Retrieval Methods using Radar and Ancillary Measurements, J. Appl. Meteor., 47, 135-163.,2008

Hagihara, Y., H. Okamoto, and R. Yoshida (2010), Development of a combined CloudSat-CALIPSO cloud mask to show global cloud distribution, *J. Geophys. Res.*, *115*, D00h33, doi:10.1029/2009jd012344.

Okamoto, H., T. Nishizawa, T. Takemura, H. Kumagai, H. Kuroiwa, N. Sugimoto, I. Matsui, A. Shimizu, S. Emori, A. Kamei, and T. Nakajima (2007), Vertical cloud structure observed from shipborne radar and lidar: Midlatitude case study during the MR01/K02 cruise of the research vessel Mirai, J. Geophys. Res., 112, D08216, doi:10.1029/2006JD007628.

Okamoto, H., T. Nishizawa, T. Takemura, K. Sato, H. Kumagai, Y. Ohno, N. Sugimoto, A. Shimizu, I. Matsui, and T. Nakajima (2008), Vertical cloud properties in the tropical western Pacific Ocean: Validation of the CCSR/NIES/FRCGC GCM by shipborne radar and lidar, J. Geophys. Res., 113, D24213, doi:10.1029/2008JD009812.

Okamoto, H., Information content of the 95GHz cloud radar signals: theoretical assessment of effect of non-sphericity by teh discrete dipole approximation, J. Geophys. Res., 107(D22), 4628, doi:10.1029/2001JD001386, 2002.

Okamoto, H., S. Iwasaki, M. Yasui, H. Horie, H. Kuroiwa, and H. Kumagai, An algorithm for retrieval of cloud microphysics using 95-GHz cloud radar and lidar. J. Geophys. Res.,

108(D7), 4226, doi:10.1029/2001JD001225, 2003

Okamoto, H., K. Sato, Y. Hagihara, Global analysis of ice microphysics from CloudSat and CALIPSO: incorporation of specular reflection in lidar signals, J. Geophys. Res., 115, D22209, doi:10.1029/2009JD013383, 2010.

Sato, K., and H. Okamoto , Characterization of Ze and LDR of nonspherical and inhomogeneous ice particles for 95-GHz cloud radar: Its implication to microphysical retrievals, J. Geophys. Res., 111, D22213, doi:10.1029/2005JD006959, 2006.

Sato, K., Okamoto, M. K. Yamamoto. S. Fukao, H. Kumagai, Y. Ohno, H. Horie,and M. Abo 95-GHz Doppler radar and lidar synergy for simultaneous ice microphysics and in-cloud vertical air motion retrieval. J. Geophys. Res., 114, D03203, doi:10.1029/2008JD010222, 2009

Yoshida, R., H. Okamoto, Y. Hagihara, and H. Ishimoto, Global analysis of cloud phase and ice crystal orientation from CALIPSO data using attenuated backscattering and depolarization ratio, J. Geophys. Res., doi:10.1029/2010JD014032, 115, D00H32, 2010.

3.1.3 Research Product (CPR Echo Product)

3.1.3.1 Introduction

This section describes the algorithm that retrieve the Research Product relating the Doppler velocity and multiple scattering effect using the radar reflectivity factor and Doppler information from CPR on EarthCARE.

3.1.3.1.1 Studies Using Doppler velocity error caused by inhomogeneity of reflectivity

Inhomogeneous reflectivity within the radar beam causes significant Doppler velocity error because the measured Doppler speeds are reflectivity-weighted Doppler speeds instead of simple average321342213 and the satellite velocity contamination to the offnadir direction is not negligible even within narrow beam width [Schutgens, 2008]. If the echo reflectivity of the forward side has stronger than the echo reflectivity of the backward side, approaching Doppler speed is measured from con-tamination of satellite velocity even though echo has no vertical speed. Although 500 m horizontal integration reduces the error caused by the inhomogeneous reflectivity, some error still remains. In order to correct this error, the method using the inclination of horizontal reflectivity is proposed and studied in several papers [Uematsu et al. 2007, Schutgens 2008, Sy et al. 2014, Kollias et al. 2014]. In those papers, relation between error caused by inhomogeneous reflectivity and inclina-tion of horizontal reflectivity is statistically analyzed using various ground base results. The Dop-pler correction factor is estimated using this relation.

Instead of using the inclination of horizontal reflectivity, we propose here more general method of Doppler error correction as follows [Ohno et al. 2013]. Sy et al. (2014) already shows the

Doppler estimation error ($\varepsilon_{\text{Ideal}}$) caused by inhomogeneous reflectivity in general equation form as follows.

$$
\begin{aligned}
\varepsilon_{\text{Ideal}}(x_{\text{E},N}) &= \mu_{\text{Ideal}}(x_{\text{E},N}) - \mu_{\text{Ref}}(x_{\text{E},N}) \\
&= \frac{V_{\text{sat}}}{h_{\text{sat}}} \times \frac{1}{Z_{\text{Ideal},N}(x_{\text{E},N})} \int_{\mathcal{X}_N(x_{\text{E},N})} f_U(x_{\text{E}} - x_{\text{E},N}) \\
&\quad \times \int_{\mathcal{X}(x_{\text{E}})} (x - x_{\text{E}})\, \omega_{\text{X}}(x - x_{\text{E}}) Z_{\text{IN}}(x)\, dx\, dx_{\text{E}},
\end{aligned}
$$

$$
\text{and} \qquad Z_{\text{Ideal},N}(x_{\text{E},N}) = \int_{\mathcal{X}_N(x_{\text{E},N})} f_U(x_{\text{E}} - x_{\text{E},N}) \int_{\mathcal{X}(x_{\text{E}})} \omega_{\text{X}}(x - x_{\text{E}}) Z_{\text{IN}}(x)\, dx\, dx_{\text{E}}.
$$

where μ_{Ideal} and μ_{Ref} is measured Doppler including inhomogeneous reflectivity effect and real Doppler velocity without inhomogeneous reflectivity effect over horizontal integration. V_{sat} and h_{sat} is satellite horizontal velocity and altitude. The integration of $\mathcal{X}_N(x_{\text{E},N})$ is an horizontal integration over several pulses N, which represents 500m or 1km, 10km horizontal integration and f_U is a uniform weighting function over $\mathcal{X}_N(x_{\text{E},N})$. The inner integration of $\mathcal{X}_N(x_{\text{E}})$ is a beam footprint integration with its beam pattern $\omega_{\text{X}}(x)$ at beam center x_{E}. $Z_{\text{Ideal},N}(x_{\text{E},N})$ and $Z_{\text{IN}}(x)$ are horizontally

integrated reflectivity and local reflectivity at x. The variable x is a distance to the along-track direction.

Using above equation, we firstly calculate the known integration part except Z_{IN} multiplication. If we use Gaussian beam pattern for $\omega_X(x)$ of the beam width as 0.098 degree, V_{sat} as 7500m/s and h_{sat} as 400km, the error contribution factor at each location is shown in Fig. 3.1.3.1.1.1. From this figure in case of 2km integration, the area around -1000m position contributes negative Doppler error and the area around +1000m position contributes positive Doppler error. Considering the reflectivity data of EarthCARE/CPR is available for 500m interval, the integrated reflectivity at -1000m and +1000m should be use for correction of Doppler error of 2km integration. Multiplying this factor to the local reflectivity and integrating all of them, then final Doppler error caused by inhomogeneous reflectivity can be estimated.
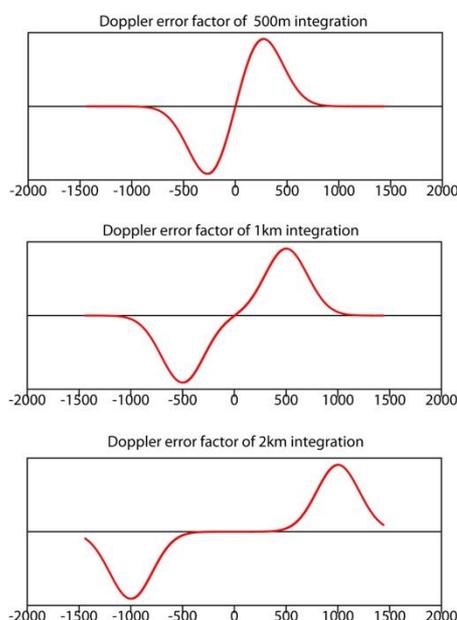

Fig.3.1.2.2.1 Doppler error contribution factor in case of 500m (top), 1000m (middle), 2000m (bottom) integration

Now we discuss Doppler folding of Doppler velocity error, which mentioned in the 3.1.1.2.1 (3). Doppler velocity error caused by inhomogeneity of reflectivity sometimes exceeds the maximum Doppler velocity. In order to including with such folding case, we consider the phase of the pulse-pair covariance instead of the velocity itself. The real and imaginary part of the 500m integrated covariance are provided from the CPR science telemetry and L1 products.

Normally, Doppler velocity V is estimated from pulse-pair complex covariance $R(T)$ as follows.

$$ V = \frac{\lambda}{4\pi T} \tan^{-1}\left(\frac{\operatorname{Im} R(T)}{\operatorname{Re} R(T)} \right) $$

Where λ is a wave length of radar and T is a time interval between pulses. The distance from the beam center (x_{max}) that causes Doppler folding by satellite velocity contamination is calculated as

follows.

$$x_{max} = \frac{\lambda \cdot PRF}{4} \bullet \frac{hsat}{Vsat}$$

In case of the EarthCARE/CPR, x_{max} is about 270m in PRF6100Hz, 332m in PRF7500Hz. If we think a similar formalization of the Doppler velocity error that mentioned above, the Doppler estimation error (ε_{Ideal}) caused by inhomogeneous reflectivity is calculated from the following equations.

$$c(x) = \mathrm{Re}\, R(T) = \cos(x / x_{max} \cdot \pi)$$
$$q(x) = \mathrm{Im}\, R(T) = \sin(x / x_{max} \cdot \pi)$$

$$C(x_E) = \int c(x - x_E)\omega_E(x - x_E)z(x)dx \Big/ Z_{IN}(x_E)$$
$$Q(x_E) = \int q(x - x_E)\omega_E(x - x_E)z(x)dx \Big/ Z_{IN}(x_E)$$
$$Z_{IN}(x_E) = \int \omega_E(x - x_E)z(x)dx$$

$$\varepsilon_{Ideal}(x_E, N) = \frac{\lambda \cdot PRF}{4\pi} \arctan\left(\int_{\chi(X_E, N)} Q(x_E)Z_{IN}(x_E)dx \Big/ \int_{\chi(X_E, N)} C(x_E)Z_{IN}(x_E)dx \right)$$

Where c(x) and q(x) are real and imaginary part of the pulse-pair covariance R(T) corresponding to local phase shift values of Doppler error caused by the satellite velocity contamination. $C(x_E)$ and $Q(x_E)$ are integrated values of c(x) and q(x) within one beam footprint area. Then, the Doppler estimation error (ε_{Ideal}) caused by inhomogeneous reflectivity is calculated with the bottom equation including horizontal integration. Horizontally integrated $C(x_E)$ and $Q(x_E)$ are shown in Fig.3.1.2.2.2. From this figure, the real part of covariance R(T) ($C(x_E)$) is larger positive value within integration length and small negative outside of integration length. In case of the imaginary part of covariance R(T) ($Q(x_E)$), positive peak is located at the end of horizontal integration in the forward side and negative peak is located at the beginning of horizontal integration in the backward side, although it is small within the integration length. This mean the reflectivity within the integration length mainly contributing to the $C(x_E)$ and reflectivity around both edges of the horizontal integration contributing to the $Q(x_E)$.

Although in above formula, we assume that z(x) is given as continuous function, z(x) is actually given as 500m integrated value with 500m interval. Then, we firstly calculated 500m integrated value of c(X_E) ω_X(X) and q(X_E) ω_X(X) corresponding to the position of 500m integrated z(x).

Fol-lowing that, multiplication of those two and integration of 1km and/or 10km of C(X_E) and

Q(X_E) are calculated, then, the Doppler estimation error (ε_{Ideal}) caused by inhomogeneous reflectivity is calculated every 1km interval. Since above formula is assuming the same PRF through the hori-zontal integration, if its PRF is changed around gap time within this 1km and/or 10km integration, we set the Doppler estimation error (ε_{Ideal}) to missing value and the NUBF correction ray flag to non-zero value (error).
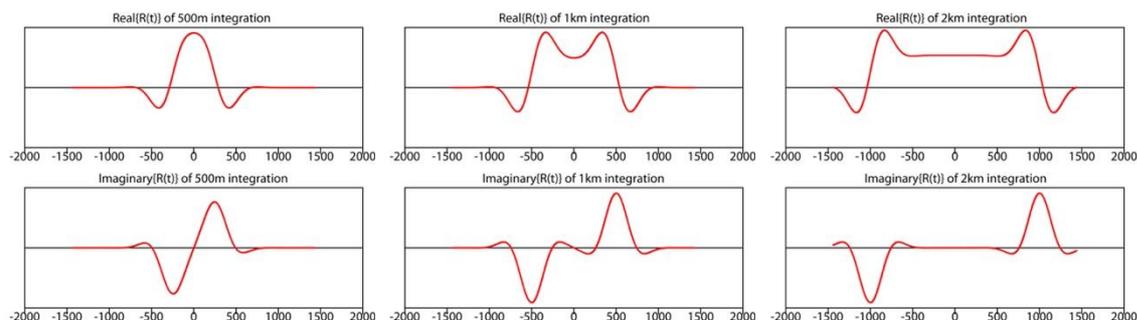

Fig.3.1.2.2.2 Horizontally integrated $C(X_E)$ and $Q(X_E)$ in case of 500m (left), 1km (middle), 2km (right) integration

This Doppler error estimation Algorithm including above consideration is under development now.

Reference

Kollias, P., S. Tanelli, A. Battagllia, A Tatarevic 2014: Evaluation of EarthCARE cloud profiling radar Doppler velocity measurements in particle sedimentation regimes. J. Atmos. Oceanic Technol., 31, 366–386.

Schutgens, N., 2008: Simulated Doppler radar observations of inhomogeneous clouds: Application to the EarthCARE space mission. J. Atmos. Oceanic Technol., 25, 26–42.

Sy, O.O., S. Tanelli, N. Takahashi, Y. Ohno, H. Horie, P. Kollias 2014: Simulation of EarthCARE spaceborne Doppler radar products using ground-based and airborne data: Effects of aliasing and nonuniform beam-filling, IEEE Transactions on Geoscience and Remote Sensing, vol.52, no.2, pp.1463-1479, 014. doi: 10.1109/TGRS.2013.2251639

Uematsu, A., Y. Ohno, H. Horie, H. Kumagai, N. Schutgens 2007: Evaluation of Doppler Velocity Bias with a Spaceborne Cloud Doppler Radar. EarthCARE Workshop at Noortwijk Netherland May 2007.

Battaglia, A.: Impact of second-trip echoes for space-borne high-pulse-repetition-frequency nadir-looking W-band cloud radars, Atmos. Meas. Tech., 14, 7809–7820, https://doi.org/10.5194/amt-14-7809-2021, 2021.

Battaglia, A., T. Augustynek, S. Tanelli, and P. Kollias (2011), Multiple scattering identification in spaceborne W-band radar measurements of deep convective cores, J. Geophys. Res., 116, D19201, doi:10.1029/2011JD016142

3.1.4 Research Product (CPR Cloud Product)

3.1.4.1 Introduction

This section describes the algorithm that retrieve the Research Cloud Product. The research products include ice water content, liquid water content, rain rate, snow rate, Doppler velocity in cloud and precipitation regions, vertical air motion and sedimentation velocity of the cloud particle. Horizontal and vertical grid spacings are the same as those for standard products.

It is crucial to estimate (1) hydrometeor (cloud particles and precipitation particles) microphysics and (2) separation of vertical air motion and particle terminal velocity from the Doppler velocity (Vd) and (3) contribution of multiple scattering on Ze and Vd. The precipitation (rain and snow) microphysics and their vertical velocity is retrieved by using the radar reflectivity factor, the normalized radar cross section, σ^0_{att} and Vd from CPR and atmospheric condition such as temperature, pressure and humidity from ECMWF.

Doppler velocity by CPR will be affected due to aliasing such as when the large precipitation particles exists or large air motion occurred in convections. Prior to the analysis of cloud particle type and microphysics and terminal velocity of cloud and precipitation particles, Doppler velocity has been corrected by de-aliasing method [Shaik et al., 2024 in preparation].

3.1.4.2 Improvement of cloud particle type by the information of Vd from CPR

The improvement of the cloud particle type discrimination is expected by introducing Vd in addition to Ze compared with the algorithm without using Vd. In general, terminal velocity of the cloud and precipitation particle reflects particle shape, type (including particle-orientation) and size. Vd is given the sum of vertical air motion and reflectivity weighted terminal velocity, Vtz, which is given by backscattering cross section of each particle and terminal velocity (equation (5)).

$$V_{tz} = \frac{\int_{r_{eq,min}}^{r_{eq,max}} V_t(r_{eq}) Z_e(r_{eq}) \frac{dn(r_{eq})}{dr_{eq}} dr_{eq}}{\int_{r_{eq,min}}^{r_{eq,max}} Z_e(r_{eq}) \frac{dn(r_{eq})}{dr_{eq}} dr_{eq}}.$$

(5)

Terminal velocity depends on particle size, shape, orientation and atmospheric condition such as temperature and pressure. Therefore V_d can be included for the cloud particle type algorithm, provided that the effect of vertical air-motion can be subtracted from V_d and V_{tz} can be estimated prior to the use of information of V_d for particle type discrimination in the research product. Relation between V_d, V_{tz} and V_{airs} is given by equation (6),

$$V_d = V_{tz} + V_{air}. \quad (6)$$

When large V_d and large Z_e are observed, the bin of interest can be considered to be precipitation. In such case, the effect of vertical air motion might be smaller than the Vtz and the discrimination of Vtz and vertical air motion might not always have to be performed prior to the type classification. The combination of Ze and Vd can be used to infer the phase of precipitation.

Correction of the vertical air-motion to V_d is needed prior to the algorithm for cloud particle type. Separation of vertical air motion and terminal velocity in V_d will be described in the description

of algorithms for the research cloud microphysical products.

In order to evaluate the algorithm for the type discrimination of large size, lidar with polarization function can be used and synergy analysis of X-, Ka- and W-band radar can be used to discriminate particle type [Okamoto et al., 2009, Okamoto 2013]. The dual wavelength ratio (DWR) and the Doppler velocity between the two different wavelengths contain information of cloud microphysics when the particle size exceeds 100μm and are used to derive empirical formula to determine particle type by CPR only.

3.1.4.3 Precipitation Microphysics, Terminal Velocity and vertical air-motion
3.1.4.1.1 Algorithm

In order to make V_d useful, correction for the effect of horizontal inhomogeneous cloud properties (non-uniform beam filling) on the V_d is required. It is recognized that the effect becomes important in case of space-borne Doppler measurements [Schutgen 2008]. The effect can be evaluated by the Doppler simulation to develop the correction method for V_d due to the effect.

In addition, as noted in previous section, we need to estimate Z_e-weighted velocity (V_{tz}) that corresponds to Doppler velocity without the effect of air motion prior to using V_d in the retrieval algorithms for cloud and precipitation microphysics.

The dependence of V_{tz} on the temperature and pressure is also taken into account to relate Vtz and cloud microphysics [Heymsfield et al., 2002].

The LUT of V_{tz} is tabulated as a function of particle radius, habits and temperature and pressure [Sato et al., 2009]. We develop algorithms using vertical profile of Z_e without using V_d to produce rain amount and snow amount. We also develop algorithms using the vertical profile of Z_e and V_d to produce rain amount and snow amount. Snow model is taken to be similar to ice model such as fractal aggregates, spherical, column, plates, bullet-rosette and the scattering properties of these particles are estimated by the DDA and are tabulated as look up tables for CPR. The whole profile of the vertical distribution of Z_e and V_d and sea-surface return signal are used to retrieve microphysics with the look up tables. For the validation of the formula used in the algorithms, we use the multi-wavelength and multi-parameter radar data already taken during several field campaigns [Okamoto et al., 2009].

The normalized surface backscattering cross section of the sea surface are planned to be used as additional input parameter to estimate rain/snow amount and rain/snow rate as tried by Haynes et al., [2008] for sea surface. When the rain (or snow) rate exceeds certain threshold such as 3 -5 mm/h, multiple scattering effect becomes significant. To model the multiple scattering effect on Z_e and V_d due to precipitating particles at 94GHz, we extend the physical model (PM) [Sato et al., 2018] for multiple scattering (detail described in section 4) where scattering properties of water is calculated by the Mie theory or T-matrix methods and ice properties single scattering properties are calculated by the DDA.

When cloud products are retrieved, the sedimentation velocity of the particles and the vertical air motion are also simultaneously retrieved. Levenberg-Marquardt algorithm is applied to retrieve cloud microphysics as well as vertical air motion and sedimentation velocity. Vd is simulated by the retrieved effective radius and particle type by CloudSat and CALIPSO analysis.

3.1.4.1.2 Evaluation of algorithms that use Vd

Full one-to-one validation of the retrieved V_{air} was performed, for the first time, by collocated VHF Doppler radar measurement (Equatorial Atmospheric Radar) every 3 min for a cloud observed on 14 November 2005, at Kototabang, West Sumatra, Indonesia. The spatial structure of the retrieved up-/downward V_{air} in cloud agreed closely with direct measurements. A large improvement in the microphysical retrieval was achieved due to the accurate estimation of the Z_e-weighted particle fall velocity V_{tz} from V_D [Sato et al., 2009]. Using the synergy data sets from EarthCARE CPR with Doppler capability and ATLID, it will be possible to derive global distribution of vertical air motion and terminal velocity of cloud particles in addition to the cloud microphysics. It is expected that the information will help to understand the link between cloud formation process, atmospheric dynamics, cloud microphysics and atmospheric radiations.

The clouds detected by at least one of CPR or ATLID can be analyzed by the algorithm originally developed by Sato and Okamoto [2011] and further modified [Sato et al., in preparation].

For the evaluation of the algorithms, we use the results from the field campaigns conducted in Niigata and Kouchi regions for winter and summer seasons, respectively. There were three wavelengths radar observations in winter and Doppler cloud radar data and lidar data in summer [Okamoto et al., 2015]. The ice and water microphysics were retrieved by using these instruments and in-situ data were also collected by aircraft.

3.2 ATLID

3.2.1 Standard Product

3.2.1.1 Introduction

Aerosols substantially affect the radiation budget of the earth-atmosphere system in both direct and indirect ways. The direct effect is directly related to scattering and absorption of solar radiation by aerosol particles [Charlson et al. 1992; Kiehl and Briegleb 1993]. The indirect effect is seen in the way aerosols influence optical properties and the lifetime of clouds through cloud formation processes [Twomey 1977; Albrecht 1989]. Further, it has been recently pointed out that absorbing aerosols (such as black carbon) reduce cloud formation by absorbing sunlight, thereby cooling the surface and heating the atmosphere [Koren et al. 2004] and also affect the large-scale circulation and hydrologic cycle by altering regional atmospheric stability and vertical motions [Menon et al. 2002]. The International Panel on Climate Change (IPCC) Forth Assessment Report (AR4) [Solomon, 2007] point out that there are still not negligible uncertainties in the estimation of the direct and indirect radiative forcing. Thus, it is important to reveal the global distributions of the microphysical and optical properties of aerosols and clouds and the chemical and physical processes regarding to aerosols and clouds.

Lidar is a powerful tool for capturing vertical distributions and temporal variations in aerosols and clouds. The vertical distributions of aerosols and clouds are a key parameter for assessing their effects on radiative impacts on the climate system: for example, it was reported that the signs of direct radiative forcing simulated by numerical models were negative/positive when absorbing aerosol layers were below/above cloud layers [Haywood and Ramaswamy 1998; Takemura et al. 2002]. A Mie-scattering lidar (MSL) is the most frequently used active instrument for studying aerosol and cloud optical properties (e.g., CALIOP/NASA [Winker et al., 2009]). Extinction and backscatter coefficients for aerosols and cirrus clouds are derived from MSL data by assuming an extinction-to-backscatter ratio (lidar ratio). Improved aerosol observation has recently been conducted using the lidar technology with High Spectral Resolution Lidar (HSRL) [e.g., Liu et al. 1999] and Raman lidar [e.g., Ansmann et al. 1992]. HSRL and Raman lidar are more useful than Mie-scattering lidar as they can provide extinction and backscatter coefficients for total aerosols without assuming a lidar ratio. The HSRL technique at the wavelength of 355nm is used in ATLID (the ATmospheric LIDar) and enables us to obtain the extinction and backscatter coefficients at 355nm without the lidar ratio assumption.

The optical and microphysical properties of aerosols and clouds are essential parameters for assessing the effects of aerosols on the radiative impacts. Multichannel lidar data such as extinction and backscatter coefficients and depolarization ratios for several wavelengths allow us to simultaneously capture the vertical distributions of several aerosol and cloud properties. Several aerosol retrieval algorithms using the multichannel lidar data have been developed. For example, the algorithms that use multichannel Raman lidar data have been developed [Müller et al. 1999; Böckmann 2001; Veselovskii et al. 2002]. Their algorithms retrieve the size distribution and complex refractive index of total aerosols. The algorithms using multichannel Mie-scattering lidar data have been also developed [e.g., Sugimoto et al. 2003; Nishizawa et al. 2007]; their algorithms classify aerosol components and estimate their extinction coefficients.

Satellite-borne passive remote sensor (e.g., AVHRR, MODIS, and SeaWIFS) is an also powerful tool to provide information on sizes of aerosols (e.g., angstrom exponent) and aerosol types (e.g., soil dust, carbonaceous) in globe, partly using the feature that the spectral property of the measured radiance data is sensitive to particle size [e.g., Higurashi and Nakajima, 1999, 2002; Kaufman et al., 2003]. The combined use of active and passive sensor data enables us to estimate various optical properties simultaneously and to reduce the potential uncertainty of estimates.

On the basis of the background abovementioned, we intend to develop an ATLID L2 and ATLID-MSI L2 algorithms to derive information on global distributions for aerosols and clouds in the atmosphere from the ATLID L1B and MSI L1B data and to reveal the occurrence for aerosol components and cloud types and their vertical distribution.

The parameters retrieved by the developed algorithms are summarized in Table 3.2.1.1.1. The algorithm for the ATLID data (hereafter, ATLID algorithm) provides the following products: (1) indicators representing molecules, aerosols, clouds, and so on in each slab layer; extinction coefficients (α_p), backscatter coefficients (β_p), depolarization ratio (δ_p), and lidar ratio (S_p) of aerosols (2) and clouds (3); (4) indicators representing cloud type (e.g., warm-water cloud) and aerosol type (e.g., maritime aerosols); (5) planetary boundary layer (PBL) height. The extinction coefficients of four major aerosol components in the atmosphere are also estimated as research products using ATLID (see section 3.2.2). In addition, the mode radii of fine-mode and coarse-mode aerosols are also estimated by the synergy between ATLID and MSI, along with the extinction coefficients of the four aerosol components as research products (see section 4.2.1).

Table 3.2.1.1.1 ATLID L2A and ATLID-MSI L2B product list[*a]

Status	Algorithm	Product name	Primary parameters	Resolution	
				Horizontal (km)	Vertical (km)
S	A	Feature mask product	Feature mask	1[*]/1/0.3	0.1
S	A	Aerosol Product	α_p, β_p, δ_p, S_p	1[*]	0.1
S	A	Cloud Products	α_p, β_p, δ_p, S_p	1[*]/1	0.1
S	A	Target mask product	Target Mask	1[*]/1	0.1
S	A	Boundary layer height	PBL height	1[*]	—
R	A	Aerosol component	α_p (Water-soluble)	1[*]	0.1
R	A		α_p (Dust)	1[*]	0.1
R	A		α_p (Sea salt)	1[*]	0.1
R	A		α_p (Light-absorbing)	1[*]	0.1
R	A-M	Aerosol component	α_p (Water-soluble)	1[*]	0.1
R	A-M		α_p (Dust)	1[*]	0.1
R	A-M		α_p (Sea salt)	1[*]	0.1
R	A-M		α_p (Light-absorbing)	1[*]	0.1
R	A-M		R_m (Fine-mode)	1[*]	0.1

| R | A-M | | R_m (Coarse-mode) | 1^* | 0.1 |

^{*a} The "Status" indicates a standard product (S) or a research product (R). The "Algorithm" indicates the ATLID algorithm (A) or the ATLID-MSI algorithm (A-M). R_m is a mode radius (see equation 2.8). α_p is a particle extinction coefficient; β_p is a particle backscatter coefficient; δ_p is a particle depolarization ratio; S_p is a particle lidar ratio. The term 1^* indicates 1km horizontal resolution running-averaged in 10km horizontal range

Figure 3.2.1.1.1 depicts the analysis flow of the algorithm developed to provide the products. The products are produced in each procedure: "Feature mask" for product (1); "particle optical properties (POP) retrieval" for products (2) and (3), Target mask" for product (4), "PBL height retrieval" for product (5) and "aerosol component retrieval" for research products. Detailed descriptions of these procedures are provided in the following sections.
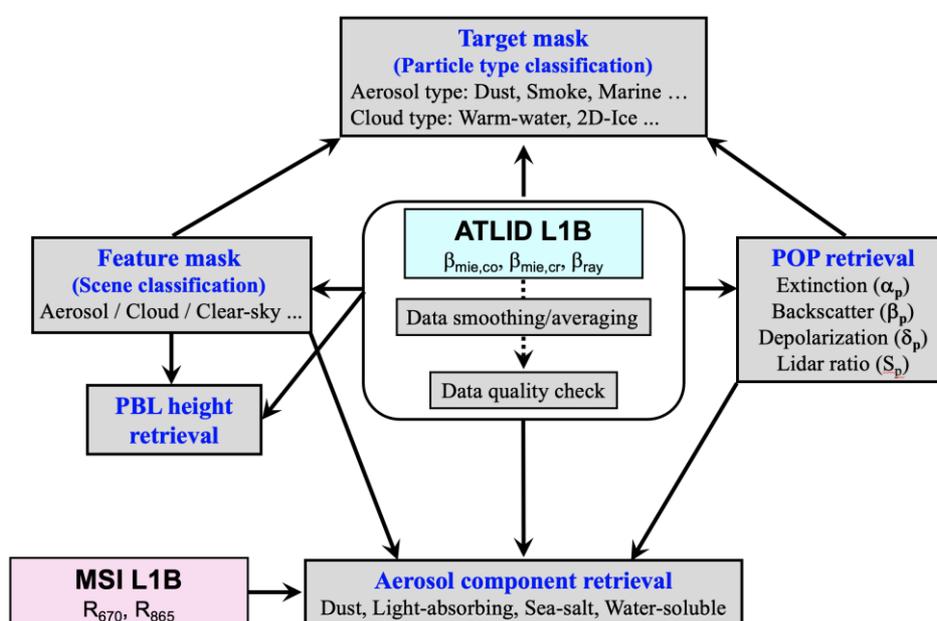
Figure 3.2.1.1.1 Analysis flow of the ATLID algorithms.

This section describes the algorithm flow. The algorithm produces the L2a ATLID standard/research products and L2b ATLID-MSI synergy research products using the L1B ATLID data of three-channel attenuated backscatter coefficients for Mie co-polar ($\beta_{mie,co}$), Rayleigh (β_{ray}), and Mie cross-polar ($\beta_{mie,cr}$) components at 355nm and L1b MSI data of two-channel radiances in the visible band (670nm) and the near-infrared band (865nm). The algorithm first applies wavelet analysis to the ATLID L1b original data with minimum horizontal resolution (0.3km) to reduce signal random noises and averages the noise-reduced data horizontally to obtain the needed resolution data. The noise reduction scheme using wavelet analysis is described in section 3.2.1.2. Next, the algorithm checks data quality and sequentially conducts each procedure (i.e., Feature mask => POP retrieval => Target mask => PBL height => Aerosol component retrieval). The ATLID algorithm will be developed to use all the three-channel data (3ch method) of the L1B data as well as use only two- (2ch method) or one-channel (1ch method) data of the L1B data, anticipating that some of the L1B ATLID data will be insufficient or blank. We design these methods to produce similar products; however, it should be noted that the 3ch method produces the most products with the best quality (i.e., 3ch

> 2ch > 1ch). In the sections that follow, the algorithms for creating the individual products are described. A performance evaluation of the individual algorithms for standard products using simulated data is given in Nishizawa et al. [2024].

3.2.1.2 Noise reduction scheme

It has been reported that a noise reduction based on discrete wavelet transform (DWT) is useful to improve the signal to noise ratio (SN) of lidar measurements [e.g., Fang and Huang 2004]. A noise-reduction scheme using the DWT is developed for ATLID analysis. Two types of support number 2 (D2) and 4 (D4) of Daubechies wavelets are used in the scheme. To reduce random noises more, the developed scheme applies the DWT method using D2 and D4 to lidar signals repeatedly alternately (i.e., D2→D4→D2→D4→…). Examples of noise-reduction analysis using the developed scheme are presented in Fig. 3.2.1.2.1 The scheme is applied to ATLID L1b data simulated using outputs of global aerosol transport model SPRINTARS [Takemura et al., 2002] and added random noise corresponding to an SN of 5. The results indicate that the SN is improved by more than twice for (SN > 10) excepting for Mie-copolar signals for cloudy case.

It should be noted that the smoothing schemes like this developed scheme using wavelet analysis and running average are effective to reduce random noises, while it blunts the signals especially where the signal strengths change significantly (e.g., ground/sea surface and edges of clouds) as presented in Fig. 3.2.1.2.1. To reduce the dulling of the surface return signal and its contamination to the atmospheric signal, the smoothing is applied from the sky to an altitude of 500 m, referring to the Digital Elevation Model (DEM) surface altitude from the EarthCARE auxiliary data.
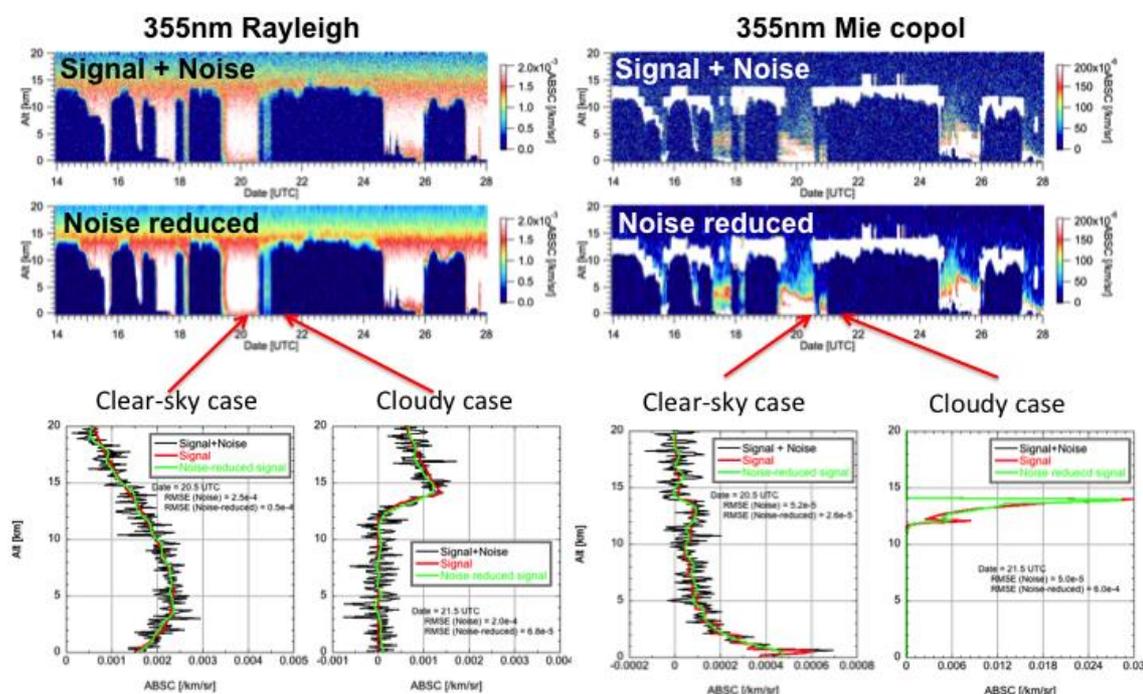

Figure 3.2.1.2.1 Examples applying the noise reduction scheme to the simulated ATLID data. The simulated signals with random noise (upper), noise-reduced signals (middle), and vertical profiles of the signals (lower) are presented. The left figures are signals for the Rayleigh component; the right figures

are signals for the Mie co-polar component.

3.2.1.3 Feature mask product

The scene classification schemes were developed by using ground-based Mie-scattering lidar data [Shimizu et al. 2004; Nishizawa et al. 2007 and 2008a; Okamoto et al. 2007 and 2008] and by using satellite borne Mie-scattering lidar data of CALIOP [Vaughan et al. 2009; Hagihara et al. 2010]. The algorithms identify clear-sky (molecules), aerosols, or cloud layers as well as the surface, subsurface, or layers, where the signal is fully attenuated under optically thick layers using the lidar backscatter signals as well as the supplemental information such as temperature, altitude, and location.

The copolar ($\beta_{atn.M,co}$) and crosspolar ($\beta_{atn.M,cr}$) components of the Mie attenuated backscatter coefficient and Rayleigh attenuated backscatter coefficient ($\beta_{atn.R}$) are given as ATLID L1 data and are described by the following equations with atmospheric parameters:

$$\beta_{atn,M,co} = \beta_{p,co}(z)exp\left\{-2\int_z^{Z_{ATLID}}\left(\alpha_p\left(z^{'}\right)+\alpha_m\left(z^{'}\right)\right)dz^{'}\right\}, \quad (3.2.1.3.1a)$$

$$\beta_{atn,M,cr} = \beta_{p,cr}(z)exp\left\{-2\int_z^{Z_{ATLID}}\left(\alpha_p\left(z^{'}\right)+\alpha_m\left(z^{'}\right)\right)dz^{'}\right\}, \quad (3.2.1.3.1b)$$

$$\beta_{atn,R} = \beta_m(z)exp\left\{-2\int_z^{Z_{ATLID}}\left(\alpha_p\left(z^{'}\right)+\alpha_m\left(z^{'}\right)\right)dz^{'}\right\}. \quad (3.2.1.3.1c)$$

$$\beta_{p,co}(z) = \beta_p(z)\frac{1}{1+\delta_p(z)}, \quad (3.2.1.3.1d)$$

$$\beta_{p,cr}(z) = \beta_p(z)\frac{\delta_p(z)}{1+\delta_p(z)}, \quad (3.2.1.3.1e)$$

where, α_p and δ_p are the extinction coefficient and depolarization ratio of particles (aerosols and clouds), respectively; $\beta_{p,co}$ and $\beta_{p,cr}$ are the copolar and cross-polar components of the particular backscatter coefficient, respectively; α_m and β_m are the molecular extinction coefficient and the molecular backscatter coefficient, respectively; Z is the altitude; and Z_{ATLID} is the altitude of ATLID. The Mie-attenuated backscatter coefficient ($\beta_{atn.M}$) is defined as the sum of the copolar and cross-polar components (i.e., $\beta_{atn.M} = \beta_{atn.M,co} + \beta_{atn.M,cr}$). We use $\beta_{atn,M}$ and $\beta_{atn,R}$ as the diagnostic parameters for P_M and P_R, respectively. The parameter corresponding to the particle backscatter coefficient ($\beta_p = \beta_{p,co} + \beta_{p,cr}$) calculated from the following equation is used as the diagnostic parameter (P_P):

$$P_P = \beta_m(z)\beta_{atn,M}(z)/\beta_{atn,R}(z). \quad (3.2.1.3.2)$$

First, a diagnosis is made on the 0.3 km horizontal resolution data in each layer, according to the following criteria (Fig. 3.2.1.3.1).
(a) If P_M and P_R are not significant due to signal noise and missing data, no diagnosis is made in that layer (classified as "Invalid").
(b) If P_R is significant and P_M is not significant, the layer is classified as "Clear-sky."
(c) P_M is significant, the layer is classified as "Aerosol, Cloud, or Surface."
The significance of P_R and P_M is determined by the magnitude of the SNR (here, an SNR > 3 is adopted).

For layers diagnosed as "aerosol, cloud, or surface," further diagnosis is performed in the following process.

For the surface detection, the criterion is that the P_M is above the threshold value set based on actual ATLID observed data and the relevant layer is below +500 m with respect to the altitude of the DEM surface altitude to prevent misdetection due to clouds with large backscatter coefficients. The layer below the surface is classified as "Sub-surface." It should be noted that P_M is subject to attenuation by clouds, aerosols, and molecules above, this variability increases the uncertainty of surface detection. Therefore, the surface detection is conducted using P_M corrected for attenuation using near-surface and significant $\beta_{atn,R}$. Several instances were observed where surface detection failed, and the surface was not detected. To overcome this, the following improvements were implemented:

(1) This was particularly evident in the horizontal 1 km average product and the horizontal 10 km moving average product. The primary cause was the reduction of the surface reflection signal strength due to signal smoothing in the L1 data, including averaging. Therefore, the surface detection flag (Feature mask product) estimated using the 0.3 km horizontal data was extended to the 1 km horizontal and 10 km moving average products to improve surface detection.

(2) When the Mie signal from the upper layer contacting the detected surface layer is large, that layer is considered the surface, considering the vertical continuity of the signal.

(3) For profiles where the surface could not be detected, the surface is determined by referencing Digital Elevation Model (DEM) data. If the Mie signal from the upper layer contacting the determined surface is large, that layer is classified as "Unknown" layer.

In addition, some cases were observed where relatively strong atmospheric signals contaminated by surface return signals were misidentified as clouds. These cases of cloud-surface misidentification were also reduced by the aforementioned improvements.

For the cloud detection, two procedures are performed based on the cloud-mask scheme developed for the CALIOP and shipborne lidar measurements [Hagihara et al. 2010 and Okamoto et al. 2008]. First, the cloud layer is detected using the following vertically variable criteria.

$$P_M > P_{th} = 0.5\beta_{c,th} \exp(-2\tau_m)\{1 - \tanh(z - z_c)\}, \qquad (3.2.1.3.3a)$$

$$P_P > P_{th} = 0.5\beta_{c,th}\{1 - \tanh(z - z_c)\}. \qquad (3.2.1.3.3b)$$

where, τ_m is the molecular optical thickness up to an altitude (z) from the altitude of the ATLID. z_c is given as 5 km, and $\beta_{c,th}=10^{-5.25}$ ($\sim5.6\times10^{-6}$) [/m/sr]. The validity of these threshold values was discussed in detail by Hagihara et al. [2010] and Okamoto et al. [2008]. Statistical analyses of cloud and aerosol backscatter coefficient data over several years from long-term ground-based observations by HSRL [Jin et al. 2020] and Raman lidar [Nishizawa et al. 2017] also supported the value of $\beta_{c,th}$. If the P_R of the target layer is significant, the Equation 3.2.1.3.3b is used as the criteria; otherwise, Equation 3.2.1.3.3a, is used. The advantage of using P_P as a diagnostic parameter is that it can eliminate attenuation due to clouds/aerosols from the ATLID to the target layer. However, the calculation of the P_P requires $\beta_{atn.R}$ in addition to $\beta_{atn.M}$, which has a disadvantage in that it cannot be diagnosed if the SNR of $\beta_{atn.R}$ is insufficient. Therefore, a hybrid method is used here, where P_M is used if P_P cannot be used as a diagnostic parameter. After identifying the cloud layer using these criteria, a continuity test is performed to suppress misdetection due to signal noise [Hagihara et al. 2010]. The continuity test is conducted on a 5-bin horizontal and 3-bin vertical window centered on the diagnostic layer, in accordance with the continuity test method used by Hagihara et al. [2010]. If more than half (i.e. more than 8 bins) of the total 15 bins are clouds, the target layer is determined to be a "Cloud". However, if the number of cloud layers was less than half of the total, but at

least one of the cloud layers was included, the layer was designated as "Unknown." For 0.3 km and 1 km resolution products, the clear-sky or aerosol layer are not diagnosed separately from the SN's point of view, and together they are classified as "Clear-sky or aerosol." The fully attenuated layer is diagnosed when no surface is detected; the layers below the lowest layer of "clear-sky or aerosol" or "cloud" are classified as "Fully attenuated."
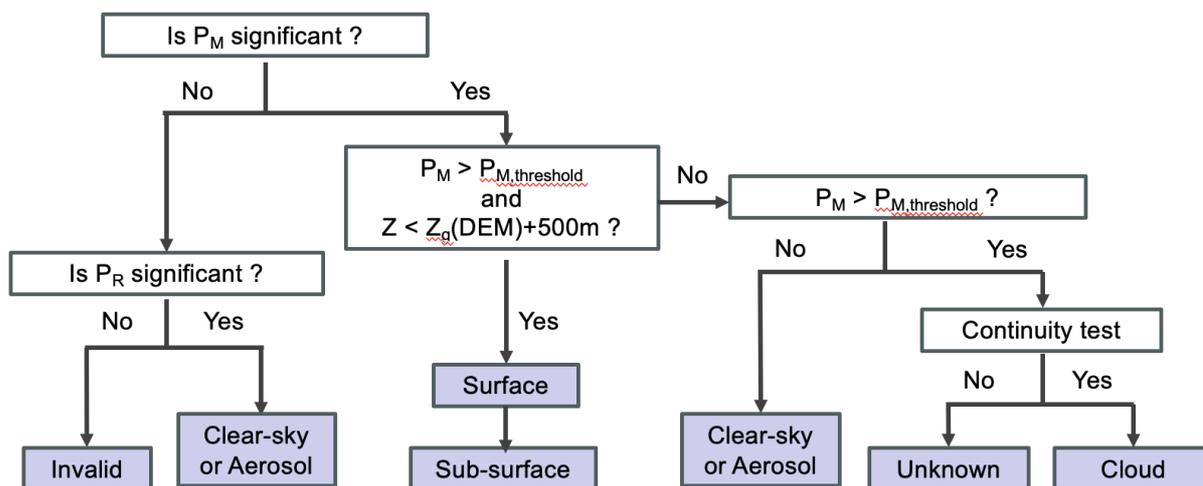

Figure 3.2.1.3.1. Identification flow of feature mask scheme for 0.3km-horizontal resolution data.

Next, a diagnosis is made on the 1 km horizontal resolution data (Fig. 3.2.1.3.2). Diagnostics similar to those performed on the 0.3 km horizontal data are performed; the layer types of "Cloud," "Clear-sky or aerosol," "Surface," " Sub-surface," "Fully attenuated," "Invalid," or "Unknown" are identified. The following method is used to identify the cloud layers. The 1 km horizontal resolution data is calculated by averaging several horizontal layers (~4 bins) of the 0.3 km horizontal resolution data. This improves the SNR, but it also causes dulling of the signal at the cloud edges, which leads to cloud layer misidentification. To suppress this, we use the FM product estimated using the 0.3 km horizontal resolution data (FM(0.3)); if more than half of the total number of the layers of the FM (0.3) product in the target layer for the 1 km horizontal resolution data is identified as "Cloud", the target layer for the 1 km horizontal resolution data is determined to be "Cloud" [Hagihara et al. 2010]. However, if the number of cloud layers (N_C) is less than half of the total, but at least one of the cloud layers is included, the target layer is designated as "Unknown." In addition, the possibility of identifying optically thin clouds or aerosols compared to the 0.3 km data, especially at high altitudes, also arises because of the improved SNR by the horizontal averaging. Equations 3.2.1.3.4a and 3.2.1.3.4b are then applied to the 1 km horizontal resolution data with the addition of a criterion for high altitude to Equations 3.2.1.3.3a and 3.2.1.3.3b.

$$P_M > P_{th} = 0.5\beta_{c,th}\exp(-2\tau_m)\{1 - \tanh(z - z_c)\} + 0.5\beta_{c,th2}\exp(-2\tau_m)\{1 + \tanh(z - z_c)\}, \quad (3.2.1.3.4a)$$

$$P_P > P_{th} = 0.5\beta_{c,th}\{1 - \tanh(z - z_c)\} + 0.5\beta_{c,th2}\{1 + \tanh(z - z_c)\}. \quad (3.2.1.3.4b)$$

$\beta_{c,th2}$ is the threshold for identifying the layer that may be a cloud at high altitudes and is set based on actual ATLID data. If the criteria is satisfied, the layer is marked as "Unknown," and if not, it is marked as "Aerosol or clear-sky."

Finally, a diagnosis is made on the 1[*] km horizontal resolution data (Fig. 3.2.1.3.2). Diagnostics similar to those performed on the 1 km horizontal resolution data are performed; the layer types of "Cloud," "Aerosol," "Clear-sky," "Surface," "Sub-surface," "Fully attenuated," "Invalid," or "Unknown" are identified.

Unlike the FM for the 1 km horizontal resolution data, the layer diagnosed as "Aerosol or clear-sky" is classified into the "Aerosol" when the P_M is significant or "Clear-sky" when the P_M is not significant.
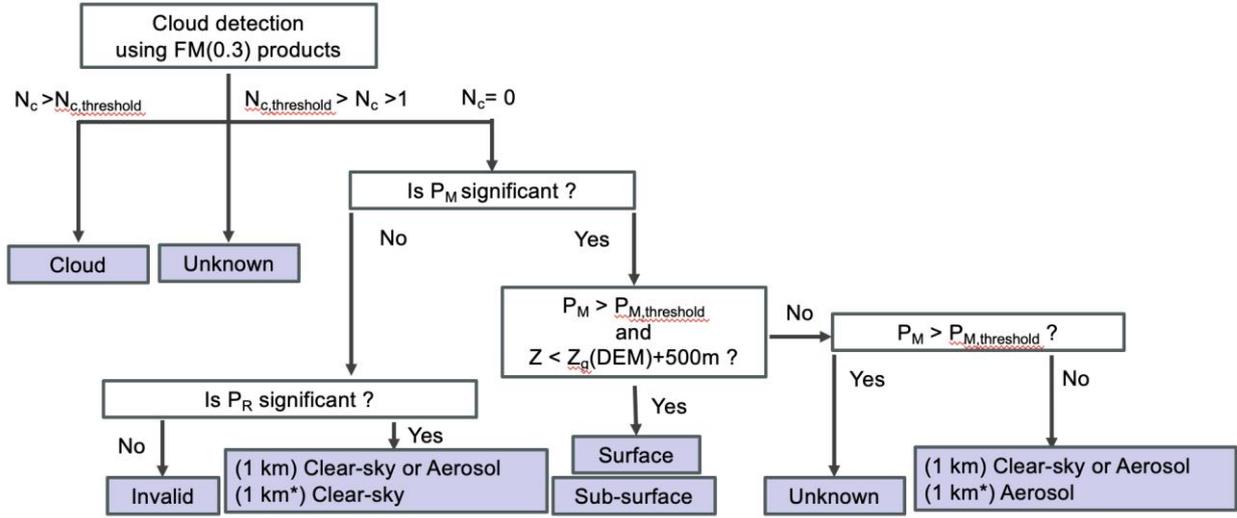

Figure 3.2.1.3.2. Identification flow of feature mask scheme for 1km- or 1*km-horizontal resolution data.

3.2.1.4 Particle optical properties (POP) products

In theoretical, extinction coefficient α_p, backscatter coefficient β_p lidar ratio S_p, and depolarization ratio δ_p of particles can be directly derived using the observed parameters of $\beta_{mie,co}$, $\beta_{mie,cr}$, and β_{ray} by the following equations,

$$\alpha_p = 0.5 \frac{\partial}{\partial z} ln \frac{\beta_m}{\beta_{ray}} - \alpha_m - \alpha_{O3} \qquad (3.2.1.4.1a)$$

$$\beta_p = \frac{\beta_{mie,co}+\beta_{mie,cr}}{\beta_{ray}} \beta_m \qquad (3.2.1.4.1b)$$

$$\delta_p = \frac{\beta_{mie,cr}}{\beta_{mie,co}} \qquad (3.2.1.4.1c)$$

$$S_p = \frac{\alpha_p}{\beta_p} \qquad (3.2.1.4.1d)$$

Observed data with a sufficient signal-to-noise ratio (SN ratio) are needed to derive the above parameters (α_p, β_p, S_p, and δ_p) with sufficient precision. In particular, the retrieval precision of α_p is very sensitive to the SN ratio [e.g., Liu et al., 1999]. It is essential to average and/or smooth the observed data to improve the SN ratio (see section 3.2.1.2). Even if the noise reduction scheme in 3.2.1.2 is applied to the lidar data, the SN ratios do not become sufficiently small, making it difficult to derive the POP from the observations. Therefore, we simultaneously optimize the vertical profiles of the POP to the measurements with the smoothness constraints for the vertical profiles of the POP. The optimization based on the method of the maximum likelihood was employed. The state vector x is the vertical profiles of α_p, S_p, and δ_p, and the best solution of the state vector minimizes the following cost function:

$$f(x) = \sum_i \frac{\left\{ ln\left(\beta_{mie,co}^{obs}(z_i) - \beta_{mie,co}^{min}\right) - ln\left(\beta_{mie,co}^{cal}(z_i) - \beta_{mie,co}^{min}\right)\right\}^2}{w_{mie,co}^2(z_i)}$$

$$+\sum_i \frac{\left\{ln\left(\beta_{mie,cr}^{obs}(z_i)-\beta_{mie,cr}^{min}\right)-ln\left(\beta_{mie,cr}^{cal}(z_i)-\beta_{mie,cr}^{min}\right)\right\}^2}{w_{mie,cr}^2(z_i)}$$

$$+\sum_i \frac{\left\{ln\left(\beta_{ray}^{obs}(z_i)-\beta_{ray}^{min}\right)-ln\left(\beta_{ray}^{cal}(z_i)-\beta_{ray}^{min}\right)\right\}^2}{w_{ray}^2(z_i)}$$

$$+\sum_i \frac{\left\{ln\left(\alpha_p(z_i)\right)-ln\left(\alpha_p(z_{i+1})\right)\right\}^2}{w_{\alpha_p}^2}$$

$$+\sum_i \frac{\left\{ln\left(S_p(z_i)\right)-ln\left(S_p(z_{i+1})\right)\right\}^2}{w_{S_p}^2}$$

$$+\sum_i \frac{\left\{ln\left(\delta_p(z_i)\right)-ln\left(\delta_p(z_{i+1})\right)\right\}^2}{w_{\delta_p}^2}, \qquad (3.2.1.4.2)$$

where z_i is i-th altitude, "*obs*" indicates the measurements, "*cal*" indicates the values calculated from $\boldsymbol{x}$ by Equations 3.2.1.3a-c, $w_{mie,co/mie,cr/ray}$ is measurements uncertainties, $w_{\alpha_p/S_p/\delta_p}$ is weight for determine the strength of the smoothness constraint, and "*min*" indicates the possible minimum values of each measurement. The measurement uncertainties $w_{mie,co/mie,cr/ray}$ are calculated from the signal noises such as shot noise, dark noise, and CCD read-out noise which are evaluated before the launch of the Earth-CARE satellite. The values of $w_{\alpha_p/S_p/\delta_p}$ are given by 1.0. A logarithmic transformation is applied to the measured and calculated values because the transformation reduces the differences of the dynamic ranges of each term in Eq. 3.2.1.4.2 and enables a fast and stable minimization of $f(\boldsymbol{x})$ [Kudo et al., 2016]. However, the measurements may have negative values due to noises, and the logarithmic transformation cannot be applied to the negative values. Therefore, we subtracted the possible minimum values from the measured and calculated values. The fourth, fifth, and sixth terms in Eq. 3.2.1.4.2 are the smoothness constraints for the vertical profiles of α_p, S_p, and δ_p. The smoothness of the vertical profile is obtained by minimizing the differences of the values at two adjacent altitudes. The minimization of $f(\boldsymbol{x})$ is conducted by the iteration of $ln(\boldsymbol{x}_{i+1}) = ln(\boldsymbol{x}_i) + \gamma\Delta\boldsymbol{x}_i$ in $ln(\boldsymbol{x})$ space. The vector $\Delta\boldsymbol{x}_i$ at the i-th step is determined by the Gauss-Newton method, and the scalar γ is determined by a line search method with Armijo rule [Nocedal and Wright, 2006]. The convergence criterion for the iteration is that the difference between $f(\boldsymbol{x}_i)$ and $f(\boldsymbol{x}_{i+1})$ should be smaller than a given threshold.

To estimate the optical properties of optically thick scatterers such as clouds, it is essential to consider multiple scattering. The multiple scattering has been considered in CALIPSO and ground-based lidar analysis by introducing η-factor (e.g., Chen et al. 2002, Young 2013, Cairo et al. 2021), and thus the η-factor is introduced into this algorithm to estimate the optical properties of clouds. Sato et al. (2018) developed a practical model to determine the time-dependent lidar attenuated backscatter coefficient, in which an analytical expression for the high-order phase function was implemented to reduce computational cost; furthermore, Sato et al. (2019) developed a vectorized physical model (VPM) which is a physical model extended with a polarization function, to analyze the observed depolarization ratio due to multiple scattering from water clouds. The introduction of these physical models is a promising as a more advanced and accurate approach in estimating cloud optical properties, considering multiple scattering from clouds.

EARTHCARE

NICT JAXA
宇宙航空研究開発機構
Japan Aerospace Exploration Agency

Fig. 3.2.1.4.2 shows an example of estimating the optical properties of atmospheric particles. Pseudo-L1 data of ATLID is calculated using the aerosol and cloud distribution observed by CALIOP from the African continent to the Atlantic Ocean. To facilitate comparison with the application result, α_p, S_p, and δ_p at 355nm of clouds are 10 km^{-1}, 20 sr, and 0, respectively; those of aerosols are 0.1 km^{-1}, 50 sr, and 0.05, respectively. Therefore, the layer (red or green) in which the value of $\beta_{mie,co}$ exceeds 0.008$km^{-1}sr^{-1}$ corresponds to the cloud layer or the uppermost layer of the cloud. The layer with a value lower than that (blue, light blue, white) corresponds to aerosols, atmospheric molecular layers, or, if there are clouds in the sky, the layers where the signal is attenuated by the clouds. Random noise such that the SN is about 5 is added to all the pseudo-L1 data. The estimated α_p, S_p, and δ_p for clouds and aerosols are estimated with an error of about 30%.
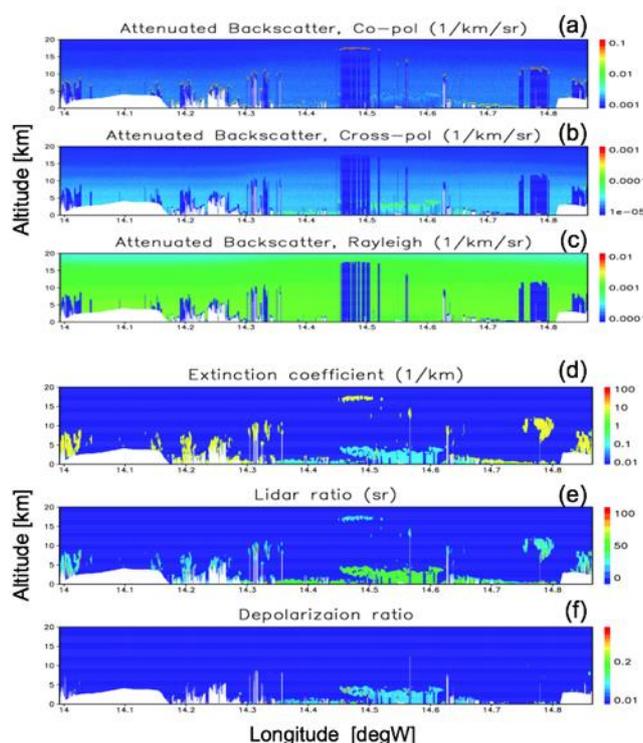
Figure 3.2.1.4.2 Examples of particle optical property retrieval.
(a) $\beta_{mie,co}$, (b) $\beta_{mie,cr}$, and (c) β_{ray} are simulated attenuated backscatter coefficients with signal noises. (d) α_p, (e) S_p, and (f) δ_p are retrieved by MAP method using the simulated $\beta_{mie,co}$, $\beta_{mie,cr}$, and β_{ray}.

3.2.1.5 Target mask products

Particle type classification schemes using satellite-borne MSL data of CALIOP have been developed [e.g., Omar et al. 2009, Yoshida et al. 2010]. These schemes identify aerosol types (e.g., maritime and polluted dust) and cloud types (e.g., water-droplet and ice-crystal clouds) using the intensity, color ratio, and depolarization ratio of the MSL backscatter signals, as well as supplemental information (e.g., temperature, altitude, and location). Since ATLID is an HSRL with a polarization measurement function, extinction data and lidar ratio data as well as depolarization ratio data can be used for aerosol and cloud type classification. However, the color ratio information cannot be used, since ATLID is a single-wavelength lidar.

The developed ATLID algorithm uses the derived feature-mask products and POP products as well as L1 data. The algorithm classifies aerosol type for the slab-layer that the feature-mask scheme identifies as "Aerosol", and it classifies cloud type for the slab-layer that the feature-mask scheme identifies as "Cloud".

Aerosol particles are classified as six aerosol types ("Smoke," "Pollution," "Marine," "Pristine," "Dust," and "Dusty mixture") with "Unknown" in Figure 3.2.1.5.1. We perform a cluster analysis of the aerosol optical properties estimated from data of the AErosol RObotic NETwork (AERONET) sun/sky photometer [e.g. Holben et al., 1998; Giles et al., 2019] and determined the aerosol optical properties at 355 nm. The optical properties of the four aerosol types (smoke, pollution, marine, and pristine) are determined using cluster analysis of the AERONET level 2 product for years of 1992 to 2012. First, δ_a and S_a at 355, 532, and 1064 nm, which are usually observed by the HSRL and Raman lidar measurements, are calculated using the refractive indices at 440, 675, 870, and 1020 nm, size distributions of fine and coarse modes, and the sphericity of scattering light derived from the AERONET inversion algorithm [Dubovik et al., 2006] for each AERONET data sample. The refractive indices at 532 nm are interpolated and those at 355 and 1064 nm are extrapolated using those of AERONET product from 440 to 1020 nm. The non-spherical particle shape is assumed to be the AERONET spheroid model [Dubovik et al., 2006]. Next, we adopt the fuzzy c-means method [Dunn, 1973; Bezdek, 1981] to conduct a cluster analysis. This method is based on minimizing the following objective function:

$$J = \sum_{i=1}^{N} \sum_{k=1}^{K} g_{ik}^2 \left\| x_i - c_k \right\|^2 . \quad (3.2.1.6.1)$$

where g_{ik} is the degree of membership of xi to the k-th cluster, x_i is the observed data, c_k is the center of the k-th cluster. Partitioning is conducted through an iterative optimization of the J with updates of g_{ik} and c_k. Based on this cluster analysis, the center of cluster c_k is assumed to be the representative value of the selected cluster parameter. We select 12 parameters used in the cluster analysis to classify the aerosol properties. These parameters are δ_a and S_a at 355, 532, and 1064 nm and the imaginary part of the refractive index and fine mode fraction (FMF) to the total (fine+coarse) AOT at 440, 675, and 870 nm. Finally, we define the characteristic results of the cluster as the optical properties of the aerosol type. The cluster, which is fine-mode dominated and light-absorbing aerosol, derived from the cluster analysis of the source regions of African biomass burning aerosols, is assumed as the smoke type. The cluster, which is fine-mode dominated and light-absorbing aerosol, derived from the cluster analysis of the source regions of Asian air pollution, is assumed as the pollution type. The marine and pristine types are defined based on islands analysis. The marine type has the largest particle size with single scattering albedo (SSA) of 0.98. The pristine type has a smaller particle size than the marine type, with the SSA of 0.98.

The difference in δ_a and S_a of non-spherical dust particles between observations and theoretical calculations remain large [Tesche et al., 2019], so that δ_a and S_a of the dust type at 355 nm are referred to as the averaged values of the Raman lidar observations in Morocco [Freudenthaler et al. 2009; Tesche et al. 2009], Germany [Wiegner et al. 2011], and Tajikistan [Hofer et al. 2017]. The dusty mixture type is defined as a mixture of dust and smoke in ratios of 0.65 and 0.35, respectively. Aerosol particles with high depolarization ratios and low lidar ratios are rarely observed; therefore, the unknown aerosol type is defined as aerosols with δ_a > 0.12 and S_a < 21 sr, which are determined by the values of the intersection of the border line between dust and pristine types and that between marine and pristine types, as shown in Figure 3.2.1.5.1.
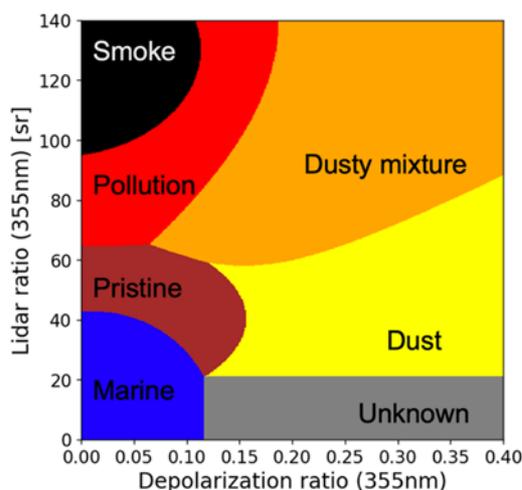
Figure 3.2.1.5.1 Lidar ratio – depolarization ratio diagram for classifying aerosol types [Nishizawa et al., 2024].

For clouds, four types of "warm water," "supercooled water," two-dimensional ice (2D-ice)," or three-dimensional ice (3D-ice)" are identified by a two-dimensional diagrammatic method using signal attenuation and depolarization ratio. The two-dimensional diagrammatic method using signal attenuation and depolarization ratio was developed by Yoshida et al. [2010] for cloud type classification using CALIOP data and is adopted and improved for ATLID. Details of the method are given in section 4.1.1.3.

3.2.1.6 Planetary boundary layer (PBL) Height

The planetary boundary layer (PBL) height can be detected by aerosol lidars using the gradient method (Lammert and Bösenberg, 2006), the wavelet covariance transform (WCT) method (Brooks, 2003), or other methods (e.g., the standard deviation method by Menut et al., 1999). Among above methods, the WCT method is less affected by noise (Qu et al., 2017), and is promising for the spaceborne lidar (Kim et al., 2021).

Based on the WCT method, we developed an algorithm of PBL height detection for ATLID. As input data, lidar data altitude, Mie attenuated backscatter ($\beta_{mie,co}+\beta_{mie,cr}$), Rayleigh attenuated backscatter (β_{ray}), and feature mask are used. The WCT is calculated from the following equation:

$$WCT(a,b) = \frac{1}{a}\int_{z_{min}}^{z_{max}} B(z)h\left(\frac{z-b}{a}\right)dz, \qquad (3.2.1.6.1)$$

Where B is the normalized backscattering ratio (the ratio of Mie attenuated backscatter to Rayleigh attenuated backscatter), a and b are the dilation and the centered location of the Haar function h, which is defined as

$$h\left(\frac{z-b}{a}\right) = \begin{cases} +1: b - \frac{a}{2} \leq z < b, \\ -1: b \leq z \leq b + \frac{a}{2}, \\ 0: \text{elswere.} \end{cases} \qquad (3.2.1.6.2)$$

Here, the target altitude (height above the surface) is set in between z_{min} and z_{max}, which are 0.3 and 5 km, respectively. B is normalized to 1.0 for the height from the surface to 1 km to reduce the dependency of aerosol concentrations. For the cases where the WCT exceeds a threshold value, the first WCT peak from z_{min} is determined as the PBL height. The threshold and dilation width are determined from a simulated lidar signals based on ground-based HSRL data (Jin et al., 2020) with random noise according to the errors in the ATLID attenuated backscatter reported by do Carmo et al., (2021), and are set to 0.2 and 1.0 km, respectively. If cloud pixels are found in the feature mask from z_{min} to PBL height, the record are excluded from the PBL height detection.

3.2.2 Research Product

3.2.2.1 Introduction

We have developed algorithms to retrieve vertical profiles of several main aerosol components in the atmosphere such as dust, sea-salt, light absorbing particle (e.g., black carbon), and water-soluble particles (e.g., sulfates, nitrates) using ground-based lidar data [Sugimoto et al. 2003; Nishizawa et al., 2007, 2008a,b, 2011, 2017] and applied them to actual data. These retrieval algorithms have also been applied to the space-borne lidar CALIOP, and the retrieved global aerosol data has been published as EarthCARE Research A-train product by JAXA (https://www.eorc.jaxa.jp/EARTHCARE/A-train/A-train_monitor.html). In the above algorithms and analysis, Mie scattering lidar, Raman lidar, and HSRL using lasers at 532nm and 1064nm are used mainly. On the other hand, ATLID uses a laser at 355nm, which is a different wavelength, but promises to improve on the above retrieval techniques to enable global 3D (horizontal and altitude) estimation for each aerosol components.

3.2.2.2 Aerosol component product (ATLID stand-alone algorithm)

Extinction coefficients at 355nm for aerosol components at each slab layer are retrieved. This method assumes the external mixture of four main aerosol components in the atmosphere that are dust, sea-salt, water-soluble particles, and light-absorbing particles such as black carbon. Water-soluble particles are defined as small particles with weak light absorption, consisting of sulfates, nitrates, and organic substances. It should be noted that "Aerosol type" (see section 3.2.1.5) is defined as the compound of several kinds of "aerosol components".

The algorithm retrieves extinction coefficients at 355nm for four aerosol components at each slab layer using α_p, $\beta_{p,co}$, and $\beta_{p,cr}$ data derived in the POP retrieval procedure (section 3.2.1.4). Note that the backscatter coefficient $\beta_p = \beta_{p,co} + \beta_{p,cr}$, the depolarization ratio $\delta_p = \beta_{p,cr} / \beta_{p,co}$, and the lidar ratio $S_p = \alpha_p / \beta_p$.

For land, the method discriminates water-soluble, light-absorbing, and dust particles and retrieves their extinction coefficients at each slab layer. The method for ocean also retrieves the extinction coefficients for the four aerosol components (water-soluble, light-absorbing, dust, and sea-salt) at each slab layer using the ATLID data as well as sea-surface wind data. In developing the methods, we effectively use the ideas and techniques of Nishizawa et al. [2008b, 2011, 2017].

At first, the method for land is described (Fig. 3.2.2.2.1). The method uses the absorption and depolarization properties of aerosols to classify the aerosol components. S_p is sensitive to the absorption property, and the

S_p value of strong light-absorbing particles (e.g., black carbon) is higher (see Table 3.2.2.2.1). Nishizawa et al. [2008b] developed an algorithm to retrieve extinction coefficients at 532nm for water-soluble, black carbon, and dust particles in each slab layer using the 1α (532nm) + 2β (532 and 1064nm) data measured with a HSRL ($1\alpha+2\beta$ algorithm), and demonstrated that extinction data were effective in retrieving black carbon particles. The depolarization ratio δ_p, which is sensitive to particle shape, has been used to discriminate between spherical and nonspherical particles [Sugimoto et al., 2003]. Nishizawa et al. [2011] computed the δ_p value as well as other optical properties of dust particles assuming that the dust is spheroidal. They used the spheroid dust optical model in dust retrieval from the 2β (532 and 1064nm) + 1δ (532) Mie scattering lidar data ($2\beta+1\delta$ algorithm). Nishizawa et al. [2017] integrates these methods, achieves simultaneous estimation of four aerosol components, and demonstrates the performance using $1\alpha+2\beta+1\delta$ Raman lidar data. Thus, we can discriminate between strong-absorption and weak-absorption particles using S_p, and between spherical and non-spherical particles using δ_p.
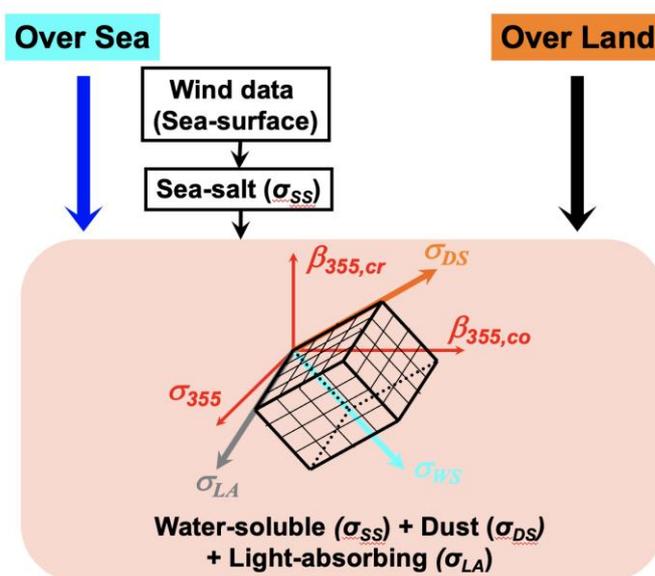
Fig. 3.2.2.2.1 Conceptual diagram of the algorithm.

The relationship between α_p, $\beta_{p,co}$, and $\beta_{p,cr}$ and the estimated parameter $\sigma_{i,355}$ are represented by the following equations.

$$\alpha_p = \sum_{i=1}^{3} \sigma_{i,355} \qquad (3.2.2.2.1a)$$

$$\beta_{p,co} = \sum_{i=1}^{3} \frac{\sigma_{i,355}}{S_{i,355}(1+\delta_{i,355})} \qquad (3.2.2.2.1b)$$

$$\beta_{p,cr} = \sum_{i=1}^{3} \frac{\sigma_{i,355}\delta_{i,355}}{S_{i,355}(1+\delta_{i,355})} \qquad (3.2.2.2.1c)$$

Subscript i denotes aerosol components (e.g., water-soluble (i = 1), light-absorbing (i = 2), or dust (i = 3)). The $S_{i,355}$ and $\delta_{i,355}$ for each aerosol component are modeled to retrieve $\sigma_{i,355}$ for the aerosol components. We specify the microphysical properties (e.g., size distribution and refractive index) of each aerosol component. We assume a volume lognormal size distribution for each aerosol component.

$$\frac{dV}{dlnr} = \frac{V_o}{\sqrt{2\pi}lnS_d} exp\left\{-0.5\frac{(lnr-lnR_m)^2}{lnS_d^2}\right\} \qquad (3.2.2.2.2)$$

The $S_{i,355}$ values for water-soluble, light-absorbing, and sea-salt particles are computed from the prescribed size distribution and refractive index using the Mie theory, assuming that the particles are spherical. The

values of $\delta_{i,355}$ for water-soluble, light-absorbing, and sea-salt particles are given empirically. The values of $S_{i,355}$ and $\delta_{i,355}$ for dust particles are computed using software developed by Dubovik et al. [2006], assuming that the particles are spheroidal.

The size distribution and refractive index for each aerosol component should be prescribed appropriately. As an example, we indicate the optical properties of each aerosol component computed by using the size distribution and refractive index prescribed in Nishizawa et al. [2008a, b, 2011, 2017] in Table 3.2.2.2.1. Here, $S_{i,355}$ and $\delta_{i,355}$ are key parameters in estimating $\sigma_{i,532}$ (Eqs. 3.2.2.2.1). If $S_{i,355}$ and $\delta_{i,355}$ for each aerosol component are similar, we cannot obtain an independent solution for $\sigma_{i,532}$. However, as indicated in Table 3.2.2.2.1, $S_{i,355}$ and $\delta_{i,355}$ for each aerosol component differ considerably. Hence, we can retrieve the extinction coefficients for each aerosol component in a given slab layer.

Table 3.2.2.2.1 Microphysical and optical properties of aerosol components[a]

Property	Water-soluble	light-absorbing	Sea-salt	Dust
R_m	0.19	0.05	3.0	2.0
s_d	1.6	2.0	2.1	2.2
$m_{r,355}$, $m_{i,355}$	1.42, 2×10^{-3}	1.75, 5×10^{-1}	1.37, 6×10^{-8}	1.51, 9×10^{-3}
S_{355}	56	101	16	80
δ_{355}	0	0	0	0.28

[a]The mode radius (R_m), standard deviation (s_d), and complex refractive index ($m_r - i\, m_i$) for the four aerosol components used in Nishizawa et al. [2008a,b, 2011, 2017] are listed. The optical parameters of the lidar ratio (S_{355}) and depolarization ratio (δ_{355}) for the four aerosol components are calculated using the size distribution and complex refractive index. The unit of R_m is μm, and that of S is sr. The theoretical δ_{355} value for spherical particles ($\delta_{355} = 0$) is listed as the δ_{355} value for each aerosol component except for dust.

Next, the method for the ocean is described. We consider estimating the extinction coefficients of the sea-salt component from sea-surface wind data, as in the aerosol transport model [e.g., Takemura et al., 2002]. This means that the four aerosol components (water-soluble, dust, light-absorbing, and sea-salt) can be retrieved simultaneously from the three-channel ATLID data and the sea-surface wind data. Reanalysis data provide global sea-surface wind data. The volume concentration at the surface is calculated using the surface wind speed [Erickson et al., 1986]. The vertical profiles are given by assuming the same profile as that of water-soluble particle. We retrieve extinction coefficients for dust, light-absorbing, and water-soluble components using α_p, $\beta_{p,co}$, and $\beta_{p,cr}$ corrected for the sea-salt component (α_c, $\beta_{c,co}$, and $\beta_{c,cr}$) as follows.

$$\alpha_c = \alpha_p - \sigma_{SS,355} \qquad (3.2.2.2.3a)$$

$$\beta_{c,co} = \beta_{p,co} - \frac{\sigma_{SS,355}}{S_{SS,355}(1+\delta_{SS,355})} \qquad (3.2.2.2.3b)$$

$$\beta_{c,cr} = \beta_{p,cr} - \frac{\sigma_{SS,355}\delta_{SS,355}}{S_{SS,355}(1+\delta_{SS,355})} \qquad (3.2.2.2.3c)$$

The algorithms for land and ocean are applied to all layers identified as "Aerosol" by the feature mask (section 3.2.1.3). Thus, it is applied to the aerosol layer above and below cloud layers as well as under clear

skies. The algorithms estimate the vertical profiles for the three aerosol components that best reproduce the profiles of α_p, β_{co}, and β_{cr}. As a numerical solution to realize it, the MAP method used in the ATLID-MSI synergy algorithm (section 4.2.1.2) is also applied to these algorithms.

We have been testing and improving the algorithms using 532nm and 355nm HSRL data on the ground (Fig. 3.2.2.2.2). In the future, we will not only apply the algorithm to ground data, but also to real data from EarthCARE to improve and validate the algorithms.
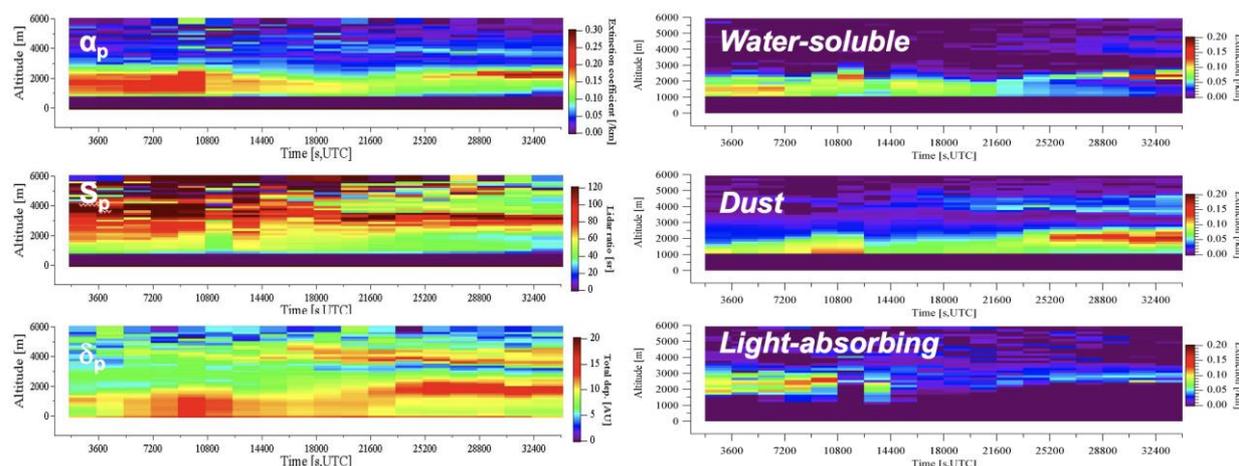
Fig. 3.2.2.2.2 Examples of application of the algorithm to ground-based HSRL data. The data used are 532nm HSRL data measure at NIES, Tsukuba, Japan. The left figures indicate derived extinction coefficients, backscatter coefficients, and total depolarization ratio. The right figures indicate retrieved extinction coefficients at 532nm for water-soluble, dust, and light-absorbing particles.

Reference

Albrecht, B. A., Aerosols, cloud microphysics, and fractional cloudiness. Science, 245, 1227–1230, 1989.

Ansmann A., M. Riebesell, U. Wandinger, C. Weitkamp, and W. Michaelis, Combined Raman elastic-backscatter LIDAR for vertical profiles of moisture, particle extinction, backscatter and LIDAR ratio, Appl. Phys., 55, 18-28, 1992.

Bezdek, J. C., Pattern recognition with fuzzy objective function algorithms, Plenum Press, 1981.

Böckmann, C., Hybrid regularization method for ill-posed inversion of multiwavelength lidar data in the retrieval of aerosol size distributions, Appl. Opt. 40, 1329–1342, 2001.

Brooks, I. M., Finding boundary layer top: application of a wavelet covariance transform to lidar backscatter profiles, J. Atmos. Oceanic Technol., 20, 1092-1105, 2003.

Cairo, F., Muro, M. D., Cnels, Marcel, Liberto, L. D., Bucci, S., Legras, B., Kottayil, A., Soccione, A., Chisu, S.: Lidar observations of cirrus clouds in Palau ((7°33′N, 134°48′E), Atmos. Chem. Phys., 21, 7947-7961, https://doi.org/10.5194/acp-21-7947-2021, 2021.

Charlson, R. J., S. E. Schwartz, J. M. Hales, R. D. Cess, J. A. Coakley, Jr., J. E. Hansen, and D. J. Hofmann, Climate forcing by anthropogenic aerosols. Science, 255, 423–430, 1992.

Chen, W.-N., Chiang, C.-W., Nee, J.-B.: Lidar ratio and depolarization ratio for cirrus clouds, Appl. Opt., 41, 6470-6476, 2002.

Do Carmo, J. P., de Villele, G., Wallace, K., Lefebvre, A., Chose, K., Kanitz, T., Chassat, F., Corselle, B., Belhadj, T., Bravetti, P. ATmospheric LIDar (ATLID): Pre-launch testing and calibration of the European Space Agency instrument that will measure aerosols and thin clouds in the atmosphere,

Atmosphere, 12, 76, 2021.

Dubovik, O., A. Sinyuk, T. Lapyonok, B. N. Holben, M. Mishchenko, P. Yang, T. F. Eck, H. Volten, O. Munoz, B. Veihelmann, W. J. van der Zande, J. Leon, M. Sorokin, and I. Slutsker, Application of spheroid models to account for aerosol particle nonsphericity in remote sensing of desert dust, J. Geophys. Res., 111, D11208, doi:10.1029/2005JD006619, 2006.

Dunn, J. C., A fuzzy relative of the ISODATA process and its use in detecting compact well-separated clusters, J. of Cybernetics, 3, 3, 32-57, 1973.

Fang, H.-T., and D.-S. Huang, Noise Reduction in Lidar Signal Based on Discrete Wavelet Transform, Opt. Comm., 233, 67-76, 2004.

Fernald, F. G., Analysis of atmospheric lidar observations: some comments, Appl. Opt., 23, 652-653, 1984.

Freudenthaler, V., M. Esselborn, M. Wiegner, B. Heese, M. Tesche, A. Ansmann, D. Müller, D. Althausen, M. Wirth, and A. Fix, Depolarization ratio profiling at several wavelengths in pure Saharan dust during SAMUM 2006, Tellus B, 61, 165–179, 2009.

Giles, D. M., A. Sinyuk, M. G. Sorokin, J. S. Schafer, A. Smirnov, I. Slutsker, T. F. Eck, B. N. Holben, J. R. Lewis, J. R. Campbell, E. J. Welton, S. V. Korkin, and A. I. Lyapustin, Advancements in the Aerosol Robotic Network (AERONET) Version 3 database – automated near-real-time quality control algorithm with improved cloud screening for Sun photometer aerosol optical depth (AOD) measurements, Atmos. Meas. Tech., 12, 169–209, 2019.

Hagihara Y., H. Okamoto, and R. Yoshida, Development of a combined CloudSat-CALIPSO cloud mask to show global cloud distribution, J. Geophys. Res., 115, D99H33, 2010.

Haywood, J. M. and V. Ramaswamy, Global sensitivity studies of the direct radiative forcing due to anthropogenic sulfate and black carbon aerosols, J. Geophys. Res., 103, 6043-6058, 1998.

Hofer, J., D. Althausen, S. F. Abdullaev, A. N. Makhmudov, B. I. Nazarov, G. Schettler, R. Engelmann, H. Baars, K. W. Fomba, K. Müller, B. Heinold, K. Kandler, and A. Ansmann, Long-term profiling of mineral dust and pollution aerosol with multiwavelength polarization Raman lidar at the Central Asian site of Dushanbe, Tajikistan: case studies, Atmos. Chem. Phys., 17, 14559–14577, 2017.

Holben, B. N., T. F. Eck, I. Slutsker, D. Tanre, J. P. Buis, A. Setzer, E. Vermote, J. A. Reagan, Y. Kaufman, T. Nakajima, F. Lavenue, I. Jankowiak, and A. Smirnov, AERONET – A federated instrument network and data archive for aerosol characterization, Remote Sens. Environ., 66, 1–16, 1998.

Hu, Y., K. Stamnes, M. Vaughan, J. Pelon, C. Weimer, D. Wu, M. Cisewski, W. Sun, P. Yang, B. Lin, A. Omar, D. Flittner, C. Hostetler, C. Trepte, D. Winker, G. Gibson, and M. Santa-Maria, Sea surface wind speed estimation from space-based lidar measurements, Atmos. Chem. Phys., 8, 3593-3601, 2008.

Hu, Y., CALIPSO/CALIOP cloud phase discrimination algorithm, J. Atmos. Ocean. Tech., 26, 2293-2309, 2009.

Jin, Y., Nishizawa, T., Sugimoto, N., Ishii, S., Aoki, M., Sato, K., and Okamoto, H. Development of a 355-nm high-spectral-resolution lidar using a scanning Michelson interferometer for aerosol profile measurement, Opt. Express, 28(16), 23209-23222, 2020.

Kiehl, J. T., and B. P. Briegleb, The relative roles of sulfate aerosols and greenhouse gases in climate forcing, Science, 260, 311–314, 1993.

Kim, M.-H., Yeo, H., Park, S., Park, D.-H., Omar, A., Nishizawa, T., Shimizu, A., and Kim, S.-W. Assessing CALIOP-derived planetary boundary layer height using ground-based lidar, Remote Sens., 13, 1496, 2021.

Koren, I., Y. J. Kaufman, L. A. Remer, and J. V. Martins, Measurement of the effect of Amazon smoke on inhibition of cloud formation, Science, 303, 1342–1344, 2004.

Kudo, R., T. Nishizawa, and T. Aoyagi, Vertical profiles of aerosol optical properties and the solar heating rate estimated by combining sky radiometer and lidar measurements, Atmos. Meas. Tech., 9, 3223-3243, 2016.

Lammert, A., and Bösenberg, J. Determination of the convective boundary-layer height with laser remote sensing, Boundary-Layer Meteorol., 119, 159-170, 2006.

Liu, Z., N. I. Matsui, and N. Sugimoto, High-spectral-resolution lidar using an iodine absorption filter for atmospheric measurements, Opt. Eng., 38, 1661-1670, 1999.

Liu, Z., et al., The CALIPSO lidar cloud and aerosol discrimination: version 2 algorithm and initial assessment of performance, J. Atmos. Ocean. Tech., 26, 2034-2050, 2009.

Menut, L., Flamant, C., Pelon, J., and Flamant P. H. Urban boundary-layer height determination from lidar measurements over the Paris area, Appl. Opt., 38(6), 945-954, 1999.

Müller, D., U. Wandinger, and A. Ansmann, Microphysical particle parameters from extinction and backscatter lidar data by inversion with regularization: theory, Appl. Opt., 38, 2346-2357, 1999.

Menon, S., J. Hansen, L. Nazarenko, Y. Luo, Climate effects of black carbon aerosols in China and India, Science, 297, 2250–2253, 2002.

Nishizawa, T., H. Okamoto, N. Sugimoto, I. Matsui, A. Shimizu, and K. Aoki, An algorithm that retrieves aerosol properties from dual-wavelength polarization lidar measurements, J. Geophys. Res., 112(D6), D06212, doi:10.1029/2006JD007435, 2007.

Nishizawa, T., H. Okamoto, T. Takemura, N. Sugimoto, I. Matsui, and A. Shimizu, Aerosol retrieval from two-wavelength backscatter and one-wavelnegth polarization lidar measurements taken during the MR01K02 cruise of the R/V Mirai and evaluation of a global aerosol transport model, J. Geophys. Res., 113, D21201, doi:10.1029/2007JD009640, 2008a.

Nishizawa, T., et al., Algorithm to retrieve aerosol optical properties from high spectral resolution lidar and polarization Mie-scattering lidar measurements, IEEE Trans. Geos. Rem. Sens., 46, 4094-4103, 2008b.

Nishizawa, T., et al., Algorithm to Retrieve Aerosol Optical Properties from Two-Wavelength Backscatter and One-Wavelength Polarization Lidar Considering Nonsphericity of Dust, submitted to J. Quant. Spectr. Radiat, 2011.

Nishizawa T., et al., Ground-based network observation using Mie-Raman lidars and multi-wavelength Raman lidars and algorithm to retrieve distributions of aerosol components. Journal of Quantitative Spectroscopy and Radiative Transfer, 188, 79-93, 2017.

Nishizawa, T., R. Kudo, E. Oikawa, A. Higurashi, Y. Jin, N. Sugimoto, K. Sato, and H. Okamoto, Algorithm to retrieve aerosol optical properties using lidar measurements on board the EarthCARE satellite, Atmos. Meas. Tech. Discuss. [preprint], https://doi.org/10.5194/amt-2024-100, in review, 2024.

Nocedal, J., and Wright, S. J., Numerical optimization, 2nd edition, Springer Series in Operations Research and Financial Engineering, 664 pp., Springer Science+Busiginess Media, LCC, New York, 2006.

Okamoto, H., et al., Vertical cloud structure observed from shipborne radar and lidar: Midlatitude case study during the MR01/K02 cruise of the research vessel Mirai, J. Geophys. Res., 112, D08216, doi:10.1029/2006JD007628, 2007.

Okamoto, H., et al., Vertical cloud properties in the tropical western Pacific Ocean: Validation of the

CCSR/NIES/FRCGC GCM by shipborne radar and lidar, J. Geophys. Res., 113, D24213, doi:10.1029/2008JD009812, 2008.

Omar, A. H., Winker, D. M., Kittaka, C., Vaughan, M. A., Liu, Z., Hu, Y., Trepte, C. R., Rogers, R. R., Ferrare, R. A., Lee, K.-P., Kuehn, R. E., and Hostetler, C. A.: The CALIPSO automated aerosol classification and lidar ratio selection algorithm, J. Atmos. Ocean. Tech., 26, 1994–2014, https://doi.org/10.1175/2009JTECHA1231.1, 2009.

Qu, Y., Han, Y., Wu, Y., Gao, P., and Wang, T. Study of PBLH and its correlation with particulate matter from one-year observation over Nanjing, Southeast China, Remote Sens., 9, 668, 2017.

Sato, K., Okamoto, H., and Ishimoto, H., Physical model for multiple scattered space- borne lidar returns from clouds, Opt. Exp., 26, 322629, doi.org/10.1364/OE.26.00A301, 2018.

Sato, K., Okamoto, H., and Ishimoto, H., Modeling the depolarization of scapce-borne lidar signals, 27, 345166, doi.org/10.1364/OE.27.00A117, 2019.

Serdyuchenko A., V. Gorshelev, M. Weber, W/ Chehade, and J. P. Burrows, High spectral resolution ozone absorption cross-sections -Part2: Temperature dependence, Atmos. Meas. Tech., 7, 625-636, 2014.

She C. Y., Spectral structure of laser light scattering revisited: bandwidths of nonresonant scattering lidars, Appl. Opt., 40, 4875-4884, 2001.

Shimizu, A., et al., Continuous observations of Asian dust and other aerosols by polarization lidar in China and Japan during ACE-Asia. J. Geophys. Res.. 2004; 109: D19S17, doi:10.1029/2002JD003253.

Solomon, S., IPCC (Intergovernmental Panel on Climate Change) (2007), Climate Change 2007: The Physical Science Basis. Cambridge Univ. Press, Cambridge, UK and New York, USA., 996 pp, 2007.

Sugimoto, N., I. Uno, M. Nishikawa, A. Shimizu, I. Matsui, X. Dong, Y. Chen, and H. Quan, Record heavy Asian dust in Beijing in 2002: Observations and model analysis of recent events, Geophys. Res. Lett., 30, 1640, doi:10.1029/2002GL016349, 2003.

Takemura, T., T. Nakajima, A. Higurashi, S. Ohta, and N. Sugimoto, Aerosol distributions and radiative forcing over the Asian-pacific region simulated by Spectral Radiation-Transport Model for Aerosol Species (SPRINTARS), J. Geophys. Res., 108(D23), 8659, doi:10.1029/2002JD003210, 2002.

Tesche, M., A. Kolgotin, M. Haarig, S. P. Burton, R. A. Ferrare, C. A. Hostetler, and D. Müller, 3+2 + X: what is the most useful depolarization input for retrieving microphysical properties of non-spherical particles from lidar measurements using the spheroid model of Dubovik et al. (2006)?, Atmos. Meas. Tech., 12, 4421–4437, 2019.

Twomey, S., The influence of pollution on the shortwave albedo of clouds. J. Atmos. Sci., 34, 1149–1152, 1977.

Veselovskii, I., A. Kolgotin, V. Griaznov, D. Muller, U. Wandinger, and D. N. Whiteman, Inversion with regularization for the retrieval of tropospheric aerosol parameters from multiwavelength lidar sounding, Appl. Opt. 41, 3685–3699, 2002.

Vaughan, M. A., et al., Fully automated detection of cloud and aerosol layers in the CALIPSO lidar measurements, J. Atmos. Ocean. Tech., 26, 2034-2050, 2009.

Wiegner, M., S. Groß, V. Freudenthaler, F. Schnell, and J. Gasteiger, The May/June 2008 Saharan dust event over Munich: Intensive aerosol parameters from lidar measurements, J. Geophys. Res.-Atmos., 116, D23213, 2011.

Winker, D. M., et al., Overview of the CALIPSO Mission and CALIOP data processing algorithms, J, Atmos. Ocean. Tech., 26, 2310-2323, 2009.

Yoshida, R., H. Okamoto, Y. Hagihara, and H. Ishimoto, Global analysis of cloud phase and ice crystal

orientation from CALIPSO data using attenuated backscattering and depolarization ratio, J. Geophys. Res., doi:10.1029/2010JD014032, 115, D00H32, 2010.

Young, S., A., Vaughan, M. A., Kuehn, R. E., Winker D. M.: The retrieval of profiles of particulate extinction from Cloud‑Aerosol Lidar and Infrared Pathfinder Satellite Observations (CALIPSO) Data: Uncertainty and Error Sensitivity Analyses, J. Atmos. Ocean. Tech., 30, 395-428, DOI: 10.1175/JTECH-D-12-00046.1, 2013.

3.3 MSI

3.3.1 Standard Product

3.3.1.1 Introduction

We have developed L2A algorithms to retrieve (1) discrimination of cloudy and clear sky and (2) cloud optical properties. The methods to provide these products and the plans for the improvements of the algorithms are described in the following sections.

Table 3.3.1.1.1 Expected products as standard band in use.

Algorithm			Cloud Screening	Water / Ice Cloud Properties		
Estimated Parameters			Confidence Level at each pixel	Optical Thickness	Effective Particle Radius	Cloud Top Temperature
M S I B A N D	1	VIS	+	+		
	2	NIR	+			
	3	SWIR1	+	+		
	4	SWIR2		+		
	5	TIR 1				
	6	TIR 2	+	+		
	7	TIR 3				

3.3.1.2 Cloud Screening

3.3.1.2.1 Algorithm

3.3.1.2.1.1 Approach

For development of CLAUDIA, we refer to the multiple threshold method employed in the MOD35 [Ackerman et al, 1998] algorithm, but substantially re-construct the structure of the algorithm to meet our aim of sustaining the neutral position. In order to realize neutral cloud screening, we apply clear confidence level and the categorization of threshold tests according to their characteristics. The clear confidence level, which can be considered as an index of the likelihood of clear condition, is estimated by applying the threshold test with two thresholds, an upper limit and a lower limit, rather than a single value. The concept of the confidence level has been introduced by MOD35. However, the MOD35 algorithm used the confidence level only as an intermediate product to divide pixels into four levels (clear, probably clear, uncertain, and cloudy). Our idea is the use of the clear confidence level consistently to the final solution. To achieve this idea we examined, categorized, and rearranged the several threshold tests of MOD35, thus not only the overall concept but also the flow of data analysis were different from MOD35. If the measured

value of a pixel is between the lower and upper limit, the algorithm does not identify the pixel as cloudy or clear but calculates the clear confidence level. Consequently, the CLAUDIA is not biased toward cloudy or clear-sky, but is neutral.

3.3.1.2.1.2 Threshold test

The CLAUDIA consists of the calculation of clear confidence levels for every threshold test and the comprehensive integration of them. Every threshold test has strong and weak points. Here we briefly explain the theoretical basis of the individual threshold tests and their characteristics.

3.3.1.2.1.2.1 Single reflectance tests

Optically thick clouds usually have a large reflectance at wavelengths in non-absorption bands in the visible and near infrared regions. Over ocean, the reflectance in the near infrared (e.g., 0.865 µm of the MSI) is efficient, because the effect of Rayleigh scattering by air molecules is smaller than that in the visible region. Over land, however, the reflectance in the visible region (e.g., 0.67 µm) must be used, because leaves of plants have a large reflectance in the near infrared region. The reflectance test may falsely identify bright surfaces, such as deserts, snow-covered areas, coral reefs, as clouds. In order to avoid incorrect identification, we apply the "minimum albedo" map, which is constructed from the minimum reflectance for a month before the date of satellite data for cloud screening. The reflectance is compared to the minimum albedo, instead of using a static threshold like MOD35. This scheme is consistent with the assumption that at least one time in a month will be clear and the minimum value for a month must represent the reflectance of the surface. It is expected that clouds and sunglint areas can be generally excluded from the minimum albedo data. However, the minimum albedo sometimes includes larger reflectance than the surfaces due to lasting clouds. Vemury et al. [2001] applied a similar procedure, i.e., dynamic and regional threshold values, to cloud screening for AVHRR data.

3.3.1.2.1.2.2 Reflectance ratio tests

The ratio and the difference of reflectance between two wavelengths in the solar radiation region can be applied to detect optically thick clouds. The reflectance of cloud at a wavelength in the solar radiation region is almost independent of the wavelength if the absorption by air molecules is very small, whereas the reflectance of land and ocean usually varies with the wavelength, depending on the condition of the surface. However, certain combinations of wavelengths for the reflectance ratio test are not appropriate for surfaces whose reflectance does not vary with the wavelength. For example, the ratio of reflectances at 0.67 µm and 0.865 µm is sensitive to clouds over ocean but mistakes sun glint regions and bright deserts for cloud. The ratio of reflectances at 0.865 µm and 1.65 µm can be applied to discriminate clouds from bright desert surfaces, because the reflectance of desert in the near infrared increases with increasing wavelength [Irish 2000]. The Normalized Difference of Vegetation Index (NDVI), which is based on the large reflectance of leaves in the near infrared region and their small reflectance in the visible region to estimate vegetation density (e.g., Zeng et al., [2000]), can be used to identify clouds over deep forests.

Several reflectance ratio and difference tests judge pixels according to whether the observation value is within a given range: such a test has both an upper and a lower limit. In addition, possibility of snow cover is estimated from the difference of reflectance between 0.67 μm and 1.65 μm, which is named as the Normalized Difference of Snow Index (NDSI [Salomonson and Appel, 2006]).

3.3.1.2.1.2.3 Brightness temperature tests

Threshold tests using the infrared channels have the advantage of being able to detect cloud at night as well as daytime. A threshold test based on brightness temperature in the window region (where gaseous absorption is very small, e.g., 10.8 μm) can be applied to detect high clouds over ocean. However, this threshold test cannot discriminate low cloud from the surfaces (i.e., clear-sky areas).

3.3.1.2.1.3 Estimation of the clear confidence level

Fig. 3.3.1.2.1.3.1 illustrates the concept of the estimation of the clear confidence level for each threshold test. The observed value is compared to the upper limit and the lower limit. If the observed value is larger (smaller) than the upper limit (lower limit), the pixel is discriminated with high confidence as clear (cloudy) and assigned the confidence level of 1 (0). Otherwise a value of between 0 and 1 is assigned to the clear confidence level by linear interpolation. This procedure is based on the assumption that a pixel with an observed value of between the upper limit and the lower limit is ambiguous, but the nearer the observed value is to the upper limit, the larger is the probability of a clear sky.

The upper and lower limits are determined from validation by comparison to other observations or theoretical calculations. We have compared threshold test values measured by MODIS to RGB images and MOD35 product, and then have broadly estimated the upper and lower limits of each threshold test. We will tentatively apply these values for early MSI observation. Table 3.3.1.2.1.3.1 lists the tentative values of upper and lower limits for MSI observation over water, land and the polar region, referring to results of cloud screening with MODIS. These values are obviously optimized for MODIS observation, and are expected to be changed through validation of actual cloud screening results by MSI, because the wavelengths of channels of MSI are slightly different from those of MODIS.
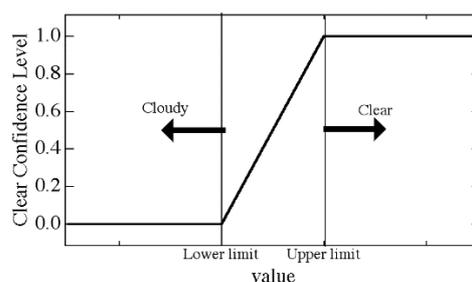
Fig. 3.3.1.2.1.3.1 Concept of the clear confidence level with two threshold values, the upper limit and the lower limit.

Table 3.3.1.2.1.3.1 Tentative upper and Lower limits for each threshold tests.

(a) Water

Gr.	Threshold tests		Lower limit	Upper limit
1	R(0.865 µm)		minimum albedo +0.195	minimum albedo +0.045
	R(0.865 µm)/R(0.67 µm)	Smaller end	0.9	0.66
		Larger end	1.15	1.35
	NDVI	Smaller end	-0.1	-0.22
		Larger end	0.22	0.46
2	T_b(10.8 µm)		261 K	273 K

(b) Land

Gr.	Threshold tests		Lower limit	Upper limit
1	R(0.67 µm)		minimum albedo +0.195	minimum albedo +0.045
	R(0.865 µm)/R(0.67 µm)	Smaller end	0.9	0.66
		Larger end	1.1	1.7
	NDVI	Smaller end	-0.1	-0.22
		Larger end	0.22	0.46
	R(0.865 µm)/R(1.65 µm)		0.86	1.06
2	T_b(10.8 µm)[1]		-	297.5 K

(c) Polar Region

Gr.	Threshold tests		Lower limit	Upper limit
1	NDVI	Smaller end	-0.1	-0.22
		Larger end	0.22	0.46

1) A pixel with T_b(10.8 µm) > 297.5 K is identified as clear, regardless of other tests

3.3.1.2.1.4 Categorization of each individual threshold test into two groups

The threshold tests are categorized into two groups, according to their weak point. The first group is efficient for finding clouds but has a possibility of incorrectly identifying clear sky areas as cloudy if the surface under the clear sky is confusing. For example, the reflectance ratio of 0.865 µm to 1.65 µm can discriminate clouds from the desert surface, but the ratio for clouds is similar

to that for forest beneath clear sky so it is not effective for cloud discrimination over thick vegetation. Threshold tests derived from the specific features of individual surfaces (e.g., the NDVI test) tend to be categorized into this first group. On the other hand, threshold tests of the second group are able to correctly identify pixels as clouds but have a possibility of missing some types of cloud and falsely identifying cloudy pixels as clear. For example, the brightness temperature of 10.8 μm is appropriate to detect high or geometrically thick clouds, but is not sensitive to low clouds even if they are optically thick. Therefore, CLAUDIA estimates a representative value of the confidence level for each group. For example, Table 3.3.1.2.1.4.1 lists the MSI channels used for the cloud detection, and the threshold tests for each group and main targets are given in Table 3.3.1.2.1.4.2. The representative value of the clear confidence level for group 1, G_1, is derived from the geometric mean as follows,

$$G_1 = 1 - \sqrt[n]{(1-F_1) \cdot (1-F_2) \cdots (1-F_k) \cdots (1-F_n)}, \qquad (3.1)$$

where F_k is the clear confidence level of the k-th threshold test. Eq. (3.1) implies that the representative value of the first group is calculated to be "cloud conservative": even if only one threshold test takes the clear confidence level of 1 then $G_1 = 1$ (clear), whereas $G_1 = 0$ (cloudy) only if all the F_k are 0. This determination is valid if at least one of the threshold tests in the group is able to distinguish clouds from the surface. On the other hand, the representative value for group 2, G_2, is calculated by

$$G_2 = \sqrt[n]{F_1 \cdot F_2 \cdots F_k \cdots F_n}. \qquad (3.2)$$

Eq. (3.2) implies that the representative value of the second group is considered to be "clear conservative". The grouping of threshold tests is also applied to MOD35, but the MOD35 is designed to make the calculation of the confidence level of all the groups be "clear conservative", employing Eq. (3.2) for the tests of group 1. The CLAUDIA is designed to be neutral considering characteristics and habits of each threshold tests. This is one of the major differences between MOD35 and CLAUDIA.

Table 3.3.1.2.1.4.1 EarthCARE/MSI channel specifications

Band	Center wave-length (μm)	Max signal [W/m2/sr/μm]	L_low (SNR) [W/m2/sr/μm]	L_high (SNR) [W/m2/sr/μm]
B1 VIS	0.67	489.1	30 (75)	444.6 (500)
B2 NIR	0.865	311.0	17 (65)	282.7 (500)
B3 SWIR1	1.65	69.3	1.5 (18)	67.9 (500)
B4 SWIR2	2.21	24.6	0.5 (21)	24.6 (500)
		Max signal [K]	B_low (NEDT1, NEDT2) [K]	B_high (NEDT1, NEDT2) [K]
B5 TIR1	8.80	350K	220 (0.8K, 0.6K)	350 (0.25K, 0.1K)
B6 TIR2	10.80	350K	220 (0.8K, 0.7K)	350 (0.25K, 0.15K)
B7 TIR3	12.00	350K	220 (0.8K, 0.8K)	350 (0.25K, 0.15K)

Reference: EarthCARE SRD

Table 3.3.1.2.1.4.2. Threshold tests and the targets

Group	Threshold tests	Targets
1	R(0.865 μm)	Optically thick clouds over ocean
	R(0.67 μm)	Optically thick clouds over land
	R(0.865 μm)/R(0.67 μm)	Optically thick clouds
	NDVI	Clouds over deep forest
	R(0.865 μm)/R(1.65 μm)	Clouds over bright desert
2	T_b(10.8 μm)	High (geometrically thick) clouds

3.3.1.2.1.5 Calculation of the overall confidence level

CLAUDIA finally obtains the overall clear confidence level (Q) from the geometric mean of the representative values for the two groups as follows,

$$Q = \sqrt{G_1 \cdot G_2} \ , \qquad (3.3)$$

which means that if the clear confidence level of either one group of two is 0 (i.e., cloudy), the overall clear confidence level results in 0. The flow of the algorithm is briefly explained in Fig. 3.3.1.2.1.5.1. It is indicated that the CLAUDIA is not a cascade or decision-tree type, which means an algorithm applying threshold tests as decision nodes such as CLAVR-1 [Stowe et al. 1999]. This means that the CLAUDIA is versatile enough to be applied to various satellites equipped with different channels, because it can be adjusted simply by adding or removing certain threshold tests according to the wavelength of the available channels. In contrast, the adaptation of a cascade algorithm may require substantial changes. The CLAUDIA can make an unbiased discrimination between cloudy and clear areas, assigning an overall clear confidence level of between 0 and 1 to ambiguous pixels. Users of the cloud detection results are allowed to select an arbitrary value of the clear confidence level according to their purposes and targets, by identifying pixels whose confidence level is less than the value selected as cloudy. For example, if a user wants to exclude any small effects of cloud, the confidence level of 1 should be selected to result in clear conservative cloud detection. It should be noted that the overall confidence level of between 0 and 1 suggests a vague area that possibly contains clouds, but the clear confidence level does not directly represent either the optical thickness of cloud or cloud amount in the pixel.
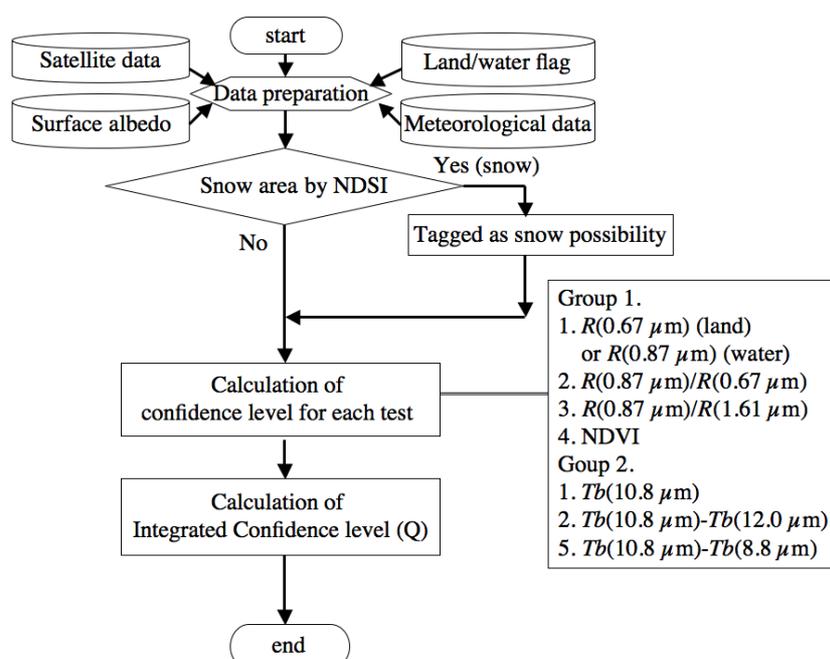
Fig. 3.3.1.2.1.5.1 Flow of the cloud detection algorithm.

3.3.1.3 Water Cloud Properties
3.3.1.3.1 Algorithm

When EarthCARE MSI is in its descending node (moving from north to south), the nadir pixel is basically located around the 102nd pixel counted from the west (Fig. 3.3.1.2.1.1). However, in actual observation, the location of the nadir will fluctuate slightly according to the location of the satellite.
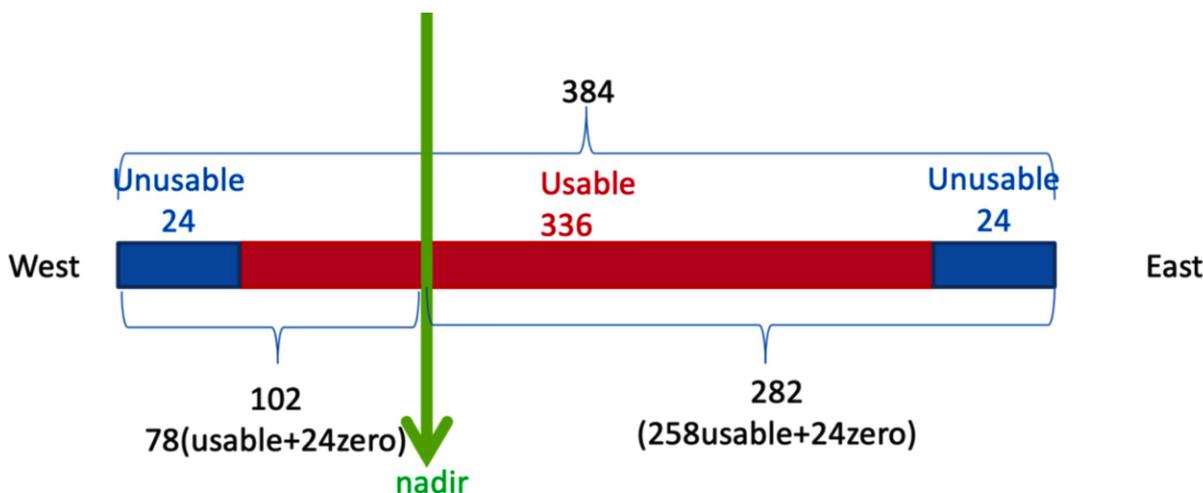
- Start pixel is from west for descending on daytime

Fig. 3.3.1.2.1.1 Pixel distribution of the MSI swath (descending node).

3.3.1.3.1.1 Approach and methodology

The CAPCOM uses LUT (Look up Table)-Iteration Method (LIM) to retrieve the target geo-physical parameters from satellite-derived radiance data. The LUT was updated in JFY2023, which is based on the response function at the nadir pixel of MSI.

In the CAPCOM, a non-absorption band (Band 1), an absorption band (Band 3,4), and a thermal band (Band 6) are used to derive cloud optical thickness (CLOP), cloud effective particle radius (CLER), and cloud top temperature (CLTT). Adding to these radiance data, some ancillary input data, such as the vertical profile of the temperature, pressure, water vapor, ground albedo, are also used to calculate related geophysical parameters; cloud top height (CLHT) and cloud top pressure (CLTP) are retrieved by comparing cloud top temperature and temperature profile from ancillary data; liquid water path (CLWP) is calculated by cloud optical thickness and effective particle radius (Eq. (3.4)).

3.3.1.3.1.2 Logic Flow

Four LUTs are prepared for this purpose, i. e., LUT of cloud-reflected radiance in bands 1, 3 and 4, transmissivities and reflectivity in bands 1, 3, and 4, band 6 transmissivity. Table 3.3.1.3.1.2.1 summarizes the grid system of the LUTs and Fig. 3.3.1.3.1.2.1 illustrates the flow of the analysis. The grid system of τ_c has been optimized so that the retrieval accuracy in thinner clouds becomes better in 2013. We used Newton-Raphson method to iterate a main loop in the

program. Some related parameters, such as cloud liquid water path and cloud top height are also calculated in the CAPCOM with temperature slicing data from objective analysis such as JMA GANAL or ECMWF dataset. We found that the iteration does not converge in some cases of optically thin clouds when the removed radiation significantly dominates over the signal. In this case we cancel the analysis.

Table 3.3.1.3.1.2.1 The grid system of the look up tables for water cloud; θ, θ_0, ϕ are the satellite and solar zenith angle, and relative azimuth angle. τ_c and r_e are cloud optical thickness and effective particle radius.

Quantities	Grid point values
θ (degrees)	0, 5, 10, 20, 30, 35, 50, 45, 50, 55, 60, 65, 70, 75, 80
θ_0 (degrees)	0, 5, 10, 20, 30, 35, 50, 45, 50, 55, 60, 65, 70, 75, 80
ϕ (degrees)	0 to 180 (divided by every 10 degrees)
τ_c (Water cloud)	0.2,0.5,1.,2.,3.,4.,5.,8.,12.,17.,23.,31.,41.,54.,70.,80.,90., 100.
r_e (Water cloud)	4., 7., 9., 11., 14., 17., 22., 30., 38., 46., 54., 62.
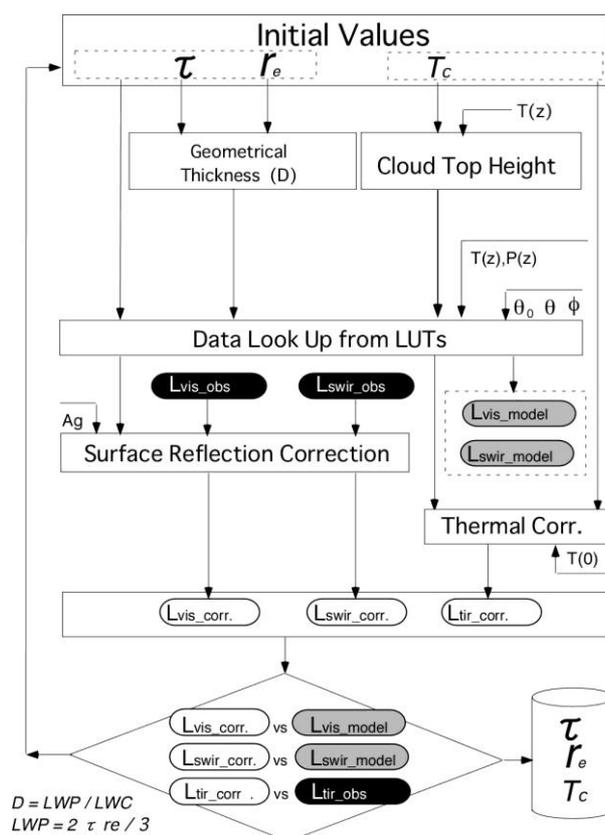
Fig. 3.3.1.3.1.2.1 Flow chart of the CAPCOM; L_{vis}, L_{swir} and L_{tir} are the radiances at visible, shortwave infrared and thermal infrared wavelength, respectively. $L_{obs.}$, $L_{corr.}$, and L_{model} mean the satellite-retrieved radiance, the radiance by correcting surface reflectance effect, and the radiance reflected by cloud layer in retrieval model with microphysical properties τ_c, r_e and T_c. $T(z)$ and $P(z)$ are temperature and pressure at altitude z above surface. $T(0)$ and Ag are surface

temperature and ground albedo.

3.3.1.3.1.3 Physical and Mathematical aspects of the CAPCOM

The solar reflectance method utilizes non-absorbing visible (Vis) and water-absorbing short-wave infrared (SWIR) wavelengths, such as 1.6, 2.2 and 3.7 µm, for the simultaneous retrieval of the cloud optical thickness at the 0.5µm wavelength and the effective particle radius. In this paper, we mainly discuss the solar reflectance method making use of MSI Band 1 (0.67 µm), 3 (1.65 µm) and/or 4 (2.21 mm), and 6 (10.8 µm). The effective particle radius of the clouds (r_e) is defined by

$$r_e \equiv \frac{\int_0^\infty r^3 n(r) dr}{\int_0^\infty r^2 n(r) dr}, \qquad (3.4)$$

where $n(r)$ is the number size distribution as a function of the particle radius **r**. We used a log-normal size distribution in the calculations,

$$n(r) = \frac{c}{r} \exp\left[-\frac{(\ln r - \ln r_0)^2}{2\sigma^2} \right], \qquad (3.5)$$

where **c** is a constant, r_0 is the mode radius, which is related to the effective particle radius as $r_e = r_0 e^{2.5\sigma^2}$, and σ is the log-standard deviation of the size distribution. Here, $\sigma = 0.35$ was assumed for marine stratocumulus clouds in our analyses. For the satellite signal simulation, we used an accurate and efficient radiative transfer scheme [Nakajima and Tanaka 1986, 1988] extended to include the thermal radiative transfer (Stamnes et al. 1988). We assumed a Lambert surface for the underlying surface. This assumption will not introduce a significant error in the analyses if we use an equivalent flux albedo for cloudy atmospheres [Nakajima et al. 1991].

We retrieved τ_c at the 0.5-µm wavelength and r_e from MSI Band 1 and 3 (and/or 4) on the basis of the fact that Band 1 and 3 primarily depend on the cloud optical thickness and the effective particle radius, respectively. Although the concept of the retrieval is simple, some difficulties occur when determining the cloud properties from the measured MSI spectral radiance. It is necessary to remove the unexpected radiation components (e.g. solar radiation reflected by the ground) from the observed radiance.

3.3.1.3.1.4 Formulations of the radiative components

According to the radiative transfer theory for parallel plane layers with an underlying Lambert surface, we remove the unexpected radiation components, such as the solar radiation reflected by the ground surface and the thermal radiation emitted from the cloud layer and the ground surface, from the satellite-received radiance, L$_{obs}$, in order to decouple the radiation component reflected by the cloud layer, L, as follows:

$$
\begin{aligned}
&L(Z_c, D_c, \tau_c, r_e; \mu, \mu_0, \phi) \\
&= L_{obs}(Z_c, D_c, \tau_c, r_e; \mu, \mu_0, \phi) \\
&- t(Z_c, D_c, \tau_c, r_e; \mu) \frac{A_g}{1 - \bar{r}(Z_c, D_c, \tau_c, r_e) A_g} t(Z_c, D_c, \tau_c, r_e; \mu_0) \frac{\mu_0 F_0}{\pi}
\end{aligned}
\tag{3.6}
$$

where F_0 is the extraterrestrial solar flux, and τ_c and τ_u are the optical thicknesses of the cloud layer, and the atmosphere above the cloud layer, respectively. μ_0 and μ are the cosines of the solar and satellite zenith angles, respectively, ϕ is the azimuthal angle of the satellite relative to the sun. $\boldsymbol{Z_c}$ and $\boldsymbol{D_c}$ are the top height and the geometrical thickness of the cloud, respectively.

The transmissivity t, the plane albedo r, and the spherical albedo $\bar{r}$ are given by

$$
\begin{aligned}
&t(\tau_c, r_e; \mu_0) \\
&= \frac{1}{\pi} \int_0^{2\pi} \int_0^1 T(\tau_c, r_e; \mu, \mu_0, \phi) \mu \, d\mu \, d\phi + e^{-\tau/\mu_0}
\end{aligned}
\tag{3.7}
$$

$$
\begin{aligned}
&r(\tau_c, r_e; \mu) \\
&= \frac{1}{\pi} \int_0^{2\pi} \int_0^1 R(\tau_c, r_e; \mu', \mu, \phi) \mu' \, d\mu' \, d\phi
\end{aligned}
\tag{3.8}
$$

$$
\bar{r}(\tau_c, r_e) = 2 \int_0^1 r(\tau_c, r_e; \mu) \mu \, d\mu ,
\tag{3.9}
$$

where $T(\tau_c, r_e; \mu, \mu_0, \phi)$ and $R(\tau_c, r_e; \mu', \mu, \phi)$ are bi-directional transmission and reflection functions respectively. The second term in Eq. (3.6) is ground-reflected radiation components Multiple reflections between the ground surface and the upper layer are taken into consideration in Eqs. (3.6). However, this effect is sufficiently small to regard $\bar{r}(\tau_c, r_e) A_g$ as almost zero, especially for optically thin clouds and ground surfaces with low reflectance. On the contrary, with optically thick clouds and large ground albedo, this effect is relatively large at visible wavelengths since the large cloud spherical albedo reflects radiation from the ground surface, while the relatively large transmissivity allows this radiation component to be transmitted into space. These formulations are exact when we consider monochromatic radiance. We further introduce a process of averaging of the variables in the formulations with respect to the wavelength. For example, t is averaged with a sub-channel response function of MSI as

$$
t = \sum_{n=1}^{N} \varphi_n \left\{ \sum_{k=1}^{M} \left(\xi_{n,k} \times t_{n,k} \right) \right\} / \sum_{v=1}^{n} \varphi_n ,
\tag{3.10}
$$

where φ_n is the response function of the n-<u>th</u> subchannel wavelength for each MSI Band, $\xi_{n,k}$ is the weight of the k-th k-distribution, and $t_{n,k}$ is the transmissivity for the k-th k-distribution at the n-th wavelength. This averaging process, which was applied to Eqs. (3.6) introduces a non-negligible error into the case of thin cloud layers in which the spectral variation of $t_{n,k}$ becomes large. However, in most cases in which this process is applied, the error remains small, and it is possible to estimate the undesirable radiation components in Eqs. (3.6) by using spectrally

EARTHCARE

NICT JAXA
宇宙航空研究開発機構
Japan Aerospace Exploration Agency

averaged variables for each channel.

3.3.1.4 Ice Cloud Properties

3.3.1.4.1 Introduction

We have developed L2A algorithms to retrieve optical properties for ice cloud. The methods to provide these products and the plans for the improvements of the algorithms are described in the following sections.

3.3.1.4.2 Algorithm

The algorithm flow for retrieving ice cloud properties is the same as CAPCOM that are used for retrieving water cloud optical properties in standard product of the EarthCARE. To retrieve ice cloud optical properties, the CAPCOM uses another group of look-up-tables of cloud-reflected radiance calculated in the condition of ice particles as with Table 3.3.1.4.2.1. The CAPCOM for ice clouds retrieves optical thickness, effective particle radius and cloud top temperature.

Designing an algorithm for ice cloud retrieval has the following two difficulties compared to doing one for water cloud retrieval. First is that the shape of ice particle, even hexagonal column or plate that is the typical shape, has degree of freedom in term of aspect ratio and 3-D rotational state. The selection of these parameters in retrievals model have impacts on the result of retrieval of cloud properties. Second is that any methods to solve the scattering problems of ice particle require much computational effort by which we cannot obtain the complete database of the scattering properties of ice particle with respect to continuous variation of shape, aspect ratio, rotation and refractive index.

This algorithm uses an ice scattering database that has the following features: 1) The scattering properties have been computed by use of the methods and solvers shown in Table 3.3.1.4.2.2. 2) The grid interval of refractive index is optimized for retrievals based on Letu et al. (2012). By this optimization, the impact of discretization error of refractive index becomes negligible small.

Fig.3.3.1.4.2.1 and Fig.3.3.1.4.2.2 illustrates a sample of MSI L2A cloud product, including CLOT and CLER for both water and ice clouds. In Fig.3.3.1.4.2.3 a combination between CPR cloud flag and MSI CLOT product shows how EarthCARE sensors work with each other to monitor a typical tropical cyclone in Indian Ocean. With the help from CPR we can clearly see the spatial position and the vertical structure of both think and thin clouds, and MSI retrieves their CLOT quite precisely.

Table 3.3.1.4.2.1 The grid system of the look up tables for ice cloud; θ, θ_0, ϕ are the satellite and solar zenith angle, and relative azimuth angle. τ_c and r_e are cloud optical thickness and effective particle radius.

Quantities	Grid point values
θ (degrees)	0, 5, 10, 20, 30, 35, 50, 45, 50, 55, 60, 65, 70, 75, 80
θ_0 (degrees)	0, 5, 10, 20, 30, 35, 50, 45, 50, 55, 60, 65, 70, 75, 80
ϕ (degrees)	0 to 180 (divided by every 10 degrees)
τ_c (Ice cloud)	0.1,0.5,1.,2.,4.,8.,16.,32.,48.,64.,80.,90.,100.,110.,120.,130.,140.,150.
r_e (Ice cloud)	5.,10.,20.,40.,60.,80.,100.,110.,120.,130.,140.,150.

Table 3.3.1.4.2.2 The solvers used to compute ice scattering properties

Solvers	Adapted size parameter	Calculation method	Reference
Lisas/SIEMM	1 - 20	Maxwell equation	Nakajima T. Y et al. 2009
FDTD	20 - 30	Maxwell equation	Ishimoto et al. 2010
GOM2	30-300	Ray-tracing + Electromacnetic theory	Ishimoto et al. 2012
GOM1	More than 300	Ray-tracing technique	Nakajima T Y et al 1997
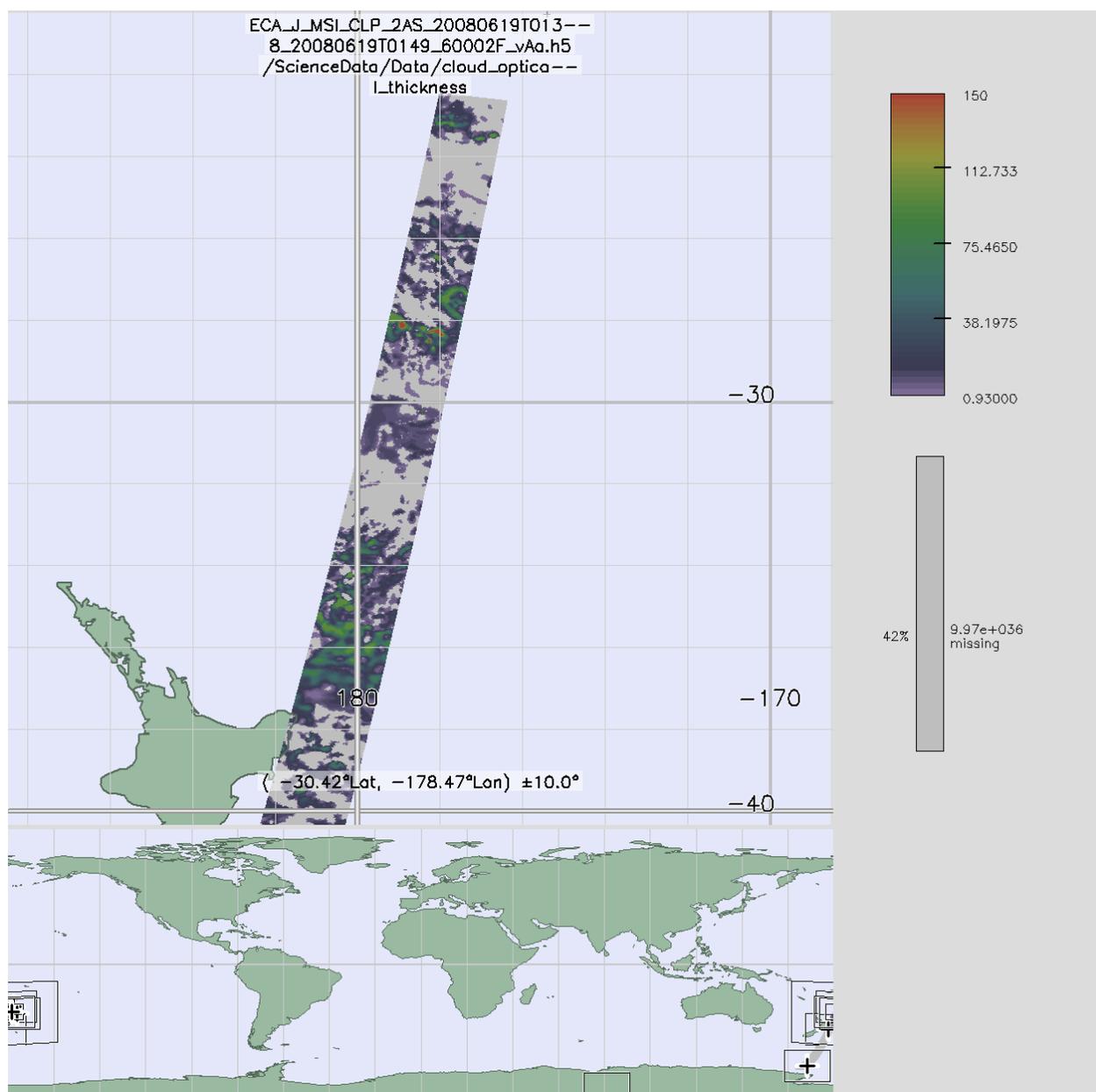
Fig.3.3.1.4.2.1 A sample of cloud optical thickness from L2A cloud product, which contains both

water and ice clouds.
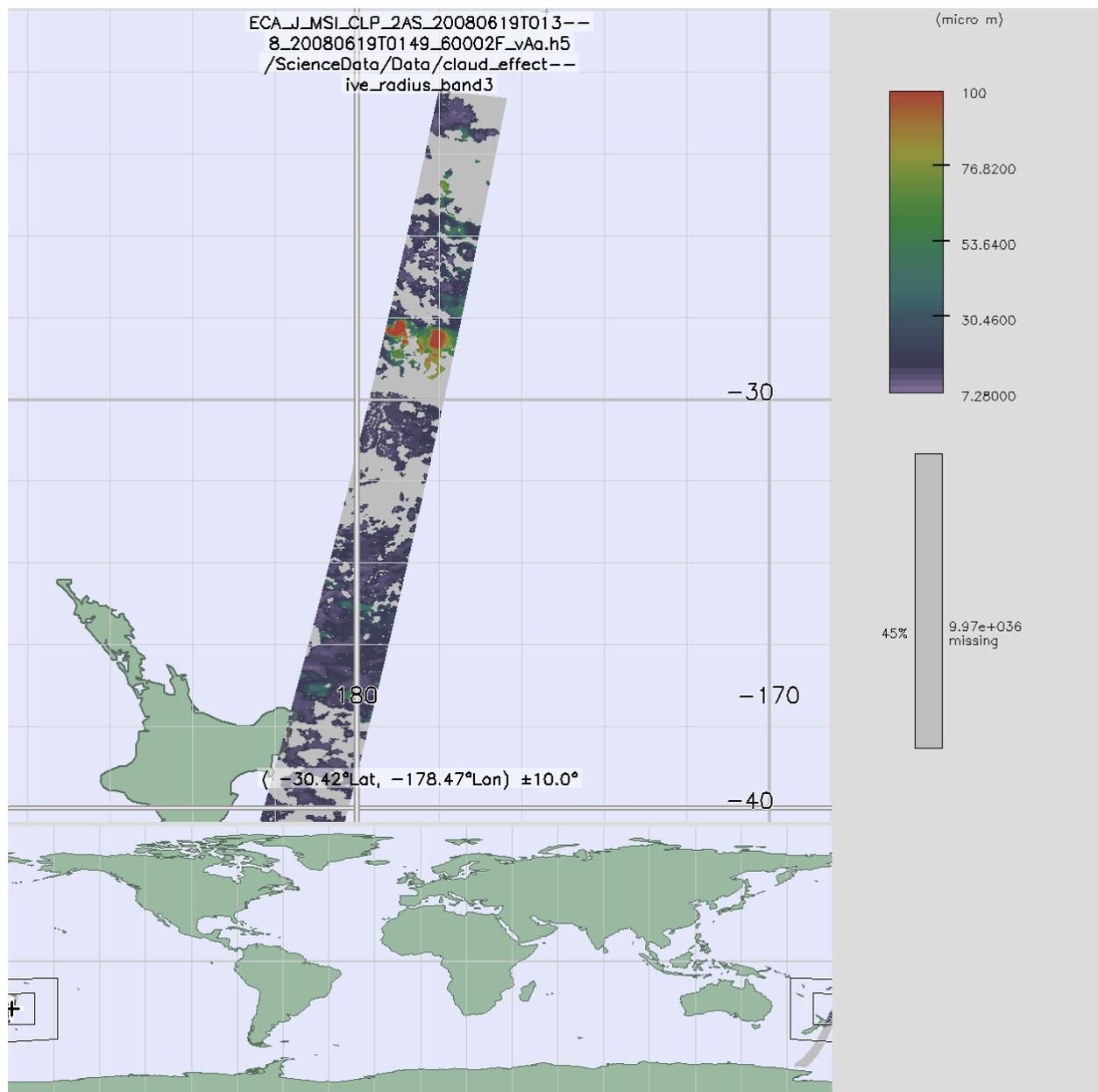
Fig.3.3.1.4.2.2 A sample of cloud effective radius from L2A cloud product, which contains both water and ice clouds.
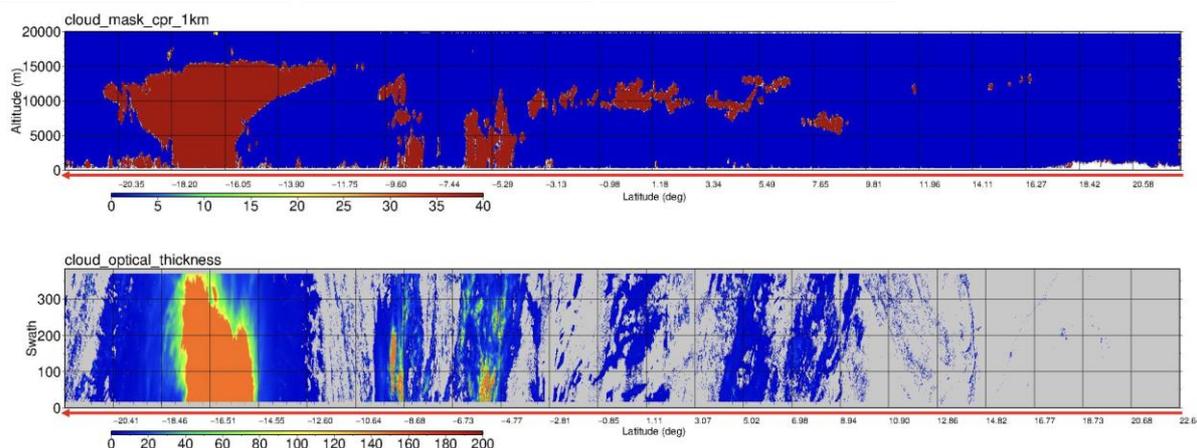
Fig.3.3.1.4.2.3 A sample of CPR cloud flag (upper) and MSI cloud optical thickness, monitoring a typical tropical cyclone in Indian Ocean on Jan.30, 2025 (03834E).

3.3.1.5 Vicarious Calibration

During the early ground base calibration and initial in-orbit validation phase from late 2024 to early 2025, it was reported that the initial version of Multi-Spectral Imager (MSI) level 1 data (MSI_RGR) had suffered some issues that compromise the data quality. To solve the issues of the MSI level 1 data, vicarious calibration is necessary particularly for VNS bands. For MSI_CLP, the vicarious calibration to MSI_RGR using the geostationary satellite Himawari-9 cloud retrieval as an intermediator was operated in middle 2025. Up to version vBa, there is a slight overestimation (about 0.93 of calibration coefficient) for VIS band, and almost no overestimation or underestimation for NIR band.
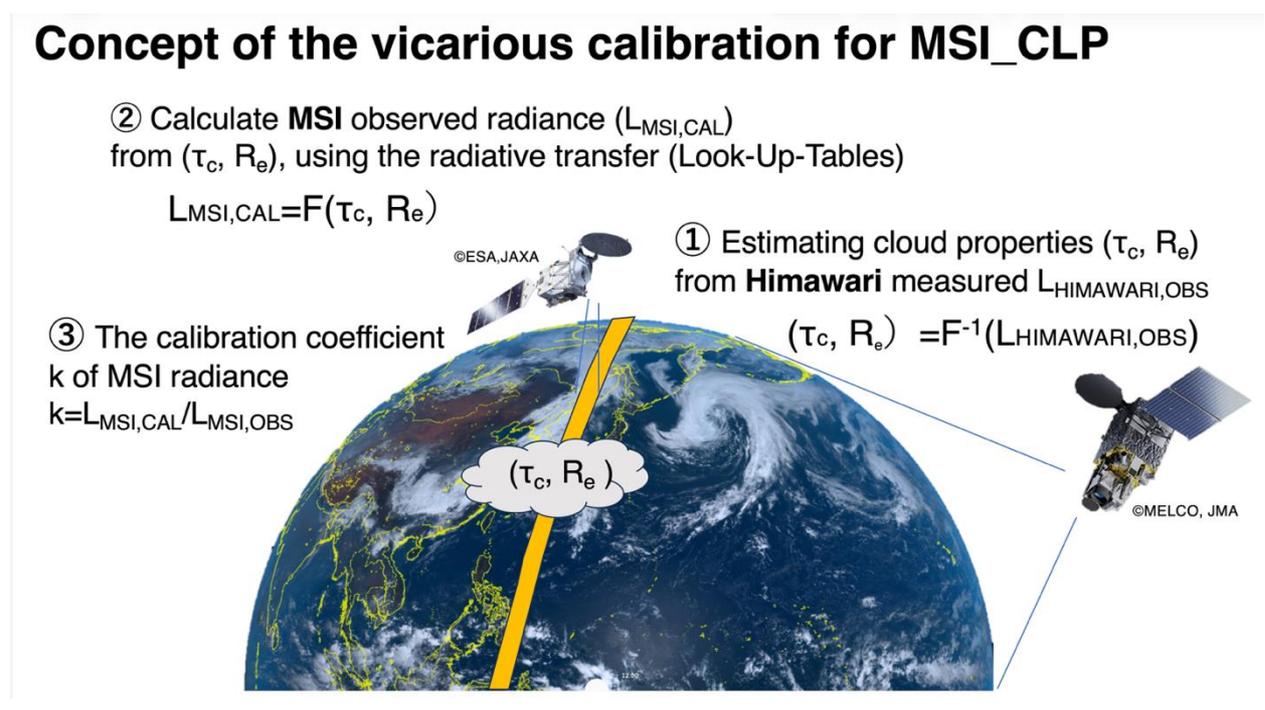
Fig.3.3.1.5.1 Concept image of the vicarious calibration for MSI_CLP.
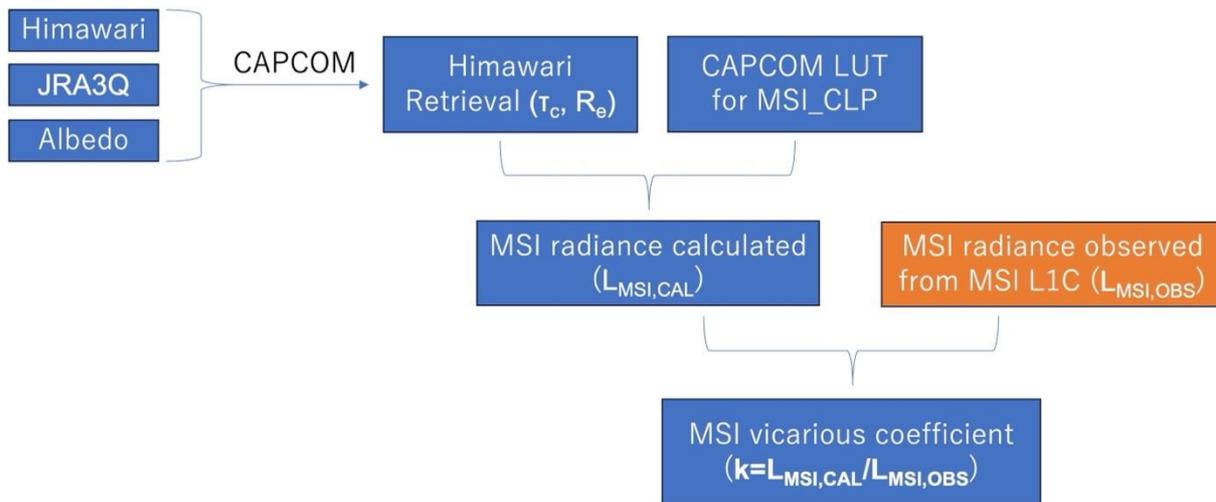
Fig.3.3.1.5.2 Flowchart of MSI_CLP vicarious calibration.

Fig.3.3.1.5.2 shows the flowchart of the vicarious calibration for MSI_CLP.

Firstly, we chose some typical scenes for water clouds as mentioned above, estimating cloud properties (COT, CER) from Himawari-9 cloud product:

$$(\tau_c, R_e) = F^{-1}(L_{Himawari,OBS})$$

where τ_c stands for COT, R_e stands for CER, and F^{-1} , the inverse function of F, infers the CAPCOM algorithm, which used in Himawari-9 cloud product.
Secondly, with the COT and CER from Himawari-9 cloud product, we operated a radiative transfer simulation using LUT of CAPCOM for EarthCARE/MSI to calculate the corresponded radiance of MSI:

$$L_{MSI,CAL} = F(\tau_c, R_e)$$

where $L_{MSI,CAL}$ stands for the radiance of MSI that based on the COT and CER we get from Himawari-9, and F infers the LUT of CAPCOM.
The cloud property algorithm CAPCOM's LUT is grid data that uses cloud top altitude as altitude information, which can be considered as a function of COT and CER:

$$F(\tau_c, R_e)$$

Normally during the activation of the algorithm, COT and CER are retrieved from the inverse function F^{-1} of the LUT from the observed radiance as input from L1C data. However, in this time, COT and CER retrieved from Himawari are used as input, and the corresponding radiance ($L_{MSI,CAL}$) is estimated by radiative transfer calculation.
Finally, we compared the values of radiance between actual MSI L1C data and what we get from above:

$$k = \frac{L_{MSI,CAL}}{L_{MSI,OBS}}$$

where k stands for the vicarious calibration coefficient of MSI radiance, and $L_{MSI,OBS}$ stands for the actual pixel value we get from MSI L1C data (which supposed to have overestimation). All these data were normalized to get the statistic scatter plots, and k is calculated from the averaged $L_{MSI, CAL}$ and $L_{MSI,OBS}$.

3.3.2.3 Aerosol Properties

3.3.2.3.1 Algorithm

We developed a new land aerosol remote sensing program, Multi-Wavelength and multi-Pixel Method (MWPM) and applied to GOSAT/CAI data. We have selected target areas of 100km x 100km where more than three surface AERONET observation sites are located: Paris area (2.15°E-2.50°E, 48.68°N-48.88°N) for 15 x 15 pixels and 42 days and Chesapeak Bay area (77.0°W-76.0°W, 38.7°N-39.4°N) for 40 x 40 pixels and 20 days. Pixels were resampled to make the pixel-to-pixel distance about 2km. Retrieval results show that a spatially smooth distribution of fine and coarse aerosol optical thicknesses (AOT) were retrieved for each area. It should be especially noted that the AOT distribution is smooth at the boundary of water and land areas indicating the smoothing constraint of MWPM can be successfully applied to the real data. Another example of the analysis is for Beijing area, China, as shown in Fig. 3.3.2.3.1.1 which indicates that the retrieved AOT values are consistent with the surface-based measurement by a sunphotometer. We also confirmed, though not shown in a figure, that seasonal variation of the retrieved Black Carbon (BC) fraction and the aerosol single scattering albedo (SSA) are consistent with the surface-observed ones by AERONET and by BC measurement (Song et al., 2013), i.e., the BC fraction increases in the winter season. These analyses suggest that our aerosol remote sensing method is significantly effective for heterogeneous surface areas including city area where conventional aerosol retrieval algorithms met a difficulty to retrieval accurate aerosol parameters.

We also extended the MWPM to an ocean area. The radiative transfer model was improved by adding a bio-optical module in the ocean part based on empirical formulations and Mie theory to consider the absorption and scattering effects of chlorophyll-a, sediment and colored dissolved organic matter (Shi et al., 2015). Fig. 3.3.2.3.1.2 shows numerical results of the upward radiance just above the ocean surface calculated by the improved code. The simulation of simultaneous retrieval of aerosol and chlorophyll was made using multi-wavelength radiance covering in and out of sunglint region. Figure 3.3.2.3.1.3 shows the simulation result by using Pstar model (Ota et al., 2009). It was demonstrated that the relative errors in simultaneously determining the optical thickness of fine, sea salt and dust particles were majorly less than approximately 10% except the dust particles in the lower concentration. The relative error for the inversion of wind velocity was less than 1.4%, due to an observation in the sun-glint direction, there are some bias for the inversion of chlorophyll-a in the relative lower an higher concentration based on simulation.

We have a plan to perform an extensive test of inversion and eventually replace our conventional ocean aerosol retrieval codes, i.e. two channel and four channel algorithms (Nakajima and Higurashi, 1998; Higurashi and Nakajima, 2002) by this general method that can accept radiances in all the channels of the imager.
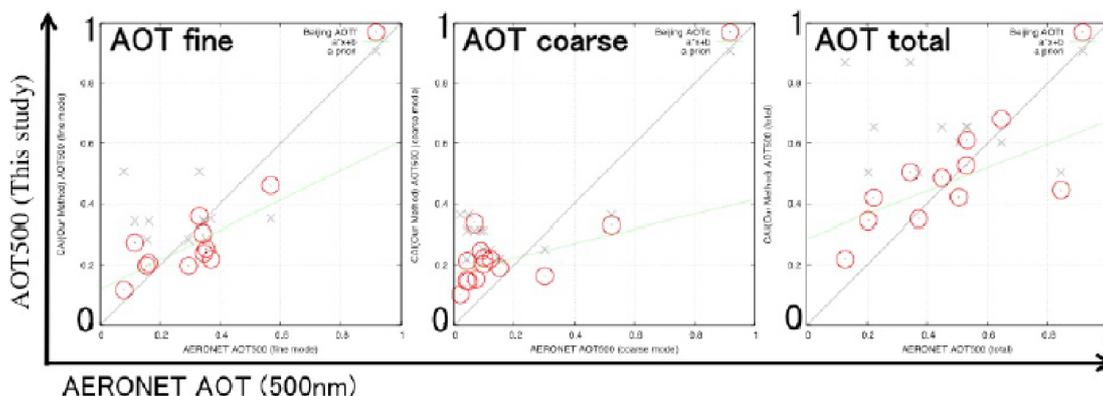
Fig. 3.3.2.3.1.1 Comparison of retrieved AOTs for fine, coarse and total aerosols with AERONET-retrieved values for a Beijing area, China, during July to December of 2009.
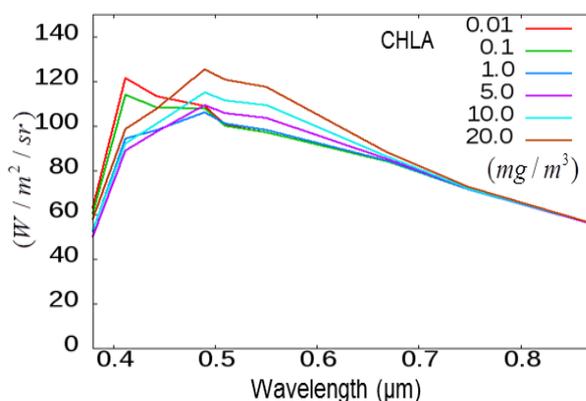

Fig. 3.3.2.3.1.2 Upward radiances above ocean surface computed by the two radiation codes (left: Rstar and molecular polarization by Pstar; right: Pstar) for various chlorophyll concentrations. Angular condition and wind velocity at 10m height are given as v_{10}= 5.0 m/s, θ_0= 30°, θ= 40° and φ - φ_0= 0°.
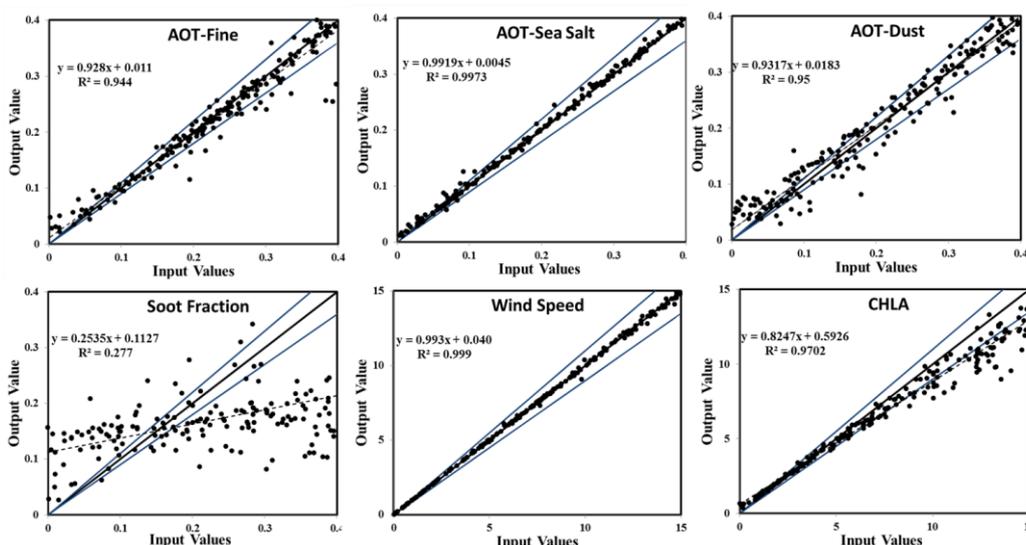
Fig. 3.3.2.3.1.3 Simulation of simultaneous retrieval of atmosphere-ocean patameters using multi-

wavelength radiance covering in and out-of sunglint. (Shi et al., 2015)

References

Higurashi, A., and T. Nakajima, 1999: Development of a two channel aerosol retrieval algorithm on global scale using NOAA/AVHRR. J. Atmos. Sci., 56, 924-941.

Higurashi, A., T. Nakajima, B. N. Holben, A. Smirnov, R. Frouin, B. Chatenet, 2000: A study of global aerosol optical climatology with two channel AVHRR remote sensing, J. Climate, 13, 2011-2027.

Higurashi, A., and T. Nakajima, 2002: Detection of aerosol types over the East China Sea near Japan from four-channel satellite data. Geophys. Res. Lett., 29(17), 1836, doi:10.1029/2002GL015357.

Nakajima, T., and A. Higurashi, 1998: A use of two-channel radiances for an aerosol characterization from space. Geophys. Res. Lett., 25, 3815-3818.

Ota, Y., A. Higurashi, T. Nakajima, and T. Yokota, 2010: Matrix formulations of radiative transfer including the polarization effect in a coupled atmosphere-ocean system. J. Quant. Spectrosc. Radiat. Transfer, 111, 878-894, doi:10.1016/j.jqsrt.2009.11.021.

Shi, C., et al., 2015: Effects of Ocean Particles on the Upwelling Radiance and Polarized Radiance in the Atmosphere–Ocean System. Advances in Atmospheric Sciences 32 1-11.

Song, S., Y. Wu, J. Xu, J., T. Ohara, S. Hasegawa, J. Li, L. Tang, and J. Hao, 2013: Black carbon at a roadside site in Beijing: temporal variations and relationships with carbon monoxide and particle number size distribution. Atmos. Environ., 77, 213-221.

4. Synergy Product

4.1 CPR-ATLID

4.1.1 Standard Product

4.1.1.1 Introduction

This section describes the synergetic algorithms that use CPR and ATLID signals to retrieve the Standard Product (1) the hydrometeor and cloud masks, (2) the discrimination of cloud particle type and (3) the cloud microphysics, using the radar reflectivity factor and Doppler information from CPR on EarthCARE.

The basic flow of the algorithms to produce standard and research cloud products from the CPR/ATLID synergy is shown in Figure 4.1.1.1.1. We first describe the algorithms to derive standard cloud products, followed by the algorithm details for the research products.

* denotes the products are produced with use of Vd
and without use of Vd
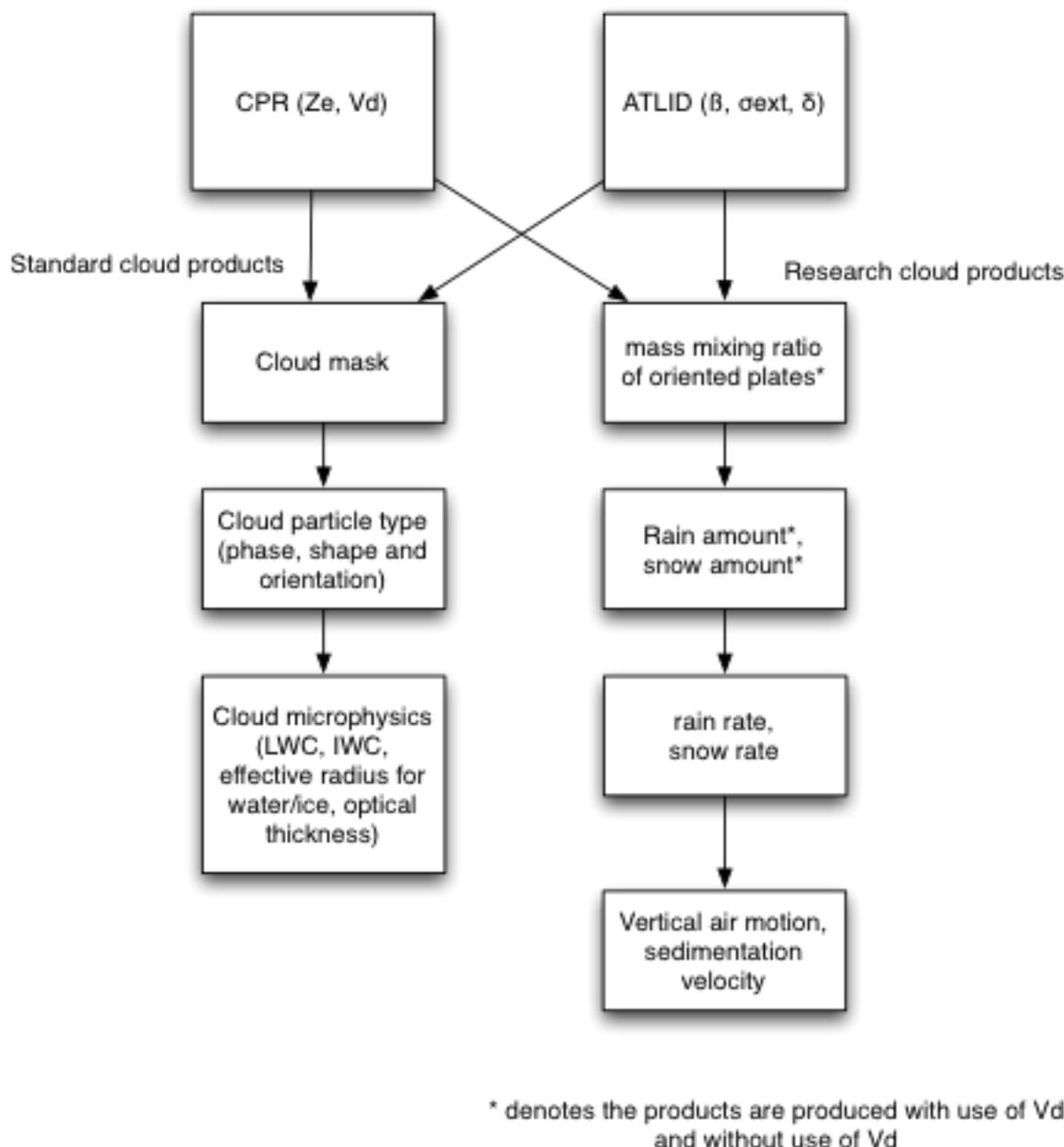
Figure 4.1.1.2.1.1 Flow of the algorithms for standard and research cloud products for CPR and ATLID synergy.

The treatments for Ze and Vd used in CPR/ATLID algorithms are similar to that for the CPR algorithm. In a similar but slightly different manner from the cloud mask for CPR, we first develop the cloud mask for the ATLID data on basis of the threshold and spatial consistency test. Since the horizontal resolution of ATLID is smaller than those of CPR, i.e., 285m for horizontal resolution for ATLID and vertical resolution of about 100m is the same as CPR, we can estimate the cloud fraction in the CPR grid to study the sub grid scale cloud feature within the CPR grid. These mask data are finally produced for the CPR gird resolution. That is, the cloud mask data from ATLID with its original resolution is averaged to the CPR resolution. Then when the cloud fraction of ATLID exceeds the threshold value of 0.5, the CPR grid box is considered to be cloud by the cloud mask scheme from ATLID. To develop the ATLID cloud mask, first, we modified a cloud mask

scheme originally developed for CALIPSO using a threshold of the attenuated total backscattering coefficient and a spatial consistency test.

4.1.1.2 Cloud Mask

4.1.1.2.1 Algorithm

We describe the cloud mask for ATLID. The ATLID cloud mask scheme is based on two criteria. The first criterion is that the attenuated total backscattering coefficient at 0.355 nm, $\beta'_{355}(z)$, exceeds a threshold value β_{th} that depends on the altitude z and the range r from the satellite to the bin of interest. This criterion is calculated for the original resolutions of the ATLID by

$$\beta_{th}(z,r) = \frac{\beta_{th,aerosol} + \beta_{th,noise}(z,r)}{2} - \frac{\beta_{th,aerosol} - \beta_{th,noise}(z,r)}{2}\tanh(z-5),$$

(6)

in which,

$$\beta_{th,aerosol} = 10^{-5.25}[1/m/ster]$$

(7)

and

$$\beta_{th,noise}(z,r) = (P_m(z,r) + P_n + \sigma_n)r^2,$$

(8)

where $P_m(z, r) = \beta_m(z)/r^2$, $\beta_m(z)$ is the volume molecular backscattering coefficient derived from ECMWF data. P_n and σ are the noise signals and the standard deviation of the background noise. The standard deviation is estimated using the P_n averaged horizontally at upper altitude than 20 km for 5 km. The second criterion is the spatial consistency test, introduced to eliminate pixels associated with aerosol and noise contaminations. At first, a "sliding data window," including information from neighboring bins in both the horizontal and vertical dimensions were created. We consider a data window made up of two-dimensional 5 × 5 bins. Each bin is surrounded by 24 pixels. If half of these 25 pixels satisfy the first criterion, the pixel of interest is considered as cloud in the ATLID mask scheme. We then applied this test to the original resolution of the ATLID data. The criterion expressed in equation (7) and the size of the window might be changed after the investigation of the background noise in the configuration of the ATLID observations.

Since the CPR and ATLID cloud mask results have differences in spatial resolution and pointing angle, an averaging procedure is necessary to interpolate the two data sets onto a common grid, Joint Standard Grid. Consequently, we will create four cloud mask schemes: (C1) CPR only cloud mask, (C2) ATLID only mask, (C3) CPR and ATLID cloud mask and (C4) CPR or ATLID cloud mask form these two sensors. The cloud mask (C4), by definition, gives the largest number of cloud grid boxes among the four schemes (for further details about C1-C4 masks, see Okamoto et

al., [2007, 2008]). The cloud mask (C4), by definition, gives the largest number of cloud grid boxes among the four schemes.

4.1.1.2.2 Evaluation of CPR-ATLID cloud mask algorithms

For the demonstration purposes of how synergetic data provide complement information on cloud detection, the cloud mask schemes were applied to CloudSat and CALIOP data and the results are summarized (Fig. 4.1.1.2.2.1). Similar method will be applied not only to CPR but also to ATLID, and these sensors will give us the improved picture of global distribution of clouds.

We examined the zonal mean cloud fractions obtained by each mask as well as the differences between the results for September–November 2006. The cloud fraction at a given altitude was defined as the number of cloud bins (mask values >0.5) divided by the total number of observations at that level. The vertical resolution was 240 m, and the horizontal resolution was 2.0° latitude. We defined C1 to be radar cloud mask scheme, C2 to be lidar cloud mask scheme. C3 is the scheme that detects cloud when both the C1 and C2 detect cloud. Therefore, C3 scheme indicates the smallest occurrence of cloud among the four schemes. C4 is the scheme that detects cloud when either of the C1 or the C2 detects the cloud. Note that the C1 and C4 results include hydrometeor fractions, i.e., clouds and drizzle. The vertical distributions of zonal mean cloud fractions and cloud coverage were analyzed [Hagihara et al., 2010]. The C1 result clearly shows a Hadley cell, illustrated by the deep convection column located near 7.5° and the nearly cloud free subtropical high. The mid-latitude storm track regions in both hemispheres have substantial cloud fractions (55%). Cloud top height in the upper troposphere observed by CALIPSO is higher than that by CloudSat by 1–2 km depending on the latitude. Fig. 3.1.1.3.2.2 (e) also shows improved detection by CALIPSO in areas below 720 m, where surface clutter hinders detection by CloudSat. CPR of the EarthCARE will reduce the contamination due to surface clutter in lower bins by its specification. It has generally been accepted that lidar cloud top is the same or higher than those detected by cloud radar in case of spaceborne observations. We investigated the cloud top height differences between CloudSat and CALIPSO lidar and found that 26% of low level clouds has its cloud top detected by the CloudSat higher than that by CALIPSO lidar and 39% is the value in mid-level clouds and 10% for high level [Hagihara et al., 2014]. Theoretical studies showed that when large particles exist in such cloud portion, radar-cloud top is higher. Since the sensitivity of the EarthCARE CPR is 7dB higher than that of CloudSat, the fraction of such clouds might increase and reducing the sensitivity of CPR to CloudSat value of about -30dBZ, the similar fraction to the findings in Hagihara et al., 2014 will be achieved provided that the ATLID sensitivity to clouds is similar to that of CALIPSO lidar. These will be one approach to evaluate the products.

4.1.1.3 Cloud Particle Type

Here we describe the synergy cloud particle type algorithm, where the cloud particle type for ATLID extended from that for CALIPSO [Yoshida et al., 2010] are introduced first and then the algorithm using the synergy data of CPR and ATLID are described.

4.1.1.3.1 Algorithm

We used the vertical profile of backscattering coefficient and depolarization ratio (δ) at the 355 nm wavelength measured by ATLID for cloud type discrimination. The approach is taken to

be similar to the one for the analysis of CALIPSO [Yoshida et al., 2010] with modification [Oka-moto and Sato 2018]. When a single-scattering process is dominant, spherical particles in water clouds do not show $\delta > 0$. In contrast, the randomly oriented ice crystals in ice clouds produce large δ (about 40%). Therefore, δ has been used for cloud phase discrimination in cases of ground-based polarization lidar measurements. However, satellite-borne lidar instruments, such as CA-LIOP and ATLID observe much larger footprints (e.g., 90 m for CALIOP and about 30m for ATLID) on Earth's surface than does ground-based lidar (generally less than 10 m). Similar dis-crimination is thus not straightforward for satellite observations because of large δ values caused by multiple scattering in water clouds. To estimate the multiple scattering effects on δ quantita-tively in water clouds, we adopted a backward Monte Carlo (MC) method developed by Ishimoto and Masuda [2002] at the wavelength of 355nm. The MC method was developed to solve the Stokes vector of multiple scattered light for an optional scattering medium with arbitrary bounda-ries. This method enables estimation of δ and the backscattering coefficient at 355 nm as a function of the penetration depth for a given extinction coefficient. CALIOP has a 0.13 mrad field of view (FOV) and orbits Earth at a distance of ~ 700 km above the ground. ATLID has different observa-tion condition, e.g., smaller FOV (0.08 mrad) and orbits Earth at a distance of ~400 km, The scat-tering matrix is calculated from Mie theory for water clouds and proper scattering theories such as geometrical optics with physical optics for ice clouds [Borovoi and Kustova 2009, Borovoi et al., 2012].

In the analysis of CALIOP at 532 nm, we found that the value of δ for water clouds was sometimes larger than 40% and comparable to or larger than values for randomly oriented ice crystals. For ATLID, we expect smaller value of δ but there are still overlap between ice and water clouds. Therefore, we will take the similar discrimination scheme for cloud particle type as in the analysis of CALIPSO that there is a fundamental difficulty in discriminating water from ice when we only use the measured δ value from CALIOP.

In order to overcome the above-mentioned problem, we introduced an additional parameter for the cloud particle type. According to Okamoto et al. [2003], the attenuated backscattering co-efficient with finite geometrical thickness for the 355 nm wavelength of layer i can be written as

$$\beta'_{355} = \beta_{355}(R_i)\exp[-2\tau_{355}(R_{i-1/2})] \cdot \left\{ \frac{\exp[-2\sigma_{355}(R_i)\Delta R] - 1}{-2\sigma_{355}(R_i)\Delta R} \right\} \quad (9)$$

, where β_{355} is the backscattering coefficient for the 355 nm wavelength, ΔR is the vertical resolu-tion (here equal to 100 m), R_i denotes the distance to the center of layer i, and $R_{i-1/2}$ is the top boundary of layer i viewed from the satellite. The geometrical thickness of a layer is 100 m. The ratio of the attenuated backscattering coefficient of layer i to that of the next layer (i + 1) is esti-mated. The ratio is known to proportional to transmittance of the layer when the cloud microphys-ics of the layer was assumed to be homogeneous. We estimate two-dimensional frequency distri-butions of the ratio and δ for all cloud observations for different temperature (T) categories from the existing data such as CALIPSO. Then the empirically derived frequency distribution expressed in δ and the ratio plane can be also checked by the theoretical curves calculated by the scattering method where the near field is calculated by the geometrical optics and the far field is calculated

from the information of near field by the Physics Optics such as Kirchhoff approximation [Iwasaki and Okamoto 2001, Borovoi et al., 2012, Okamoto et al., 2019, 2020]. Since the ATLID is a high spectral resolution lidar (HSRL), it can directly produce σ_{ext} without any assumption made. If the measured extinction will be obtained with sufficient accuracy, we can replace the ratio of two attenuated β's by σ_{ext} for the cloud particle classification. For example, when both σ_{ext} and δ are large, the particle is categorized to be water. When σ_{ext} and δ are small and large, the cloud particle is categorized to be randomly oriented ice crystals. When both of σ_{ext} and δ are small, the cloud particle is considered to be oriented plate in horizontal plane.

The ice particle type can be specified by the relation of lidar ratio (S) defined as σ_{ext}/β and δ. We estimated the average backscattering coefficient (β), backscatter color ratio (χ), and depolarization ratio (δ) for ice particles with a wide range of effective radii for five randomly oriented three-dimensional (3D) and three quasi-horizontally oriented two-dimensional (2D) types of ice particle using physical optics and geometrical integral equation methods [Okamoto et al., 2019, 2020]. The following ice particle types and orientations are considered; quasi 2D- and 3D-Voronoi, Droxtal, Bullet, quasi 2D- and 3D-Columns and quasi 2D and 3D-Plates. The algorithm based on S- δ relationship produces robust classification of ice particle type. In addition, in order to improve the discrimination of dust and ice particles, lidar ratio–depolarization ratio relations at 355nm produced by super-spheroid dust models were comprehensively investigated, and the optimal super-spheroid parameters to parameterize dust shapes were determined through combined theoretical and airborne HSRL observation studies (Kong et. al., 2022).

Finally, the CPR- and ATLID- type classification schemes are combined as the CPR-ATLID synergy classification scheme, which is applicable to CPR only detected regions, ATLID only detected regions and CPR and ATLID detected regions [Kikuchi et al., 2017]. In the CPR-ATLID synergy classification scheme, information of the particle types assigned independently by the CPR- and ATLID- type classification scheme at each observation grid is used to re-classify the particle type based on the developed classification rule. Further, a radar reflectivity and temperature-based melting layer detection scheme is developed and implemented in the hydrometeor type classification scheme to determine the ice-water mixing layers. Accordingly, the following 14 hydrometeor types are considered: warm water, super-cooled water, randomly oriented ice crystal (3D-ice), horizontally oriented plate (2D-plate), 3D-ice + 2D-plate, liquid drizzle, mixed-phase drizzle, rain, snow, mixed-phase cloud, water + liquid drizzle, water + rain, melting layer, and unknown. From sensitivity studies, the total retrieval uncertainty of the method due to measurement errors was estimated to be 5.8%. The hydrometeor type classification scheme was adapted to different laser tilting angle configurations [Kikuchi et al., 2021]. The synergy algorithm was also applied to CloudSat-CALIPSO data and validated by collocated aircraft in-Situ observation data and by collocated HSRL, including recently developed a 355-nm HSRL using a scanning Michelson interferometer [Jin et al., 2020, 2022], Doppler lidar and Doppler cloud radar.

4.1.1.3.2 Application Study

We examined cloud particle types from CALIOP observations taken on 8 October 2006 in the area 33°S–58°S, 114°W–123°W over ocean. We also examined the CloudSat radar reflectivity, CALIOP backscattering coefficient at 532 nm, depolarization ratio, the resulting cloud particle type by our method and the Vertical Feature Mask (VFM) cloud phase product. The VFM cloud phase is derived from the ice water algorithm (IWA) [Liu et al., 2005] and distributed by the CALIPSO team based at the National Aeronautics and Space Administration (NASA), Langley. The VFM product generally showed more cloudy pixels than were found in our product. The differences reflect differences in the cloud mask schemes [Okamoto et al., 2007, 2008; Hagihara et al., 2010]. CloudSat and CALIOP detected southern mid-latitude storm tracks. These were typical storm tracks in that latitude zone and are known to be associated with extratropical cyclones. CloudSat CPR detected clouds with precipitation having top heights of ~10 km and horizontal scales larger than 200 km. We could infer the vertically resolved particle type inside the same cloud layer. The method was further applied to CALIOP data for September–November 2006. We found that 3-D ice generally occurred colder than −20°C, whereas 2-D plate occurred between −10°C and −20°C, with high-occurrence frequency in high-latitude regions. The Vertical Feature Mask (VFM), which is a set of standard products distributed from NASA, tended to show a homogeneous cloud type through the entire cloud layer in vertical directions and misclassified 2-D plate as water. The ratio of water particles relative to ice particles decreased with decreasing temperature. By the proposed method, water cloud occurrence in subtropical and high-latitude regions was greater (up to 20%) than in the other regions below −10°C; however, the VFM results did not show such dependence on latitude [Yoshida et al, 2010]. Water/ice partitioning derived from the analyses here has been used to evaluate the representation in the Atmospheric General Circulation Model [Watanabe et al., 2010]. Synergy use of CPR and ATLID on EarthCARE will enable to obtain more robust cloud type classification owning to the higher sensitivity of CPR on Earth-CARE compared with CloudSat, Doppler capability for the ability to discriminate precipitation from clouds and the capability of direct measurement of extinction.

4.1.1.4 Cloud Microphysics

4.1.1.4.1 Ice microphysics algorithm

We first describe the algorithm for ice microphysics and that for water cloud microphysics will be given later in the next sub section.

Once we obtain the cloud particle types for the whole cloud grids detected by the CPR and/or ATLID, we can apply the radar-lidar algorithms for the CPR-ATLID overlapping region as performed for CloudSat and CALIPSO data [Okamoto et al., 2010] . By using the solutions for the CPR-ATLID overlapping region, it is also possible to derive the cloud microphysics for CPR or ATLID only regions as demonstrated in Sato and Okamoto [2011]. Products obtained by the algorithm are effective radius for ice and water clouds, IWC and LWC. Mass mixing ratio of oriented plates (2D-plate) are obtained by the algorithm but the product is in the research cloud products.

The radar-lidar approach is applied to the data corresponding to the grid boxes that detected cloud by both the radar and lidar, and the cloud microphysics, i.e. effective radius and IWC, are retrieved. The main characteristic of the radar-lidar algorithm is the followings; (a) this is a forward type approach where the microphysics of cloud top layer is first retrieved (b) attenuation correction due to clouds and precipitation for the next layer is performed using the knowledge of the microphysics retrieved for the first layer. Prior to the application of radar-lidar algorithm to the CPR and ATLID data, the attenuation in radar signals due to gaseous absorption is taken into account. The attenuation correction due to molecule scattering and aerosols is also performed for ATLID. For the latter correction, aerosol products produced from lidar method is used. These corrections are especially effective for the retrieval of water cloud.

For the cloud grids only detected by the CPR, the microphysics are not retrieved by the original radar-lidar approach. Radar reflectivity-Doppler velocity-lidar algorithm can be applied to these grids when Doppler velocity is available.

We first describe the basis for the retrieval of cloud microphysics by the radar-lidar algorithm without Doppler velocity. The algorithm uses Z_e from CPR and attenuated backscattering coefficient β' and δ from ATLID. To develop the algorithm, we used the CloudSat and CALIPSO data. Input observation parameters are Z_e [dBZ] at 94 GHz (3.16 mm) measured by CloudSat, and $\beta_{tot,m}$ [1/m/sr] and δ [%] at 532 nm measured by CALIOP; δ is introduced as an additional input parameter in the original version of the radar-lidar algorithm described in Okamoto et al., [2003]. Four look-up tables (LUTs) are created in the algorithm: two for CloudSat and two for CALIOP. We considered two types of particle: CB50 model as an analog to 3D ice category, and a 2D plate category. The effective radius, IWC and mass mixing ratio of 2D-plate to the total IWC are retrieved for radar and lidar overlap regions with high accuracy.

To treat the mixture of 2D plate and 3D ice categories on the same grid, Z_e, β and δ were expressed in terms of the cloud microphysics of 2D plate and 3D ice categories, with β for parallel channel for 3D and 2D-plate.

$$\beta_{co,r} = \beta_{co,r1} I_r,$$

$$\beta_{co,h} = \beta_{co,h1} I_h, \quad (10)$$

where I_r and I_h denote IWC for 3D ice and 2D plate categories, respectively, and $\beta_{co,r1}$ and $\beta_{co,h1}$ are defined as $\beta_{co,r}$ with $I_r = 1$ g/m^3 and $\beta_{co,h}$ with $I_h = 1$ g/m^3, respectively. Similarly, the backscattering coefficients for the perpendicular channel were expressed as

$$\beta_{cr,r} = \beta_{cr,r1} I_r,$$

$$\beta_{cr,h} = \beta_{cr,h1} I_h, \tag{11}$$

where $\beta_{cr,r1}$ and $\beta_{cr,h1}$ are defined as $\beta_{cr,r}$ with $I_r = 1$ g/m3 and $\beta_{cr,h}$ with $I_h = 1$ g/m3, respectively.

The values of $\beta_{co,m}$ and $\beta_{cr,m}$ measured by the ATLID were written using the discretized form of attenuation introduced by Okamoto et al. [2003]

$$\beta_{co,m} = \left(\beta_{co,r1} \frac{I_r}{I_t} + \beta_{co,h1} \frac{I_h}{I_t} \right) I_t \exp\left(-2\tau'_{li}\eta \right)$$
$$\times \left\{ \frac{\exp\left[-2I_t \left(\sigma_{ext,li,r1} \frac{I_r}{I_t} + \sigma_{ext,li,h1} \frac{I_h}{I_t} \right) \Delta R\eta \right] - 1}{-2I_t \left(\sigma_{ext,li,r1} \frac{I_r}{I_t} + \sigma_{ext,li,h1} \frac{I_h}{I_t} \right) \Delta R\eta} \right\}, \tag{12}$$

Here, η was assumed to be 0.5 in Okamoto et al. [2010]. We introduce X_h, defined as the mass ratio between 2D plate category and 3D ice I_h/I_r, and the total IWC, I_t as $I_r + I_h$, the mass mixing ratio of 3D ice category to the total ice mass. We can then write I_r/I_t as $1/(1 + X_h)$, and the mass mixing ratio of 2D plate category is $I_h/I_t = X_h/(1 + X_h)$. Then $\beta_{co,m}$ can be written in terms of X_h as

$$\beta_{co,m} = \left(\beta_{co,r1} \frac{1}{1 + X_h} + \beta_{co,h1} \frac{X_h}{1 + X_h} \right) I_t \exp\left(-2\tau'_{li}\eta \right)$$
$$\times \left\{ \frac{\exp\left[-2I_t \left(\sigma_{ext,li,r1} \frac{1}{1 + X_h} + \sigma_{ext,li,h1} \frac{X_h}{1 + X_h} \right) \Delta R\eta \right] - 1}{-2I_t \left(\sigma_{ext,li,r1} \frac{1}{1 + X_h} + \sigma_{ext,li,h1} \frac{X_h}{1 + X_h} \right) \Delta R\eta} \right\}, \tag{13}$$

In a similar manner, $Z_{e,m}$ can be written in terms of r_{eff}, I_t, and X_h as

$$Z_{e,m} = \left(Z_{e,r1} \frac{1}{1 + X_h} + Z_{e,h1} \frac{X_h}{1 + X_h} \right) I_t \exp\left(-2\tau'_{ra} \right)$$
$$\times \left\{ \frac{\exp\left[-2I_t \left(\sigma_{ext,ra,r1} \frac{1}{1 + X_h} + \sigma_{ext,ra,h1} \frac{X_h}{1 + X_h} \right) \Delta R \right] - 1}{-2I_t \left(\sigma_{ext,ra,r1} \frac{1}{1 + X_h} + \sigma_{ext,ra,h1} \frac{X_h}{1 + X_h} \right) \Delta R} \right\}, \tag{14}.$$

For the mixture of 2D plate and 3D ice categories, δ_m can be written as

$$\delta_m = \frac{\beta_{cr,r1}I_r + \beta_{cr,h1}I_h}{\beta_{co,r1}I_r + \beta_{co,h1}I_h}.$$
(15)

Because $\beta_{cr,h1} = 0$ and $\delta_r = \beta_{cr,r1}/\beta_{co,r1} = 0.4$, equation above can be further simplified to

$$\delta_m = \frac{\delta_r}{\dfrac{\beta_{co,h1}}{\beta_{co,r1}}X_h + 1}$$
(16)

X_h can be expressed as

$$X_h = \frac{\beta_{co,rl}}{\beta_{co,hl}}\left(\frac{\delta_r}{\delta_m} - 1\right)$$
(17)

,where $\beta_{co,h1}$ and $\delta_{co,r1}$ are given as functions of R_{eff} in the LUTs.

Note that δ_r can be given according to the result of ice particle category described above and now δ_r depends on radius and category [Okamoto et al., 2019, 2020]. Same can be said for β. Thus the radar-lidar algorithm can be extended to incorporate the replacement of CB50 by ice particle category by retrieved ice category.

The R_{eff} of the 2D plate category is assumed to be the same as that of 3D ice category in the cloud grid. Then X_h solely depends on R_{eff} for a given δ_m. Thus for each R_{eff}, every possible X_h can be calculated. The equations related $\beta_{co,m}$ and $Z_{e,m}$ to R_{eff} and I_t. Therefore, we could estimate R_{eff}, I_t and X_h from the three observables, Z_e, $\beta_{co,m}$ and δ_m for the cloud top layer. Attenuation correction to the next top layer is performed by using the retrieved microphysics for the top layer. By repeating the procedure, we obtain all cloud microphysics such as effective radius of ice, IWC and mass mixing ratio of 2D-plate. Lidar backscattering coefficient and extinction are obtained by the physical optics [Iwasaki and Okamoto 2001, Borovoi et al., 2012, Okamoto et al., 2012, Okamoto et al., 2019, 2020].

Use of fixed ice model leads to large errors in the retrieved microphysics. Based on physical optics and geometrical optics integral equation method, Okamoto et al., [2019] found that β differed more than one order of magnitude among the particle types for the same effective radius and IWC. Thus, introducing particle category can reduce retrieval errors of microphysics. Other source of errors in the retrievals is the use of constant η of 0.5 for multiple scattering correction. For the EarthCARE CPR/ATLID algorithm, several updates on the treatment of single scattering and multiple scattering by non-spehrical ice particles are considered to minimize the uncertainties in the retrieved cloud microphysics. For multiple scattering, the constant $\eta = 0.5$ model can be replaced by the physical model (PM) which directly simulates the multiple scattering effects with input single scattering properties based on the geometrical optics with physics optics approach. Detail of the PM is described later in subsection 4.1.1.4.2.

In order to treat the cloud microphysics for CPR or ATLID only detected regions, we can follow the approach introduced by Sato and Okamoto [2011]. The algorithm extended the retrieval algorithm of cloud microphysics in Okamoto et al., 2010 as follows: (1) it increases the applicability of the radar- lidar overlap cloud region to the radar- or lidar-only cloud regions and (2) it gives an optimal estimation of the microphysics and their retrieval uncertainties with the Levenberg-Marquardt algorithm [Marquardt 1963]. The basic concept behind the microphysical retrieval in the radar- or lidar only region is as follows; for the radar-lidar overlap region, the dependence of the ratio of Z_e and β' for two vertically consecutive grids on those of r_{eff} and IWC can be inferred. For the radar (or lidar) only region, β (or Z_e) is estimated by projection of such a relationship between the ratio of Z_e and the ratio of β in the two consecutive grids, i.e., grid of interest and previous grid. The r_{eff} and IWC are retrieved within 10% uncertainties except for extreme cases where IWC is retrieved within 40%. Once we obtain the vertical profile of all variables such as Z_e, β and δ, by estimating them at grids where they are not observed, it is possible to estimate the vertical profile of cloud microphysics. Further, an improved version of the retrieval algorithm is developed for EarthCARE, and when applied to the A-train data, it was found to have good agreement between the cloud optical thickness estimates by CloudSat and CALIPSO and that from MODIS.

4.1.1.4.2 Water microphysics algorithm

For water cloud, an approach similar to the ice cloud algorithm is applied to analyze the vertical profile of Ze, β and δ to obtain cloud microphysical properties, but with replaced forward models. In case of water cloud microphysics retrieval, the forward models for ATLID and CPR observables are based on Mie theory with log-normal particle size distribution function. Different size distribution functions are taken into account to assess such effect on the retrieved cloud microphysics. As mentioned in previous subsection for the cloud particle type algorithm, treatment of multiple scattering effects including pulse-stretching effects on β and δ is essential for the retrievals. In order to provide accurate and fast estimates of the time-space dependent multiple scattering backscattered irradiance for lidar signal simulations, a physical model (PM) was developed [Sato et al., 2018]. Further, the PM was extended with a polarization function to create a vectorized physical model (VPM) [Sato et al., 2019]. The PM decomposes the backscatter irradiance into contributions from the singles scattering component (SS), on-beam multiple scattering component (MS,on) and the off-beam multiple scattering component (MS,off). These are further modeled by introducing an analytical expression for the high-order phase function to significantly reduce computational cost, and the decay rate of the multiple scattering backscattered irradiance was estimated by incorporating the dependence on the scattering angle and the scattering order on the basis of the path integral formulation [R. P. Feynman, 1949]. The VPM includes a high-order scattering matrix and accommodates mechanisms that modify the polarization state of the incoming wave during multiple scattering processes by considering the horizontal spread of the photons for the MS,on and MS,off components. By the VPM, transition from the SS-dominant regimes to the MS,on, and MS,off - dominant regimes for the total backscattering and depolarization ratio can be naturally estimated. The VPM can treat β and δ for arbitrary space-borne lidar specification. Intensive error analyses of β and δ estimated over time and range by the PM/VPM against those

from Monte Carlo simulations for vertically homogeneous and inhomogeneous cloud profiles and those from literatures revealed that the PM/VPM had good agreement with Monte Carlo simulations and had wide applicability. Further, it was found that the PM had smaller mean relative error and standard deviation than existing statistical method for β.

The VPM is incorporated into the EarthCare ATLID and CPR water cloud algorithm, which combines forward calculations with a multidimensional optimization algorithm. Incorporation of cloud extinction measurement in the algorithm framework is straightforward when it becomes available. In the actual process, water, ice cloud microphysics and aerosol extinction are simultaneously retrieved. Additional information of V_d enables better estimate of the cloud microphysics as mentioned in the CPR only section especially for CPR only detected cloud regions.

With V_d, the accuracy of radar only region will be greatly enhanced [Sato et al., 2009, Sato et al., 2010]. The product from the approach includes effective radius, IWC/LWC, mass mixing ratio of 2D-plate and air motion. At first the algorithm uses the information of cloud microphysics derived from the radar-lidar algorithm for the C3-masked grids. From the retrieved microphysics, the Doppler velocity solely due to the particle microphysics V_{tz} is estimated, i.e., no effects of air motion on the Doppler velocity. The difference between the measured Doppler velocity and V_{tz} corresponds to the air-motion. For the radar only region, the normalized structure of radar reflectivity and that for Doppler velocities in vertical direction are constructed and the differences between the two with the information of retrieved air motion are used to derive the air motion for the C1 clouds. Then the correction of air-motion to the Doppler velocity is performed to estimate the particle terminal velocity and the particle size is obtained. Finally radar reflectivity factor and the size information determine IWC. Similar to the ice cloud case, the precipitation and water cloud microphysics can be obtained by using the same framework used in the algorithm. For the cloud regions only detected by the lidar, the lidar approach and/or empirical formula developed by the radar-lidar approach are used.

The accuracy for the radar-lidar method and radar reflectivity and Doppler velocity has been assessed by the comparison of in-situ data [Heymsfield et al., 2008]. The former approach introduced here turns out to be the most accurate one among the participating algorithms, i.e., smallest bias and standard deviation. The latter also turns to gives the smallest standard deviation among the categories. Validation activities for space-borne radar and lidar data are ongoing for the radar-lidar and reflectivity and temperature approaches for the CloudSat and CALIPSO data with collocated air-craft data. The radar reflectivity-Doppler-lidar method will be also tested for the airborne radar data with in-situ data.

As an example of the CPR-ATLID cloud microphysical product, simulated backscattering coefficient, extinction coefficient and depolarization ratio for ATLID are calculated. And retrieved effective radius and cloud water content from the synergy use of CPR and ATLID observables are derived.

4.1.1.4.3 Evaluation of cloud microphysics algorithm

Global analyses of ice microphysics for CloudSat-CALIPSO overlap regions were performed (Fig. 4.1.1.4.1.7). The effective radius decreased as the altitude increased. The effective radius in the specular reflection ranged from 100 to 300 μm. The ice water content (IWC) ranged from 10−4

to several tenths of a gram per cubic meter. Both effective radius and IWC increased as the altitude (temperature) decreased (increased). The largest mixing ratio of oriented particles occurred between −20 and −5°C. The IWC had two maxima in the tropics above 15 km and around 5 km. We also examined the differences in ice microphysics over land and ocean (Fig 4.1.1.4.1.8). The effective radius was similar over land and ocean, but the IWC tended to be larger over land [Okamoto et al., 2010]. Synergy data of CPR and ATLID will provide more reliable information of cloud microphysics. The ice effective radii in cloud top regions are compared between the Cloud-Sat-CALIPSO retrieval results and that by MODIS infrared channels. The general agreement has been achieved in spite of applying totally different techniques [Iwabuchi et al., 2014]. Ze-IWC relationship derived for CloudSat-CALIPSOP over-rapping regions have been compared with those derived from aircraft measurements in the CIRCLE-2 campaign [Gayet et al., 2012]. General agreement was found in especially the clouds that do not contain cloud cores [Seiki et al., 2019].

For further evaluation of the cloud microphysics retrieval, we have developed a new type of ground-based multiple scattering lidar called the Multiple-Field-of-View Multiple-Scattering Polarization Lidar (MFMSPL) [Okamoto et al., 2016, Nishizawa et al., 2021] and a newly developed 355-nm and 532-nm high-spectral-resolution lidar (HSRL) with a scanning interferometer [Jin et al., 2020, 2022]. This system consists from several parallel and perpendicular channels mounted with different zenith angles to measure backscattering and depolarization ratio comparable to space-borne lidars, but with much higher resolution. The performance of the MFMSPL was investigated by collocated observation with the 95-GHz cloud radar and from theoretical simulations by Monte Carlo method. These showed that the MFMSPL could observe the actual cloud top height of optically thick cloud and the lidar signals that are affected by multiple scattering. The MFMSPL system has the capability to simulate satellite signals and test the developed retrieval algorithms for ATLID as well as ATLID-CPR synergy [Sato and Okamoto, 2020].

References

Borovoi, A., A. Konoshonkin, N. Kusutova and H. Okamoto, Backscattering Mueller matrix for quasi- horizontally oriented ice plates of cirrus clouds: application to CALIPSO signals, Opt. Express, 20, 28222-28233, 2012

Brown, P. R. A., and P. N. Francis, Improved measurements of the ice water content in cirrus using a total-water probe, J. Atmos. Oceanic Technol, 12, 410–414, 1995.

Hagihara, Y., H. Okamoto, and R. Yoshida (2010), Development of a combined CloudSat-CALIPSO cloud mask to show global cloud distribution, *J. Geophys. Res.*, *115*, D00h33, doi:10.1029/2009jd012344.

Hagihara, Y., H. Okamoto, Z. Luo, Joint analysis of cloud-top heights from CloudSat and CALIPSO: New insights into cloud-top microphysics, J. Geophys. Res., , 119, 4087-4106, doi:10.1002/2013JD020919, 2014.

Hashino, T, M. Satoh, Y. Hagihara, T. Kubotai, T. Matsui T. Nasuno, H. Okamoto, Evaluating cloud microphysics from NICAM against CloudSat and CALIPSO,118,7273-7292, J. Geophys. Res. Atmos., 118, 7273–7292, doi:10.1002/jgrd.50564.,2013.

Heymsfield, A. J., A. Protat, R. Austin, D. Bouniol, R. Hogan, J. Delaoe, H. Okamoto, K. Sato, G. Zadelhoff, D. Donovan, Z. Wang, Testing and Evaluation of Ice Water Content Retrieval Methods using Radar and Ancillary Measurements, J. Appl. Meteor., 47, 135-

163.,2008

Ishimoto, H., and K. Masuda, A Monte Carlo approach for the calculation of polarized light: Application to an incident narrow beam, J. Quant. Spectrosc. Radiat. Transfer, 72, 467–483, doi:10.1016/S0022-4073(01)00136-4, 2002.

Iwabuchi, H., S. Yamada, S. Katagiri, P. Yang and H. Okamoto, J. Appl. Meteor and Clim., Radiative and microphysical properties of cirrus cloud inferred from the infrared measurements made by the Moderate Resolution Imaging Spectrometer (MODIS). Part I: Retrieval method, accepted. J. Appl. Meteor. And Clim., 10.1175/JAMC-D-13-0215.1, 53, 5, 1297-1316, 2013.

Jin, Y., T. Nishizawa, N. Sugimoto, S. Ishii, M. Aoki, K. Sato and H. Okamoto, Development of a 355-nm high-spectral-resolution lidar using a scanning Michelson interferometer for aerosol profile measurement, Optics Exprees 28(16), 23209-23222, 2020.

Jin, Y., T. Nishizawa, N. Sugimoto, S. Takakura, M. Aoki, S. Ishii, A. Yamazaki, R. Kudo, K. Yumimoto, K. Sato and H. Okamoto, Demonstration of aerosol profile measurement with a dual-wavelength high-spectral-resolution lidar using a scanning interferometer, Applied Optics, 2022, in press.

Kikuchi, M., H. Okamoto, K. Sato, K. Suzuki, G. Cesana, Y. Hagihara, N. Takahashi, T. Hayasaka, R. Oki (2017), Development of algorithm for discriminating hydrometeor particle types with a synergistic Use of CloudSat and CALIPSO. Journal of Geophysical Research: Atmospheres, 122, 11,022–11,044. https://doi.org/10.1002/ 2017JD027113

Kikuchi, M., Okamoto, H., Sato, K., A climatological view of horizontal ice plates in clouds: Findings from nadir and off-nadir CALIPSO observations. Journal of Geophysical Research: Atmospheres, 126, e2020JD033562. doi.org/10.1029/2020JD033562, 2021

Kong, S., Sato, K., Bi, L. (2022). Lidar ratio–depolarization ratio relations of atmospheric dust aerosols: The super-spheroid model and high spectral resolution lidar observations. Journal of Geophysical Research: Atmospheres, 127, e2021JD035629. https://doi. org/10.1029/2021JD035629

Liu, Z., et al., CALIOP Algorithm Theoretical Basis Document: Scene Classification Algorithms, 56 pp., NASA Langley Res. Cent., Hampton, Va, 2005.

Nishizawa T, Jin Y, Sugimoto N, Sato K., Fujikawa M., Ishii S., Aoki M., Nakagawa K., Okamoto H., Observation of clouds, aerosols, and precipitation by multiple-field-of-view multiple-scattering polarization lidar at 355nm, Journal of Quantitative Spectroscopy and Radiative Transfer, Vol.271, 107710, doi.org/10.1016j.jqsrt. 2021.107710, 2021

Okamoto, H., T. Nishizawa, T. Takemura, H. Kumagai, H. Kuroiwa, N. Sugimoto, I. Matsui, A. Shimizu, S. Emori, A. Kamei, and T. Nakajima (2007), Vertical cloud structure observed from shipborne radar and lidar: Midlatitude case study during the MR01/K02 cruise of the research vessel Mirai, J. Geophys. Res., 112, D08216, doi:10.1029/2006JD007628.

Okamoto, H., T. Nishizawa, T. Takemura, K. Sato, H. Kumagai, Y. Ohno, N. Sugimoto, A. Shimizu, I. Matsui, and T. Nakajima (2008), Vertical cloud properties in the tropical western Pacific Ocean: Validation of the CCSR/NIES/FRCGC GCM by shipborne radar and lidar, J. Geophys. Res., 113, D24213, doi:10.1029/2008JD009812.

Okamoto, H., S. Iwasaki, M. Yasui, H. Horie, H. Kuroiwa, and H. Kumagai (2003), An algorithm for retrieval of cloud microphysics using 95-GHz cloud radar and lidar. J. Geophys.

Res., 108(D7), 4226, doi:10.1029/2001JD001225.

Okamoto, H., (2002) Information content of the 95GHz cloud radar signals: theoretical assessment of effect of non-sphericity by the discrete dipole approximation, J. Geophys. Res., 107(D22), 4628, doi:10.1029/2001JD001386, 2002.

Okamoto, H., K. Sato, Y. Hagihara, Global analysis of ice microphysics from CloudSat and CALIPSO: incorporation of specular reflection in lidar signals, J. Geophys. Res., 115, D22209, doi:10.1029/2009JD013383, 2010.

Okamoto, H., A.Macke, M.Quante, E.Raschke, Modeling of backscattering by non-spherical ice particles for the interpretation of cloud radar signals at 94GHz. An error analysis, Contr. Atmos. Phys, 68, 319-334, 1995.

Okamoto, H., K. Sato, T. Nishizawa, N. Sugimoto, T. Makino, Y. Jin, A. Shimizu, T. Takano, and M. Fujikawa (2016), Development of a multiple-field-of-view multiple-scattering polarization lidar: comparison with cloud radar, Opt. Express **24**, 30053-30067. doi: 10.1364/OE.24.030053.

Okamoto, H., and K. Sato (2018) Remote sensing of clouds and precipitation, Springer Remote Sensing/Photometry, doi:10.1007/978-3-319-72583-3_8.

Okamoto, H., Sato, K., Borovoi, A., Ishimoto, H., Masuda, K., Konoshonkin A., Kustova, N., (2019), Interpretation of lidar ratio and depolarization ratio of ice clouds using space-borne high-spectral-resolution polarization lidar, Optics Express, 27, 36587-36600. doi: 10.1364/OE.27.036587.

Okamoto, H., K. Sato, A. Borovoi, H. Ishimoto, K. Masuda, A. Knoshonkin and N, Kustova, Wavelength dependence of ice cloud backscatter properties for space-borne polarization lidar applications, Optics Express, 28, 29178-29191 doi:10.1364/OE.400510. 2020.

Sato, K., and H. Okamoto, Characterization of Ze and LDR of nonspherical and inhomogeneous ice particles for 95-GHz cloud radar: Its implication to microphysical retrievals, J. Geophys. Res., 111, D22213, doi:10.1029/2005JD006959, 2006.

Sato, K. and H. Okamoto (2011), Refinement of global ice microphysics using spaceborne active sensors, J. Geophys. Res., *116*, D20202, doi:10.1029/2011JD015885.

Sato, K., H. Okamoto, H. Ishimoto, Physical model for multiple scattered space-borne lidar returns from clouds, Opt. Express 26, A301-A319, doi.org/10.1364/O E.26.00A301 (2018).

Sato, K., H. Okamoto, H. Ishimoto, Modeling the depolarization of space-borne lidar signals. Opt. Express, 27, A117-A132, doi:10.1364/OE.27.00A117 (2019)

Sato, K., H. Okamoto, T. Takemura, H. Kumagai and N. Sugimoto, Characterization of ice cloud properties obtained by shipborne radar/lidar over the tropical western Pacific Ocean for evaluation of an atmospheric general circulation model, J. Geophys. Res., doi:10.1029/2009JD012944, 115, D15203, 2010.

Sato, K., Okamoto, M. K. Yamamoto. S. Fukao, H. Kumagai, Y. Ohno, H. Horie,and M. Abo 95-GHz Doppler radar and lidar synergy for simultaneous ice microphysics and in-cloud vertical air motion retrieval. J. Geophys. Res., 114, D03203, doi:10.1029/2008JD010222, 2009

Sato, K., Okamoto, H., (2020), Application of single and multiple-scattering theories to analysis of space-borne cloud radar and lidar data, Springer Nature, Springer Series in Light Scattering, Vol.5, pp.1-37, doi:10.1007/978-3-030-38696-2

Sato, K., Okamoto, H., (2020), Global Analysis of height-resolved ice particle categories from space-borne lidar, Geophysical Research Letters, 50, 1-10, e2023GL.105522. https://doi.oorg/10.1029/2023GL105523.

Seiki, T., C. Kodama, M. Satoh, Y. Hagihara and H. Okamoto, Characteristics of ice clouds over mountain regions detected by CALIPSO and CloudSat satellite observations, J. Geophys. Res., 124, doi:10.1029/2019JD030519, 2019. Vaughan, M. A., D. M. Winker, and K. A. Powell (2005), CALIOP algorithm theoretical basis document, part 2, feature detection and layer properties algorithms, Rep. PC-SCI-202.02, NASA Langley Res. Cent., Hampton, Va.

Yoshida, R., H. Okamoto, Y. Hagihara, and H. Ishimoto, Global analysis of cloud phase and ice crystal orientation from CALIPSO data using attenuated backscattering and depolarization ratio, J. Geophys. Res., doi:10.1029/2010JD014032, 115, D00H32, 2010.

4.1.2 Research Product

4.1.2.1 Introduction

This section describes the algorithm that retrieve the precipitation and vertical velocity-related Research Products using the radar reflectivity factor and Doppler information from CPR on Earth-CARE.

4.1.2.2 Rain, Snow and Vertical Velocity

4.1.2.2.1 Algorithm

By using the algorithms described in previous section, we can also derive research cloud products by the synergy of CPR and ATLID, i.e., mass mixing ratio of 2D-plate to the total IWC, rain and snow amount, rain and snow rate, and vertical air motion in the cloud regions and sedimentation velocity of the cloud particles. Particle models for rain and snow are the same as in CPR only section and scattering properties for CPR and ATLID can be calculated by the DDA and the geometrical optics with physical optics, respectively. The normalized surface cross section at 94GHz and path integral attenuation (PIA) for rain and snow retrievals are estimated by synergy use of cloud radar and lidar. Once we retrieve the cloud microphysics, sedimentation velocity of the particle can be basically estimated and by subtraction the velocity component from the V_d, it is possible to estimate vertical air motion. In actual retrievals, we consider the simultaneous retrievals of vertical air motion and cloud microphysics, including rain and snow microphysics, in a similar manner as in Sato et al., [2009] but this time with the Levenberg-Marquardt algorithm framework. This allows to estimate the error for each retrieved parameter and is expected to better characterize algorithm errors.

4.2 ATLID-MSI

4.2.1 Research Product

4.2.1.1 Introduction

Not only the lidar described in Section 3.2, satellite-borne passive remote sensor (e.g., AVHRR, MODIS, and SeaWIFS) is an also powerful tool to provide information on sizes of aerosols (e.g., angstrom exponent) and aerosol types (e.g., soil dust, carbonaceous) in globe, partly using the feature that the spectral property of the measured radiance data is sensitive to particle size [e.g., Higurashi and Nakajima, 1999, 2002; Kaufman et al., 2003]. The combined use of active and passive sensor data enables us to estimate various optical properties simultaneously and to reduce the potential uncertainty of estimates.

On the basis of this background, we intend to develop an ATLID-MSI L2 algorithm to derive information on global distributions for aerosols and clouds in the atmosphere from the ATLID L1B and MSI L1B data and to reveal the occurrence for aerosol components and cloud types and their vertical distribution. The algorithm produces the L2b ATLID-MSI products using the L1B ATLID data of three-channel attenuated backscatter coefficients for particle Mie co-polar ($\beta_{\text{mie,co}}$), molecule Rayleigh co-polar ($\beta_{\text{ray,co}}$), and total cross-polar ($\beta_{mie+ray,cr}$) components at 355nm and L1b MSI data of two-channel radiances in the visible band (670nm) and the near-infrared band (865nm). The parameters retrieved by the developed algorithms are summarized in Table 3.2.1.1.1.

4.2.1.2 Aerosol component product (ATLID-MSI algorithm)

4.2.1.2.1 Algorithm

The ATLID-MSI algorithm provides extinction coefficients at 355nm for water-soluble, light-absorbing (black carbon), dust, and sea-salt particles in each slab layer and vertically mean mode-radii for fine (water-soluble and light-absorbing) particles and coarse (dust) particle. This algorithm uses $\beta_{\text{mie,co}}$, $\beta_{\text{ray,co}}$, and $\beta_{mie+ray,cr}$ data of ATLID L1b products and radiance data at 670 and 865nm of MSI L1c data (R_{670} and R_{865}). This algorithm is not applied to the data under cloudy conditions.

As discussed in section 3.2.2.2, the ATLID 3ch method can provide vertical profiles of the extinction coefficients for the aerosol components, but with potentially uncertain assumption that the mode-radii and refractive indexes for each aerosol component are prescribed. Previous studies using satellite-borne passive remote sensors provide information on particle sizes of aerosols (e.g., Ångström exponent) and aerosol types (e.g., soil dust, carbonaceous) partly using the feature that the spectral property of the measured radiance data is sensitive to particle size [e.g., Higurashi and Nakajima, 1999, 2002; Kaufman et al., 2003]. Thus, the combined use of passive and active sensor data enables us to estimate the mode-radii for aerosol components. We have developed the synergistic retrieval method using CALIPSO/CALIOP and Aqua/MODIS observations [Kudo et al., 2023] for the retrieval of extinction coefficients of water-soluble, light-absorbing, dust, and sea-salt, and the vertically mean mode-radii for fine and coarse particles. The ATLID-MSI algorithm is developed based on the CALIOP-MODIS algorithm.

The retrieval procedure is illustrated schematically in Fig. 4.2.1.2.1. The inputs are the observation vector $\boldsymbol{y}^{obs}$ of ATLID L1b and MSI L1c data. The state vector $\boldsymbol{x}$ is parameters to be optimized to $\boldsymbol{y}^{obs}$ and consists of the volume concentrations of water-soluble, light-absorbing, dust, and sea-salt particles (v_{WS},

v_{LA}, v_{DS}, v_{SS}), and the mode-radii of fine (water-soluble and light-absorbing) and coarse (dust) particles ($r_{m,fine}$ and $r_{m,coarse}$). Note that the mode-radius of light-absorbing was assumed to be same as that of water-soluble. The mode-radius of sea-salt is calculated by the parameterization using the ocean surface wind speed [Erickson and Duce, 1988]. The optimization of $\boldsymbol{x}$ is based on the maximum a posteriori (MAP) scheme. The final results of the extinction coefficients of water-soluble, light-absorbing, dust, and sea-salt particles ($\alpha_{WS,355}$, $\alpha_{LA,355}$, $\alpha_{DS,355}$, $\alpha_{SS,355}$,) are calculated from the optimized state vector $\boldsymbol{x}$.

According to the MAP scheme, the best solution of $\boldsymbol{x}$ is obtained by minimizing the cost function which is defined as the sum of square differences between observations and ones calculated from $\boldsymbol{x}$ using forward models, and a priori constraints. Here, we define the cost function as

$$f(\boldsymbol{x}) = \left(\boldsymbol{y}^{obs} - \boldsymbol{y}(\boldsymbol{x})\right)^T (\boldsymbol{W}^2)^{-1} \left(\boldsymbol{y}^{obs} - \boldsymbol{y}(\boldsymbol{x})\right) + \boldsymbol{y}_a(\boldsymbol{x})^T (\boldsymbol{W}_a^2)^{-1} \boldsymbol{y}_a(\boldsymbol{x}) \qquad (4.2.1.2.1)$$

where the vector $\boldsymbol{y}(\boldsymbol{x})$ is the calculated values from $\boldsymbol{x}$ using the forward models for ATLID L1b and MSI L1c data. The $\boldsymbol{W}$ is the weight matrix and is assumed to be diagonal. The weight values are given by the observation accuracies. The vector $\boldsymbol{y}_a(\boldsymbol{x})$ is a priori constraints for $\boldsymbol{x}$. The diagonal matrix $\boldsymbol{W}_a$ is the weight matrix to determine the strength of constraints. The details of the a priori constraints are described later.

In the forward model $\boldsymbol{y}(\boldsymbol{x})$, the aerosol optical properties are calculated from the volume concentrations and the mode-radii of the four components. The particle shapes of water-soluble, and sea-salt are assumed to be spherical. The non-spherical shapes are assumed for light-absorbing and dust particles. Voronoi aggregate model was assumed for dust particles [Ishimoto et al., 2010]. For the light-absorbing particle, the internally mixed aggregate model developed by Ishimoto et al. [2019] was employed. The model has an aggregate shape of soot particles as a core, and the non-spherical core is covered with the shell of water-soluble. The volume ratio of shell to core is fixed by about 30 % This lies among the values observed in the A-FORCE aircraft campaign in East Asia [Matsui, et al. 2013].

The volume size distributions of each particle are assumed to be lognormal distribution. The values of mode-radii are inputs from the state vector, and the standard deviations are given from the database of Hess et al. [1998]. Note that the mode-radii for water-soluble and light-absorbing particles are assumed to be same, and the mode-radius of sea-salt particle is obtained by parameterization using the ocean surface wind speed [Erickson and Duce, 1988]. The refractive index of water-soluble, shell of light-absorbing, and sea-salt particles are also given from the database of Hess et al. [1998]. That of a soot aggregate core of light-absorbing is given from the data of the flame soot [Chang and Charalampopoulos, 1990]. That of dust is given from the data of Asian dust [Aoki et al., 2005]. The hygroscopic growth with relative humidity for water-soluble, the shell of light-absorbing, and sea-salt particles is considered. The refractive index of aerosols mixed with water is calculated by the volume weighting mixing rule [Hess et al. 1998]. The single-scattering properties (extinction coefficient, single-scattering albedo, and phase matrix) of water-soluble and sea-salt particles are calculated by Mie theory. Those for light-absorbing and dust are calculated using the data table of Ishimoto et al. [2010; 2019].

For the forward calculations for R_{670} and R_{865} of MSI L1c, we employed a vector radiative transfer code,

PSTAR [Ota et al., 2010]. For the rapid computation, the atmosphere in the MSI forward model is divided into five vertical layers from the surface to 120 km altitude and the smallest resolution is 1 km near the surface, although the vertical resolution of ATLID L1b is about 100 m. The influence of this approximation on the radiances of MSI is less than 1 %. The surface reflectance on the land is calculated by the given surface albedo. For the ocean surface, the PSTASR calculates the surface reflectance depending on the surface wind speed. The forward calculations of ATLID L1b are conducted by Eqs. 3.2.1.3a-c.

For reducing the influences of the large signal noises in ATLID data, the smoothness constraints for the vertical profiles of the volume concentrations for each component are introduced by using the same method as Kudo et al. [2023]. The vector $y_a(x)$ in Eq. (4.2.1.2.1) is defined as the second derivatives of the vertical profiles of the volume concentrations for water-soluble, light-absorbing, dust and sea-salt particles as follows:

$$y_a(x) = (\cdots \quad \ln v_{WS/LA/DS/SS}(z_{i-1}) - 2\ln v_{WS/LA/DS/SS}(z_i) + \ln v_{WS/LA/DS/SS}(z_{i+1}) \quad \cdots).$$
$$(4.2.1.2.2)$$

When the vertical profiles of aerosols are smooth, the value of $y_a(x)$ becomes small, and the value of $f(x)$ also becomes small.

It is difficult to retrieve the volume concentrations of water-soluble and light-absorbing particles separately. Therefore, we introduced two a priori constraints [Kudo et al., 2023]. One is the similarity of the vertical profiles of water-soluble and light-absorbing particles, and the other is inequality of aerosol optical depth of water-soluble and light-absorbing particles. The similarity constraint is introduced by

$$y_a(x) = (\cdots \quad \ln[v_{LA}(z_i)/v_{LA}(z_{i+1})] - \ln[v_{WS}(z_i)/v_{WS}(z_{i+1})] \quad \cdots). \qquad (4.2.1.2.3)$$

The vertical changes in water-soluble and light-absorbing particles approach the same value when Eq. (4.2.1.2.3) is minimized. For the inequality constraint, the following log barrier function is introduced:

$$y_a(x) = -\ln\left(1 - \frac{\tau_{LA}(355nm)}{\tau_{WS}(355nm)}\right), \qquad (4.2.1.2.4)$$

where $\tau_{LA/WS(355nm)}$ is aerosol optical depth at 355 nm for light-absorbing and water-soluble particles. When τ_{LA} approaches to τ_{WS}, Eq. (4.2.1.2.4) becomes infinity.

The ATLID and MSI has information of particles sizes but it is difficult to retrieve the mode-radii due to the signal noises of the ATLID and MSI measurements. Therefore, we give a priori values for mode-radii of fine (water-soluble and light-absorbing) and coarse (dust) mode as follows:

$$y_a(x) = r_{m,fine/coarse} - r_{m,fine/coarse}^{a\ priori}, \qquad (4.2.1.2.5)$$

where $r_{m,fine/coarse}^{a\ priori}$ is the a priori values and is 0.15 μ m for fine particles and 2.0 μm for coarse particle.

The minimization of $f(x)$ is conducted by the Gauss-Newton method combined with the line search [Kudo et al. 2016]. This method searches the minimum value of $f(x)$ in the x space by the iteration of $x_{i+1} = x_i + \alpha d_i$, where the vector d_i is a direction to minimize $f(x)$, and the scalar α is a value to minimize $f(x)$ in the direction of d_i. Firstly, the scalar α is defined as 1, and the vector d_i is determined by solving the normal equation

$$[J(x_i)^T(w^2)^{-1}J(x_i) + (w_a^2)^{-1}]d_i = J(x_i)^T(w^2)^{-1}\left(y^{obs} - y(x_i)\right) + (w_a^2)^{-1}y_a(x_i) \qquad ,$$

(4.2.1.2.6)

where the matrix $\boldsymbol{J}(\boldsymbol{x}_i)$ is the Jacobi matrix for $\boldsymbol{y}(\boldsymbol{x}_i)$. We solve this equation by the Singular Value De-composition [Press et al., 1992]. Secondly, the scalar α is searched by the iteration of $\alpha_{j+1} = \eta\alpha_j$, where the value of η is set to 0.5. The value of α_j is decreased until the Armijo condition is satisfied:

$$f\big(\boldsymbol{x}_i + \alpha_j\boldsymbol{d}_i\big) \le f(\boldsymbol{x}_i) + \gamma\alpha_j\nabla f(\boldsymbol{x}_i)^T\boldsymbol{d}_i, \ 0 < \gamma < 1, \quad (4.2.1.2.7)$$

where γ is an arbitrary constant that we set to 0.001. The line search inhibits unstable oscillation in the Gauss-Newton method by limiting the length of $\|\boldsymbol{x}_{i+1} - \boldsymbol{x}_i\|$, and the monotonic and stable convergence is obtained. Additionally, for the rapid and stable convergence of the iteration of the Gauss-Newton method, we applied the logarithmic transformations for $\boldsymbol{x}$, $\boldsymbol{y}(\boldsymbol{x})$, and $\boldsymbol{y}^{obs}$ [Kudo et al. 2016]. However, the AT-LID L1b data may have negative values due to signal noises. Therefore, the ATLID L1b data was trans-formed by $Y = \ln(y - y_{min})$. Introducing these transformations, the first term $\big(\boldsymbol{y}^{obs} - \boldsymbol{y}(\boldsymbol{x})\big)$ of Eq.

(4.2.1.2.1) becomes dimensionless, $\ln\big(\boldsymbol{y}^{obs}/\boldsymbol{y}(\boldsymbol{x})\big)$. The $\boldsymbol{J}(\boldsymbol{x}_i)$ in Eq. (4.2.1.2.6) also becomes dimen-sionless. This has a scaling effect on the minimization problem of the cost function [Nocedal and Wright, 2006], and the rapid and stable convergence is expected in the cases that the state vector and the observation vector have different units and values varying over a wide range of magnitudes.

The ATLID-MSI algorithm was applied to the simulated data of ATLID L1b and MSI L1c. Fig. 4.2.1.2.2 is an example. The retrievals of the ATLID stand-alone method (Section 3.2.2.2) might have larger errors due to the fixed mode-radius of dust particles than the ATLID-MSI synergy algorithm. The ATLID-MSI algo-rithm can significantly improve the retrievals by estimating the mode-radius.
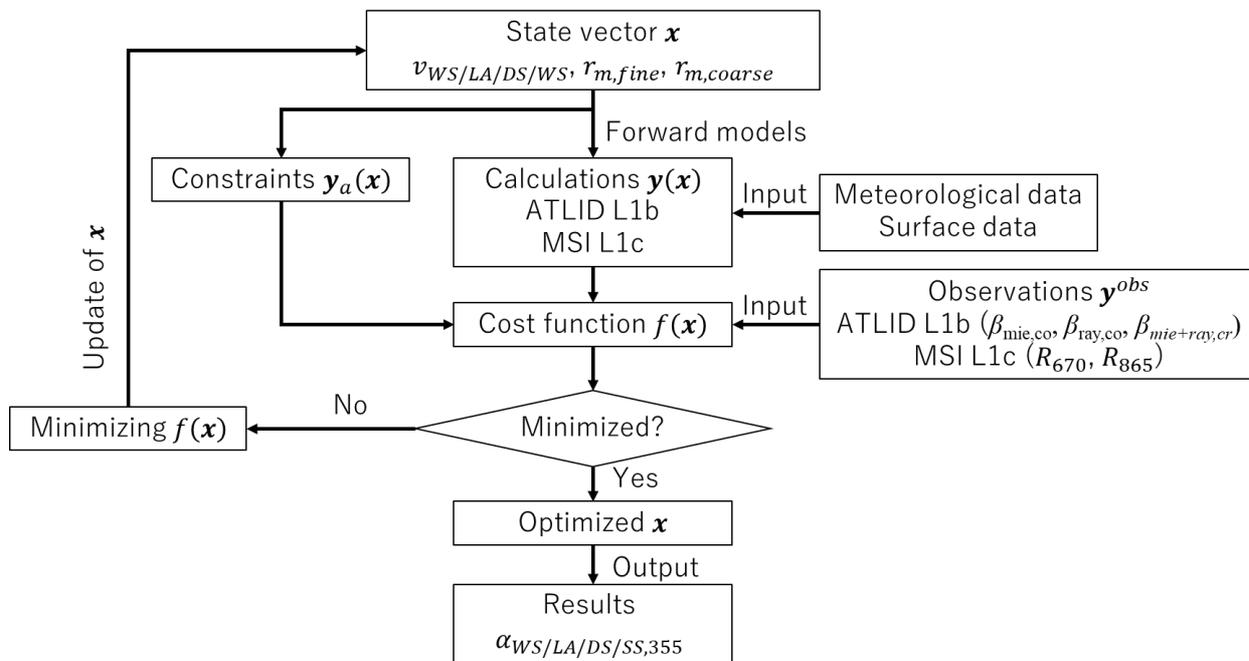
Fig. 4.2.1.2.1 Schematic diagram of the ATLID-MSI algorithm.
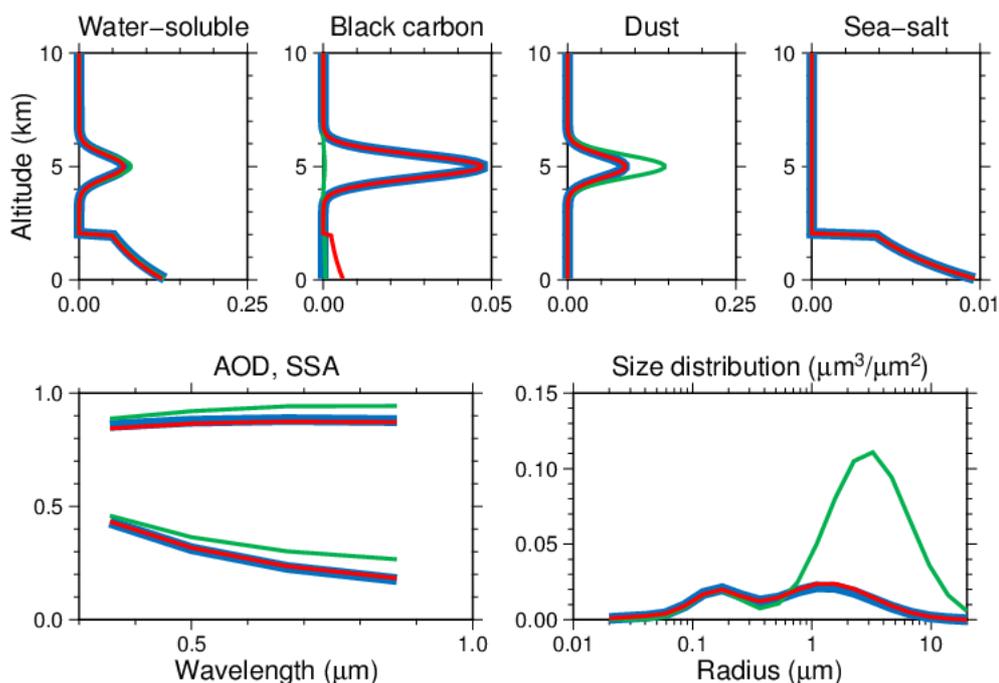
Fig. 4.2.1.2.2 An example of application of ATLID-MSI algorithm to the simulated data of ATLID L1b and MSI L1c. The vertical profiles of the extinction coefficients at 355 nm for water-soluble, light-absorbing, dust, and sea-salt particles (upper), the aerosol optical depth and single-scattering albedo in the column (bottom, left), and the volume size distribution integrated in the column (bottom, right). The line color indicates truth (blue), retrievals of ATLID stand-alone method (green), and retrievals of ATLID-MSI algorithm (red).

Reference

Aoki, T., T. Y. Tanaka, A. Uchiyama, M. Chiba, M. Mikami, S, Yabuki, and J. R. Key, Sensitivity experiments of direct radiative forcing caused by mineral dust simulated with a chemical transport model, J. Meteorol. Soc. Jpn., 83A, 315-331, 2005.

d'Almeida, G. A., P. Koepke, and E. P. Shettle, Atmospheric aerosols: Global climatology and radiative characteristics, 561 pp., A. Deepak, Hampton, Virginia, 1991.

Chang, H., and T. T. Charalampopoulos, Determination of the wavelength dependence of refractive indices of flame soot, Proc. R. Soc. Lond., A430, 577-591, 1990.

Erickson, D. J., and R. A. Duce, On the global flux of atmospheric sea salt, J. Geophys. Res., 93, 14079-14088, 1988.

Hess, M., P. Koepke, and I. Schult, Optical properties of aerosols and clouds: The software package OPAC, Bull. Am. Meteorol., 37, 414-435, 1998.

Ishimoto, H., Y. Zaizen, A. Uchiyama, K. Masuda, and Y. Mano, Shape modeling of mineral dust particles for light-scattering calculations using the spatial Poisson–Voronoi tessellation, J. Quant. Spectrosoc. Ra., 111, 2434–2443, https://doi.org/10.1016/j.jqsrt.2010.06.018, 2010.

Ishimoto, H., R. Kudo, and K. Adachi, A shape model of internally mixed soot particles derived from

artificial surface tension, Atmos. Meas. Tech., 12, 107–118, https://doi.org/10.5194/amt-12-107-2019, 2019.

Kaufman, Y. J., D. Tanré, J.-F. Léon and J. Pelon. Retrievals of Profiles of Fine and Coarse Aerosols Using Lidar and Radiometric Space Measurements. IEEE Trans. Geosci. Rem. Sens.. 2003; 41: 1743-1754.

Kudo, R., T. Nishizawa, and T. Aoyagi, Vertical profiles of aerosol optical properties and the solar heating rate estimated by combining sky radiometer and lidar measurements, Atmos. Meas. Tech., 9, 3223-3243, 2016.

Kudo, R, A. Higurashi, E. Oikawa, M. Fujikawa, H. Ishimoto, and T. Nishizawa, Global 3-D distribution of aerosol composition by synergistic use of CALIOP and MODIS observations, Atmos. Meas. Tech., 16, 3835–3863, https://doi.org/10.5194/amt-16-3835-2023, 2023.

Matsui, H., M. Koike, Y. Kondo, N. Moteki, J. D. Fast, and R. A. Zaven, Development and validation of a black carbon mixing state resolved three-dimensional model: Aging processes and radiative impact, J. Geophys. Res., 118, 2304-2326, 2013.

Nocedal, J., and S. J. Wright, Numerical optimization, 664 pp., Springer Science+Business Media, New York, 2006.

Ota, Y., A. Higurashi, T. Nakajima, and T. Yokota, Matrix formulations of radiative transfer including the polarization effect in a coupled atmosphere-ocean system, J. Quant. Spectr. Rad. Trans., 111, 878-894, 2010.

Press, W. H., S. A. Teukolsky, W. T. Vetterling, and B. P. Flannery, Numerical recipes in FORTRAN, The Art of Scientific Computing, 965 pp., Cambridge Univ., New York, 1992.

4.3 CPR-ATLID-MSI

4.3.1 Standard Product

The flow of the algorithm and standard and research cloud products is found in figure 3. MSI provide the radiances at seven channels, i.e., 0.67, 0.865, 1.65, 2.21, 8.8, 10.8 and 12.0μm. MSI L2a product includes optical thickness and effective radius for water and ice clouds. These additional input parameters will be combined with the observables from CPR and ATLID to derive standard and research cloud products. We first describe the algorithms to derive standard cloud products. Then the detail of the algorithms for the research products are provided.

4.3.1.1 Introduction

This section describes the algorithm that retrieve the Standard cloud products, using CPR, ATLID and MSI on EarthCARE.

The cloud particle models and treatment of scattering properties is the same as described in the CPR/ATLID section except for MSI infrared channels. The radiances measured by MSI are calculated by radiative transfer codes for the input single scattering properties. Note that the DDA cannot be applied to the large particles compared with the wavelength due to the requirement of memory and computing time. For radiance calculations due to ice particles in the infrared channels, we can apply the DDA for the size parameter X up to 30 and above, we apply the geometrical optics with physical optics approach [Borovoi and Kustova 2009, Borovoi et al., 2012] when X>30 to cover the possible range of size parameter in each wavelength of MSI. Then we can achieve the consistency in the treatment of scattering properties of ice particles between CPR, ATLID and MSI.

Standard cloud products include cloud mask, cloud particle type (phase and orientation), cloud microphysics including effective radius of water, that of ice, LWC, IWC, optical thickness, liquid water path (LWP), ice water path (IWP). MSI information can be used complementary to the vertically resolved information provided from the CPR and ATLID.
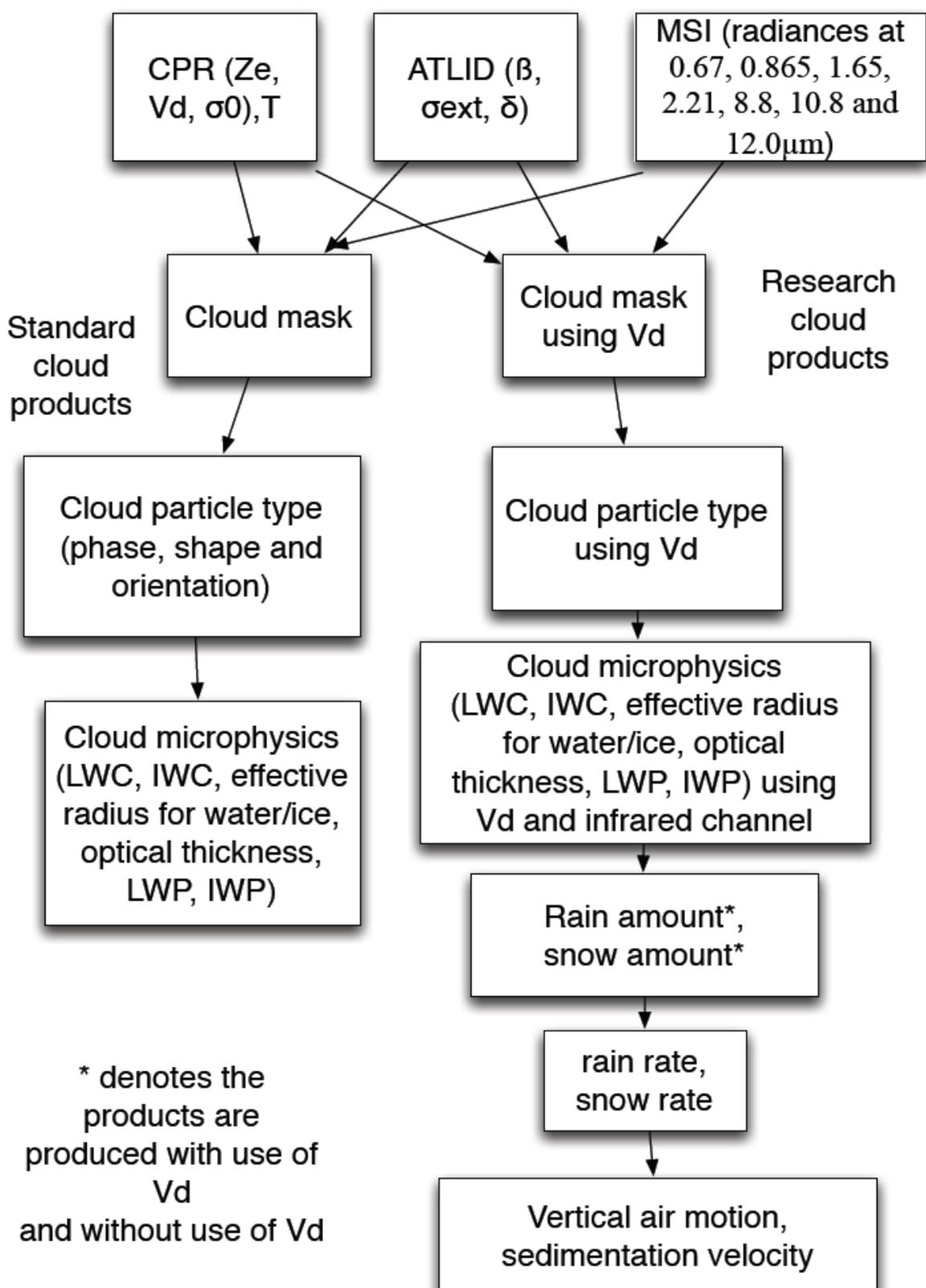
4.3.1.2 Cloud Mask

4.3.1.2.1 Algorithm

For cloud mask, the ATLID alone may have a difficulty in discriminating dust from thin ice clouds when CPR does not have a sensitivity. MSI is expected to help the information. Radiances at 8.8, 10.8 and 12.0μm can be used to discriminate dust and ice clouds.

4.3.1.3 Cloud Particle Type

4.3.1.3.1 Algorithm

For the cloud particle type, combinational use of MSI with CPR and ATLID is expected to improve the discrimination of water and ice by CPR or ATLID as performed in cloud mask using the three radiance channels at far-infrared wavelengths. MSI information can be used for the constraint of the existence of super-cooled water or ice [Delanoë, J., and R. J. Hogan 2010].

4.3.1.4 Cloud Microphysics

4.3.1.4.1 Algorithm

For the cloud microphysical retrievals, MSI also helps to improve the retrieval accuracy compared with the combination of CPR/ATLID synergy. For CPR-ATLID-MSI algorithms, radiances and optical thickness for both of water and ice clouds from MSI are used. For example, when CPR does not have enough sensitivity to detect thin ice, MSI information with ATLID is effective to improve the accuracy of the retrieval of ice microphysics in these regions. When cloud optical thickness is large, ATLID signal may not be observed after some distance from the cloud top. MSI information will be combined with CPR observables to reduce the uncertainties in the retrieved values for CPR only or CPR/ATLID cloud products. We use optical thickness retrieved from imager to constrain the result from CPR or CPR/ATLID. That is, we compare the estimated optical thickness from CloudSat and CALIPSO and retrieved optical thickness from MODIS to improve the microphysics. Radiance will be also used instead of retrieved optical thickness. Overall, we plan to use Levenberg-Marquardt algorithm for the retrieval of cloud microphysics as for the analysis of the CPR-ATLID synergy data. That is, all observables from CPR, ATLID and MSI are used as input parameters and retrieval of cloud microphysics are performed on the basis of optimal estimation approach. We found the improvement of the retrieved microphysics by the additional information provided from the imager to the active sensors observables [Okamoto et al., in preparation].

When full observables including Vd are used, the retrieval cloud products are categorized as research cloud products. Since we chose Levenberg-Marquardt approach, it is easy to construct algorithms that include or exclude Vd as a input parameter. In the regards, the basic structure of algorithm with Vd is almost the same with the CPR/ATLID/MSI standard cloud product algorithm without Vd. The research cloud products include cloud mask, cloud particle type, cloud microphysics such as effective radius of water, effective radius of ice, LWC, IWC, optical thickness, LWP, IWP. Rain and snow amount are also provided with Vd and without Vd as input. rain and snow rate are provided. Vertical air motion and sedimentation velocity are retrieved. Finally ice effective radius and optical thickness is retrieved by using visible, infrared and the thermal

channels as additional information from MSI to CPR and ATLID. Consistency among the LUTs of CPR, ATLID and MSI is kept by taking into account the same ice particle shape assumptions.

To test the CPR/ATLID/MSI algorithm, similar approaches to the evaluations of CPR and CPR-ATLID algorithms are considered; we use the three data sets; (1) Cloud-Sat/CALIPSO/MODIS data. In addition to the satellite data, (2) ground-based synergetic instruments located at NICT in Koganei, Tokyo and at NIES in Tsukuba, Ibaraki, (3) Simulated observables by using J-simulators and output values from NICAM. Concerning (1), comparisons of statistics of L2 products of clouds will be carried out to evaluate the algorithms for EarthCARE. We produce global mean values of clouds microphysics from these for the purpose. For (2), evaluation examples are as follows. Ground-based observation system consists of Multiple-Field-of-View Multiple Scattering Polarization lidar at 355nm (Nishizawa et al., 2021), extended from the precursor at 532nm (Okamoto et al., 2016), High Spectral Resolution Lidar(HSRL) at 355nm (Jin et al., 2021, 2022), direct detection Doppler lidar (Ishii et al., 2022), coherent Doppler lidar at 2.05μm and HG-Spider radar at 94GHz. These instruments have been used to evaluate algorithms of cloud mask, cloud particle type and cloud microphysics by using CPR-only, CPR-ATLID and CPR-ATLID-MSI. For (3), we apply algorithms to the simulated observables such as radar reflectivity factor , extinction coefficient, and depolarization ratio to derive such as microphysics and compare with the model output of microphysics. Through these processes, errors of the algorithms are established.

4.3.2 Research Product

4.3.2.1 Introduction

This section describes the algorithm that retrieve the research product relating the ice cloud properties, using the CPR, ATLID and MSI on EarthCARE.

4.3.2.2 Cloud Microphysics

4.3.2.2.1 Algorithm

MWP method (Multi-wavelength and multi-pixel method) is developing as application of the emission method to retrieve ice cloud optical properties such as optical thickness and effective radius in research product of the EarthCARE. This method expands the principle of Kaufman Neutral method (Kaufman et al., 1987). At regions with various ground albedo in wavelength and spatial direction, ice cloud cover over the regions are analyzed by simultaneous calculation.

"Sub-domain" is cut off from the region. Several observation points are included in sub-domain. The minimum unit of sub-domain is 5×5 pixels (Fig. 4.3.2.2.1.1). It is assumed that ice cloud cover over the sub-domain is distributed smoothly and little changes in the properties.
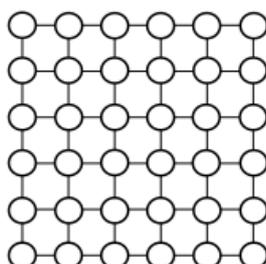
Fig. 4.3.2.2.1.1 Sub-domain minimum unit (5×5 pixels). Circles indicate observation points.

Ice cloud optical properties are estimated by inversion analysis at all observation points in a sub-domain at a time. As shown in Fig. 4.3.2.2.1.2, observed data are analyzed in sequence sub-domains under boundary condition of retrieved ice cloud parameters at between two sub-domains.
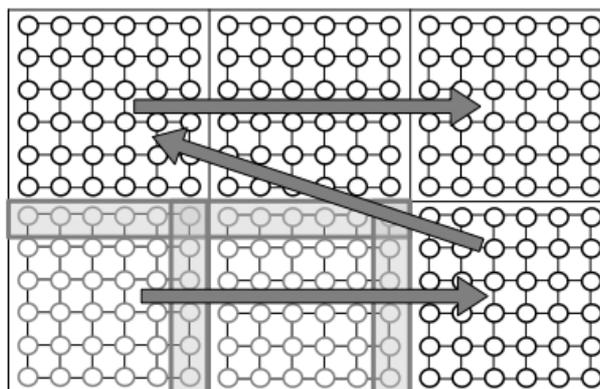
Fig. 4.3.2.2.1.2 Description of analysis procedure. Square areas surrounded by borders are sub-domains. Gray circles are for analyzed points while black circles for unanalyzed points. Ice cloud optical properties are estimated in sequence sub-domains in the direction of arrows. Shaded areas are used as boundary condition to adjacent sub-domain.

The inversion method is combination of the MAP method (Maximum a posteriori method, Rogers, 2000) and Phillips-Twomey method (Pillips, 1982; Twomey, 1963) as smoothing constraint for the stated vector. In MAP method, solution $\boldsymbol{u}$ is obtained when posterior probability $P(\boldsymbol{u}|\boldsymbol{R})$ reach a maximum level by means of Bayer' theorem (Eq. (4.1)).

$$P(u \mid R) = \frac{P(R \mid u)P(u)}{P(R)} \; , \qquad (4.1)$$

where $P(A)$ is probability density function of event $\boldsymbol{A}$, $P(A|B)$ is conditional probability of event A given that another event $\boldsymbol{B}$ has occurred. Gaussian distribution is applied to probability density function.

Cost function is given as follows (Eq. (4.2)) .

$$
\begin{aligned}
\phi &= \phi_{\mathrm{MAP}} + \phi_{\mathrm{PT}} \\
&= [\boldsymbol{R} - \boldsymbol{f}(\boldsymbol{u})]^{\mathrm{T}} \mathbf{S}_e^{-1} [\boldsymbol{R} - \boldsymbol{f}(\boldsymbol{u})] + (\boldsymbol{u} - \boldsymbol{u}_a)^{\mathrm{T}} \mathbf{S}_a^{-1} (\boldsymbol{u} - \boldsymbol{u}_a) \quad \text{... MAP method} \\
&\quad + \sum_{ix} \boldsymbol{\gamma}^{\mathrm{T}} (\boldsymbol{u}_{b,ix} + \mathbf{D}_{ix}\boldsymbol{u})^{\mathrm{T}} (\boldsymbol{u}_{b,ix} + \mathbf{D}_{ix}\boldsymbol{u}) \qquad\qquad \text{... Phillips-Twomey method}
\end{aligned}
\text{,} \qquad (4.2)
$$

$$\boldsymbol{u}_{b,x} = [\quad \boldsymbol{u}_0 \quad 0 \quad 0 \quad \cdots \quad 0 \quad \boldsymbol{u}_{Nx+1} \quad]^{\mathrm{T}}, \qquad (4.3)$$

$$u_{b,y} = [\quad u_0^{\mathrm{T}} \quad 0 \quad 0 \quad \cdots \quad 0 \quad u_{Ny+1}^{\mathrm{T}} \quad]^{\mathrm{T}}, \qquad (4.4)$$

where R is observation vector and $f(u)$ is radiation transfer model. $\mathbf{S}_e$ and $\mathbf{S}_a$ are observation error covariance matrix and priori covariance matrix of R, respectively. u_a and u_b are priori value and boundary condition of u, respectively. ix is direction of smoothing constraint condition (longitude, latitude, time). γ is smoothing parameter and shows amplitude of smoothing. $\mathbf{D}$ is smoothing operator matrix. To minimize the cost function ($d\phi \rightarrow 0$), Eq. (4.5) is obtained with Newton-Gauss method, and the optimized solution may be obtained by several iterations. When $\varepsilon = 0.001$ (Eq. (4.7)) or maximum iteration counts reach to 15 times, solution u is considered as estimate value.

$$u_{k+1} = u_k + \left[(K_k^T S_e^{-1} K_k + S_a^{-1}) + \sum_{ix} \gamma_{ix} D_{ix}^T D_{ix} \right]^{-1}$$
$$\times \left\{ K_k^T S_e^{-1} [R - f(u_k)] - S_a^{-1}(u_k - u_a) - \sum_{ix} \gamma_k (D_{ix}^T D_{ix} u_k + D_{ix}^T u_{b,ix}) \right\} \qquad (4.5)$$

$$K \equiv \nabla_u f_{\mathrm{model}}, \qquad (4.6)$$

$$\sum_{i=1}^{n} \left| \frac{u_{i,(k+1)} - u_{i,k}}{u_{i,(k+1)}} \right| \leq \varepsilon . \qquad (4.7)$$

where u_k is solution of k-th count in iteration and $\mathbf{K}_{ij} = k_{ij} = (\partial f / \partial u)_{ij}$ is Jacobian matrix.

Estimate value is adopted when root-mean-square error (RMSE, Eq. (4.8)) is less than 0.07 (= 7 %).

$$RMSE = \sqrt{\left(\frac{f(u_{\mathrm{retrieved},k})}{R^{\mathrm{meas}}} - 1 \right)^2} . \qquad (4.8)$$

EARTHCARE

NICT JAXA
宇宙航空研究開発機構
Japan Aerospace Exploration Agency

The MWP method has been originally developed to derive aerosol optical properties and described in detail in M. Hashimoto doctoral thesis 2014. In this study, we applied the MWP method to MODIS/Aqua radiance data at the infrared wavelengths (8.550 μm, 11.03 μm, and 12.02 μm) for retrieving cirrus cloud optical properties in several regions for the first time. Figs. 4.3.2.2.1.3 and 4.3.2.2.1.4 show the area analyzed in this study.
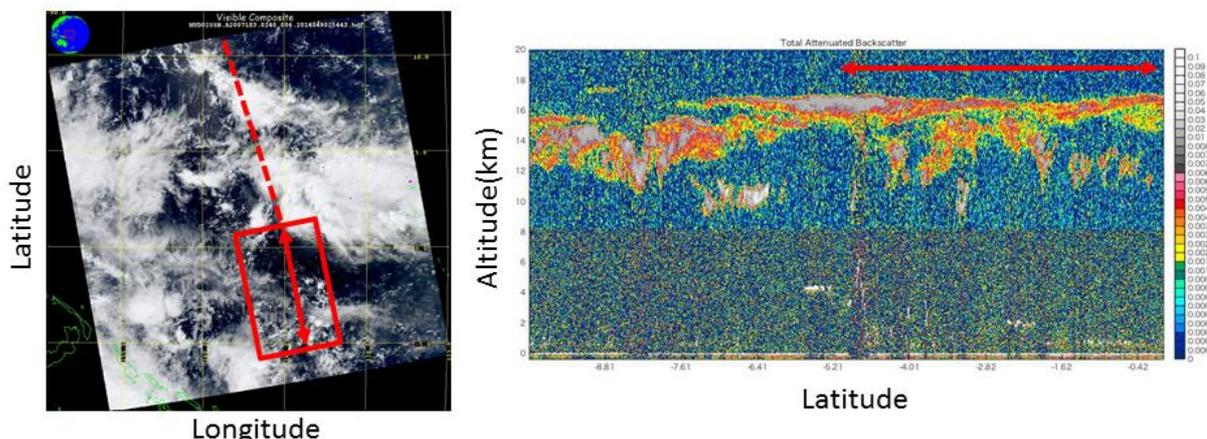
Fig. 4.3.2.2.1.3 (Left) MODIS/Aqua RGB image acquired over East coast of Papua New Guinea (10S-10N, 155-175E) at 02:40 UTC on July 2, 2007. Red square and line show analyzed area and trajectory of CALIOP. (Right) CALIOP backscatter intensity profile. Red line shows analyzed area. Cirrus clouds exist at 10-15 km altitude.
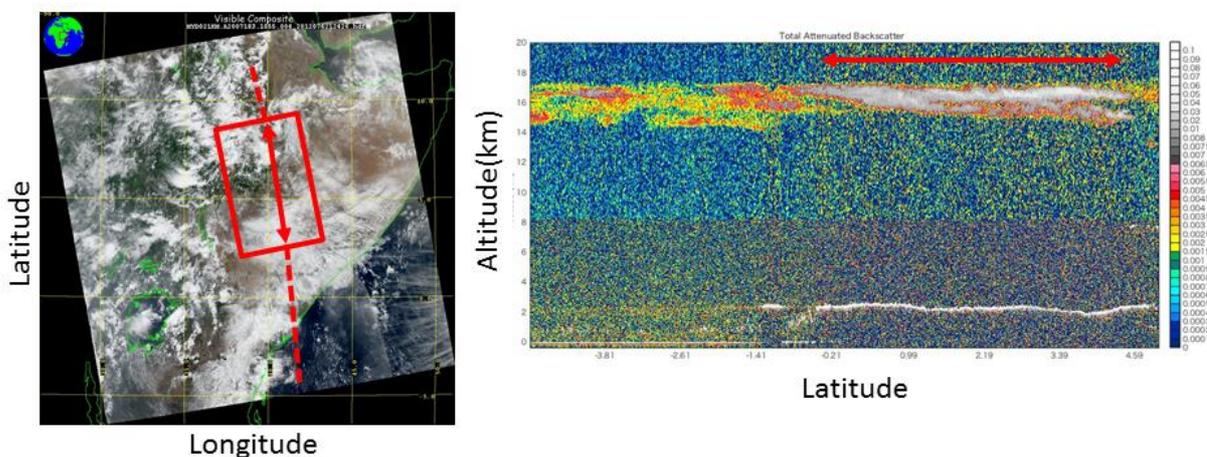
Fig. 4.3.2.2.1.4 As in Fig. 4.3.2.2.1.3 except for (Left) MODIS/Aqua RGB image acquired on the east side of Ethiopia (5S-15N, 30-50E) at 10:55 UTC on July 2, 2007.

Figs. 4.3.2.2.1.5 and 4.3.2.2.1.6 show horizontal distributions of cirrus optical thickness retrieved by the MWP method over the ocean and land, respectively. In both ocean and land regions, retrieved optical thickness was slightly different by the selected infrared wavelength. The optical thickness obtained using 11.03 μm band was smaller than that from 8.550 μm and 12.02 μm bands. We also investigated the geometrical effect of the ice for preparing single scattering properties. The geometrical effect of ice crystal was rather small over the ocean. On the other hand, the shape of ice crystal became important over the land, especially at 8.550 μm band.

Fig. 4.3.2.2.1.5 Retrieved optical thickness obtained from MODIS/Aqua radiance with MWP method over East coast of Papua New Guinea (10S-10N, 155-175E) at 02:40 UTC on July 2, 2007 at (Left) 8.550 μm, (Center) 11.03 μm, and (Right) 12.02 μm. Upper panels show optical thickness retrieved using spherical ice crystal model. Lower panels show optical thickness retrieved using spheroid ice crystal model.

Optical thickness of Spherical ice
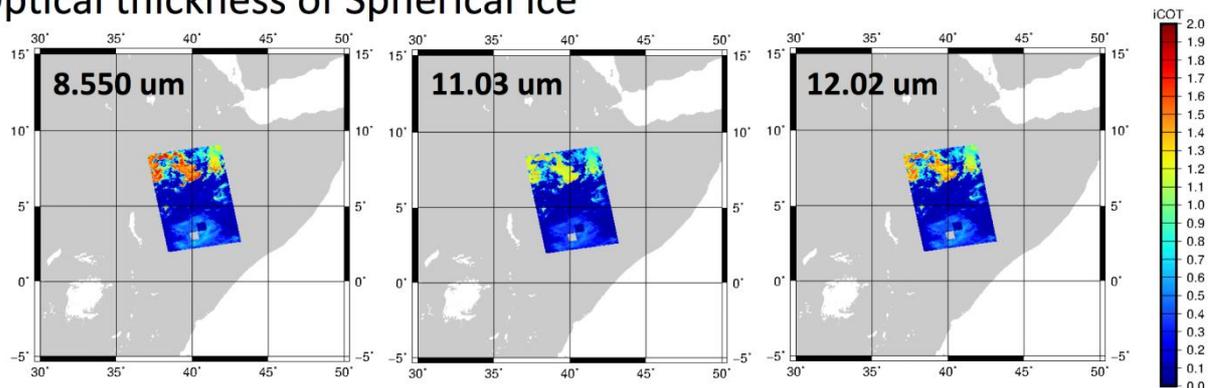
Optical thickness of Spheroid ice
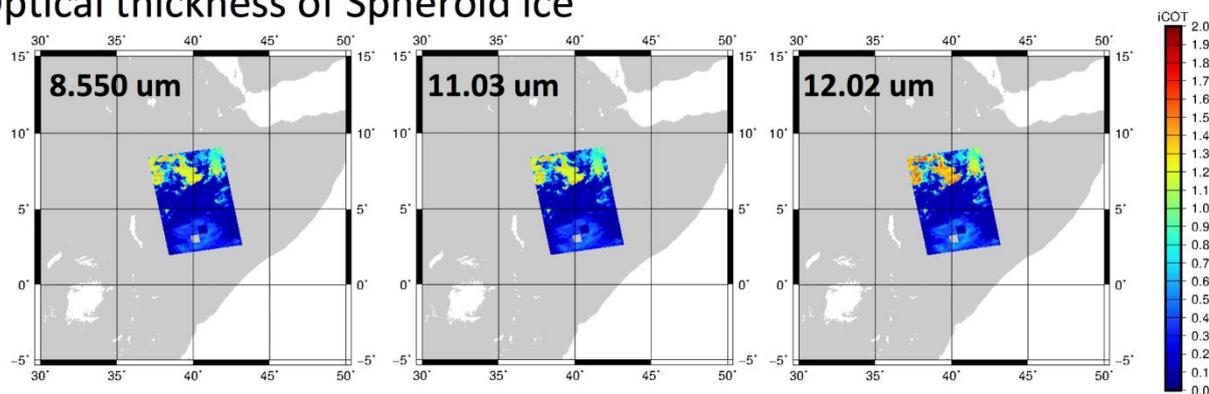
Fig. 4.3.2.2.1.6 As in Fig. 4.3.2.2.1.5 except for Retrieved optical thickness obtained from MODIS/Aqua radiance with MWP method on the east side of Ethiopia (5S-15N, 30-50E) at 10:55 UTC on July 2, 2007.

4.4 All Four Sensor Synergy

4.4.1 Standard Product

4.4.1.1 Introduction

This section describes the algorithm that generates the Standard Product of the four-sensor synergy radiation budget, referred to as ALL_RAD. The algorithm uses cloud and aerosol properties provided by the Level-2 AC_CLP, ATL_CLA, and MSI_CLP products as input to estimate radiative fluxes and radiative heating-rate profiles through one-dimensional radiative-transfer simulations. The top-of-atmosphere radiative fluxes produced by this algorithm are compared with the Level-2 BMA_FLX radiative-flux product from ESA to evaluate radiative closure.

4.4.1.2 Radiative flux computation with 1D RTM

The radiative-transfer framework implemented in ALL_RAD is based on Yamauchi *et al.* (2024). The algorithm first generates composite profiles of aerosol and cloud properties obtained from the Level-2 AC_CLP, ATL_CLA, and MSI_CLP products, together with atmospheric and surface variables provided by AUX_3JH (derived from the X-MET meteorological auxiliary product) along the EarthCARE orbit. The composite profiles are then input into a one-dimensional plane-parallel radiative-transfer simulation to compute shortwave (SW) and longwave (LW) radiative fluxes and radiative heating-rate profiles.

To construct the composite profiles, vertically resolved cloud and aerosol properties from AC_CLP (Sato et al., 2025) and ATL_CLA (Nishizawa et al., 2024) are used as primary inputs, with corrections applied using MSI column-integrated cloud optical thickness when available. For clouds, the extinction coefficient at each layer is computed from the liquid water content (LWC) and ice water content (IWC), together with the effective radius of liquid and ice clouds (Reff$_{water}$ and Reff$_{ice}$) provided by the AC_CLP product. When the MSI_CLP cloud optical thickness is available, the layerwise extinction coefficients are scaled so that their vertical integral matches the MSI_CLP-retrieved cloud optical thickness. When the MSI_CLP cloud optical thickness is not available, the extinction coefficients provided by AC_CLP and ATL_CLA are used directly. Aerosol extinction coefficients and aerosol types (smoke, pollution, marine, pristine, dusty-mixture, and dust) are obtained from ATL_CLA.

Meteorological variables required for the radiative transfer computation—including pressure, temperature, specific humidity, and ozone mass mixing ratio for atmospheric conditions, as well as 10-m wind speed, sea ice cover, snow depth, surface albedo in the UV/VIS and near-IR, and sea surface and skin temperature for surface conditions—are taken from AUX_3JH.

These composite profiles are used as inputs to the one-dimensional radiative-transfer code *MstrnX* (Sekiguchi and Nakajima, 2008; Nakajima et al., 2000) to compute radiative fluxes and radiative heating-rate profiles. To ensure consistency with the assumptions used in the MSI_CLP algorithm (Wang et al., 2023), *MstrnX* employs optical parameter tables based on the Voronoi aggregate model. This radiative transfer computational framework has been tested using aerosol and cloud products from the A-Train constellation prior to the launch of EarthCARE (Yamauchi et al, 2024), as shown in Fig. 4.4.1. In addition, Fig. 4.4.2 presents an example of the radiative fluxes and heating-rate profiles obtained from actual EarthCARE observations, demonstrating the

current performance of the ALL_RAD product using the operational Level-2 inputs.

The radiative flux and heating-rate profiles thus obtained are further used to estimate direct aerosol radiative effect (ARE) and cloud radiative effect (CRE). These quantities are derived by taking differences between the "full-atmosphere" fluxes and those additionally simulated for virtual atmospheres in which aerosols or clouds are removed. The ARE and CRE estimates are produced along the EarthCARE orbit. Taking advantage of EarthCARE's vertical profiling capability, AREs are estimated for different stratification cases of aerosols and clouds with the method of Oikawa et al. (2013, 2018), who classified the stratifications according to location of aerosol layers relative to cloud layers into four scenarios that have distinctly different radiative characteristics.

The estimates of radiative fluxes, heating rates and ARE/CRE are then compiled into a global radiation budget to provide an updated picture of Earth's energy budget. This facilitates comparisons with previous satellite-based studies (e.g. CERES, CloudSat, CALIPSO, and MODIS) and supports updates to the observed global radiation budget. The EarthCARE-derived global radiation budget also serves as an observation-based reference for comparison with climate models. Such comparisons will enable us to evaluate the models in their representation of aerosol and cloud radiative effects and their influences on global radiation budget.

4.4.2 Research Product
4.4.2.1 Introduction

This section describes the algorithm that retrieves the Research Product relevant to the radiative flux properties, using all four sensors on EarthCARE. The research product of radiative flux is obtained from three-dimensional radiative transfer simulation.

4.4.2.2 3D RTM development

This task is to develop a system of calculating the profile of atmospheric radiative flux using a three dimensional (3D) Monte-Carlo radiative transfer code. Input data are Level-2 products of CPR, ATLID, MSI and BBR; Outputs are radiative flux profiles along the EarthCARE orbit (Fig 4.4.3).

For this research purpose, we have developed a 3D Monte-Carlo radiative transfer code (Okata, 2016; Okata et al. 2017). This code is implemented with k-distribution parameters of Sekiguchi and Nakajima (2008), adopted from OpenCLASTR Rstar radiation code (http://157.82.240.167/~clastr/), for broad band solar flux calculation, so that it can be used in the manner consistent with the Rstar code, which has been used by JAXA and other communities in the world. We plan to use this code for generating the radiative flux profile and heating rate profile in the atmosphere including broken clouds.

For testing the 3D radiative transfer code, 3D cloud fields are constructed based on available A-Train satellite measurements by the method of Minimum Information Deviation Profiling Method (MIDPM) of Howard Barker, Meteorological Service of Canada, and David Donovan, KNMI (private communication).

In the MIDPM method, as illustrated in Fig. 4.4.4, we first construct a library of the pair of observed parameters from CPR and collocated imager products at the footprint of CPR along the EarthCARE orbit, i.e. the profile of effective radar reflectivity factor, dBZe(z), spectral MSI radiances, cloud optical thickness (COT), effective particle radius (RE) and cloud top temperature (T_c).

We then select a best matched radar reflectivity factor profile from the library for each of off nadir pixels of MSI where CPR profile is not available, by minimizing the deviation between library MSI parameters and those at the pixel. We applied the MIDPM method to CloudSat CPR-retrieved radar reflectivity profiles, and AQUA MODIS-retrieved COT, RE, and T_c for a case of summer stratus cloud off California coast on July 2, 2007. The CloudSat data are provided by NASA, and MODIS products are provided by Takashi Nakajima. As illustrated in Fig. 4.4.4, we constructed a 3D cloud system in a target region of 100km x 100km area at location (22N, 138W).

Using these constructed 3D cloud systems and assuming the periodic boundary condition, we calculated the radiation field by our Monte-Carlo radiative transfer code in the visible spectral region assuming optical molecular and water cloud particle models derived from Rstar code. Figure 4.4.5 shows differences ΔR between area mean reflectivities of the 3D clouds and two approximations. The figure indicates that the Independent Pixel Approximation (IPA) is a good approximation to the area-averaged flux reflectivity in most cases, but there are cases of better approximation by the Plane Parallel Approximation (PPA).

References

Nakajima, T., M. Tsukamoto, Y. Tsushima, A. Numaguti, and T. Kimura, 2000: Modeling of the radiative process in an atmospheric general circulation model. *Appl. Opt.*, **39**, 4869-4878, doi:10.1364/AO.39.004869.

Nishizawa, T., Kudo, R., Oikawa, E., Higurashi, A., Jin, Y., Sugimoto, N., Sato, K., and Okamoto, H., 2024: Algorithm to retrieve aerosol optical properties using lidar measurements on board the EarthCARE satellite. *Atmos. Meas. Tech. Discuss.* [preprint], https://doi.org/10.5194/amt-2024-100, in review.

Oikawa, E., T. Nakajima, T. Inoue, and D. Winker, 2013: A study of the shortwave direct aerosol forcing using ESSP/CALIPSO observation and GCM simulation. *J. Geophys. Res.*, **118**, 3687-3708, 2012, doi:10.1002/jgrd.50227.

Oikawa, E., 2014: An evaluation of the direct aerosol radiative forcing from satellite remote sensing and climate modeling. 博士論文, 2014年12月, 東京大学大学院理学系研究科地球惑星科学専攻.

Oikawa, E., T. Nakajima, and D. Winker, 2018: An evaluation of the shortwave direct aerosol radiative forcing using CALIOP and MODIS observations. *J. Geophys. Res. Atmos.*, **123**, 1211-1233, doi:10.1002/2017JD027247.

Okata, M., T. Nakajima, K. Suzuki, T. Inoue, T. Y. Nakajima, and H. Okamoto, 2017: A study on radiative transfer effects in 3-D cloudy atmosphere using satellite data, *J. Geophys. Res. Atmos.*, 122, doi:10.1002/2016JD025441.

Okata, M., 2016: A study on radiative transfer effects in 3D cloudy atmospheres using Monte Carlo numerical simulation. 博士論文, 2016年12月, 東京大学大学院理学系研究科地球惑星科学専攻

Sato, K., Okamoto, H., Nishizawa, T., Jin, Y., Nakajima, T. Y., Wang, M., Satoh, M., Roh, W., Ishimoto, H., and Kudo, R., 2025: JAXA Level 2 cloud and precipitation microphysics retrievals based on EarthCARE radar, lidar, and imager: the CPR_CLP, AC_CLP, and ACM_CLP products. *Atmos. Meas. Tech.*, **18**, 1325–1338, https://doi.org/10.5194/amt-18-1325-2025.

Sekiguchi, M., and T. Nakaima, 2008: A k-distribution-based radiation code and its computational optimization for an atmospheric general circulation model. *J. Quant. Spectrosc. Radiat. Transfer*, **109**, 2779-2793.

Wang, M., T. Y. Nakajima, W. Roh, M. Satoh, K. Suzuki, T. Kubota, and M. Yoshida, 2023: Evaluation of the spectral misalignment on the Earth Clouds, Aerosols and Radiation Explorer/multi-spectral imager cloud product. *Atmospheric Measurement Techniques*, **16**(2), 603–623, doi:10.5194/amt-16-603-2023.

Yamauchi, A., K. Suzuki, E. Oikawa, M. Sekiguchi, T. M. Nagao, and H. Ishida, 2024: Description and validation of the Japanese algorithm for radiative flux and heating rate products with all four EarthCARE instruments: pre-launch test with A-Train. *Atmospheric Measurement Techniques*, **17**(22), 6751–6767, doi:10.5194/amt-17-6751-2024.
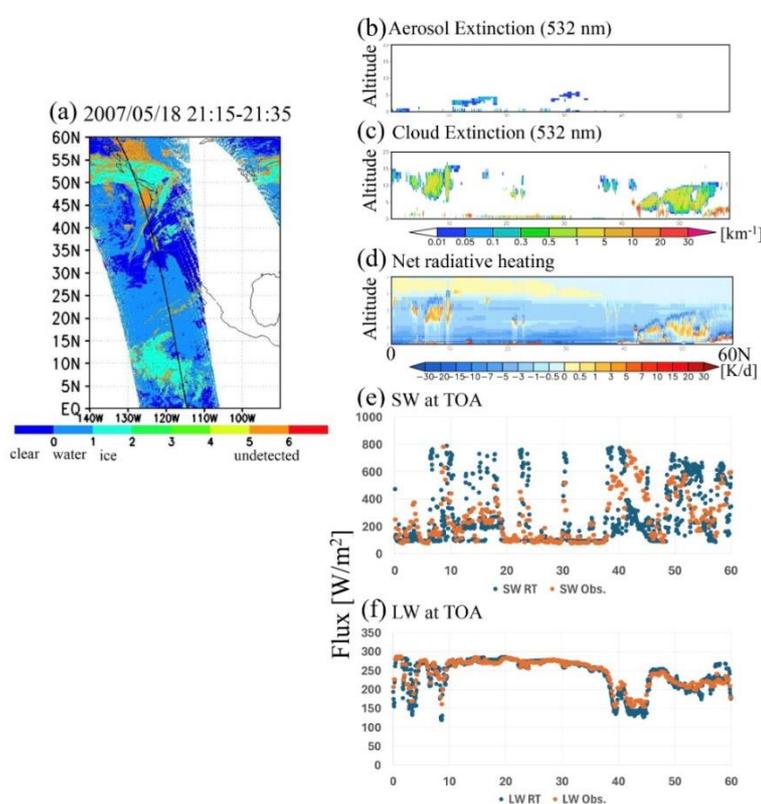
Figure 4.4.1. Example of a pre-launch test using A-Train data. (a) Cloud phase information from MODIS, with the A-Train footprint (solid line). (b) Aerosol extinction and (c) cloud extinction (km^{-1}) used as input. (d) Net radiative heating (K/day) as output. (e) Comparison of SW fluxes at the TOA estimated from 1-D RT calculations (blue) and CERES observations (orange). (f) Same as (e), but for LW at the TOA. (Adapted from Yamauchi et al., 2024)
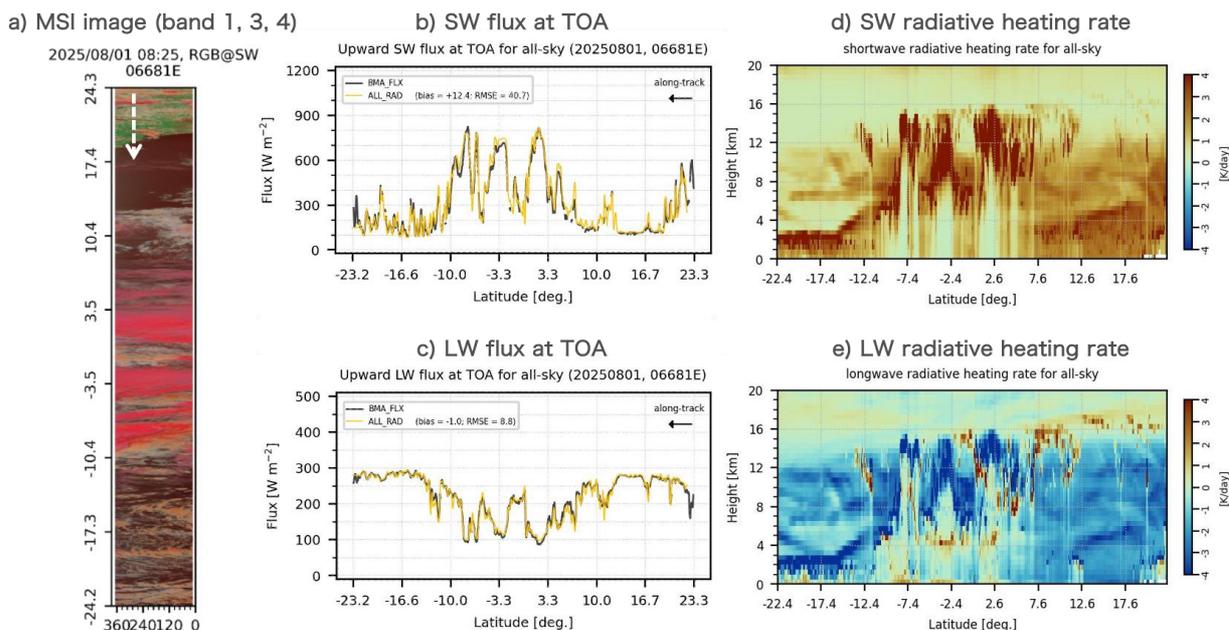
Figure 4.4.2. Example of the ALL_RAD inputs and outputs derived from actual EarthCARE observations. (a) MSI RGB composite using Bands 1, 3, and 4. (b) Shortwave radiative fluxes at the top of the atmosphere derived from ALL_RAD (yellow), compared with those from the BMA_FLX product based on BBR observations (black). (c) Same as (b), but for longwave radiative fluxes. (d) Shortwave heating-rate profiles derived from ALL_RAD. (e) Same as (d), but for longwave heating-rate profiles.
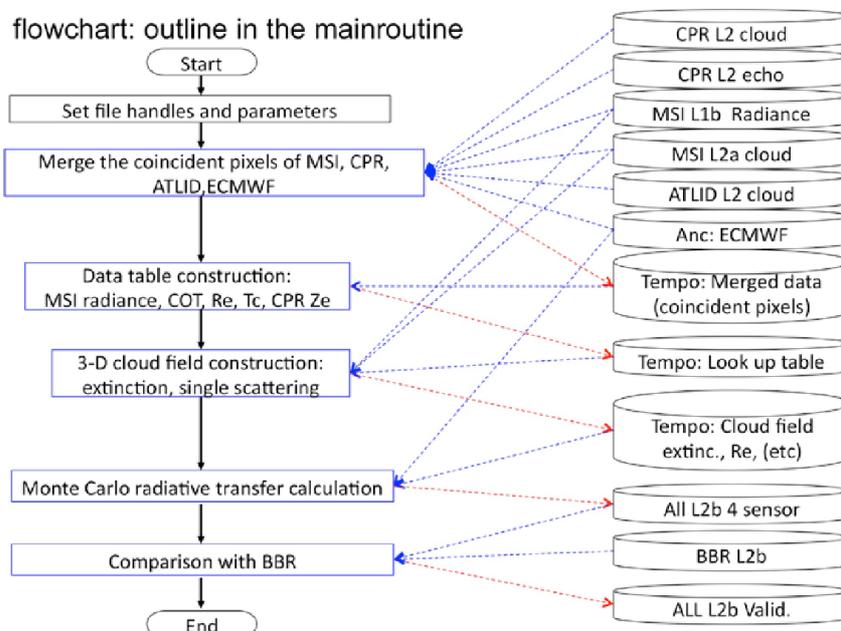
Figure 4.4.3. A flow chart of the 4 sensor radiative flux estimates with 3D RTM and MIDPM.
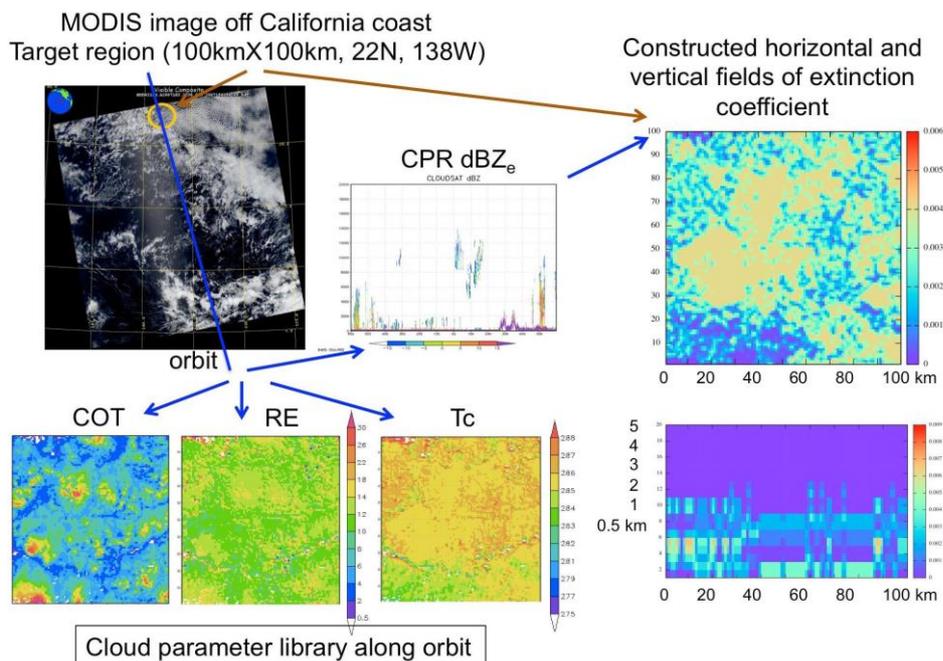
Fig. 4.4.4. A method of constructing a 3D extinction coefficient field from CPR and imager data. CLOUDSAT and AQUA MODIS cases on July 2, 2007.
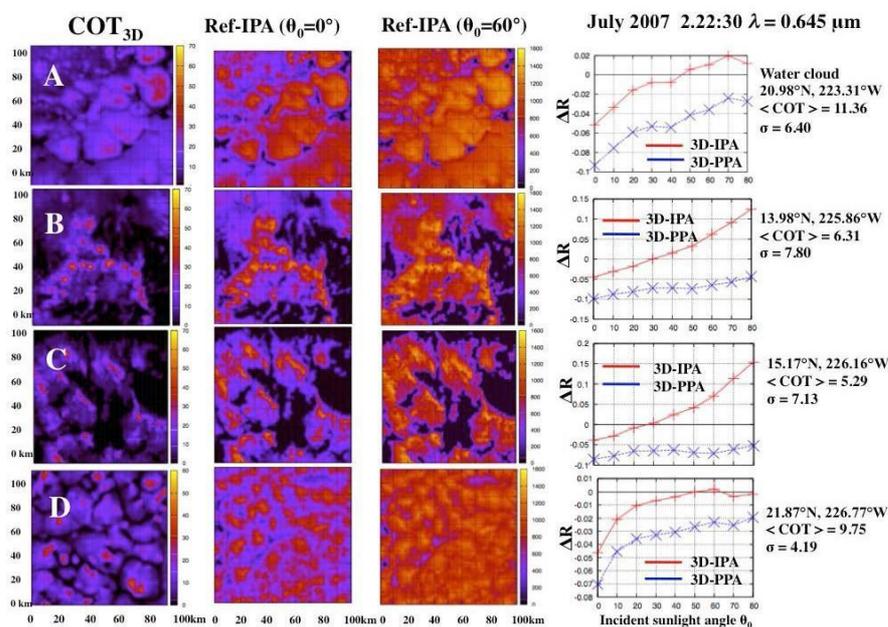
Fig. 4.4.5. Four scenes of 100kmx100km areas reconstructed by the MIDPM. Distributions of the Cloud Optical Thickness (COT) and flux reflectivity by the Independent Pixel Approximation (IPA) for two solar zenith angles $\theta_0 = 0°$ and $60°$. Right column panels shows the dependence of the difference between reflectances by *MCstar* and IPA or Plane Parallel Approximation (PPA) on the incident solar zenith angle θ_0.

5. Joint-Simulator

This section describes a suite of forward simulators for the radiometric quantities called Joint-simulator. Joint-simulator simulates the signals for all four sensors onboard EarthCARE based on cloud-resolving model (CRM) outputs and general circulation model (GCM) outputs. It provides synthetic observation that can be used for retrieval development as well as a way of evaluating the aerosol and clouds simulated with the numerical models directly against satellite observations.

5.1 Introduction

EarthCARE has four sensors: CPR with Doppler measurement, ATLID, Multi-Spectral Imager (MSI), and Broadband Radiometer (BBR). To implement forward simulation of the sen-sor signals from geophysical variables simulated by CRMs and GCMs, the Joint-Simulator (Joint Simulator for Satellite Sensors) is being developed. The main features are

- The radiative signatures of a vertical column of the atmosphere are calculated with the assumption of a plane-parallel atmosphere.
- The simulated sensors (Table 5.1.1.) are
    - o Visible and infrared (IR) imagers (visir)
    - o Microwave radiometers and sounders (micro)
    - o Radars (radar, ease)
    - o Lidars (lidar, ease)
    - o Broadband radiometers (broad)
- Joint-Simulator can be run with a single processor or multiple processors using Message Passing Interface (MPI).
- It has a universal interface for CRMs with use of netCDF format.
- Joint-Simulator has a universal interface that can be applied for various aerosol-cloud mi-crophysical outputs. The setup for particle size distributions (PSDs), mass-diameter rela-tionship, and terminal-velocity relationship can be easily done with use of namelist.
- There is an option to write out inputs for a 3D radiative transfer model, MCARaTS,
- A beam convolution scheme for spherical coordinates is available.
- A simple sub-grid data generator is provided to make the output from GCMs to be a CRM-like output.

The basic structure of Joint-Simulator is inherited from SDSU and NASA Goddard SDSU (Masunaga et al. 2010). As shown in Fig. 5.1.1, the sensors of EarthCARE are simulated by Earth-CARE Active Sensor Simulator (EASE) (Okamoto et al. 2007, 2008; Nishizawa et al. 2008) for CPR and ATLID, RSTAR (Nakajima and Tanaka 1986, 1988) for MSI, and MSTRN (Sekiguchi and Nakajima 2008) for BBR, and all the components are ready for application. 'module_simula-tor.F' in Fig. 5.1.1 has subroutines that read in atmospheric, surface, and aero-sol-cloud micro-physical variables simulated by CRMs and GCMs. 'main_SDSU.F' is the driver of Joint-Simulator that calls the sensor simulators and others based on a namelist 'Configure_SDSU.F'. In addition to the sensor simulators, Joint-Simulator is equipped with a beam-convolution simulator, an orbit-scan simulator, and a ground-validation simulator.

At present Joint-Simulator has been applied to the following models:

- Atmospheric models: NICAM (Satoh et al. 2008), JMA-NHM (Saito et al. 2006), WRF (Klemp et al. 2007; Skamarock and Klemp 2008), and MIROC (Watanabe et al. 2010).
- Aerosol microphysical models: SPRINTARS (Takemura et al. 2003) and GOCART (Chin et al. 2000)
- Cloud microphysical models: NICAM single and double-moment bulk schemes (Tomita 2008; Seiki et al. 2012), Hebrai University spectral bin model (Khain et al. 2000), and WRF microphysical schemes (e.g., Chapman et al. 2009).

It is noted that the aerosol and cloud optical parameters such as extinction cross-section and phase functions are calculated differently among some sensors (Fig. 5.1.2):

- visir, lidar, broad: uses KRNL.OUT of RSTAR6b which is a lookup table for Mie solutions.
- micro, radar: uses a built-in Mie subroutine.
- ease: uses its own lookup tables for Mie and non-spherical particles.

5.2 1D sensor simulators for EarthCARE

In the following, a brief description of EASE, RSTAR, and MSTRN is given. EASE simulates 95GHz cloud profiling radar with Dopplar velocity and backscatter Lidar for 532nm, 1064nm, and 355nm. Three kinds of configuration can be chosen with a run-time option: MIRAI, CALIPSO/CLOUDSAT, and EarthCARE. The MIRAI setup is for vertically pointing ground-based sensors. The CLIPSO/CLOUDSAT and EarthCARE setups are different in the altitude where the satellite flies and the output variables. EASE takes into account the attenuation of the radar and lidar signals by hydrometeors. In addition, the molecular attenuation and backscattering are simulated for the lidar. EASE has a set of scattering tables for non-spherical ice particles (Fig. 5.1.2). The default is set to CB50, i.e., the mixture of 50% of 3D bullet and 50% of 2D column (Okamoto et al. 2010; Sato and Okamoto 2006). This option is effective only for the radar and 532nm lidar at this moment. Scattering properties for aggregates and particles with liquid layer are not available. The cross-polarization signals at 355nm and 532nm are calculated for aerosol particles, while the signals due to hydrometeors are diagnosed based on empirical relations of depolarization to other parameters. Effect of the multiple scattering on extinction by liquid hydrometeors in the lidar signals is considered with use of a correction factor that was parameterized based on Mote Carlo simulation (Ishimoto and Masuda, 2002). However, EASE does not have capability of simulating the multiple scattering in the radar signals yet, which is important for deep convective clouds.

RSTAR6b is a general package for simulating radiation fields in the atmosphere-land-ocean system at wavelengths between 0.17 and 1000 μm. It assumes a plane parallel atmosphere divided into homogeneous sub-layers with underlying ground or ocean surface. The transfer engine is that of Nakajima and Tanaka (1986), which derives the solution of the discrete-ordinate method with use of eigen-space transformations of symmetric matrices. The number of streams set in Joint-Simulator is three in the hemisphere (six-stream method). The gaseous absorption is accounted through the non-linear fitting k-distribution method of Nakajima et al. (2000) and Sekiguchi et al. (2008). It contains a k-distribution table with HITRAN2004, and this version treats the major seven gases, H_2O, CO_2, O_3, N_2O, CO, CH_4, and O_2. The followings are the major differences

from the original RSTAR6b package:
- Look-up table option for single scattering of cloud particles
- Look-up table option for water surface reflection matrix and surface source matrix
- Lidar option

Use of the above two options makes it run 10~30 times faster than the original. Currently, only monochromatic intensity and brightness temperature are calculated.

MSTRN-X uses the correlated-k distribution (CKD) method to model the gas absorption, in which the quadrature points and weights are optimized for use in GCMs (Sekiguchi and Nakajima 2008). MSTRN-X considers 28 species compiled in HITRAN2004. The radiative transfer solver uses the two-stream approximation, but in a form of the discrete-ordinate method/adding method. There are three versions: standard version (18 Bands 40 integration points), global warming version (29 Bands 111 integration points), and chemical transport version (37 Bands 126 integration points).

An example of satellite observation simulated with Joint-Simulator is shown in Fig. 5.2.1. The signals were calculated from a 3.5 km-horizontal resolution simulation with NICAM for 2008 Tropical Cyclone Fengshen (Nasuno et al. 2009). Upper panel left: simulated visible 0.62 μm with a blue marble: next generation, NASA, right: simulated TOA Longwave upwelling flux. Lower panel left: simulated 94 GHz radar reflectivity, middle: simulated 532 nm lidar backscattering coefficient, and right: simulated Doppler velocity at 10 km. The ability to simulate the satellite signals from visible to microwave for passive and active sensors is vital for retrieval development and comprehensive validation of the aerosols and clouds simulated by GCMs and CRMs.

a. Modules and options added in 2012 fiscal year

In the following, the documents, modules and options that are added or improved in 2012 fiscal year are described.

User's guide

The user's guide has been updated to version 1.1 and 1.2, according to the development of Joint-Simulator.

General interfaces for CRMs

- Cloud microphysical schemes

  The native horizontal grid of NICAM is the icosahedral grid, which is usually converted into lat-lon grids for analysis. However, the relations among the aerosol and cloud variables can be altered during the conversion. The interface was modified to digest the icosahedral data. Also, the direct input of the icosahedral grid help reducing the grid points in the polar regions that are increased more than the actual model resolution during the lat-lon conversion.

- Aerosol microphysical schemes

  Previously, only EASE was able to digest the aerosol-particle input from CRMs. This year visible-IR and broadband simulators were connected to the input. In addition, users can choose a model for hygroscopic growth and specify internal mixing of aerosol species

in the configure file. The interface is applicable to single-moment schemes such as SPRINTARS (Takemura et al. 2003) and GOCART (Chin et al. 2000).

To validate the calculation of optical properties with Joint-Simulator, the aerosol optical depth (AOD) at 0.55 μm was calculated from the mass density of aerosol particles output from NICAM-SPRINTARS (provided by Dr. K. Suzuki at Jet Propulsion Laboratory, NASA). In Joint-Simulator, the optical properties of aerosol particles are calculated using RSTAR database based on SPRINTARS parameters for aerosol particles. As shown in Fig. 5.2.2, the AOD of carbonaceous aerosol particles from Joint-Simulator agree well with the output from NICAM-SPRINTARS. The AOD of dust particles also show a good agreement, but some difference can be seen. This is probably because the SPRINTARS uses bins to represent the size distribution of dust but the Joint-Simulator uses a lognormal distribution to the dust category.

The effects of aerosol particles on the visible-IR radiance and broadband fluxes can be investigated with Joint-Simulator. Fig. 5.2.3 shows 0.55μm radiance simulated with RSTAR and the difference by including aerosol particles (aerosol radiative forcing). It can be seen that the radiance is increased over the Sahara desert due to the scattering by dust particles. The absorbing carbonaceous aerosol particles decrease the radiance in the south of Gulf of Guinea.

IO options

The model outputs from CRMs may contain time-series of data set. Therefore, the interface and driver of Joint-Simulator was modified to calculate the signals over time series. The netcdf format was added for the output option. This format is superior to the simple binary like grads format since it is self-explanatory and compression capability.

EASE

- Interpolation

  Previously, the atmospheric fields from CRMs were vertically interpolated onto the CloudSat/CALIPSO/EarthCARE grid in EASE. Then, the signals were calculated. This can cause a difference in the relations between cloud microphysical variables. So, a new option has been added in which the signals are first calculated in the vertical grid of the CRMs, and then they are vertically interpolated onto the grid defined with the satellite data.

RSTAR

- Response function

  Previously, the Joint-Simulator assumed monochromatic inputs. The original RSTAR has the capability of using response function based on the simulated visible-IR imager, which is widely used in the satellite operational community. Therefore, the configure file was modified to read in the information of response function and lookup tables of optical properties were modified to cope with it.

Broadband simulators

- Surface albedo option

    Previously, the two broadband simulators used different surface albedo data; CLIRAD used MODIS-derived albedo lookup tables based on IGBP land-cover type, while MSTRN-X used the default albedo data. A new option was added to enable users to choose the above two albedo data as well as the albedo data used in their CRMs.

Unified single scattering library

- Microwave data

    The construction of unified single scattering library has begun this year. As shown in Fig. 5.2.4, individual developers of scattering models submit their data in any formats to us (level-0). The format converter was developed to adjust and organize the original data into the unified format (level-1). The extinction cross section, scattering cross section, asymmetry parameter, and scattering phase matrix are stored in terms of size parameter calculated with melt-mass equivalent radius, air temperature, and frequency for the microwave range. Then, users can create lookup tables (level-2) for the sensor simulator of interest based on user's cloud microphysical scheme through the RTM input creator.

    This year, Dr. Ishimoto at Japan Meteorological Agency Meteorological Research Institute let us use his scattering data for aggregate models calculated with the finite discrete time domain (FDTD) method (Table 5.2.1). Prof. Liu at Florida State University, USA, agreed for storing and re-distributing his data (called SCATDB) with discrete dipole approximation (DDA), which has 11 crystal habits (Table 5.2.2).

We tested the scattering models to see the sensitivity of the simulated signals. The single scattering look-up tables were calculated by assuming inverse exponential size distribution, $N(D) = N_0 \exp(-\lambda D)$, for snow category ($N_0 = 0.03$ cm^{-4}, $\rho_s = 0.1$ gm^{-3}, and ice water content of 1 g m^{-3}). Fig. 5.2.5 shows volume extinction, single scattering albedo, asymmetry parameter, and backscattering phase function as a function of effective radius. The size integration is limited from 0.1 to 2 cm. MG-MIE1 uses the oblique Maxwell-Garnet mixing rule (ice inclusion within air matrix) and Mie sphere solution that is a default in Joint-Simulator. ISMT-SF1, ISMT-SF2, and ISMT-SF3 were calculated with the aggregate models provided by Dr. Ishimoto. These use slightly different fractal dimensions, thus different mass-dimensional relationships. Compared to MG-MIE1, the maximum extinction of ISMT-SF1 and ISMT-SF2 are small. The asymmetry parameter of the aggregate models is smaller than MG-MIE1 over large sizes, while the backscattering phase functions of the aggregate models are larger. These imply that the microwave brightness temperature is more depressed and the radar reflectivity is larger with the aggregate models than those with MG-MIE1. The simulated 89 GHz brightness temperature with horizontal polarization and the difference from MG-MIE1 are calculated for Tropical Cyclone Fengshen (Fig. 5.2.6). Indeed, the ISMT-SF2 results in more depression of the brightness temperature, up to 5 K.

b. Modules and options added in 2013 fiscal year

In the following, the documents, modules and options that are added or improved in 2013 fiscal year are described.

User's guide

The user's guide has been updated to version 1.3 and 1.5, according to the development of Joint-Simulator.

General interfaces for CRMs

- Reading in effective radius

  Some models diagnose and output the effective radius of particles along with mass mixing ratio. Therefore, we have added an option to read in the effective radius, which is directly used for calculation of single scattering properties.

- Surface albedo diagnosis

  A diagnosis option has been added for NICAM simulations that implement a land-surface model (bucket model).

- Diagnosis of melt fraction for ice particles

  Most of the cloud microphysical schemes do no predict the melt water on ice particles in the melting layer. This is critical information to simulate the bright band observed by microwave sensors, so a simple diagnosis has been added, following the other SDSUs. Also, the stratiform cloud type is identified with a simple diagnosis based on the vertical motion input. If your model predicts or diagnoses the melt water, then you can input them through the netcdf file. This applies to Radar and Micro simulators.

EASE

- Scattering calculation

  Previously, when the signals from hydrometeors were calculated, one mass-equivalent effective radius was calculated for each phase of hydrometeor categories and then a corresponding signal value was picked up from the lookup tables.

  This time, we decided to calculate the effective radius for each category and look for the signal value in the lookup tables. Compared to the previous method, this approach can calculate the contribution better from large particles when multiple categories with cloud and precipitation particles exist.

  In calculating radar and lidar signals, the previous version applies only one scattering lookup table to all the ice categories. This time, for example, if you have three categories of ice particles, such as cloud ice, snow, and graupel, you can choose one of the seven tables for each category.

- Beam convolution

  Previously, EASE did not have the beam convolution functionality, although vertical interpolation is already available. In order to accommodate high-resolution simulations, the beam convolution scheme has been made available for EASE, too.

- Bin model

  Previously, EASE could not deal with a bin model that has an arbitrary number of bins. This modification enables it to calculate the signals as long as a set of single scattering lookup tables for the hydrometeors beforehand. The tools to make the single scattering lookup tables are being prepared for public release.

- Vertical interpolation

  We added an option to calculate the signals in the vertical grid of the model.

Radar

- Vertical interpolation

  Calculation of the signals in radar simulator is done in the vertical grid defined by the input model. In order to cope with arbitrary vertical grids of satellite data, a new option has been added for vertical interpolation. The beam convolution function can be also applied at the same time. In this case the signals are interpolated vertically first, and then the Gaussian beam pattern is applied. This option allows WRF users to output the signals in the user-defined grid directly.

Lidar

- Vertical interpolation

  The same option as Radar has been added.

Passive microwave

- Slant-path option

  In the passive microwave sensor simulator, there is a slant-path option that allows users to input the atmospheric information in a slanted angle, not perpendicularly, based on the sensor viewing zenith angle. But, when the domain division is used in the parallel computation, some threads have to obtain data outside of their sub-domain through MPI communication. At this time, this problem was solved by implementing the MPI. Note that the slant-path direction is taken to be north-south direction, and outgoing path is set to the south.

Unified single scattering library

- Mie solution

  As shown in Fig. 5.2.4, the format converter is used to create the scattering database and the RTM input creator is utilized to create the lookup tables that are specifically tailored for input models. This year, the RTM input creator has been updated 1) to include Mie approximation, 2) to write outputs for visible-IR, Lidar, and EASE simulators, and 3) to cope with general bin models.

Sub-grid data generator

  The conventional general circulation models (GCMs) have coarse horizontal resolution such as 2.5 degrees for computational efficiency. In such resolution, the clouds and

precipitation are not explicitly resolved, but they are spatially distributed based on a sub-grid scheme. Correspondingly, the model outputs on hydrometeors are given in the coarse resolution along with grid-average cloud fraction. In order to apply Joint-Simulator to GCMs, it is necessary to generate sub-grid data based on the coarse grid-average data. We have developed a simple sub-grid data generator for this purpose. Currently, a maximum-random cloud overlap scheme is available for cloud particles or large-scale condensates, and precipitating hydrometeors that are represented by only mass flux are not taken into consideration.

c. Modules and options added in 2014 fiscal year

In the following, the documents, modules and options that are added or improved in 2014 fiscal year are described.

User's guide

The user's guide has been updated to version 1.6, according to the development of Joint-Simulator.

EASE

- Depolarization parameterization

    The CALIPSO lidar has a 532 nm cross polarization channel, which is used to calculate depolarization ratio. This parameter is useful for identifying particle types (Yoshida et al. 2010). Previously, signals in the channel were not calculated for hydrometeors at 532 nm, but only for aerosol particles at 355 nm. This time, we incorporated lookup tables of depolarization that was made from CALIPSO observation. For liquid hydrometeors, the depolarization is given as a function of nadir angle (time of operation), temperature (above or sub freezing temperature), total attenuated backscattering, extinction between two consecutive layers, and order of liquid layers. For solid hydrometeors, the depolarization is given as a function of nadir angle, temperature, and total attenuated backscattering. The order of liquid layers is calculated by employing a simplified lidar mask (Hashino et al. 2013). For mixed-phase cloud boxes, we apply the above tables separately to the attenuated backscatter calculated only with liquid or ice in the box. Then, the two cross polarization signals are weighted by the attenuated total backscattering coefficients. Note this approach is purely empirical and does not use information of the particle shape from the atmospheric models.

Broadband

- RRTMG

    RRTMG package (RRTMG_LW and RRTMG_SW, Iacono et al. 2008) is widely used in operational global models and climate/weather models, including ECMWF IFS, MPI ECHAM5, NCEP GFS, NCAR WRF, NCAR CAM5, and NASA GEOS-5. Both utilize correlated-k approach and two-stream approximation, although RRTMG_LW modifies the diffusivity angle in some spectral bands based on water vapor amounts. The longwave scheme consists of 16 bands from wavelength of 3.08 to 1000 microns, and the shortwave

one 14 bands covering from 0.2 to 12.2 microns. More details are found at http://rtweb.aer.com/rrtm_frame.html. Note that McICA (Monte-Carlo Independent Column Approximation) for sub-grid cloud representation is not available in Joint-Simulator.

An example of global averages of depolarization ratio was calculated with a NICAM simulation dataset (Fig. 5.2.7.). Fig. 5.2.7.a) matches with the lookup tables except for 'all' samples, indicating correct implementation of the parameterization. For the liquid clouds, the depolarization ratio mostly matches with those for 1st layer of liquid clouds likely because the signals are totally attenuated by one layer of liquid cloud.

To understand relative performance of the three broadband simulators, we calculated fluxes under clear sky and full sky assuming ocean surface from a NICAM-SPRINTARS dataset. For example, a good agreement on TOA longwave upward flux was found between MSTRNX and RRTMG in the clear sky case (Fig. 5.2.8e). But RRTMG underestimates the flux for the full sky case up to 50 W/m^2 (Fig. 5.2.8f). CliRAD overestimates the flux for the clear sky case due to less absorption by water vapor (Fig. 5.2.8c), while it simulates differences up to 48 W/m^2 both in positive and negative directions for the full sky case (Fig. 5.2.8d). It turned out that MSTRNX and RRTMG give similar LW and SW fluxes under clear sky (within 5 W/m^2).

Passive microwave

- Test of Liu's microwave model

    Liu's microwave model is a microwave radiative transfer model, developed by Prof. Liu at Florida State University (Liu 1998), which uses a plane–parallel and various ice shape assumption. This model uses the four-stream discrete ordinate method, while the Joint-Simulator is based on the two-stream Eddington model (Kummerow 1993). Liu's model is used to evaluate and data assimilation of nonhydrostatic mesoscale model of the Japan Meteorological Agency (Eito and Aonashi 2009). Liu's model use an empirical approach to calculate surface emissivity over land, and a detailed description is given in Table 5.2.3 We tested and compared it with the Joint-Simulator before implementation in the Joint-Simulator as an option.

We compared Liu's model and the Joint-Simulator using AMSR-E data collected over a tropical open ocean in January 2008 using stretched NICAM. Figure 5.2.9 shows comparisons of brightness temperatures of microwave channels of AMSR-E, the Joint-simulator, and the Liu model. The figure shows the horizontal distribution for 19 GHz horizontally polarized brightness temperature (T19H) and for 89 GHz polarization collected brightness temperature (PCT89). NICAM simulations reproduce the convective bands between 0 and 5 degrees north latitude. The deep convective systems are shifted westward in comparison with the observation. The simulated PCT89 shows similar size convective systems to the observation, while the size of the simulated T19H is smaller than in the observation. This means that NICAM reproduces scattered precipitation systems compared with the observation Liu's model and the Joint-Simulator show almost the same distribution over the ocean.

General interfaces for CRMs

- Implementation of size distribution of Roh and Satoh 2014

  We added an option to factor in temperature and vertical wind in bulk microphysics. In addition, the size distributions of Roh and Satoh 2014 are implemented.

d. Modules and options added in 2015 fiscal year

In the following, modules and options that are added or improved in 2015 fiscal year are described.

EASE

- Minor changes in L1 data simulator

  There are minor changes such as addition of surface elevation data, changed product frame from 10 minute to 11.25 minute, and consideration of tilting angle in ATLID data by interpolation in NICAM in L1 data simulator

VIS/IR

- Maxwell-Garnett model in VIS/IR simulator

  We added calculation modules with a similar method of scattering and absorption, which has constancy in microwave and radar simulator. The original VIS/IR simulator assumed wet particle polydispersions and compute refractive index for internal mixture, including hygroscopic growth based on RSTAR. In microwave and radar simulator, the dielectric function of frozen hydrometeors is calculated based on the Maxwell-Garnett model with an ice matrix and air inclusions, where the volume fraction of the inclusions is estimated from a given particle density. We added same calculation module for scattering and absorption like the microwave simulator. These codes have been developed by Prof. Masunaga of Nagoya university to compute the scattering phase function for use by visible/IR simulations in SDSU (Masunaga et al. 2010).

Passive microwave

- Implementation of 4 stream model

  We implemented 4 stream approximation model (Liu 1998) for passive microwave sensors in Joint-simulator, in courtesy of Prof. Liu of Florida university. According to Liu (1998), the 4 stream model was more accurate while only using about 20 % more computer time comparing to a 2 stream model. Especially, the maximum error of the 2 stream Eddington model was about 7 K for ice clouds, while that of the 4 stream model was only about 2K comparing with two 32 stream models.

e. Modules and options added in 2016 fiscal year

In the following, modules and options that are added or improved in 2016 fiscal year are described.

User's guide

The user's guide has been updated to version 1.5 and 1.7, according to the development

of Joint-Simulator.

General interfaces for CRMs

- Lookup Table (LUT) approach for Spectral Bin cloud microphysics schemes

  In previous versions, when spectral bin schemes are the inputs, Joint-Simulator calculates the single-scattering optical properties for each size (mass) bin and each spatial grid. This was a time-consuming approach, though it is accurate. Also, old versions could not handle the broadband simulations for bin schemes.

  This updates allow us to read Lookup Tables of the single-scattering optical properties that are prepared beforehand and outside of Joint-Simulator, so that it saves time. In case of spectral bin schemes, we define bins by mass (not size) of particles and the optical parameters in the LUT such as extinction coefficients are given as a function of these mass bins.

EASE

- Consideration of 2D plate ice for 0.3 and 3 degree tilting angle

  The tilting angle of spaceborne lidar is one of issues for evaluation and retrievals of cloud properties and cloud fractions (Hu et al. 2009). The database of optical properties is implemented for 2D plate when lidar is off nadir 0.3 and 3 degree.

- Implementation of Hogan's multiple scattering models in the EASE simulator

  Multiple scatterings in the previous version were considered using the look up table from Ishimoto and Masuda (2002) by liquid hydrometeors in the lidar signals in the EASE simulator. Lidar observations of clouds are affected by multiple scattering of the lidar signals. According to Hogan (2006), the retrieved optical depth will be underestimated by around 40% due to no consideration of lidar multiple scattering effects in combined radar-lidar retrievals of ice clouds from space. We implemented two fast algorithms developed by professor Hogan of University of Reading: the Photon Variance-Covariance (PVC) method for quasi-small-angle (Hogan 2006; Hogan 2008) and the Time-Dependent Two-Stream method for wide-angle multiple scattering (TDTS) method of Hogan and Battaglia (2008). The PVC method is suitable for ground lidar and airborne lidar with small footprint on the cloud. The TDTS method is suitable for spaceborne lidar with a large field of view and spaceborne millimeter-wave radar observation of deep convective clouds. This module helps to interpret effects of multiple scatterings of ice crystals on the lidar signals.

f. Modules and options added in 2017 fiscal year

In the following, modules and options that are added or improved in 2017 fiscal year are described.

General interfaces for CRMs

- Reading in precipitation mass flux

  GCMs typically do not predict mass contents for precipitating hydrometeors, and instead diagnose precipitation mass fluxes. The subroutine was updated to diagnose the parameters of particle size distributions with use of terminal velocity and mass dimensional relationships.

EASE

- Noise simulator for Doppler velocity

  We introduced noises using the pulse pair method and standard deviation of Doppler velocity error using a perturbation approximation (Doviak and Zrnic 1993) in courtesy of Dr. Hagihara in JAXA. This noise simulator can simulate uncertainties from noises by the setting of CPR such as PRF and antenna beam-width.

- Water vapor absorption

  Previously, water vapor absorption was neglected in calculation of radar reflectivity. The subroutine available in microwave module is now simply called to take that into account.

Microwave

- Implementation of monthly land emissivity data

  Previously, NESDIS model (Weng et al. 2001) is used for microwave emissivity over land in Joint-simulator. Climatological emissivity data are widely used for data assimilation for rain and rain retrievals over land. We implemented two kinds of climatological surface microwave emissivity data.

  First, TELSEM data (Aires et al. 2011), which is global land surface microwave emissivity with 0.25-degree grid size for 12 years (1993-2004). These data are calculated from SSM/I measurements, ISCCP and NCEP-NCAR reanalysis. It covers the globe.

  Second, emissivity data of Nagoya university (Furuzawa et al. 2012), which is land surface microwave emissivity with 0.2-degree for 15 years (1998 – 2012). These data are calculated from TRMM TMI, PR, and JRA25. It covers only from 36.2S to 36.2N.

VIS-IR

- RSTAR6b to RSTAR7a

  The visible-IR simulator was updated to version 7a. The update includes non-spherical scattering options for ice particles and for aerosol particles. The databases compiled with Yang et al. (2000, 2005) and Duvobik (2002) are directly available without use of the Joint-Simulator Scattering Database. The number of scattering angles has been increased from 74 to 112, and for application of response function variable intervals over wavelength are now allowed.

- Tuned RSTAR7a

  This version allows users to calculate signal observations of major satellites easier and faster. This was made possible by tuning evaluation points of gas absorption and the weights. Currently available sensor is Himawari 8. The task of validating the simulation against the one with response function remains for next year.

- RSTAR7a-BRDF

  A Bi-directional Reflection Distribution Function option was added to RSTAR7a. Currently 9 models are available. This option is still under development and feedback from users is expected to improve it.

- Viewing zenith and azimuth angles for geostationary satellites

    In general, users prepare viewing zenith angle and difference of viewing and Solar azimuth angles (Fig. 5.2.10 and 5.2.11). This option allows one to specify the name of geostationary satellite and Joint-Simulator calculates these angles over the globe automatically.

JSSD

- Habit mixing module

    A habit-mixture module has been provided by Dr. Baum at Space Science and Engineering Center, including the mixing model used for MODIS Collection 5 (Baum et al. 2014). This mixture model is supposed to be used for visible-IR and broadband calculation of ice clouds (Fig. 5.2.12).

g. Modules and options added in 2018 fiscal year

    In the following, modules and options that are added or improved in 2018 fiscal year are described.

The modules about technical information of instruments

- Consideration for a closed version

    The Joint-Simulator for L1 data has a detail technical information about the instruments such as noise simulator and surface clutter model. This information is limited to public people. We will support the code about noise simulators to people which have permission from JAXA or NICT.

EASE

- Noise simulator for ATLID

    The noise model for ATLID is implemented by courtesy of Dr. Nishizawa of NICT and ESA. The noise model is based on gaussian random noises in L1 data from shot noise, dark count rate, solar background counts and so on. The noise model can investigate the uncertainties from instrument noises for cloud and aerosol properties, which are retrieved from ATLID.

- Surface clutter of EarthCARE CPR

    The surface clutter simulator is implemented by courtesy of Dr. Ohno of NICT and Dr. Hagihara of JAXA. The expected surface echo is calculated using a response function of CPR. The two settings are prepared like over ocean and land. We set up the normalized radar cross section as 10 dB over the ocean, and as 0 dB over land. The normalized radar cross section varies by SST, surface winds over the ocean, and varies by the characteristics of surfaces over land such as land use. After the launch of EarthCARE, the surface clutter model will be updated. According the expected surface clutters, the boundary layer clouds can be observed above 600m altitude by EarthCARE CPR (Fig. 5.2.13)

h. Modules and options added in 2019 fiscal year

In the following, modules and options that are added or improved in 2019 fiscal year are described.

VIS-IR

- Response functions for MSI

    All response functions of MSI are implemented by courtesy of and ESA. The 'smile effect' means a spectral distortion, which found in push-broom sensors. The smile effect can be considered for 0.67, 0.865, 1.65, and 2.21 μm channels with the response functions, depends on an across-track pixel (Fig. 5.2.14)

EASE

- Ozone module for ATLID and CALIPSO

    The ozone module for ATLID and CALIPSO is implemented by courtesy of Dr. Nishizawa of NICT (Fig. 5.2.15). The ozone absorption cross-sections are calculated based on the laboratory experiment study (Serdyuchenko et.al 2014). The monthly climatology ozone data were given in Joint-Simulator, which used in a radiation calculation in NICAM.

i. Modules and options added in 2020 fiscal year

In the following, modules and options that are added or improved in 2020 fiscal year are described.

POLARRIS-f

- An introduction to a new polarimetric radar simulator

    A POLArimetric Radar Retrieval and Instrument Simulator (POLARRIS, Matsui et al. 2019) is developed to simulate and evaluate the parameters of a polarimetric radar. The POLARRIS consists of POLARRIS-f and iPOLARRIS. POLARRIS-f is a forward model to calculate parameters of a polarimetric radar, and iPOLARRIS is hydrometeor identification (HID) tool using the parameters from a polarimetric radar. The POLARRIS-f is introduced in the Joint simulator. The.POLARRIS-f use T-matrix and Mueller-matrix modules (Vivekanandan et al., 1991).

    The POLARRIS-f can simulate the Differential reflectivity (ZDR), the specific differential phase (KDP), the copular correlation coefficient (ρHV), and Doppler velocity using T-matrix, Mueller-matrix modules, and the output data from cloud models. The POLARRIS-f makes lookup tables in terms of liquid/ice water content and effective radius for each hydrometeor. And polarimetric parameters are calculated using the lookup tables. Fig. 5.2.16 is an example of the lookup table for ran with 1 g/m^3 at 300K. The radar reflectivity is independent for radar angles. ZDR and KDP depend on the radar angle and effective radius. It is related to change of rain drop shapes from spherical shapes to oblate

spheroids.

EASE

- An introduction of observation windows of EarthCARE CPR

     The EarthCARE CPR have two modes of an observation window like low mode (–1 to 16 km) at latitudes of 60–90° and high mode (–1 to 20 km) at latitudes of 0–60° (Hagihara et al. 2021). The pulse reputation frequency (PRF) is changed in a range of 6100 – 7500 Hz with the latitude and observation window because PRF is determined by the satellite altitude as illustrated in Fig. 5.2.17 (Hagihara et al. 2021).

     The modes of observation window for EarthCARE CPR are implemented by courtesy of Dr. Hagihara of NICT. This module can help more realistic simulation of Doppler velocity of CPR depending on the latitude than the fixed PRF.

j. Modules and options added in 2021 fiscal year

     In the following, modules and options that are added or improved in 2021 fiscal year are described.

VIS-IR

- Minor updates of RSTAR7 related to smile effects of MSI

     The minor updates for the MSI smile effect have done. We changed the location on nadir and a pixel order for MSI simulation. We debugged an interface of azimuth angle from the orbit simulator. The reference response function was changed to the response function on nadir.

iPOLARRIS

- An introduction of iPOLARRIS and CSU-tool

     POLARRIS-f was implemented in Joint simulator last fiscal year. However, it is difficult to interpretate polarimetric radar signals in observation and simulation results. Hydrometeor identification (HID) is used to interpretate hydrometeor categorizations based on polarimetric variables. iPOLARRIS, has been developed to apply the same retrieval algorithms of HIDs to observations and simulation results from POLARRIS-f.

     iPOLARRIS is Python-based and incorporates a library of radar processing algorithms for an evaluation of models using POLARRI-f. iPOLARRIS is based on fuzzy logic techniques requiring membership functions (MBFs) to calculate a score from polarimetric variables and atmospheric conditions.

     The fuzzy logic HID was described in Dolan and Rutledge (2009) and Dolan et al. (2013) which used in iPOLARRIS. There are ten categories in the HID: drizzle (DZ), rain (RN), ice crystals (IC), dry snow (DS), wet snow (WS), vertical ice (VI), low-density graupel (LDG), high-density graupel (HDG), hail (HA), and big drops (BD).

     CSU-tool (Tessendorf et al. 2005; Dolan et al 2013) is also one of the HID method like iPOLARRIS using following the same fuzzy logic and similar MBFs.

     The difference between iPOLARRIS and CSU-tool is about the MBFs of radar

reflectivity for ice crystals, vertical ice, and low-density graupel. Figure 5.2.18 shows the difference between iPOLARRIS and CSU-tool. The results are almost same each other, but the fraction of low-density graupel and ice crystal is different.

k. Modules and options added in 2022 fiscal year

In the following, modules and options that are added or improved in 2022 fiscal year are described.

VIS-IR/ Broadband

- Making an interface for the MCstar

    For fine-resolution experiments like large eddy simulations (LES), the three-dimensional scattering is important for the simulations of satellite signals. The MCstar (Okata et al. 2017) is a 3D Monte Carlo radiative transfer model. This model is one of the STAR series (System for Transfer of Atmospheric radiation) developed by OpenCLASTR (Nakajima and Tanaka 1983, 1986, 1988; Sekiguchi and Nakajima 2008) like RSTAR and MSTRNX in the Joint-Simulator.

    In this fiscal year, we made an interface for the MCstar in the Joint-Simulator in courtesy of Professor Nakajima. The Joint-Simulator can make input data from the LES data for the MCstar such as atmospheric data like pressure, temperature, relative humidity, cloud optical thickness of cloud types and aerosol types, and phase functions for hydrometeors. Note that an implementation of the MCstar in the Joint-Simulator is not completed in this fiscal year.

l. Modules and options added in 2023 fiscal year

In the following, modules and options that are added or improved in 2023 fiscal year are described.

VIS-IR/ Broadband

- Making a parallel version of MCstar using OpenMP

    One of the issues of MCstar is that it takes a longer calculation time compared to the radiation code based on Rstar. We made a parallel version of MCstar using OpenMP. With the implementation of the parallel version, we've observed a sevenfold increase in processing speed over the single CPU version of MCstar. Specifically, this acceleration was benchmarked using a 16 CPU configuration. This performance improvement does not come at the cost of precision. Our validation exercises reveal that the parallel version maintains high fidelity to the original model, with an average difference in radiance calculations at the 0.6 μm radiance test case of merely 0.5%. Even at the extreme, the maximum divergence recorded was just 1.61%.

J. Modules and options added in 2024 fiscal year

In the following, modules and options that are added or improved in 2024 fiscal year are described.

VIS-IR/ Broadband

- Making lookup tables based on the Voronoi ice shapes

    We have integrated Voronoi particle databases into MSTRNX, courtesy of Dr. Tempei Hashino. These Voronoi particles are utilized in the radiative flux algorithm using MSTRNX (Yamauchi et al., 2024). To ensure consistency in model evaluations, it is essential to apply the same ice particle shape assumptions in the Joint Simulator. The lookup tables are derived from the Joint-Simulator Scattering Database, which was developed by Dr. Tempei Hashino.

References

Aires, F., C. Prigent, F. Bernardo, C. Jimenez, R. Saunders, and P. Brunel, 2011: A Tool to Estimate Land-Surface Emissivities at Microwave frequencies (TELSEM) for use in numerical weather prediction. *Q J Roy Meteor Soc*, **137,** 690-699.

Baum, B. A., P. Yang, A. J. Heymsfield, A. Bansemer, B. H. Cole, A. Merrelli, C. Schmitt, C. Wang, 2014: Ice cloud single-scattering property models with the full phase matrix at wavelengths from 0.2 to 100 □m, *J. Quantitative Spectroscopy & Radiative Transfer.*, **146**, 123-139.

Chapman, E. G., W. I. Gustafson Jr., R. C. Easter, J. C. Barnard, S. J. Ghan, M. S. Pekour, and J. D. Fast, 2009: Coupling aerosol-cloud-radiative processes in the WRF-Chem model: Investigating the radiative impact of elevated point sources, Atmos. Ghem. Phys., 9, 945-964.

Chin, M., R. B. Rood, S.-J. Lin, J. F. Muller, and A. M. Thomspon, 2000: Atmospheric sulfur cycle in the global model GOCART: Model description and global properties, J. Geophys. Res., 105, 24,671-24,687.

Chou, M. D., and M. J. Suarez, 1994: An efficient thermal infrared radiation parameterization for use in general circulation models. Technical report series on global modeling and data assimilation, NASA/TM-104606, Vol. 3.

Chou, M. D., and M. J. Suarez, 1999: A solar radiation parameterization for atmospheric studies. Technical report series on global modeling and data assimilation, NASA/TM-1999-104606, Vol. 15.

Chou, M. D., M. J. Suarez, X.-Z. Liang, and M. M.-H. Yan, 2001: A thermal infrared radiation parameterization for atmospheric studies. Technical report series on global modeling and data assimilation, NASA/TM-2001-104606, Vol. 19.

Dolan, B., & Rutledge, S. A. (2009). A theory-based hydrometeor identification algorithm for X-band polarimetric radars. Journal of Atmospheric and Oceanic Technology, 26(10), 2071-2088.

Dolan, B., Rutledge, S. A., Lim, S., Chandrasekar, V., & Thurai, M. (2013). A robust C-band hydrometeor identification algorithm and application to a long-term polarimetric radar dataset. Journal of Applied Meteorology and Climatology, 52(9), 2162-2186.

Doviak, R. J., and D. a. S. Zrni**, 1993: *Doppler radar and weather observations.* 2nd ed.   Academic Press, xix, 562 pages, 568 unnumbered pages of plates pp.

Eito, H., and K. Aonashi, 2009: Verification of Hydrometeor Properties Simulated by a Cloud-Resolving Model Using a Passive Microwave Satellite and Ground-Based Radar Observations for a Rainfall System Associated with the Baiu Front. *J. Meteor. Soc. Japan*, **87A,** 425-446.

Furuzawa, F. A., H. Masunaga, and K. Nakamura, 2012: Development of a land surface emissivity algorithm for use by microwave rain retrieval algorithms. *Proc Spie*, **8523**.

Hagihara, Y., H. Okamoto, and R. Yoshida, 2010: Development of a combined CloudSat-CALIPSO cloud mask to show global cloud distribution. *J. Geophys. Res.*, **115**, D00H33, doi:10.1029/2009JD012344.

Hagihara, Y., Ohno, Y., Horie, H., Roh, W., Satoh, M., Kubota, T., Oki, R. (2021). Assessments of Doppler velocity error of EarthCARE Cloud Profiling Radar using global cloud system

resolving simulation: Effects of Doppler broadening and folding. *The IEEE Transactions on Geoscience and Remote Sensing* (Accepted: 17 Feb. 2021). https://doi.org/10.1109/TGRS.2021.3060828.

Hashino, T., M. Satoh, Y. Hagihara, T. Kubota, T. Matsui, T. Nasuno, and H. Okamoto, 2013: Evaluating cloud microphysics from NICAM against CloudSat and CALIPSO. *J. Geophys. Res.*, 118, 1-20, doi:10.1002/jgrd.50564.

Hogan, R. J., 2006: Fast approximate calculation of multiply scattered lidar returns. *Appl Optics*, **45,** 5984-5992.

Hogan R. J., 2008: Fast Lidar and Radar Multiple-Scattering Models. Part I: Small-Angle Scattering Using the Photon Variance-Covariance Method. *J Atmos Sci*, **65,** 3621-3635.

Hogan, R. J., and A. Battaglia, 2008: Fast Lidar and Radar Multiple-Scattering Models. Part II: Wide-Angle Scattering Using the Time-Dependent Two-Stream Approximation. *J Atmos Sci*, **65,** 3636-3651.

Hu, Y. X., and Coauthors, 2009: CALIPSO/CALIOP Cloud Phase Discrimination Algorithm. *J Atmos Ocean Tech*, **26,** 2293-2309.

Iacono, M.J., J.S. Delamere, E.J. Mlawer, M.W. Shephard, S.A. Clough, and W.D. Collins, 2008: Radiative forcing by long-lived greenhouse gases: Calculations with the AER radiative transfer models, *J. Geophys. Res.*, 113, D13103, doi:10.1029/2008JD009944.

Ishimoto, H., and K. Masuda, 2002: A Monte Carlo approach for the calculation of polarized light: Application to an incident narrow beam, *J. Quant. Spectrosc. Radiat. Transfer*, 72, 467–483.

Khain, A. P., M. Ovtchinnikov, M. Pinsky, A. Pokrovsky, and H. Krugliak, 2000: Notes on the state-of-the-art numerical modeling of cloud microphysics. Atmos. Res., 55, 159–224.

Klemp, J. B., Skamarock,W. C., and Dudhia, J.: Conservative splitexplicit time integration methods for the compressible nonhydrostatic equations, Mon. Weather Rev., 135, 2897–2913, 2007.

Kummerow, C. D., 1993: On the accuracy of the Eddington approximation for radiative transfer in the microwave frequencies. *J. Geophys. Res.*, 98, 2757–2765.

Liu, G. S., 1998: A fast and accurate model for microwave radiance calculations. *J. Meteor. Soc. Japan*, **76,** 335-343.

Liu, G., 2008: A database of microwave single-scattering properties for nonspherical ice particles. *Bull. Amer. Meteor. Soc.*, 1563-1570. doi:10.1175/2008BAMS2486.1.

Masunaga, H. and C. D. Kummerow, 2005: Combined radar and radiometer analysis of precipitation profiles for a parametric retrieval algorithm. *J. Atmos. Oceanic Technol.*, 22, 909–929.

Masunaga, H., T. Matsui, W.-K. Tao, A. Y. Hou, C. D. Kummerow, T. Nakajima, P. Bauer, W. S. Olson, M. Sekiguchi, and T. Y. Nakajima, 2010: Satellite Data Simulator Unit: A multisensor, multispectral Satellite Simulator Package. Bull. Amer. Meteor. Soc., 91, 1625–1632. doi: 10.1175/2010BAMS2809.1

Matsui, T., Dolan, B., Rutledge, S. A., Tao, W. K., Iguchi, T., Barnum, J., & Lang, S. E. (2019). POLARRIS: A polarimetric radar retrieval and instrument simulator. *Journal of Geophysical Research: Atmospheres*, *124*(8), 4634-4657.

Nakajima, T. and M. Tanaka, 1986: Matrix formulations for the transfer of solar radiation in a

plane-parallel scattering atmosphere. *J. Quant. Spectrosc. Radiat. Transfer*, **35**, 13-21.

Nakajima, T. and M. Tanaka, 1988: Algorithms for radiative intensity calculations in moderately thick atmospheres using a truncation approximation. *J. Quant. Spectrosc. Radiat. Transfer*, **40**, 51-69.

Nakajima, T. and M. Tsukamoto, Y. Tsushima, A. Numaguti, and T. Kimura, 2000: Modeling of the radiative process in an atmospheric general circulation model. *Applied Optics*, **39**, 4869-4878.

Nasuno, T, M. Satoh, K. Oouchi, H. Taniguchi, H. Tomita, S. Iga, A. T. Noda, Y. Yamada, C. Kodama, H. Miura, W. Yanase, H. Yamada, H. Fudeyasu, and JAMSTEC ISV observation team, 2009: MJO Simulations/Hindcasts with NICAM. Monsoon Intraseasonal Variability Modeling Workshop, Busan, Korea.

Nishizawa, T., H. Okamoto, T. Takemura, N. Sugimoto, I. Matsui, and A. Shimizu, 2008: Aerosol retrieval from two-wavelength backscatter and one-wavelength polarization lidar measurement taken during the MR01K02 cruise of the R/V Mirai and evaluation of a global aerosol transport model, J. Geophys. Res., 113, D21201, doi:10.1029/2007JD009640.

Okamoto, H., T. Nishizawa, T. Takemura, H. Kumagai, H. Kuroiwa, N. Sugimoto, I. Matsui, A. Shimizu, A. Kamei, S. Emori, and T. Nakajima, 2007: Vertical cloud structure observed from shipborne radar and lidar,: mid-latitude case study during the MR01/K02 cruise of the R/V Mirai, J. Geophys. Res, 112, D08216, doi:10.1029/2006JD007628.

Okamoto, H., T. Nishizawa, T. Takemura, K. Sato, H. Kumagai, Y. Ohno, N. Sugimoto, A. Shimizu, I. Matsui, and T. Nakajima, 2008: Vertical cloud properties in the tropical western Pacific Ocean: Validation of the CCSR/NIES/FRCGC GCM by shipborne radar and lidar, J. Geophys. Res., 113, D24213, doi:10.1029/2008JD009812.

Okamoto, H., S. Iwasaki, M. Yasui, H. Horie, H. Kuroiwa, and H. Kumagai, 2003: An algorithm for retrieval of cloud microphysics using 95-GHz cloud radar and lidar, J. Geophys. Res., 108, D74226, doi:10.1029/2001JD001225.

Okata, M., Nakajima, T., Suzuki, K., Inoue, T., Nakajima, T. Y., and Okamoto, H.: A study on radiative transfer effects in 3-D cloudy atmosphere using satellite data, J. Geophys. Res. Atmos., 122(1), 443-468, 2017.

Roh, W., and M. Satoh, 2014: Evaluation of Precipitating Hydrometeor Parameterizations in a Single-Moment Bulk Microphysics Scheme for Deep Convective Systems over the Tropical Central Pacific. *J. Atmos. Sci.*, **71,** 2654-2673.

Saito, K., and Coauthors, 2006: The operational JMA nonhydrostatic mesoscale model. Mon. Wea. Rev., 134, 1266–1298.

Satoh, M., T. Matsuno,T., H. Tomita, H. Miura, T. Nasuno, S. Iga, 2008: Nonhydrostatic Icosahedral Atmospheric Model (NICAM) for global cloud resolving simulations. *J. Comp. Phys.*, **227**, 3486-3514.

Sato, K., and H. Okamoto, 2006: Characterization of Ze and LDR of nonspherical and inhomogeneous ice particles for 95-GHz cloud radar: Its implication to microphysical retrievals, J. Geophys. Res., 111, D22213, doi:10.1029/2005JD006959.

Sekiguchi, M. and T. Nakajima, 2008: A k-distribution-based radiation code and its computational optimization for an atmospheric general circulation model. *J. Quant. Spectrosc.*

Radiat. Transfer, **109**, 2779-2793.

Serdyuchenko, A., V. Gorshelev, M. Weber, W. Chehade, and J. P. Burrows, 2014: High spectral resolution ozone absorption cross-sections - Part 2: Temperature dependence. *Atmos Meas Tech*, **7,** 625-636.

Skamarock, W. C. and Klemp, J. B.: A time-split nonhydrostatic atmospheric model for weather research and forecasting applications, J. Comput. Phys., 227, 3465–3485, 2008.

Takemura T., T. Nakajima, A. Higurashi, S. Ohta, and N. Sugimoto, 2003: Aerosol distributions and radiative forcing over the Asian Pacific region simulated by Spectral Radiation-Transport Model for Aerosol Species (SPRINTARS). *J. Geophys. Res.*, 108, D238659, doi:10.1029/2002JD003210.

Tessendorf, S. A., Miller, L. J., Wiens, K. C., & Rutledge, S. A. (2005). The 29 June 2000 supercell observed during STEPS. Part I: Kinematics and microphysics. *Journal of the Atmospheric Sciences*, *62*(12), 4127-4150.

Tomita, H., 2008: New microphysics with five and six categories with diagnostic generation of cloud ice. *J. Meteor. Soc. Japan*, **86A**,121-142.

Vivekanandan, J. W., Adams, M., & Bringi, V. N. (1991). Rigorous approach to polarimetric radar modeling of hydrometeor orientation distributions. *Journal of Applied Meteorology*, **30**(8), 1053‑1063.

Watanabe, M., and Coauthors, 2010: Improved climate simulation by MIROC5: Mean states, variability, and climate sensitivity. J. Climate, 23, 63126335.

Weng, F. Z., B. H. Yan, and N. C. Grody, 2001: A microwave land emissivity model. *J Geophys Res-Atmos*, **106,** 20115-20123.

Yamauchi, A., Suzuki, K., Oikawa, E., Sekiguchi, M., Nagao, T. M., and Ishida, H. 2024: Description and validation of the Japanese algorithm for radiative flux and heating rate products with all four EarthCARE instruments: pre-launch test with A-Train, *Atmos. Meas. Tech.*, **17**, 6751–6767, https://doi.org/10.5194/amt-17-6751-2024.

Yoshida, R., H. Okamoto, Y. Hagihara, and H. Ishimoto, 2010: Global analysis of cloud phase and ice crystal orientation from cloud-aerosol lidar and infrared pathfinder satellite observation (CALIPSO) data using attenuated backscattering and depolarization ratio, J. Geophys. Res., 115, D00H32, doi:10.1029/2009JD012334.

Table 5.1.1. Sensor simulators and citations.

Simulator_switch	Model name, Citations
micro	Kummerow (1993)
radar	Masunaga & Kummerow (2005)
visir	RSTAR, Nakajima & Tanaka (1986, 1988)
lidar	Matsui et al. (2009)
broad	CliRad, Chou and Suarez (1994, 1999, 2001)
	MSTRN-X, Sekiguchi & Nakajima (2008)
	RRTMG, Iacono et al. (2008)
ease	EASE, Okamoto et al. (2007, 2008), Nishizawa et al. (2008)

Table 5.2.1. Ishimoto's data in unified non-spherical scattering database

Citation	Ishimoto (2008)
Method	Finite difference time domain method
Frequency (GHz)	36, 89, 95, 150
Temperature	250
Number of size parameters	9
Number of scattering angles	181
Number of phase function	6
Habits	3 aggregate models

Table 5.2.2. Liu's data in unified non-spherical scattering database

Citation	Liu (2008)
Method	Discrete dipole approximation
Frequency (GHz)	3, 5, 9, 10, 13.405, 15, 19, 24.1, 35.605, 50, 60, 70, 80, 85.5, 90, 94, 118, 150, 166, 183, 220, 340
Temperature	233.15, 243.15, 253.15, 263.15, 273.15
Number of size parameters	20
Number of scattering angles	37
Number of phase function	1
Habits	11 crystal habits: columns, plates, rosettes, sector snow-flakes, and dendrite snowflakes.

Table 5.2.3. Description of Liu's model and microwave simulator in the Joint-Simulator.

Citation	Liu's model	Joint-Simulator
Radiative transfer equation	Four-stream model (Liu 1998)	Eddington model (Kummerow 1993, two-stream model)
Scattering of non-spherical ice	Consideration of non-spherical ice particles based on DDA results (Liu 2008)	EASE simulator (94 GHz, lidar signals) has a database of non-spherical particles (Sato and Okamoto 2006; Okamoto et al. 2010) in the Joint-Simulator.
Surface emissivity over land	Using monthly climatological data with 0.25° resolution for seven-channel SSMI (Special Sensor Microwave Imager)	NESDIS land emissivity model in the Joint-Simulator (Weng et al. 2001)
Surface emissivity over ocean	1) Guillou et al. 1998 2) Klein & Swift 1977 3) Liu et al. 2009 (FASTERM-5)	Kummerow's model
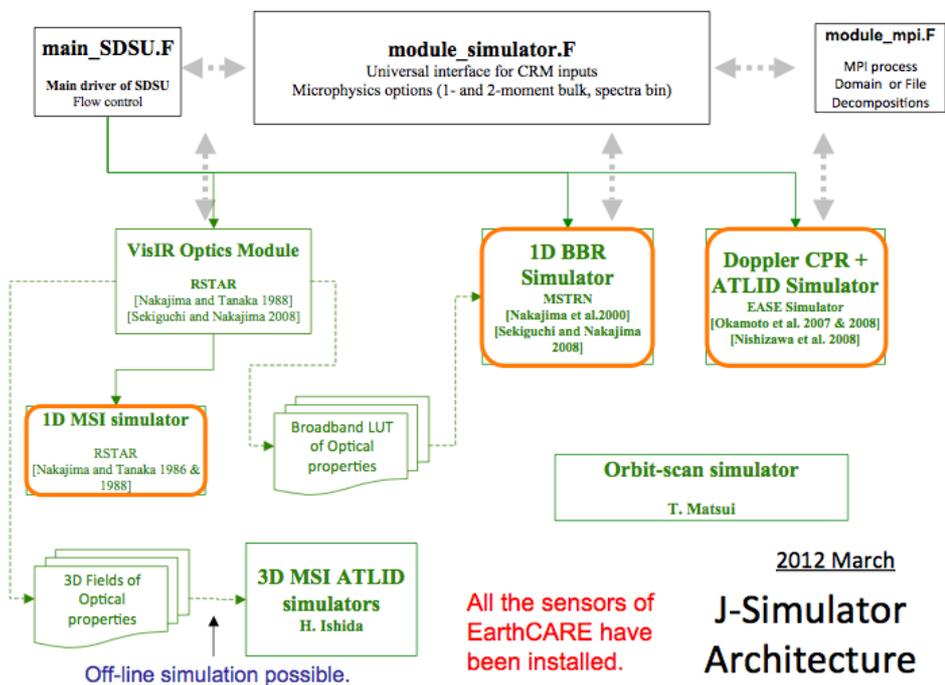
Fig. 5.1.1. Structure and simulator components of Joint-Simulator.
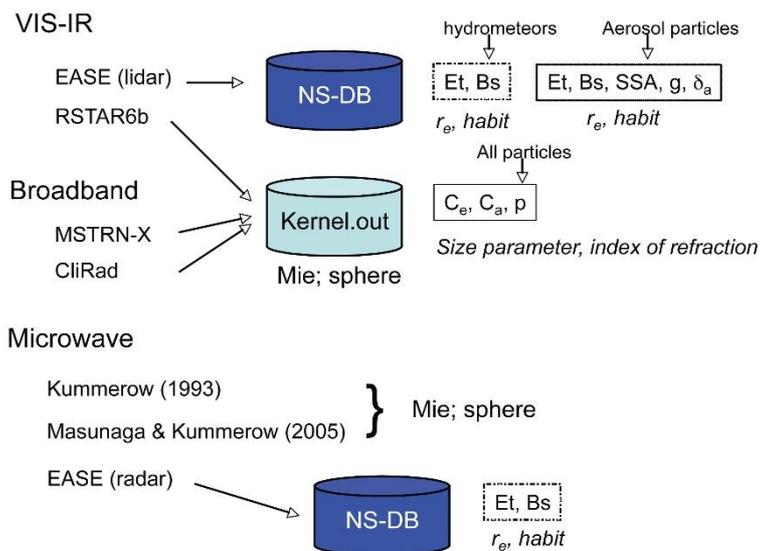
Fig. 5.1.2. Scattering library in Joint simulator.   Et: extinction coefficient, Bs: backscattering coeff., SSA: single scattering albedo, g: asymmetric parameter, d_a: depolarization ratio, C_e: extinction cross section, C_a: absorption cross section, p: phase function, r_e: effective radius.   NS-DB means non-spherical database.   The variables in the square box are tabulated in terms of the variables below.
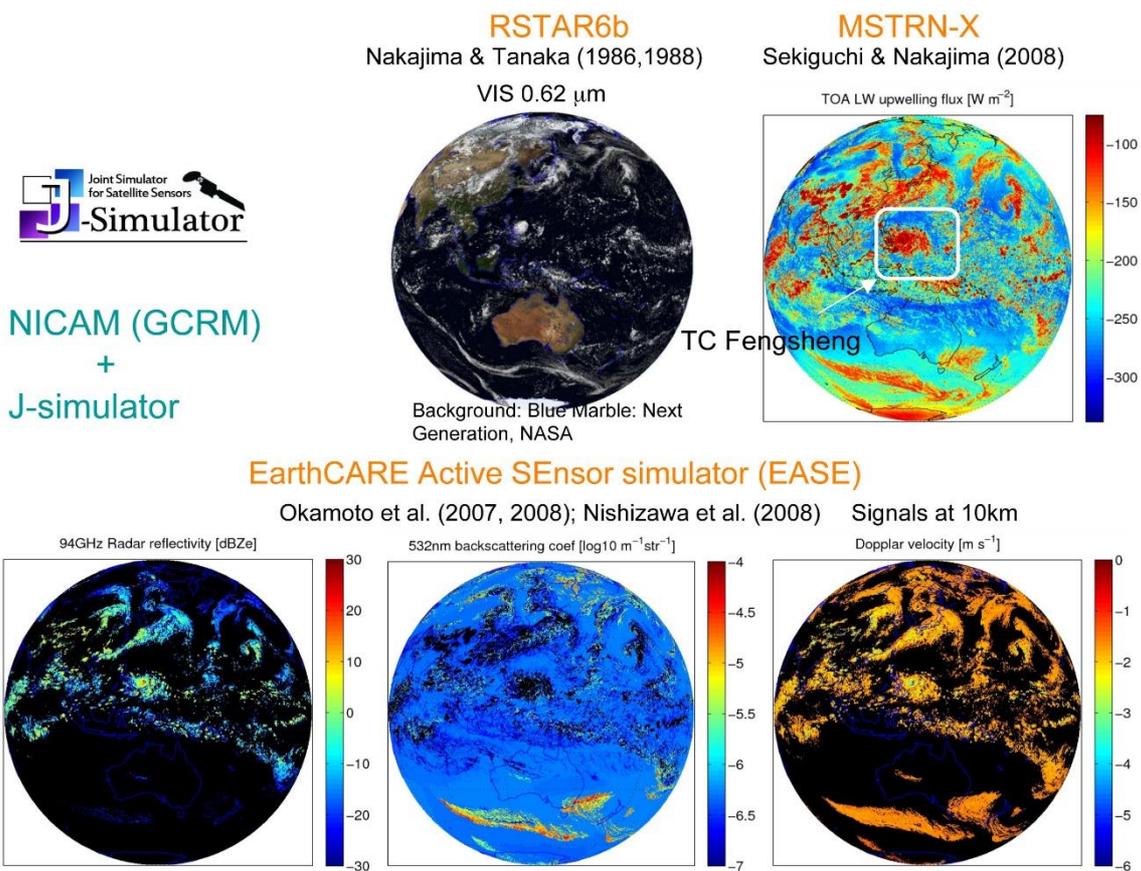
Fig. 5.2.1. Example of satellite observation simulated with Joint-simulator from a NICAM output. Upper panel left: simulated visible 0.62 μm with a blue marble: next generation, NASA, right: simulated TOA Longwave upwelling flux. Lower panel left: simulated 94 GHz radar reflectivity, middle: simulated 532 nm lidar backscattering co-efficient, and right: simulated Doppler velocity at 10 km.
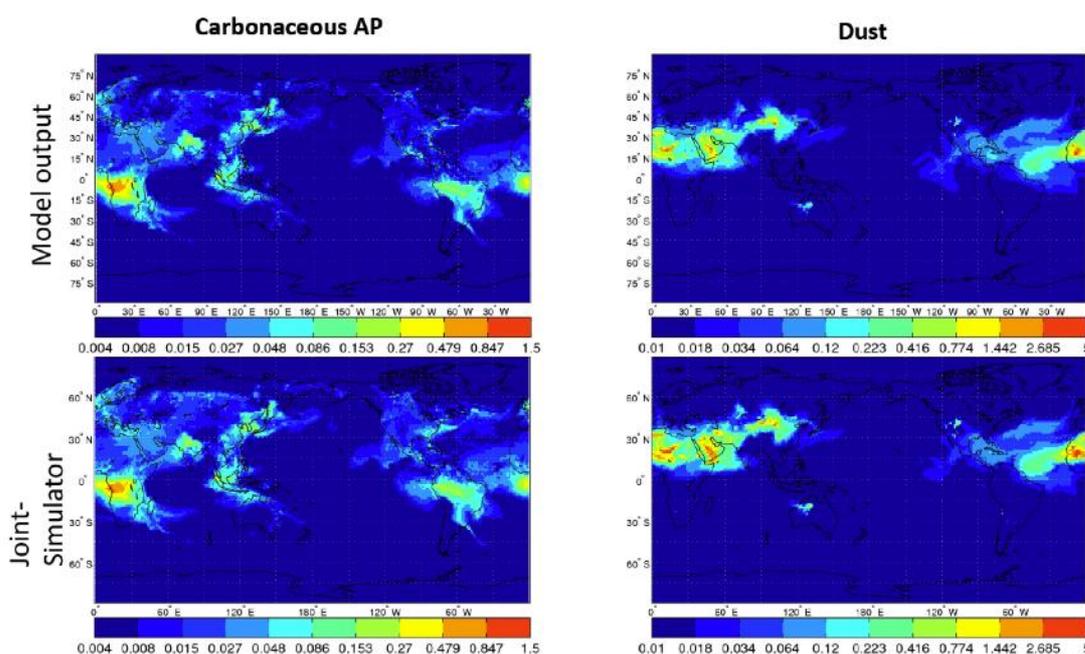
Fig. 5.2.2. Comparison of global distribution of aerosol optical depth (AOD) at 0.55 μm from NICAM-SPRINTARS (upper rows) and Joint-simulator output (bottom rows). The AOD of carbonaceous and dust particles are shown in left and right columns.
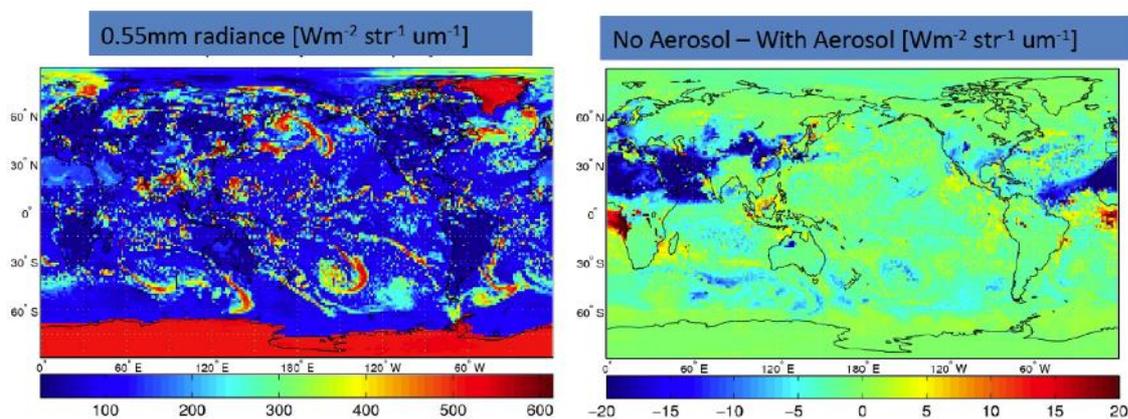
Fig. 5.2.3. 0.55 μm radiance simulated with RSTAR (left) including aerosol and clouds, and aerosol radiative forcing (right).
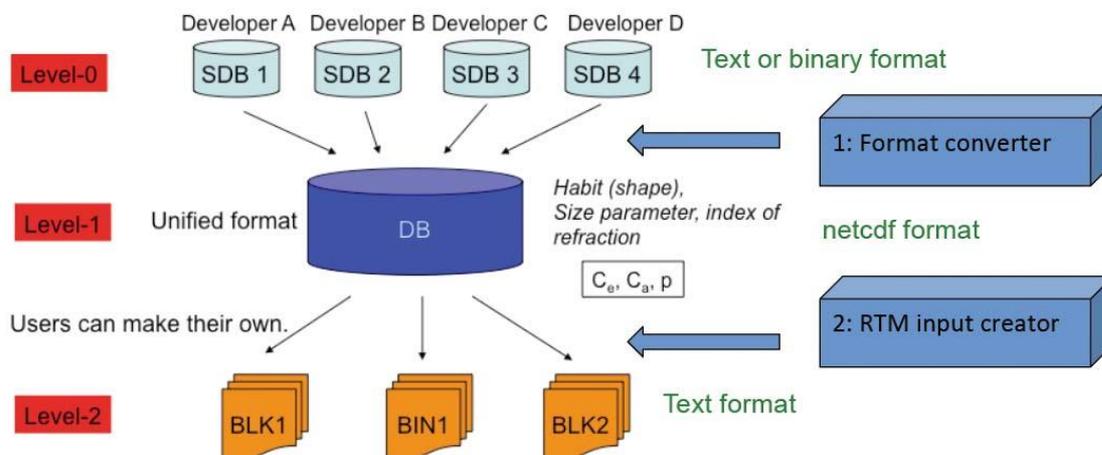
Fig. 5.2.4 Unified non-spherical scattering database.
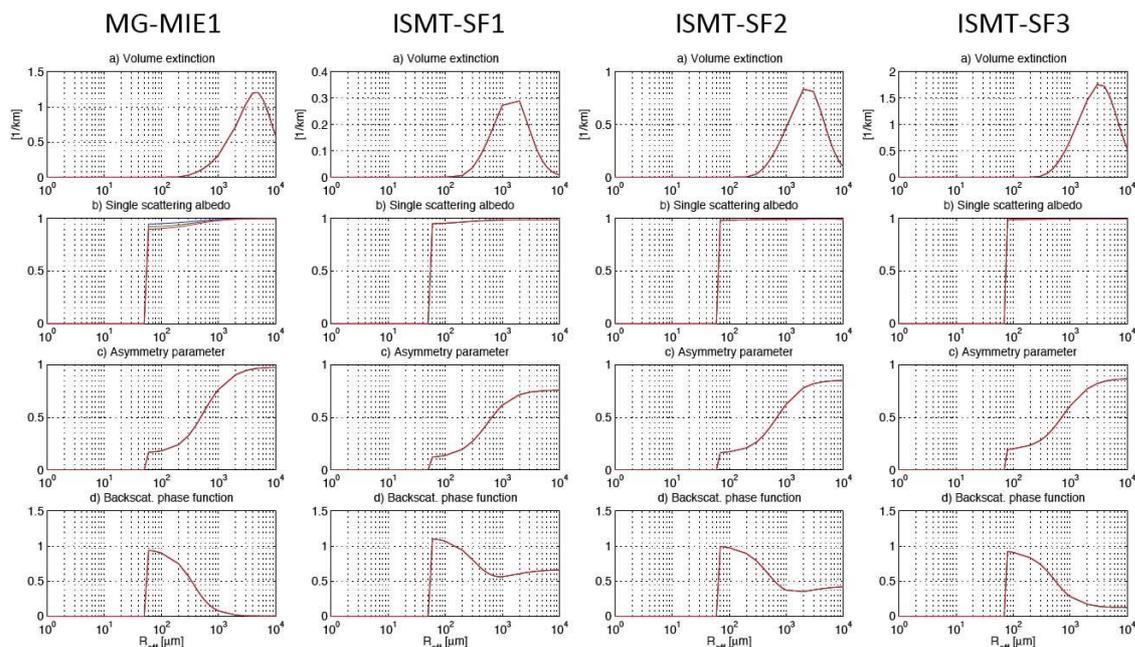
Fig. 5.2.5. Comparison of single scattering properties versus effective radius at 89 GHz. MG-MIE1 uses Mie sphere solution with Maxwell-Garnet mixing rule, and ISMT-SF1, SF2, SF3 are from Dr. Ishimoto's aggregate model with different fractal dimensions.
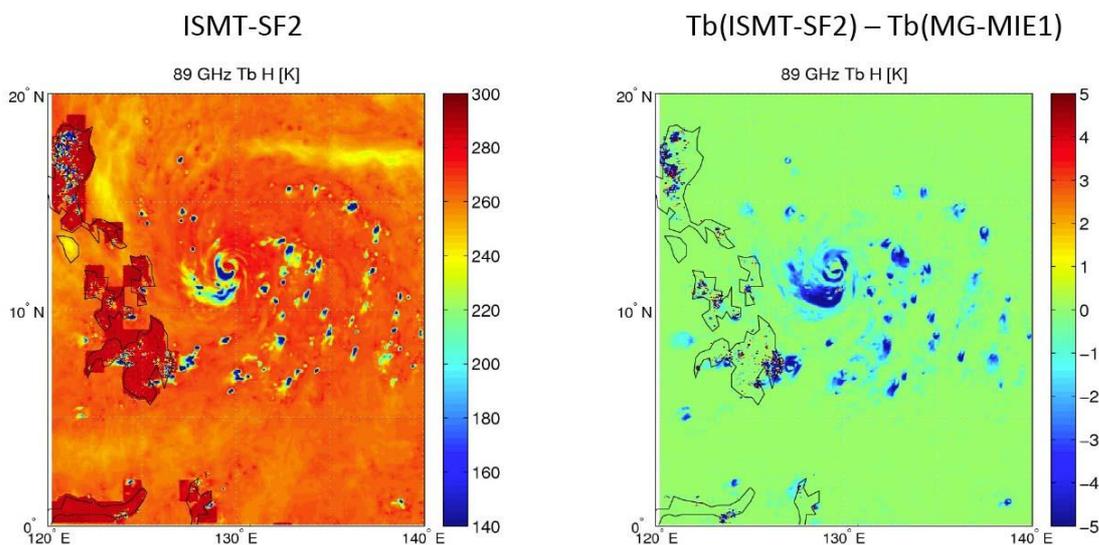
Fig. 5.2.6. Example of the sensitivity of scattering model on microwave brightness temperature.
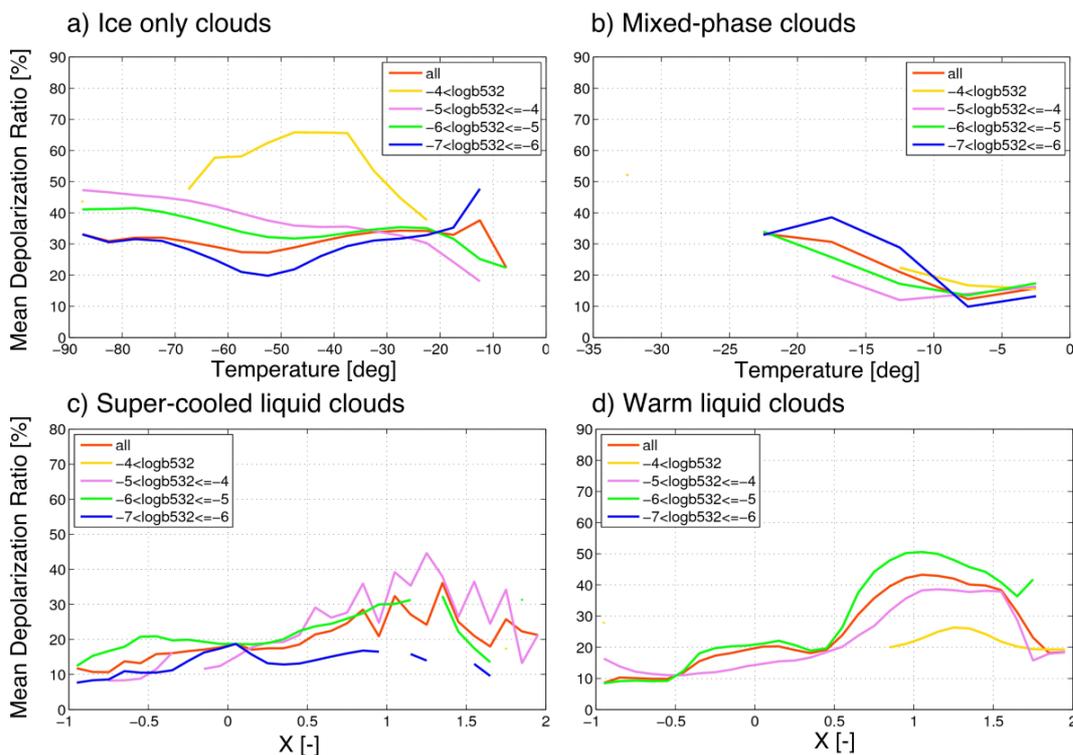
Fig. 5.2.7. Example of global averages of diagnosed depolarization for a) ice only clouds, b) mixed-phase clouds, c) super-cooled liquid clouds, and d) warm liquid clouds. X is proportional to the extinction between two consecutive layers.
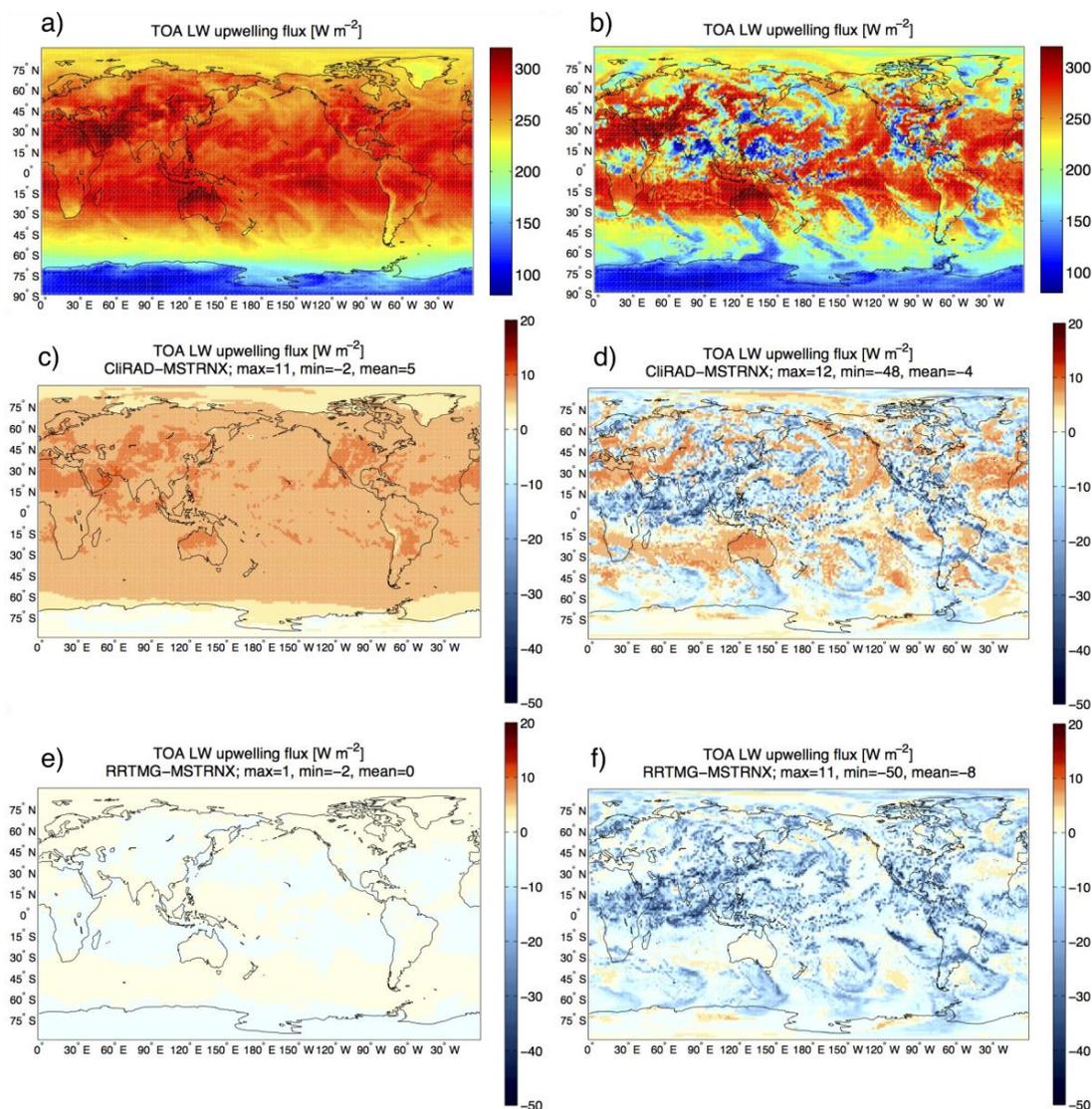
Fig. 5.2.8. Comparison of outgoing longwave flux at top of atmosphere simulated by MSTRNX, CliRAD, and RRTMG. The left column is for clear sky case, and the right column for full sky case. The fluxes by MSTRNX are shown in a) and b). Differences from MSTRNX are shown in c) and d) for CliRAD, and e) and f) for RRTMG.
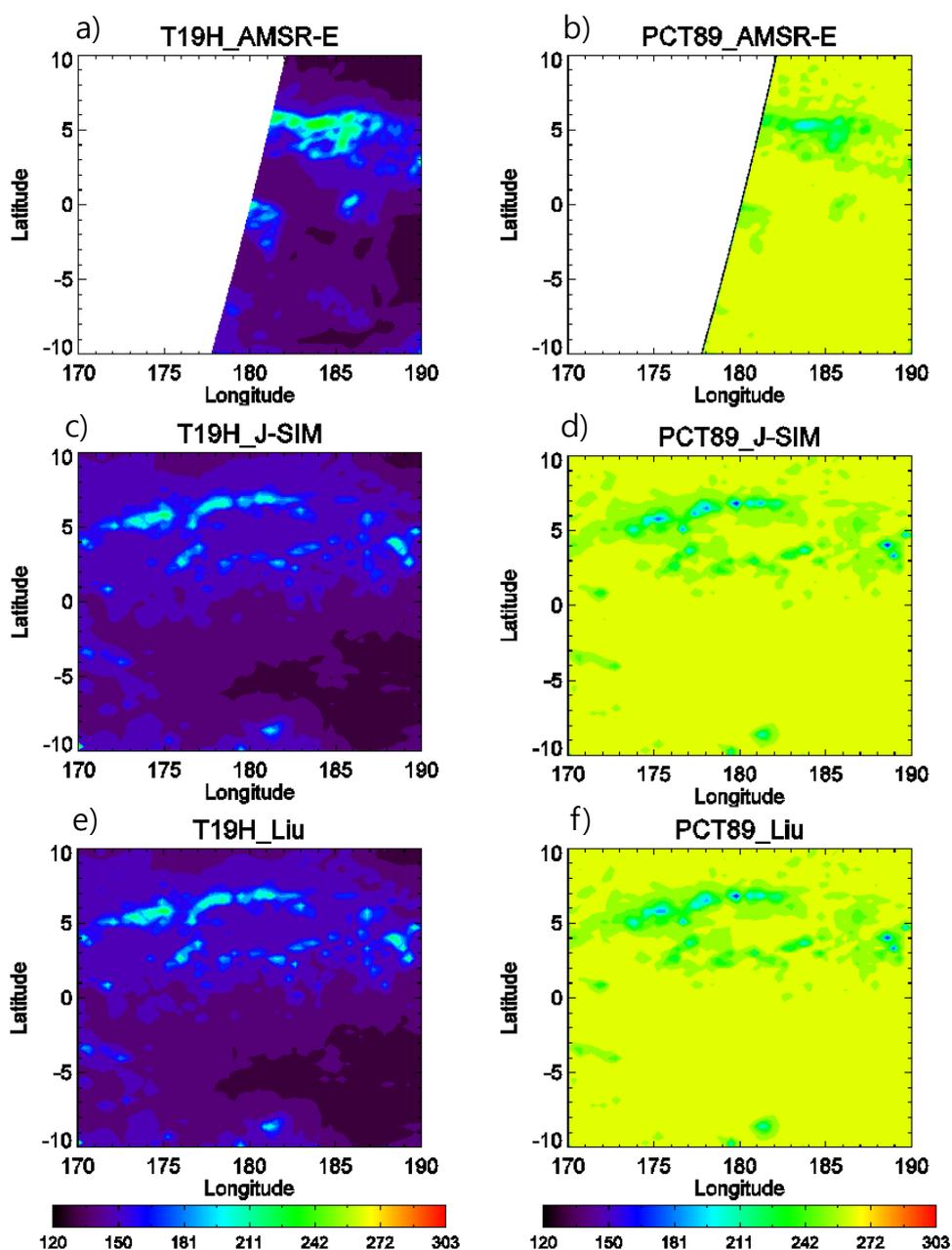
Fig. 5.2.9. Comparisons of brightness temperatures of microwave channels of AMSR-E, Joint-simulator, Liu's model on 12 UTC 2 January 2007 with a 38 km resolution. (a), (c), and (e) in the left column are 19 GHz horizontally polarized brightness temperatures (T19H). (b), (d), and (f) in the right column are 89 GHz polarization collected brightness temperatures (PCT89).

a)

b)
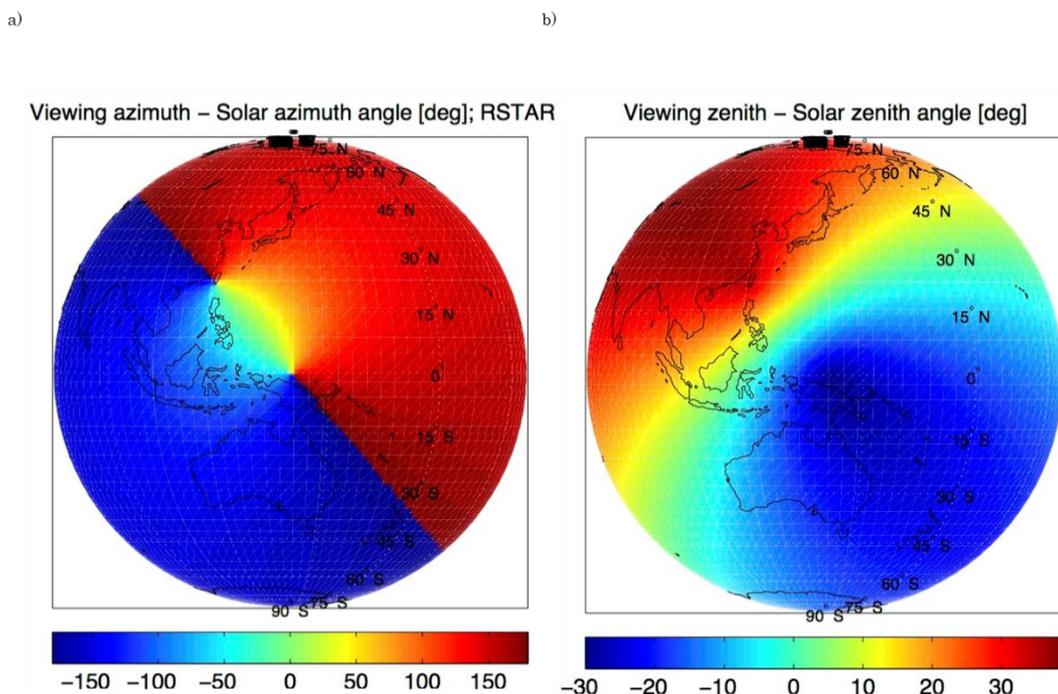
Fig. 5.2.10. Computed differences of azimuth and zenith angles between sensor and Sun.
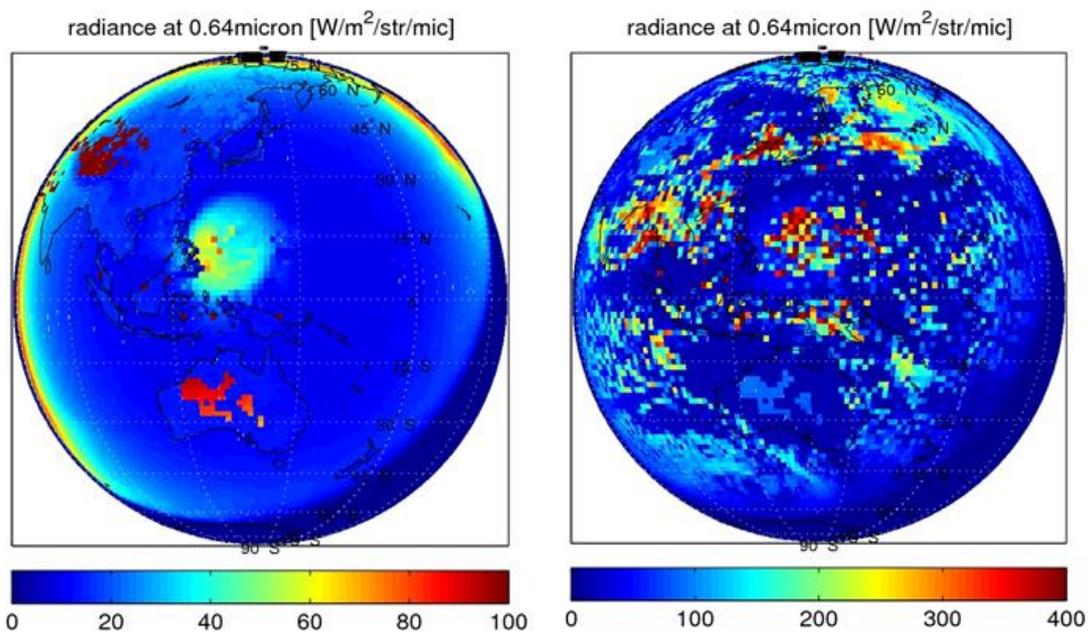
Fig. 5.2.11. Calculated radiance at 0.64 micron for Himawari 8.
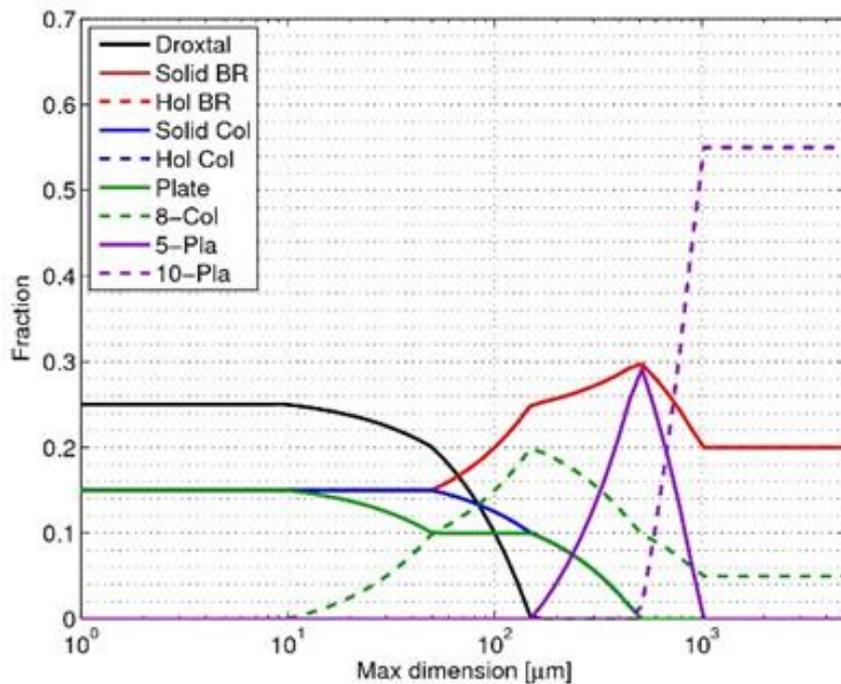
Fig. 5.2.12. Mixing model called GeneralMix3 provided by Dr. Baum.
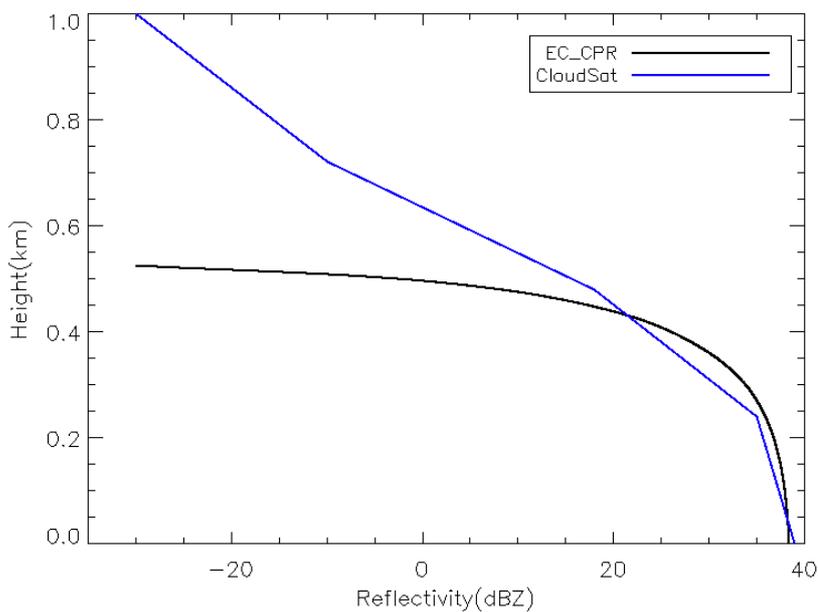
Fig. 5.2.13. Comparisons of surface clutters over the ocean between Cloudsat CPR and Earth-CARE CPR.
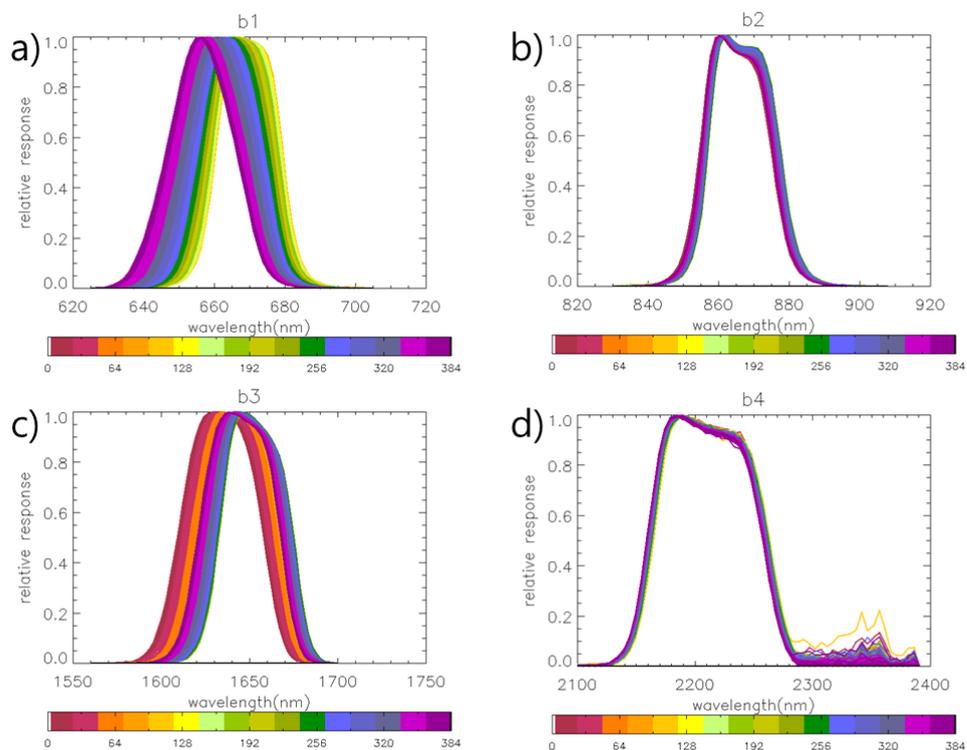
Fig. 5.2.14. The response functions for 0.67 (a), 0.865 (b), 1.65 (c), and 2.21 (d) μm channels in MSI. The contour is a cross-track pixel number.
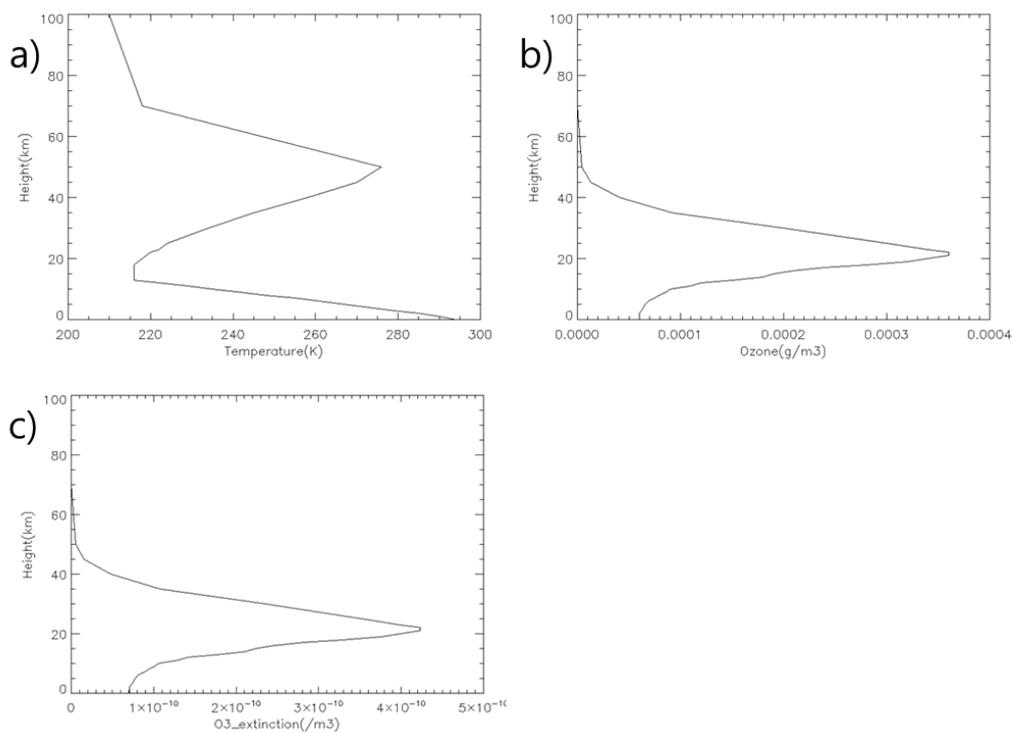
Fig. 5.2.15. A test of ozone module. Input of temperatures (a), input of ozone data, and output of extinctions of ATLID.
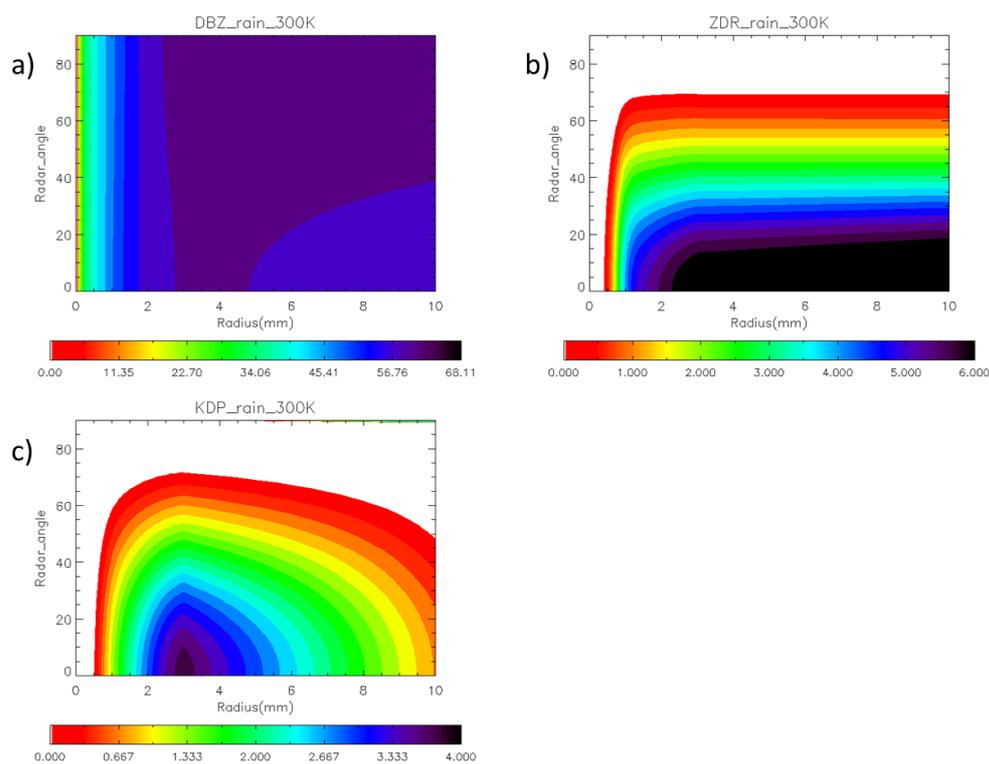
Fig. 5.2.16. The lookup table for ran for radar reflectivity (a), ZDR (b), and KDP (c) with 1 g/m3 at 300K in terms of radar angle (y-axis) and effective radius (x-axis).
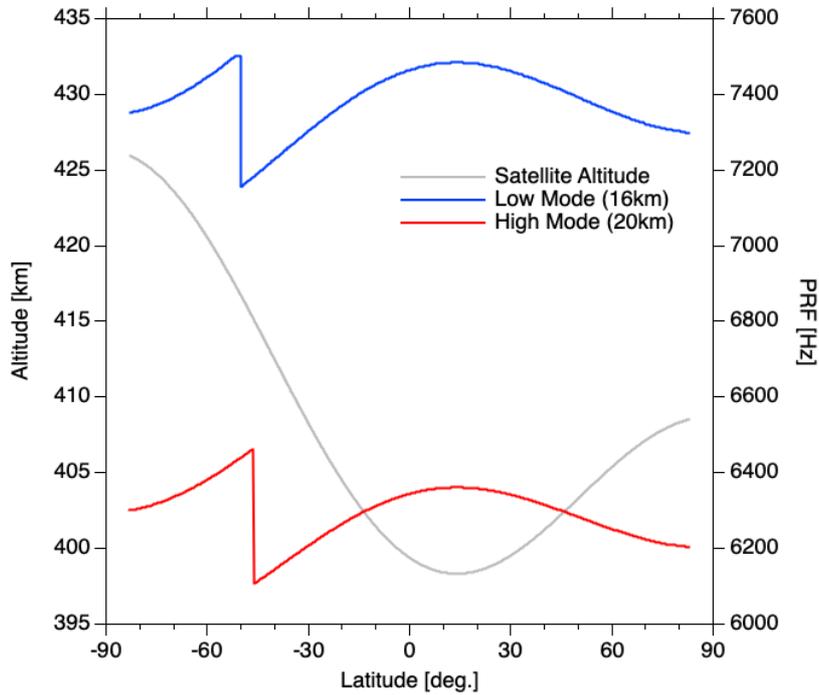
Fig. 5.2.17. The EarthCARE satellite altitude and PRF change of observation window with latitude.
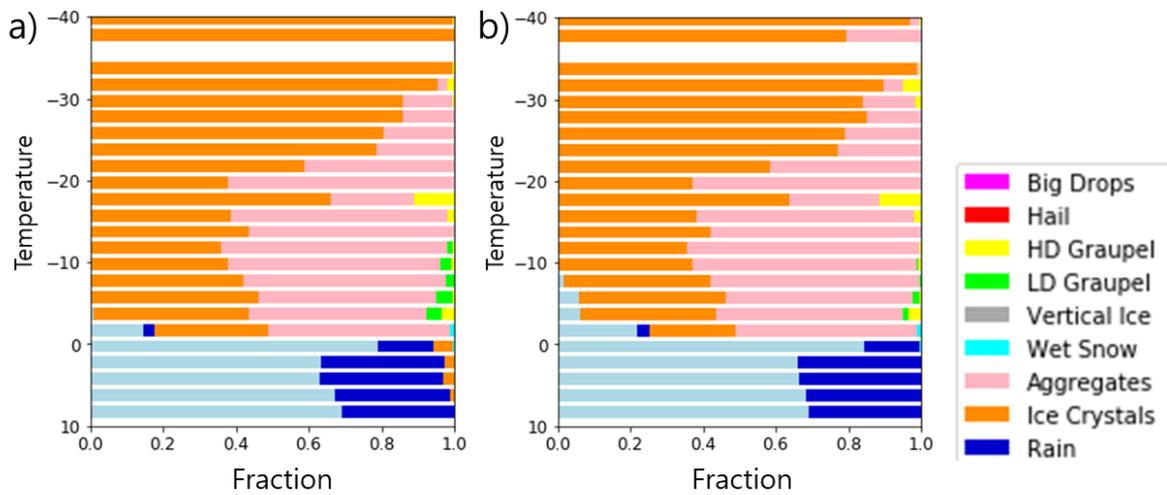
Fig. 5.2.18. Contoured Frequency by tEmperature Diagrams (CFED) of HID of iPOLARRIS (left) and CSU-tools (right) from NICAM simulation results in Narita airport on 18 UTC 15th Sep. 2019.

5.3 3D sensor simulators for EarthCARE

5.3.1 Background

Radiative transfer calculation in atmosphere is often carried out with an assumption that the atmosphere is uniform in horizontal, i.e., a one-dimensional structure (referred to as "plane-parallel") for simplifying the radiative transfer equation. This assumption is reasonable to a general atmosphere, especially without clouds, because the atmosphere always has the vertical structure but the horizontal structure is often homogenous. The retrieval algorithm of the cloud properties with MSI in Joint-simulator is also based on the plane-parallel assumption. However, some kinds of clouds, such as cumulus, sometimes have large horizontal inhomogeneity and must be considered to as a three-dimensional structure, making the plane-parallel assumption not appropriate. It is necessary for accurate calculation of radiances in the atmosphere with clouds to solve the radiative transfer equation dealing with three-dimensional structure.

Since the independent variables increases, radiative transfer in the three-dimensional atmosphere is more complicated and difficult to solve, compared to a plane-parallel case. Therefore, we plan to incorporate a radiative transfer calculation module in Joint-simulator in order to deal with the three-dimensional atmosphere and to estimate errors of radiances calculated with the plane-parallel assumption. The calculation method of this module is based on the Monte Carlo method, which is suitable and effective to calculate the radiance in the three-dimensional atmosphere. The basic algorithm of the Monte Carlo module has been developed by Iwabuchi (2006) and Iwabuchi and Kobayashi (2008), named as "MCARaTS". This program can carry out calculation of radiance on an arbitrary direction and an arbitrary position in the setting atmosphere, as well as radiative fluxes. We modify this program in order to fit measurements with sensors on satellite.

5.3.2 Algorithm description of MCARaTS

The Monte Carlo method consists on statistical calculation of photon transport. First, we set a photon packet (which is different to the term of physics) at the point of incident radiance, which corresponds to the sun for the case of solar radiation. The photon packet travels in the atmosphere and undergoes scattering and absorbing. The scattered intensity of radiance is statistically determined. For example, the ratio of scattering by cloud particles is calculated from its single scattering albedo. The direction of scattering is also statistically calculated according to the phase function of the cloud particle. The quantity of the photon packet reduces at each scattering or absorbing. If we deal with radiation including thermal emission, the quantity of the photon packet increases by emission, which is determined from the emissivity of objects (e.g., air molecular). The photon packet finally exits from the calculation area, containing information of the changes of intensity by scattering, absorbing, and emitting. Consequently, we can estimate the emittance, reflectance, and absorptance of a photon packet. If we iterate this sequence with a large number of photon packets and average these results, we can obtain probable emittance, reflectance, and absorptance.

The accuracy of calculation results primarily depends on a number of photon packets. An increase of photon packets causes an increase of calculation time: the accuracy and the calculation speed is trade-off. Before a radiance calculation, it is necessary to estimate a reasonable number to obtain reliable results of radiance, according to user demands, atmosphere settings, and intended satellite sensors. The spatial resolution of atmosphere setting and the resolution of radiance bin are

also important for the accuracy. The finer these resolutions, the more number of photon packets is required.

This calculation module for the three-dimensional atmosphere can deal with various atmosphere settings. Pixels in the atmosphere are assumed to be rectangular. An arbitrary vertical distribution of the absorption coefficient by molecular can be set, implying that the molecular concentration vertically changes but is spatially uniform. This absorption coefficient is to be prepared from another module in Joint-simulator based on the distributions of molecular. An arbitrary vertical and spatial distribution of the parameters of extinction by particles i.e., the scattering coefficient, the single scattering albedo, phase function, can be also set. These parameters have to be previously calculated according to the size distribution of particles, and electro-magnetic properties of material of the particles. In addition, the reflectance of the ground surface can be given by selecting some reflection models, e.g., the Lambert surface or a BRDF model, according to the kind of setting surface. The incident of the radiance is assumed to emit at some sources, which in general corresponds to the sun. The solar zenith angle and azimuth angle can be given and the intensity of solar incident radiance is determined.

We can set an arbitrary position of a sensor and its field of view. For a simulation of satellite observation, the radiance calculation by Monte Carlo method roughly corresponds to counting the number of photons (packets) that enter in the bin of the sensor. The number of photons varies with the direction of the sensor. The zenith and azimuth angle of the sensor can be given arbitrarily.

5.3.3 Examples

An example of calculation for three-dimensional atmosphere is shown. We simulate a certain scene observed by MSI, i.e., the reflected radiances of solar radiation. Fig. 5.3.3.1 (a) is the spatial distribution of optical thickness of clouds, generated with an atmospheric model, and (b) is the spatial distribution of reflected radiance. The sun locates at the left-hand side of the figure, with the zenith angle of 60˚ and the azimuth angle from the x-axis of 0˚. The wavelength is 0.67 μm. Clouds consist of only water particles. The reflectance of surface is assumed to be nothing. Here we only present the half of the swath of MSI, assuming that the nadir of MSI locates at 0 km of x in the figure. The radiances are calculated for each pixel, which implies that this is an expected result for an observed scene by MSI. In order to extract the effects of three-dimensional structure for radiance transport, we compare the result to the ICA calculation, which means that each column in the setting atmosphere is assumed to be plane-parallel. In other words, ICA calculation ignores the horizontal transport of radiance, corresponding to the case of radiance calculation for MSI with RSTAR6b. Fig. 5.3.3.2 is the difference between the three-dimensional case and the ICA case. This result shows that the underestimation by ICA remarkably appears at the gaps between clouds, which indicates that a clear-sky pixel sometimes obtain reflection effects due to radiances from surrounded clouds.

Reference

Iwabuchi, H., 2006: Efficient Monte Carlo methods for radiative transfer modeling. Journal of the
    Atmospheric Sciences, 63, No. 9, 2324-2339.

Iwabuchi, H., and H. Kobayashi, 2008: Modeling of radiative transfer in cloudy atmospheres and
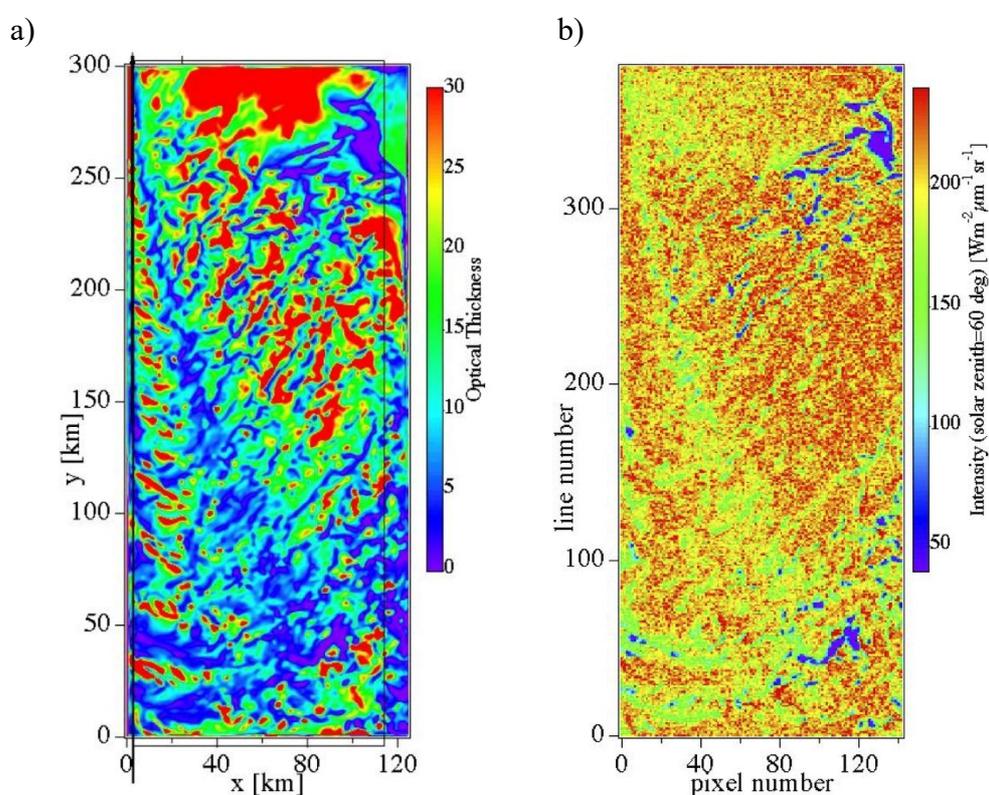   plant canopies using Monte Carlo methods. FRCGC Technical Report No. 8, 199 pp, 2008.

a) b)

Fig. 5.3.3.1. An example of radiance calculation by the Monte Carlo Method. (a)
the optical thickness of clouds, (b) the reflected upward radiances of solar radiance
at the wavelength of 0.67 μm.
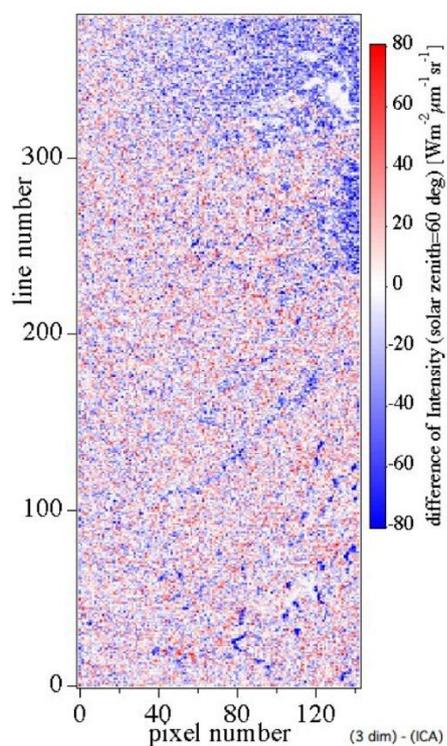
Fig. 5.3.3.2. The difference in intensities between a three-dimensional case and a ICA case. Blue (Red) means the radiances of three-dimensional case is smaller (larger) than those of ICA case.

6. ECMWF-AUX

6.1. Development of ECMWF-AUX processors

ECMWF-AUX processors, developed by the JAXA Earth Observation Research Center (EORC), interpolate meteorological field data from global model data from the European Centre for Medium-Range Weather Forecasts (ECMWF) to EarthCARE Level-2 (L2) grids. The ECMWF-AUX products generated by the processors are divided into two types: (1) public data (AUX-2D, AUX-3D) intended for combined analysis with sensor products, and (2) non-public data intended for uses of meteorological field data in JAXA's L2 processing.

The ECMWF-AUX processors input the X-MET product by ESA. Eisinger et al. (2024) described the X-MET as follows.

The X-MET processor generates the EarthCARE meteorological product, X-MET, using meteorological fields selected from output of the ECMWF Integrated Forecasting System in its highest resolution configuration and subsetting them to the EarthCARE swath, while keeping them on the original model grid.

Horizontal grid. Parameters are provided on ECMWF model grid points, which is a reduced Gaussian grid. ECMWF uses an octahedral grid, with a resolution between 8 and 10 km, and a total number of 6.59 million grid points.

Vertical grid. Pressure and geometric altitude on model levels are provided in X-MET for each point of the horizontal grid, which enables interpolation/conversion from model levels to pressure or altitude coordinates.

On the other hand, the L2 algorithm basically uses a grid system based on footprints and vertical range bins defined by the EarthCARE sensors. ESA processes the EarthCARE Joint Standard Grid product (X-JSG) from the geolocation in ATLID and CPR level 1b products (Eisinger et al. 2024). To use meteorological field data in the L2 algorithm, it is necessary to interpolate the meteorological field data from the model grid in the X-MET to the L2 grid in the X-JSG.

Thus, the ECMWF-AUX algorithms input the X-MET and the X-JSG and interpolates meteorological field data onto the X-JSG geometry. The ECMWF-AUX products generated by these processors are divided into two-dimensional (2D) and three-dimensional (3D) products depending on the geometry handled by each L2 algorithm.

6.2. Overview of ECMWF-AUX processors and products

An overview of ECMWF-AUX processors and products is shown in Table 6.2-1. The ECMWF-AUX products are generated through three different processors (ECMWF-AUX-2D, ECMWF-AUX-3D-MSI, and ECMWF-AUX-3D-JSG). The publicly released products are AUX-2D and AUX-3D. The public products (AUX-2D and AUX-3D) are archived with reduced data volumes. In addition to these, the processors generate three non-public products: AUX-2DH, AUX-3MH, and AUX-3JH, which are used as inputs for the JAXA's L2 algorithms described in Sections 3 and 4.

Table 6.2-1 ECMWF-AUX specifications. The public products (AUX-2D and AUX-3D) are shown with light blue backgrounds.

Processor name	ECMWF-AUX-2D				ECMWF-AUX-3D-MSI				ECMWF-AUX-3D-JSG	
Product name	AUX-2DH		AUX-2D		AUX-3MH		AUX-3D		AUX-3JH	
Public or Non-public	Non-public (for L2 processing)		Public		Non-public (for L2 processing)		Public		Non-public (for L2 processing)	
Grid H: Horizontal V: Vertical	H	V	H	V	H	V	H	V	H	V
	X-JSG & ATLID	X-JSG	X-JSG	X-JSG	MSI L1c（10km-interval）	X-MET	X-JSG（10km-interval）	Lower 25-layers in X-MET	X-JSG	X-JSG

The ECMWF-AUX-2D processor outputs AUX-2DH (for the L2 processing) and AUX-2D (for public release). AUX-2DH stores data interpolated onto a two-dimensional grid extending to an altitude of approximately 80 km based on the X-JSG nadir grid and ATLID sampling. The public AUX-2D product stores variables on a two-dimensional grid (satellite orbit direction x vertical direction) extracted from the X-JSG nadir grid. AUX-2DH and AUX-2D also store variables on one-dimensional grids based on surface and integrated geophysical quantities.

ECMWF-AUX-3D-MSI processor outputs AUX-3MH (for the L2 processing) and AUX-3D (for public release). AUX-3MH is a 3D grid based on the horizontal sampling of MSI L1c and the altitude profile of X-MET, with the horizontal grid composed of 10km intervals to reduce data volume. AUX-3D is a 3D grid based on the horizontal grid of 10km intervals based on X-JSG and the lower 25 layers of the altitude profile of X-MET. AUX-3MH and AUX-3D also store 2D grid variables based on surface and integrated geophysical quantities.

ECMWF-AUX-3D-JSG processing uses the AUX-3JH for the L2 processing, and its sampling is based on X-JSG, with data stored in a three-dimensional grid that is limited to within 20 km on either side of the nadir in the across-track direction and extends to approximately 80 km in the vertical direction.

Images of the publicly available AUX-2D and AUX-3D data storage is shown in Figure 6.2-1.
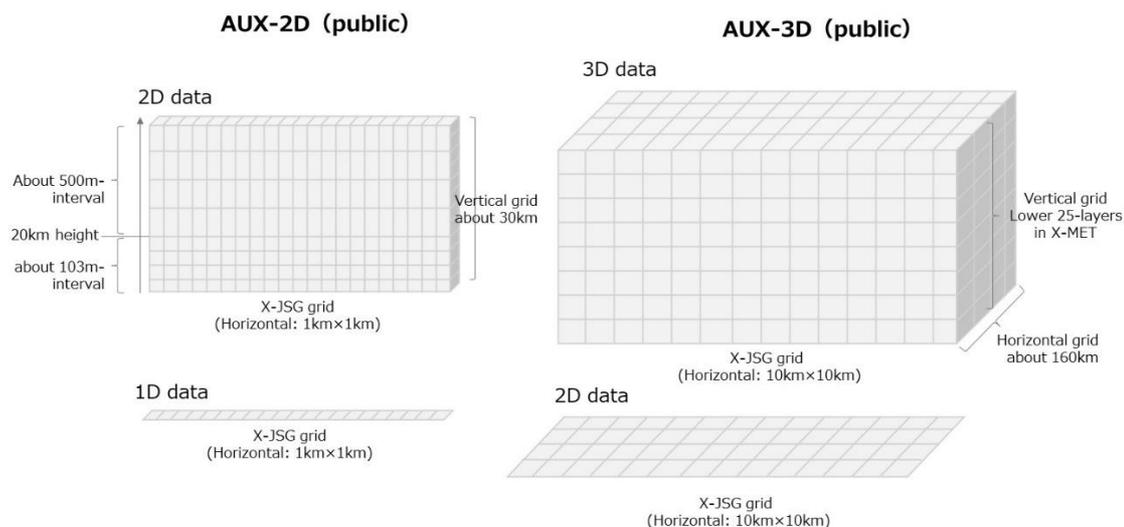
Figure. 6.2-1 Images of the publicly available AUX-2D and AUX-3D stored data. The number of pixels does not match the actual number of data. The altitude of the AUX-3D is defined by the X-MET model level, so in reality it curves to the terrain.

6.3. Details of the interpolation method used in ECMWF-AUX

The process of interpolating the X-MET meteorological field data onto the X-JSG geometry is basically linear interpolation. The details of the method are described in this section.

In the horizontal dimension, the ECMWF grid is based on latitude and longitude, so interpolation is performed in latitude-longitude space. On the other hand, in the reduced Gaussian grid of the ECMWF model, the grid point spacing in the longitude direction is coarser at higher latitudes in order to make the path along the longitude of one grid as equal as possible, as shown in Figure 6.3-1. For this reason, the unit cell is generally not rectangular

In the meridian direction, the grid points are aligned at the same latitude. Therefore, intermediate interpolation points (open square points in Figure 6.3-2) with the same longitude as X-JSG are set at the top and bottom of the X-MET longitude grid with an internal division ratio of (t1, t2) , and the physical quantities at these two intermediate interpolation points are further interpolated in the latitude

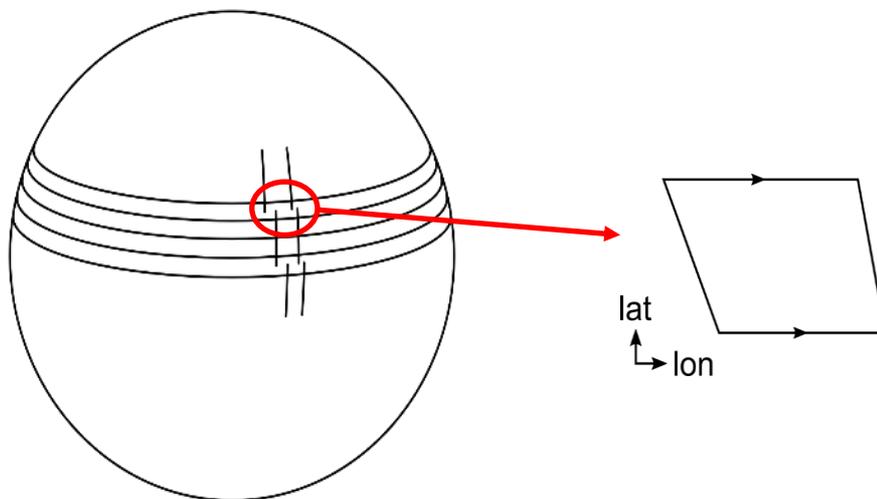direction to calculate the physical quantities at the X-JSG grid points (see Figure 6.3-2) .

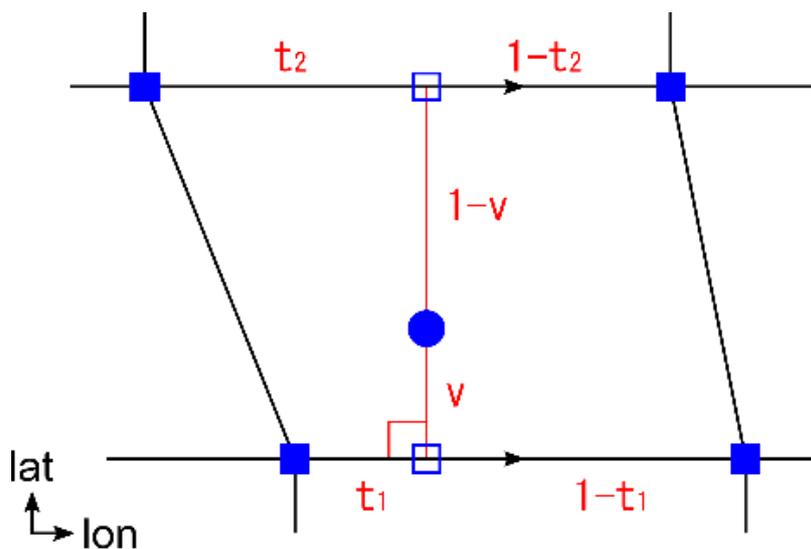Figure 6.3-1. Reduced Gaussian grid

Figure 6.3-2. ECMWF-AUX horizontal interpolation

The physical quantity p at the target point described in Fig. 6.3-2 is calculated as follows:

$$p = (1-t1)(1-u)p11 + t1(1-u)p21 + u(1-t2)p12 + t2up22 \quad (6.3\text{-}A)$$

For the vertical dimension, X-MET gives geometrical height, while X-JSG gives altitude, but these are aligned to geodetic height starting from WGS84 (World Geodetic System 1984), so interpolation is performed on this scale. However, since the model level is stretched or contracted depending on the terrain as shown in Figure 6.3-3, the unit cell is generally not rectangular.

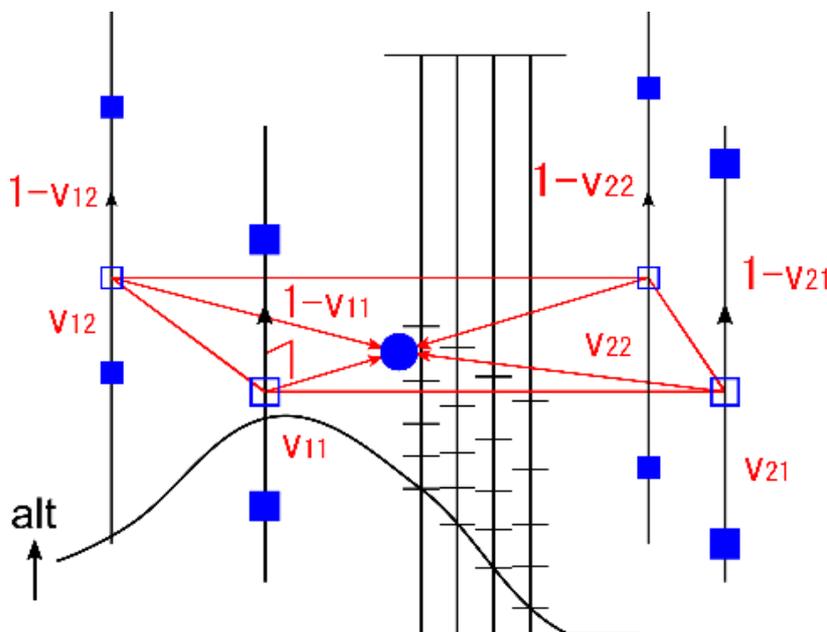Figure 6.3-3. Grid based on the ECMWF model level

Figure 6.3- 4. ECMWF-AUX spatial interpolation

Since both latitude and longitude are fixed in the vertical direction, as with horizontal interpolation, four intermediate interpolation points (open square points in Figure 6.3.4) at the same altitude as X-JSG are set on each vertical line of X-MET , and the physical quantities of the X-JSG grid points are obtained by applying the horizontal interpolation described above to these points (see Figure 6.3-4).

The interpolated physical quantity p at the target point described in Figure 6.3-4 is calculated as follows:

$$p = (1-t1)(1-u)(1-v11)p111 + (1-t1)(1-u)v11p112 \\ + t1(1-u)(1-v12)pij121 + t1(1-u)v12p122 \\ + u(1-t2)(1-v21)p211 + u(1-t2)v21p212 + t2u(1-v22)p221 + t2uv22p222$$

(6.3-B)

Based on these methods, three-dimensional physical quantities are calculated by interpolation using equation (6.3-B), and surface and integrated physical quantities are calculated by interpolation using equation (6.3-A).

Figures 6.3-5 and 6.3-6 show an example of a comparison between ECMWF -AUX and X-MET for temperature, a typical parameter of meteorological field data . AUX-2D (Figure 6.3-5) and AUX-3D

(Figure 6.3-6) show a basic spatial pattern of warm temperatures in the lower layers and cold temperatures in the upper layers, confirming that the ECMWF-AUX interpolation process is working correctly.
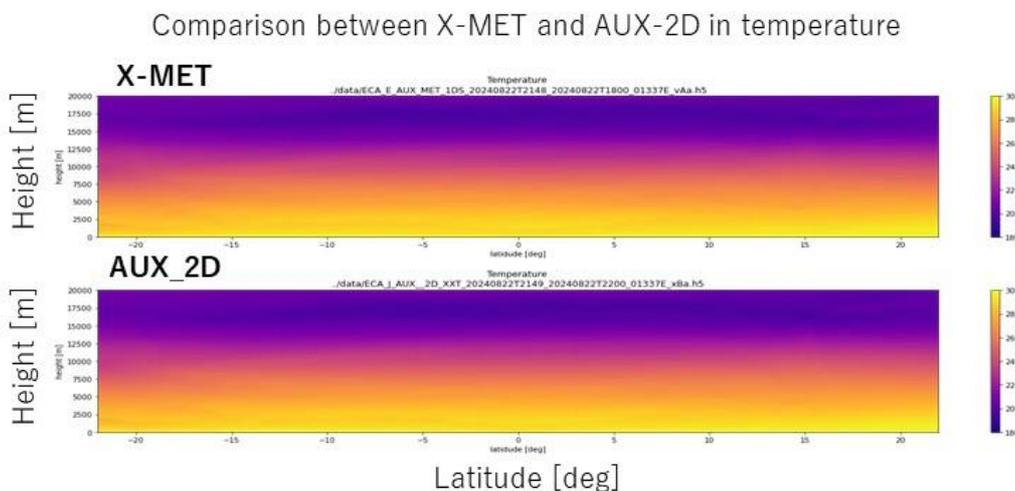

Figure 6.3.-5. Latitude -altitude cross section of temperature. Temperature distribution when the EarthCARE satellite passed by at around 21:48 on August 22, 2024. Top) X-MET, bottom) AUX-2D. Orbit number is 0 1337E. The unit of the figure is K.
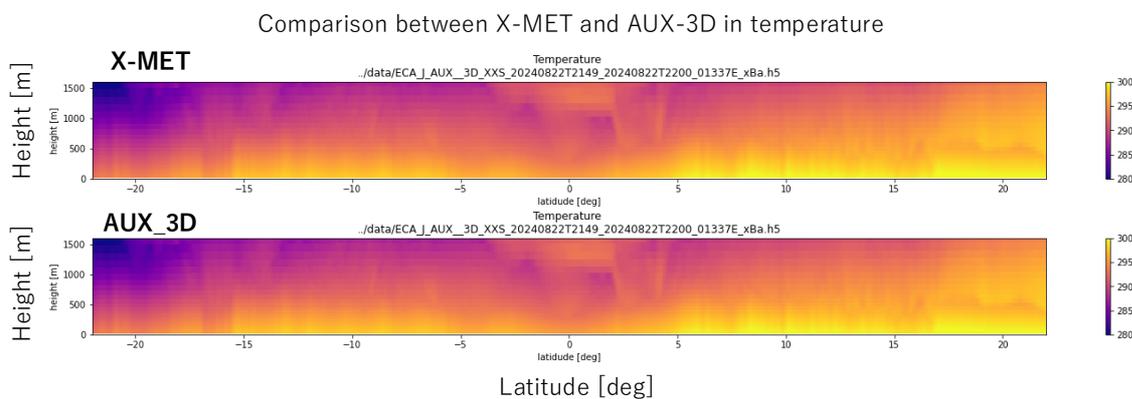

Figure 6.3-6. Latitude -altitude cross section of temperature . Temperature distribution when the EarthCARE satellite passed by at around 22:00 on August 22, 2024. Top) X-MET, bottom) AUX-3D. Orbit number is 0 1337E. The unit of the figure is K.

Reference:

Eisinger, M., Marnas, F., Wallace, K., Kubota, T., Tomiyama, N., Ohno, Y., Tanaka, T., Tomita, E., Wehr, T., and Bernaerts, D.: The EarthCARE mission: science data processing chain overview, Atmos. Meas. Tech., 17, 839–862, https://doi.org/10.5194/amt-17-839-2024, 2024.